

H124/3491

MONASH UNIVERSITY
THESIS ACCEPTED IN SATISFACTION OF THE
REQUIREMENTS FOR THE DEGREE OF
DOCTOR OF PHILOSOPHY

ON..... 20 December 2002

JCV Sec. Research Graduate School Committee

Under the copyright Act 1968, this thesis must be used only under the normal conditions of scholarly fair dealing for the purposes of research, criticism or review. In particular no results or conclusions should be extracted from it, nor should it be copied or closely paraphrased in whole or in part without the written consent of the author. Proper written acknowledgement should be made for any assistance obtained from this thesis.

IN-SITU STRUCTURAL HEALTH MONITORING OF COMPOSITE REPAIR PATCHES

by

Yeow Leung Koh B.Com B.E. (Hons)

**This thesis is submitted in the fulfilment of the requirements for the
degree of Doctor of Philosophy**

**Department of Mechanical Engineering
Monash University, Clayton,
Victoria, Australia**

June 2002

TABLE OF CONTENTS

SUMMARY	I
DECLARATION.....	III
ACKNOWLEDGEMENT.....	IV
NOMENCLATURE.....	V
CHAPTER 1	1
INTRODUCTION	1
CHAPTER 2	8
LITERATURE REVIEW	8
2.1 INTRODUCTION	8
2.2 COMPOSITE REPAIR PATCHES	9
2.2.1 <i>General background</i>	10
2.2.2 <i>Properties of bonded composite repairs</i>	11
2.2.3 <i>Recent successful applications of composite repairs</i>	17
2.3 DISBOND OF COMPOSITE REPAIR PATCHES	20
2.3.1 <i>History of composite patch disbond</i>	21
2.3.2 <i>Types and location of disbonds</i>	22
2.4 IMPACT DAMAGE OF COMPOSITE REPAIR PATCHES	23
2.5 EXISTING NDE METHODS FOR DAMAGE DETECTION	26
2.5.1 <i>Non structural parameter based analysis for non destructive evaluation</i>	26
2.5.2 <i>Wave based analysis for non destructive evaluation</i>	28
2.5.3 <i>Vibration based analysis for non destructive evaluation</i>	32
2.6 THREE POSSIBLE EXISTING METHODS FOR MONITORING THE STATED PROBLEMS	36
2.6.1 <i>The practical excitation and measurement of electromechanical impedance method</i>	36
2.6.2 <i>The practical excitation and measurement of transfer function method</i>	40
2.6.3 <i>The practical excitation and measurement of stress wave method</i>	42
2.7 PIEZOELECTRIC TRANSDUCERS	45
2.7.1 <i>Mechanical properties of piezoelectric materials</i>	46
2.7.2 <i>Applications of piezoelectric materials</i>	48
2.8 OBJECTIVES OF THE PRESENT INVESTIGATION	49
CHAPTER 3	51
EXPERIMENTAL METHODS	51
3.1 INTRODUCTION	51
3.2 SOURCE OF MATERIAL	52
3.3 SET-UP FOR THE ACQUISITION OF ELECTROMECHANICAL IMPEDANCE	54
3.4 SET-UP FOR THE ACQUISITION OF SYSTEM TRANSFER FUNCTION	56
3.5 SET-UP FOR THE ACQUISITION OF STRESS WAVE	59

3.6	SPECIMEN PREPARATION FOR IMPEDANCE METHOD AND TRANSFER FUNCTION METHOD	62
3.6.1	<i>Static experiments</i>	64
3.6.2	<i>Fatigue experiments</i>	67
3.7	SPECIMEN PREPARATION FOR STRESS WAVE METHOD	70
3.7.1	<i>Test rig</i>	70
3.7.2	<i>Specimens</i>	74
3.8	DEGRADATION OF PIEZOCERAMIC TRANSDUCERS	77
3.8.1	<i>Specimen preparation</i>	77
3.8.2	<i>Experimental equipment</i>	81
3.8.3	<i>Results and discussion</i>	84
3.9	CONCLUDING REMARKS	88
CHAPTER 4	90
	NUMERICAL MODELLING	90
4.1	INTRODUCTION	90
4.2	VALIDATION OF FINITE-ELEMENT MODEL FOR IMPEDANCE METHOD AND TRANSFER FUNCTION METHOD	91
4.3	VALIDATION OF FINITE-ELEMENT MODEL FOR SOLVING STRESS WAVE METHOD	94
4.3.1	<i>Dispersion curve and deflected shapes</i>	95
4.3.2	<i>Description of finite element model</i>	96
4.3.3	<i>Results and discussion</i>	99
4.4	CONCLUSIONS	102
CHAPTER 5	103
	EVALUATION OF THE IMPEDANCE METHOD USING NUMERICAL ANALYSIS	103
5.1	INTRODUCTION	103
5.2	BACKGROUND THEORY	104
5.3	PRELIMINARY SIMULATION STUDY	106
5.3.1	<i>Model development</i>	106
5.3.2	<i>Results and discussion</i>	108
5.4	MODELLING COMPLEX DISBOND TYPES	112
5.4.1	<i>Data analysis</i>	112
5.4.2	<i>Model development</i>	113
5.4.3	<i>Results and discussion</i>	116
5.5	CONCLUSIONS	121
CHAPTER 6	123
	EXPERIMENTAL EVALUATION OF THE IMPEDANCE METHOD	123
6.1	INTRODUCTION	123
6.3	STATIC TESTING WITH BORON/EPOXY REPAIR PATCH	125
6.3.1	<i>Experimental procedures</i>	126
6.3.2	<i>Results and discussion</i>	127
6.4	STATIC TESTING WITH GLASS FIBRE-REINFORCED PLASTIC REPAIR PATCH	129
6.4.1	<i>Experimental procedures</i>	130
6.4.2	<i>Data analysis</i>	131
6.4.3	<i>Results and discussion</i>	132

6.5	FATIGUE TESTING	136
6.5.1	<i>Experimental procedures</i>	136
6.5.2	<i>Results and discussion</i>	139
6.6	CONCLUSIONS.....	143
CHAPTER 7	144
EVALUATION OF THE TRANSFER FUNCTION METHOD USING NUMERICAL ANALYSIS		144
7.1	INTRODUCTION	144
7.2	BACKGROUND THEORY AND ANALYSIS	145
7.2.1	<i>Data analysis</i>	146
7.2.2	<i>Mathematical model</i>	147
7.3	PRELIMINARY SIMULATION STUDY	149
7.3.1	<i>Model development</i>	149
7.3.2	<i>Results and discussion</i>	152
7.3.3	<i>Comparing numerical analysis to the mathematical model</i>	162
7.4	MODELLING COMPLEX DISBOND TYPES.....	164
7.4.1	<i>Model development</i>	164
7.4.2	<i>Results and discussion</i>	167
7.5	CONCLUSIONS.....	173
CHAPTER 8	175
EXPERIMENTAL EVALUATION OF THE TRANSFER FUNCTION METHOD		175
8.1	INTRODUCTION	175
8.2	BACKGROUND THEORY	176
8.3	STATIC EVALUATION WITH BORON/EPOXY REPAIR PATCH.....	178
8.3.1	<i>Experimental procedures</i>	179
8.3.2	<i>Results and discussion</i>	180
8.4	STATIC EVALUATION WITH GLASS FIBRE-REINFORCED PLASTIC REPAIR PATCH.....	184
8.4.1	<i>Experimental procedures</i>	184
8.4.2	<i>Data analysis</i>	186
8.4.3	<i>Results and discussion</i>	186
8.5	FATIGUE TESTING	192
8.5.1	<i>Experimental procedures</i>	192
8.5.2	<i>Results and discussion</i>	194
8.6	CONCLUSIONS.....	202
CHAPTER 9	203
EVALUATION OF THE STRESS WAVE METHOD USING NUMERICAL ANALYSIS.....		203
9.1	INTRODUCTION	203
9.2	BACKGROUND THEORY AND ANALYSIS	204
9.2.1	<i>Data analysis</i>	206
9.3	PRELIMINARY SIMULATION STUDY	209
9.3.1	<i>Model development</i>	209
9.3.2	<i>Results and discussion</i>	214
9.4	MODELLING FOR DISBOND GROWTH.....	221
9.4.1	<i>Model development</i>	222

9.4.2	<i>Results and discussion</i>	225
9.5	CONCLUSIONS	232
CHAPTER 10		234
EVALUATION OF STRESS WAVE METHOD USING EXPERIMENTAL ANALYSIS		234
10.1	INTRODUCTION	234
10.2	BACKGROUND THEORY	235
10.3	PRELIMINARY STUDY OF COMPOSITE SPECIMEN	237
10.3.1	<i>Experimental procedures</i>	237
10.3.2	<i>Results and discussion</i>	240
10.4	DAMAGE CHARACTERISATION STUDY	244
10.4.1	<i>Experimental procedures</i>	244
10.4.2	<i>Results and discussion</i>	246
10.5	CONCLUSIONS	255
CHAPTER 11		257
CONCLUSIONS AND RECOMMENDATIONS FOR FUTURE WORK		257
11.1	CONCLUSIONS	257
11.1.1	<i>Electromechanical impedance method</i>	257
11.1.2	<i>Transfer function method</i>	258
11.1.3	<i>Stress wave method</i>	259
11.1.4	<i>Mechanical degradation</i>	260
11.2	RECOMMENDATIONS FOR FUTURE WORK	261
REFERENCES		263
LIST OF PUBLICATIONS		274

TABLE OF FIGURES

FIGURE 1.1 SCHEMATIC OF THE SMART PATCH.....	3
FIGURE 2.1 ALUMINIUM DOG-BONE SPECIMEN REPAIRED WITH BORON/EPOXY COMPOSITE REPAIR PATCH.....	11
FIGURE 2.2 SCHEMATIC OF A GENERIC EXTERNAL BONDED REPAIR SHOWING SAFE-LIFE ZONE AND DAMAGE TOLERANT ZONE (BAKER, 1997).	12
FIGURE 2.3 ADHESIVE JOINT TYPES (HART-SMITH, 1974)	13
FIGURE 2.4 TYPICAL CHARACTERISTICS OF AEROSPACE ADHESIVES (HART-SMITH, 1978)	14
FIGURE 2.5 THE PC-9/ A FATIGUE TEST ARTICLE (BARTHOLOMEUSZ ET AL, 2000)	20
FIGURE 2.6 PHOTOGRAPH OF THE CENTRE SECTION OF THE LOWER WING-SKIN SHOWING REPAIRS (BARTHOLOMEUSZ ET AL, 2000)	20
FIGURE 2.7 MECHANICAL IMPEDANCE AGAINST FREQUENCY FOR A THICK BEAM WITH AN ADHESIVELY BONDED SKIN 3.3-MM THICK (CAWLEY, 1984)	38
FIGURE 2.8 MINIMUM DETECTABLE DEFECT DIAMETER AGAINST DEPTH IN ALUMINIUM AND CARBON FIBRE COMPOSITE ASSUMING 3dB RELIABILITY IN IMPEDANCE MEASUREMENTS (CAWLEY, 1984)	39
FIGURE 2.9 EFFECT OF THE DISBONDING ON IMPEDANCE MAGNITUDE FROM CHAUDRY ET AL (1995)	40
FIGURE 2.10 CUMULATIVE AVERAGE DELTA SPECTRUMS WITH SUCCESSIVE DAMAGE (LICHTENWALNER ET AL, 1997).	42
FIGURE 2.11 THE CALCULATED DISPERSION CURVES OF A UNIDIRECTIONAL LAMINATE FROM GUO AND CAWLEY (1993)	45
FIGURE 3.1 IMPEDANCE ANALYSER MODEL 4192A LF	54
FIGURE 3.2 IMPEDANCE ANALYSER MODEL 4284A PRECISION LCR METER	54
FIGURE 3.3 PHOTOGRAPH OF THE AND FFT ANALYSER.....	56
FIGURE 3.4 PHOTOGRAPH OF THE PCMCIA CARD BASED FFT ANALYSER SLOTTED INTO THE LAPTOP ON THE LEFT	58
FIGURE 3.5 WAVEFORM DOWNLOAD SET-UPS.....	59
FIGURE 3.6 PHOTOGRAPH SHOWING THE COMPLETE EXPERIMENTAL SETUP TO EXCITE LAMB WAVES AS WELL AS TO ACQUIRE THE RESPONSE	60
FIGURE 3.7 PHOTOGRAPH OF THE SPECIMEN WITH PZTS AT VARIOUS LOCATIONS.....	61
FIGURE 3.8 EXPERIMENTAL SET-UP	61
FIGURE 3.9 PIEZOCERAMIC TRANSDUCERS BEFORE BONDING	62
FIGURE 3.10 REMOVAL OF PIEZOCERAMIC ELEMENT FOR DESTRUCTIVE EVALUATION OF BONDING CONDITION FROM (A) TO (D)	63
FIGURE 3.11 SCHEMATIC DRAWING OF THE SPECIMEN USED FOR THE DETECTION OF DISBOND GROWTH BY MEANS OF THE TRANSFER FUNCTION METHOD	64
FIGURE 3.12 SCHEMATIC DRAWING OF SPECIMEN (ON THE LEFT) AND THE ACTUAL SPECIMEN (ON THE RIGHT) USED FOR THE VISUALISATION OF DISBOND GROWTH ..	65
FIGURE 3.13 ALUMINIUM PLATE WITH COPPER WIRES IN THE MIDDLE SECTION	66
FIGURE 3.14 FIRST SPECIMEN USED FOR THE VERIFICATION OF METHODS.....	68
FIGURE 3.15 SECOND SPECIMEN USED FOR VERIFICATION OF METHODS.....	69
FIGURE 3.16 LOCATIONS OF STRAIN GAUGES ON THE SECOND SPECIMEN.....	69

FIGURE 3.17 SPECIMEN IN THE MTS OF DEPARTMENT OF MECHANICAL ENGINEERING, MONASH UNIVERSITY TEST MACHINE BEFORE THE START OF THE FATIGUING PROCESS	70
FIGURE 3.18 SCHEMATIC OF IMPACT TEST RIG	71
FIGURE 3.19 SCHEMATIC OF SUPPORT FRAME WITH WINDOW	72
FIGURE 3.20 SCHEMATIC OF THE BASE TABLE WITH FRAME, SPECIMEN AND CLAMPS ...	72
FIGURE 3.21 SCHEMATIC OF IMPACTOR MODULE ATTACHED TO CARRYING UNIT	73
FIGURE 3.22 SCHEMATIC OF THE NEW SPECIMENS	75
FIGURE 3.23 SCHEMATIC DRAWING OF SPECIMEN-4 WITH LOCATION PZT TRANSDUCERS	77
FIGURE 3.24 DOG BONE SHAPED SPECIMEN.....	79
FIGURE 3.25 MTS MACHINE LOCATED IN THE DEPARTMENT OF MECHANICAL ENGINEERING.....	81
FIGURE 3.26 DOG BONE CLAMPED IN POSITION WITHIN THE JAWS	82
FIGURE 3.27 TEKTRONIX OSCILLOSCOPE MODEL TDS 210	82
FIGURE 3.28 ALUMINIUM TABS ON THE DOG BONE FOR ELECTRICAL INSULATION	83
FIGURE 3.29 HEWLETT-PACKARD WAVEFORM GENERATOR	84
FIGURE 3.30 CHANGE IN $[D_{31}]$ CONSTANT WITH STRAIN AFTER 100-KCYCLES	85
FIGURE 3.31 CHANGE IN IMPEDANCE MEASUREMENT WITH STRAIN.....	86
FIGURE 3.32 TRANSFER FUNCTION MEASUREMENT RECORDED WITH DEGRADED SENSORS.....	87
FIGURE 4.1 INITIAL MESH USED FOR THE VALIDATION	91
FIGURE 4.2 SINUSOIDAL EXCITATION OF THE PLATE	92
FIGURE 4.3 OUTPUT FROM PAFEC.....	93
FIGURE 4.4 DISPERSION CURVES OF PHASE VELOCITY AT POISSON'S RATIO 0.34.....	94
FIGURE 4.5 DISPERSION CURVES OF GROUP VELOCITY AT POISSON'S RATIO 0.34.....	95
FIGURE 4.6 NORMALISED TIME HISTORY OF THE Z DISPLACEMENT AT $x = 0$ -MM USED IN ALL THE NUMERICAL TEST.....	99
FIGURE 4.7 NORMALISED TIME HISTORY OF THE Z DISPLACEMENT AT $x = 100$ -MM IN A 0.5-MM PLATE WHEN THE INPUT AT A IS DESIGNED TO EXCITE ONLY S_0	100
FIGURE 4.8 NORMALISED TIME HISTORY OF THE Z DISPLACEMENT AT $x = 164$ -MM IN A 0.5-MM PLATE WHEN THE INPUT AT A IS DESIGNED TO EXCITE ONLY S_0	100
FIGURE 4.9 NORMALISED TIME HISTORY OF THE Z DISPLACEMENT AT $x = 0$ -MM FROM ALLEYNE AND CAWLEY (1991).....	100
FIGURE 4.10 NORMALISED TIME HISTORY OF THE Z DISPLACEMENT AT $x = 100$ -MM IN A 0.5-MM PLATE FROM ALLEYNE AND CAWLEY (1991).	101
FIGURE 4.11 A COMPARISON OF THE FINITE ELEMENT PREDICTIONS WITH THE ANALYTICAL SOLUTION OF THE DISPERSION CURVES.....	101
FIGURE 4.12 3-D PLOT OF THE 2-D FFT RESULTS OF THE CASE GIVEN IN FIGURE 4.8, SHOWING A SINGLE PROPAGATING MODE, S_0	102
FIGURE 5.1 SCHEMATIC DRAWING OF NODE POSITIONS ON PZT- OR PVDF- SENSORS AND ACTUATORS	106
FIGURE 5.2 SCHEMATIC DRAWING OF THE SPECIMEN WITH SENSOR/ACTUATOR BONDED	108
FIGURE 5.3 IMPEDANCE MEASUREMENT RECORDED AT PIEZOCERAMIC LOCATION PZT1	109
FIGURE 5.4 IMPEDANCE MEASUREMENT RECORDED AT PIEZOCERAMIC LOCATION PZT2	109
FIGURE 5.5 IMPEDANCE MEASUREMENT RECORDED AT PIEZOCERAMIC LOCATION PZT3	110

FIGURE 5.6 IMPEDANCE MEASUREMENT RECORDED AT PIEZOCERAMIC LOCATION PZT4	111
FIGURE 5.7 TOP VIEW FOR DISBOND INITIATING FROM CORNER OF REPAIR PATCH (COR)	114
FIGURE 5.8 SIDE VIEW FOR DISBOND INITIATING FROM CORNER OF REPAIR PATCH (COR)	114
FIGURE 5.9 TOP VIEW FOR DISBOND UNDER THE PZT AND THE REPAIR PATCH (BLP)	115
FIGURE 5.10 SIDE VIEW FOR DISBOND UNDER THE PZT AND THE REPAIR PATCH (BLP)	115
FIGURE 5.11 TOP VIEW FOR DISBOND BETWEEN PZT (MID)	115
FIGURE 5.12 SIDE VIEW FOR DISBOND BETWEEN PZT (MID)	115
FIGURE 5.13 RESULTS OBTAINED FROM PZT BONDED ON THE EDGE OF REPAIR PATCH TAPER (SEE FIGURE 5.7, PZT3)	116
FIGURE 5.14 RESULTS OBTAINED FROM PZT ELEMENT BONDED ON THE TOP END OF THE REPAIR PATCH TAPER (SEE FIGURE 5.7, PZT2)	117
FIGURE 5.15 RESULTS OBTAINED FROM PZT ELEMENT LOCATED DIRECTLY ABOVE THE DISBOND (SEE FIGURE 5.9, PZT1B)	118
FIGURE 5.16 RESULTS OBTAINED FROM PZT ELEMENT LOCATED TO DETECT APPROACHING DISBOND (SEE FIGURE 5.9, PZT1A)	118
FIGURE 5.17 RESULTS OBTAINED FROM PZT ELEMENT LOCATED FAR FROM THE DISBOND (SEE FIGURE 5.9, PZT2B)	119
FIGURE 5.18 RESULTS OBTAINED FROM PZT ELEMENT LOCATED ABOVE THE INITIAL DISBOND (SEE FIGURE 5.11, PZT1B)	120
FIGURE 5.19 RESULTS OBTAINED FROM PZT ELEMENT LOCATED DIAGONALLY ABOVE THE INITIAL POINT OF DISBOND (SEE FIGURE 5.11, PZT1A)	121
FIGURE 6.1 SCHEMATIC DRAWING OF THE SPECIMEN USED FOR THE DETECTION OF DISBOND GROWTH BY MEANS OF THE TRANSFER FUNCTION METHOD	126
FIGURE 6.2 IMPEDANCE MEASUREMENT INTERROGATED AT LOW FREQUENCY TAKEN AT PZT LOCATION 1	127
FIGURE 6.3 IMPEDANCE MEASUREMENT INTERROGATED AT HIGH FREQUENCY TAKEN AT PZT LOCATION 1	128
FIGURE 6.4 IMPEDANCE MEASUREMENT INTERROGATED AT LOW FREQUENCY TAKEN AT PZT LOCATION 2	129
FIGURE 6.5 IMPEDANCE MEASUREMENT INTERROGATED AT HIGH FREQUENCY TAKEN AT PZT LOCATION 2	129
FIGURE 6.6 SCHEMATIC DRAWING OF SPECIMEN (ON THE LEFT) AND THE ACTUAL SPECIMEN (ON THE RIGHT) USED FOR THE VISUALISATION OF DISBOND GROWTH	130
FIGURE 6.7 SPECIMEN WITH DYE-PENETRANT SHOWING DAMAGE SIZE OF $45 \times 25\text{mm}^2$	131
FIGURE 6.8 BLADE INSERTED TO CREATE A DAMAGE SIZE OF $5 \times 5\text{-mm}^2$	132
FIGURE 6.9 IM-PARAMETER OBTAINED FROM PZT1 (SEE FIGURE 6.6)	133
FIGURE 6.10 IM-PARAMETER OBTAINED FROM PZT3 (SEE FIGURE 6.6)	133
FIGURE 6.11 IM-PARAMETER OBTAINED FROM PZT5 (SEE FIGURE 6.6)	134
FIGURE 6.12 MEAN SQUARE IMPEDANCE RESPONSE FOR PZT6 (SEE FIGURE 6.6)	135
FIGURE 6.13 MEAN SQUARE IMPEDANCE RESPONSE FOR PZT9 (SEE FIGURE 6.6)	136
FIGURE 6.14 SCHEMATIC DRAWING OF DD2 SPECIMEN USED FOR THE IMPEDANCE METHOD	137
FIGURE 6.15 SCHEMATIC DRAWING OF TTCP2 SPECIMEN USED FOR THE IMPEDANCE METHOD	138

FIGURE 6.16 LOCATIONS OF STRAIN GAUGES ON THE TTCP2 SPECIMEN	138
FIGURE 6.17 IMPEDANCE READINGS FROM SENSOR ON EDGE OF REPAIR PATCH TAPER (PP2).....	140
FIGURE 6.18 SIGNAL TO NOISE RATIO DETERMINED FOR THE EXPERIMENT	140
FIGURE 6.19 STRAIN GAUGE READING TAKEN FROM EDGE OF REPAIR PATCH TAPER, P3	141
FIGURE 6.20 RESULTS USING THE IMPEDANCE METHOD IN THE SECOND EXPERIMENT ON BPZT3.....	141
FIGURE 6.21 STRAIN GAUGE RESULTS FOR THE SECOND SPECIMEN OF STUDY.....	142
FIGURE 7.1 MATHEMATICAL MODEL WITH SPRING MASS SYSTEM	147
FIGURE 7.2 SCHEMATIC DRAWING OF THE SPECIMEN WITH BONDED PIEZOELECTRIC TRANSDUCERS.....	150
FIGURE 7.3 VARIATION OF TRANSFER FUNCTION SPECTRUM WITH RESPECT TO FREQUENCY FOR SENSOR PZT2 AND ACTUATOR PZT1	152
FIGURE 7.4 TRANSFER FUNCTION INTEGRAL BETWEEN SENSOR PZT2 AND ACTUATOR PZT1.....	153
FIGURE 7.5 TRANSFER FUNCTION INTEGRAL BETWEEN SENSOR PZT1 AND ACTUATOR PZT2.....	153
FIGURE 7.6 SPECTRAL DENSITY OF ACTUATOR PZT1, SENSOR PZT2 (ON THE LEFT) AND ACTUATOR PZT2, SENSOR PZT1 (ON THE RIGHT).....	154
FIGURE 7.7 Y-DIRECTION DISPLACEMENT OUTPUT FROM FINITE ELEMENT ANALYSIS .	155
FIGURE 7.8 TRANSFER FUNCTION INTEGRAL BETWEEN SENSOR PZT3 AND ACTUATOR PZT1.....	155
FIGURE 7.9 TRANSFER FUNCTION INTEGRAL BETWEEN SENSOR PZT3 AND ACTUATOR PZT2.....	156
FIGURE 7.10 TRANSFER FUNCTION INTEGRAL BETWEEN SENSOR PZT4 AND ACTUATOR PZT2.....	157
FIGURE 7.11 TRANSFER FUNCTION MEASUREMENT BETWEEN SENSOR PZT4 AND ACTUATOR PZT1.....	158
FIGURE 7.12 TRANSFER FUNCTION INTEGRAL BETWEEN SENSOR PZT4 AND ACTUATOR PZT3.....	158
FIGURE 7.13 TRANSFER FUNCTION MEASUREMENT FOR SENSOR PZT2 AND ACTUATOR PZT1.....	159
FIGURE 7.14 TRANSFER FUNCTION MEASUREMENT FOR SENSOR PVDF3 AND ACTUATOR PZT1.....	160
FIGURE 7.15 TRANSFER FUNCTION MEASUREMENT FOR SENSOR PZT4 AND ACTUATOR PZT1.....	160
FIGURE 7.16 TRANSFER FUNCTION MEASUREMENT FOR SENSOR PVDF3 AND ACTUATOR PZT2.....	160
FIGURE 7.17 TRANSFER FUNCTION MEASUREMENT FOR SENSOR PVDF3 AND ACTUATOR PZT4.....	161
FIGURE 7.18 CALCULATED TRANSFER FUNCTION SPECTRAL DENSITY AND MTF- PARAMETER FOR SENSOR PZT3 AND ACTUATOR PZT2	163
FIGURE 7.19 CALCULATED TRANSFER FUNCTION SPECTRAL DENSITY AND MTF- PARAMETER FOR SENSOR PZT1 AND ACTUATOR PZT3	163
FIGURE 7.20 CALCULATED TRANSFER FUNCTION SPECTRAL DENSITY AND MTF- PARAMETER FOR SENSOR PZT4 AND ACTUATOR PZT2	164
FIGURE 7.21 TOP VIEW FOR DISBOND INITIATING FROM CORNER OF REPAIR PATCH (COR).....	165

FIGURE 7.22 SIDE VIEW FOR DISBOND INITIATING FROM CORNER OF REPAIR PATCH (COR).....	165
FIGURE 7.23 TOP VIEW FOR DISBOND UNDER THE PZT AND THE REPAIR PATCH (BLP).....	166
FIGURE 7.24 SIDE VIEW FOR DISBOND UNDER THE PZT AND THE REPAIR PATCH (BLP).....	166
FIGURE 7.25 TOP VIEW FOR DISBOND BETWEEN PZT (MID).....	166
FIGURE 7.26 SIDE VIEW FOR DISBOND BETWEEN PZT (MID).....	166
FIGURE 7.27 MTF-PARAMETER BETWEEN SENSOR ON ALUMINIUM HOST FAR FIELD (SEE FIGURE 7.21, PZT4) AND ACTUATOR ON REPAIR PATCH FAR FIELD (SEE FIGURE 7.22, PZT1).....	167
FIGURE 7.28 MTF-PARAMETER BETWEEN SENSOR ON EDGE OF REPAIR TAPER (PZT3) AND ACTUATOR ON TOP END OF REPAIR PATCH TAPER (PZT2).....	168
FIGURE 7.29 MTF-PARAMETER BETWEEN SENSOR ON EDGE OF REPAIR PATCH TAPER (PZT3) AND ACTUATOR ON FAR FIELD REPAIR PATCH (PZT1).....	169
FIGURE 7.30 MTF-PARAMETER BETWEEN SENSOR ON TOP END OF REPAIR PATCH TAPER (PZT2) AND ACTUATOR ON FAR FIELD REPAIR PATCH (PZT1).....	170
FIGURE 7.31 MTF-PARAMETER BETWEEN SENSOR ON TOP RIGHT (PZT1B) AND ACTUATOR ON TOP LEFT (PZT1A).....	171
FIGURE 7.32 MTF-PARAMETER BETWEEN SENSOR ON BOTTOM RIGHT (PZT2B) AND ACTUATOR ON BOTTOM LEFT (PZT2A).....	172
FIGURE 7.33 MTF-PARAMETER BETWEEN SENSOR ON TOP RIGHT (PZT1B) AND ACTUATOR ON TOP LEFT (PZT1A).....	173
FIGURE 8.1 SCHEMATIC DRAWING OF THE PRELIMINARY INVESTIGATION SPECIMEN ..	179
FIGURE 8.2 TRANSFER FUNCTION SPECTRUM FOR NO DAMAGE AND $10 \times 10\text{-MM}^2$ DAMAGE.....	181
FIGURE 8.3 TRANSFER FUNCTION BETWEEN ACTUATOR ON COMPOSITE PATCH AND SENSOR ON ALUMINIUM.....	182
FIGURE 8.4. TRANSFER FUNCTION BETWEEN ACTUATOR ON ALUMINIUM AND SENSOR ON COMPOSITE PATCH.....	182
FIGURE 8.5 TRANSFER FUNCTION BETWEEN SENSOR ON ALUMINIUM AND ACTUATOR ON ALUMINIUM.....	183
FIGURE 8.6 SCHEMATIC DRAWING OF SPECIMEN (ON THE LEFT) AND THE ACTUAL SPECIMEN (ON THE RIGHT) USED FOR THE VISUALISATION OF DISBOND GROWTH	185
FIGURE 8.7 SPECIMEN WITH THE BLADE INSERTED FOR A DAMAGE SIZE OF $10 \times 10\text{-MM}^2$	186
FIGURE 8.8 TRANSFER FUNCTION OF SIGNAL BETWEEN SENSOR PZT 4 AND ACTUATOR PZT 7 (SEE FIGURE 8.6).....	187
FIGURE 8.9 TRANSFER FUNCTION SIGNAL BETWEEN SENSOR PZT 1 AND ACTUATOR PZT 7 (SEE FIGURE 8.6).....	187
FIGURE 8.10 SPECIMEN WITH THE BLACK COLOUR LIQUID PENETRANT HIGHLIGHTING DAMAGE SIZE OF $25 \times 25\text{-MM}^2$	188
FIGURE 8.11 TRANSFER FUNCTION BETWEEN SENSOR PZT2 AND ACTUATOR PZT8 (SEE FIGURE 8.6).....	189
FIGURE 8.12 TRANSFER FUNCTION BETWEEN SENSOR PZT 5 AND ACTUATOR PZT 8 (SEE FIGURE 8.6).....	189
FIGURE 8.13 SPECIMEN WITH THE BLACK COLOUR LIQUID PENETRANT HIGHLIGHTING DAMAGE SIZE OF $45 \times 25\text{-MM}^2$	190
FIGURE 8.14 TRANSFER FUNCTION BETWEEN SENSOR PZT 6 AND ACTUATOR PZT 9 (SEE FIGURE 8.6).....	191

FIGURE 8.15 SCHEMATIC DRAWING OF THE DD2 SPECIMEN USED FOR THE TRANSFER FUNCTION METHOD	193
FIGURE 8.16 SPECIMEN TTCP2 USED FOR VERIFICATION OF BOTH METHODS.....	194
FIGURE 8.17 LOCATION OF STRAIN GAUGES ON THE TTCP2 SPECIMEN	194
FIGURE 8.18 TRANSFER FUNCTION BETWEEN ACTUATOR PP3 AND SENSOR PP2	195
FIGURE 8.19 SIGNAL-TO-NOISE GRAPH	195
FIGURE 8.20 STRAIN GAUGE READING TAKEN FROM EDGE OF REPAIR PATCH TAPER, P3	196
FIGURE 8.21 TRANSFER FUNCTION OF ACTUATOR PP1 AND SENSOR PP2	196
FIGURE 8.22 TOP VIEW SCHEMATIC OF THE FINITE ELEMENT MODELLED SPECIMEN....	197
FIGURE 8.23 SIDE VIEW SCHEMATIC OF THE FINITE ELEMENT MODELLED SPECIMEN...	197
FIGURE 8.24 TRANSFER FUNCTION BETWEEN ACTUATOR PP1 AND PP2	197
FIGURE 8.25 VARIATION OF INTEGRATED BULK STRESS WITH DAMAGE.....	198
FIGURE 8.26 TRANSFER FUNCTION OF CONTROL GROUP ACTUATOR PP3 AND SENSOR PP1	199
FIGURE 8.27 SECOND SPECIMEN, ACTUATOR ON BPZT1 AND SENSOR BPZT3	200
FIGURE 8.28 VARIATION OF SURFACE STRAINS (SIDE B) WITH LOADING CYCLES.....	200
FIGURE 8.29 ULTRASONIC A-SCANS OF DISBOND ON SIDE B.....	200
FIGURE 9.1 PROBES USED IN EXPERIMENTS TO EXCITE LAMB WAVES	206
FIGURE 9.2 OUTPUT FROM LOWE ET AL (2000).....	208
FIGURE 9.3: CALCULATED DISPERSION CURVE OF AN 8-PLY CROSS PLY LAMINATE	210
FIGURE 9.4: THE CALCULATED DISPERSION CURVES OF ALUMINIUM PLATE.....	211
FIGURE 9.5 SCHEMATIC OF THE FE MODEL SHOWING THE PZT TRANSDUCER BONDED ON THE ALUMINIUM HOST.....	212
FIGURE 9.6 A COMPARISON OF THE FINITE ELEMENT PREDICTIONS WITH THE ANALYTICALLY GENERATED DISPERSION CURVES	212
FIGURE 9.7 2D-FFT OF THE TIME HISTORY BEFORE THE DELAMINATION ZONE.....	214
FIGURE 9.8 2D-FFT OF THE TIME HISTORY ABOVE THE DELAMINATION ZONE.....	215
FIGURE 9.9 2D-FFT OF THE TIME HISTORY AFTER THE DELAMINATION ZONE.....	216
FIGURE 9.10 2D-FFT OF THE TIME HISTORY AFTER THE DELAMINATION ZONE WITH GATING PROCEDURE.....	216
FIGURE 9.11 2D-FFT OF THE TIME HISTORY ABOVE A 25% DELAMINATION FROM THE SURFACE DEPTH	217
FIGURE 9.12 2D-FFT OF THE TIME HISTORY ABOVE A 37.5% DELAMINATION FROM THE SURFACE DEPTH	218
FIGURE 9.13: 2D-FFT FROM ALUMINIUM PLATE WITH NO DAMAGE AND 100% OF YOUNG'S MODULUS	220
FIGURE 9.14: 2D-FFT FROM ALUMINIUM PLATE WITH 04-MM AND 50% OF YOUNG'S MODULUS	220
FIGURE 9.15 2D-FFT FROM ALUMINIUM PLATE WITH 12-MM AND 90% OF YOUNG'S MODULUS	221
FIGURE 9.16 POWER TRANSMITTED ACROSS BVID-TYPE DAMAGE.....	221
FIGURE 9.17 CALCULATED DISPERSION CURVES OF ALUMINIUM PLATE.....	222
FIGURE 9.18 SCHEMATIC OF A SMALL SECTION OF THE SIMULATED MODEL.....	224
FIGURE 9.19: 2D-FFT ON THE ALUMINIUM SUBSTRATE IMMEDIATELY NEXT TO THE ACTUATOR	226
FIGURE 9.20: 2D-FFT ON THE COMPOSITE REPAIR PATCH AFTER THE DAMAGE.....	226
FIGURE 9.21 COMPARISON OF NUMERICAL AND ANALYTICAL FOR 0-MM DAMAGE	228
FIGURE 9.22 COMPARISON OF NUMERICAL AND ANALYTICAL FOR 6-MM DAMAGE	228
FIGURE 9.23 COMPARISON OF NUMERICAL AND ANALYTICAL FOR 12-MM DAMAGE ...	228

FIGURE 9.24 FINITE ELEMENT MESH USED BY DALTON ET AL (2001).....	229
FIGURE 9.25: POWER TRANSMISSION DETECTED BY PZT3	230
FIGURE 9.26 POWER TRANSMISSION DETECTED BY PZT2	231
FIGURE 9.27 POWER TRANSMISSION FOR PZT LOCATED AT THE BETWEEN PZT2 AND PZT3.....	231
FIGURE 9.28: RESULTS FROM THE EXPERIMENTAL INVESTIGATION OF THE STRESS WAVE METHOD TAKEN FROM KOH ET AL (2002)	232
FIGURE 9.29: STRAIN GAUGE READING TAKEN FROM EDGE OF REPAIR PATCH TAPER..	232
FIGURE 10.1 SCHEMATIC DRAWING OF THE ID1-SERIES SPECIMENS WITH PZT LOCATIONS.....	238
FIGURE 10.2 TIME OF FLIGHT BETWEEN ACTUATOR (PZT4) AND SENSOR (PZT1) ON ID1	240
FIGURE 10.3 TIME OF FLIGHT BETWEEN ACTUATOR (PZT4) AND SENSOR (PZT2) ON ID1	240
FIGURE 10.4 TIME OF FLIGHT BETWEEN ACTUATOR (PZT4) AND SENSOR (PZT3) ON ID1	241
FIGURE 10.5 SCHEMATIC OF THE ID1-SERIES SPECIMENS WITH NEW PZT LABELS	242
FIGURE 10.6 TIME DELAY BETWEEN ACTUATOR (PZT2) AND SENSOR (PZT4) SIGNAL FOR A LONGER DISTANCE	242
FIGURE 10.7 AMPLITUDE SPECTRUM OF THE TIME HISTORY SHOWN IN FIGURE 10.6....	244
FIGURE 10.8 SCHEMATIC OF THE ID2-SERIES SPECIMENS WITH PZT LOCATION LABELS	245
FIGURE 10.9 SPECIMEN 4 RESPONSE FOR ACTUATOR (4) AND SENSOR (8) BEFORE LAST IMPACT	246
FIGURE 10.10 RESPONSE FOR ACTUATOR (4) AND SENSOR (8) AFTER LAST IMPACT ...	246
FIGURE 10.11 SPECIMEN 4 RESPONSE FOR ACTUATOR (1) AND SENSOR (5) BEFORE LAST IMPACT	247
FIGURE 10.12 RESPONSE FOR ACTUATOR (1) AND SENSOR (5) AFTER LAST IMPACT ...	247
FIGURE 10.13 THERMAL SCAN FRONT FACE OF SPECIMEN 4 BEFORE AND AFTER LAST IMPACT.....	249
FIGURE 10.14 THERMAL SCAN OF SPECIMEN 4 (BACK) BEFORE AND AFTER LAST IMPACT	249
FIGURE 10.15 THERMAL SCAN OF SPECIMEN 5 AFTER LAST IMPACT (FRONT AND BACK)	251
FIGURE 10.16 THERMAL SCAN OF SPECIMEN 6 AFTER LAST IMPACT (FRONT AND BACK)	252
FIGURE 10.17 ATTENUATION IN % AS A FUNCTION OF IMPACT ENERGY (J)	254
FIGURE 10.18 ATTENUATION IN % AS A FUNCTION OF ABSORBED ENERGY (J).....	254
FIGURE 10.19 ATTENUATION (%) AS A FUNCTION OF ABSORBED ENERGY (%) COMPARED TO A FITTED LINE	255

LIST OF TABLES

TABLE 2.1 RELEVANT MATERIAL MECHANICAL AND PHYSICAL PROPERTIES (BAKER, 1988)	15
TABLE 2.2 BONDED APPLICATIONS ON AIRCRAFT PRIMARY STRUCTURES	18
TABLE 2.3 COMPOSITE PATCH FITMENT AND DISBOND DETECTION HISTORY (CHALKLEY AND GEDDES, 1998).....	21
TABLE 3.1 MATERIAL PROPERTIES OF FM73 ASSUMED AT ROOM TEMPERATURE	53
TABLE 3.2 MATERIAL PROPERTIES OF PZT	53
TABLE 3.3 DISBOND SIZES CONSIDERED FOR THE FRP COMPOSITE PATCH.....	67
TABLE 3.4 CHARACTERISTICS OF THE IMPACTOR	73
TABLE 3.5 TIME FROM DROP TO IMPACT	74
TABLE 3.6 IMPACT HEIGHTS FOR VARIOUS IMPACT ENERGIES	75
TABLE 3.7 INTERVALS BETWEEN THE LOADING CYCLES	78
TABLE 3.8 LOCATION OF PZT ON THE ALUMINIUM DOG BONE.....	80
TABLE 3.9 STRAIN AT EACH INDIVIDUAL PZT ON THE DOG BONE.....	80
TABLE 5.1 DISBOND SIZES SIMULATED	114
TABLE 7.1 PIEZOELECTRIC-3 WITH PZT MATERIAL PROPERTY	151
TABLE 7.2 PIEZOELECTRIC-3 WITH PVDF MATERIAL PROPERTY	151
TABLE 7.3 DISBOND SIZES SIMULATED	165
TABLE 8.1 TRANSFER FUNCTIONS USED IN VIBRATION MEASUREMENT	177
TABLE 8.2 RELATIONSHIP BETWEEN COMPOSITE THICKNESS AND SENSITIVITY	201
TABLE 9.1 THE TYPE OF IMPACT SIZE AND INTENSITY CONSIDERED	213
TABLE 10.1 COMMON MATERIAL PROPERTIES OF GRAPHITE/EPOXY COMPOSITE.....	238
TABLE 10.2 TIME DELAY FROM EMITTER TO RECEIVER.....	241
TABLE 10.3 SPEED OF FLIGHT IN DIFFERENT DIRECTIONS.....	241
TABLE 10.4 TIME DELAY FROM EMITTER TO RECEIVER.....	242
TABLE 10.5 CHARACTERISTICS OF THE SPECIMENS AFTER IMPACT DAMAGE.....	245
TABLE 10.6 RMS VALUES FOR SPECIMEN 4	248
TABLE 10.7 RMS VALUES FOR SPECIMEN 5	250
TABLE 10.8 RMS VALUES FOR SPECIMEN 6	251
TABLE 10.9 RESULTS AFTER IMPACT ON ALL THREE SPECIMENS.....	252
TABLE 10.10 RESULTS AFTER THIRD IMPACT ON ALL THREE SPECIMENS	253

SUMMARY

This research aims to assess the viability of three methods that can be implemented at once as part of an *in-situ* system to monitor the structural health of bonded composite repairs on aircraft structures. This system has the potential to reduce operating costs, increase flight safety and improve aircraft availability.

In the first stage of the research, the effective placement of the piezoelectric sensors for the detection of disbond growth underneath a composite repair patch was first established and the parameters necessary to quantify damage identified. The safe operating strain levels for the PZT elements were then quantified necessitating an investigation of the mechanical degradation of PZT elements. It was shown that there was no change in the governing constitutive relation if the PZT elements operated below the threshold strain level. When the PZT elements operated above the threshold limit, the coupling constant decreased exponentially with increasing strain levels. Impedance measurements were found to be unaffected by the changes in the coupling constant, while the transfer function measurement varied with the changes in the coupling constant.

In the second stage of the research, building on the information obtained, the applications of the impedance, the transfer function and the stress wave methods to detect damage in bonded composite repair patches were initially evaluated by numerical analysis. When the impedance and transfer function method were applied, the disbond could be detected when it came within the damage detectable zone. Both methods were not able to detect a disbond that was beyond the sensing zone of the sensors. During the application of the stress wave method, regardless of the sensor location, initiation of disbond was shown by an increase in power flow and advanced disbond was shown by a decrease in power flow, which was also confirmed by the experimental evaluation. These results suggest that, for future practical applications, more than one sensor is required to determine the underlying condition. They also

suggest that for optimum sensitivity, the sensor should be approximately equal in length and width.

In the third stage of the research, an experimental evaluation of the three methods was carried out to substantiate the results obtained from the numerical analysis. The results from the experimental evaluation showed good agreement with the results from the numerical analysis. The disbonds studied were typical disbonds that can occur in bonded repairs. All three methods could be used to detect disbond under the bonded repair patches. In addition, the stress wave method could be used for the detection of delamination between plies.

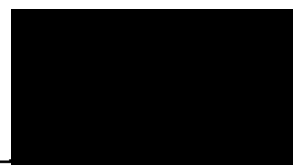
It was successfully demonstrated that by strategically locating the sensor and actuator pairs, the type, location and severity of the disbond could be determined. In the experimental evaluation, an array of surface mounted PZT elements were used for the *in-situ* detection of disbond growth in a bonded composite repair patch. The disbond growth was either artificially introduced damage or fatigue-induced damage. In the fatigue-induced damage, the detection methods were used to track the evolution of disbond growth under a boron/epoxy composite patch. Throughout the experiments, the PZT elements were reliable and robust with signals produced beyond 1,000,000 loading cycles. It was demonstrated the transducer placement relative to the disbond location was an important factor in the sensitivity of the impedance and the transfer function methods.

Additional experimental work was conducted to evaluate an impact damaged composite plate using the stress wave method. The effects of impact damage and delamination of plate-like structures on the propagating Lamb wave mode were investigated and it was found that the measured responses attenuate proportionally with the severity of damage. The type and severity of damage were confirmed using thermal scans.

DECLARATION

I hereby declare that this thesis contains no material which has been accepted for the award of any other degree or diploma in any university, and to the best of my knowledge and belief contains no material previously published or written by another person, except where due reference is made.

Signed:

A solid black rectangular box used to redact the signature of the author.

Yeow Leung Koh

Date:

15/6/02.

ACKNOWLEDGEMENT

The successful completion of this thesis is the cumulation of support of the following people. They make this an enjoyable and fruitful experience and I am most grateful to all those who helped in along the way.

- Assoc. Prof. W. K. Chiu whom it is a privilege to work under, the role of a mentor in all aspects of life. He has read every page of and checked every formula; it is a pleasure to acknowledge my debt to him for the enthusiasm needed to undertake such a task and the resolution needed to pursue it to a conclusion.
- Assoc. Prof. Ian H. Marshall who is the most charming of supervisors, kind enough to read and comment helpfully on a major part of the thesis.
- Dr. Stephen C. Galea and Dr. Niklaus Rajic at DSTO, Department of Defence, who showed me what conscientious research is all about.
- Jane Moodie for the corrections to my thesis that as a result made many useful alterations to the original manuscript.
- The Mechanical Engineering workshop staff, especially Mr Ron Laemmle who contributed immensely to the fabrication of specimens.
- My fellow colleagues in the office, Dr. Wibowo Harsonugroho and Derek Barke, whom it has been a great opportunity to be working under one roof.
- My brother Yeow Lu for his concern and sound advice at different stages of the thesis.
- My parents, the source of inspiration, for the unconditional love and undying faith in me even in my darkest hours.
- My girlfriend, Yee Meng for her unconditional love and care even in my absence, without could not have brought the thesis to completion.

"Without counsel purposes are disappointed: but in the multitude of counsellors they are established".

Proverbs 15:22

NOMENCLATURE

1-D, 2-D, 3-D	One dimensional, two dimensional and three dimensional
a	Gravitational acceleration
c_l	Longitudinal velocity
c_t	Transverse velocity
D	Flexural rigidity
D_m	Electric displacement
d_{mi}	Piezoelectric coupling between the electrical and mechanical variables
ϵ_{mk}^T	Dielectric permittivity measured at zero mechanical stress ($T=0$)
E	(i) Young's modulus (ii) Kinetic energy
E_m	Electric field
$E[]$	Denotes the ensemble averaged value of the quantity in the brackets
F	Harmonic force
f	Frequency
FEM	Finite element method
FM73	Adhesive brittle
FM400	Adhesive ductile
g_{mi}	Piezoelectric voltage coefficient
h	Plate thickness
K_j^T	Relative dielectric constant
k	Wave number
k_{mi}	Coupling coefficient
kcycles	'000 cycles
m	Mode number in the x-direction
n	Mode number in the y-direction
PZT	Lead zirconate titanate
PVDF	Polyvinylidene fluoride

r	Radial coordinate
$S_x(\omega)$	Auto-spectral density of the stationary random process $x(t)$
S_i	Surface strain
s_{ij}^E	Mechanical compliance of the material measured at zero electric field ($E=0$)
s	Displacement in metres
T_j	Stress
t	Time in seconds
u	Initial velocity
x, y, z	Orthogonal directions (Cartesian coordinate system)
γ_j^E	Elastic modulus
Z	Point impedance

Greek symbols

π	Constant – Pi = 3.1482
ρ	Density
ν	Poisson's ratio
υ	Response velocity
ξ	Strain
ω	Circular frequency

CHAPTER 1

INTRODUCTION

The ability of the morning glory to bloom with the rising of the sun and the chameleon blending with its surrounding background are universally admired. A similar adaptability in synthetic materials is desirable - imagine a self-colouring carpet optimising its design to its immediate environment, and a building adjusting its dynamic properties to minimise discomfort to the occupants in high winds or under earth tremor conditions. Smart structures offer this potential as they are structures that sense their internal state and external environments and, based on the information-gained, respond in a manner that fulfils their functional requirements (Islam et al, 1994).

During the past two centuries, material science has witnessed the emergence of a research and development thrust, which has evolved in parallel with those activities focused on the development of new generations of structural materials. This thrust has focused on the development of functional materials; namely, materials whose principal functional characteristics rather than inherent structural properties are exploited in the fields of science and technology. Thus, for example when germanium, which is a photoconductive material, is exposed to a light source, it generates an electric current as the photons of light are absorbed at the surface of the material and electrons are subsequently released from the atomic structure. Using an amplifying

circuit, this phenomenon can be employed for commercial application. Another example of a functional material is a vibration transducer, which typically features a piezoelectric element. When fixed to a vibrating structure, it is subjected to dynamic deformations and thereby develops an appropriate time-dependent electrical signal, which can be used to measure the vibrational response of the structure. The mechanical strength of the piezoelectric element is not exploited in this application; rather it is the functional piezoelectric characteristics of the material, which combine the mechanical and electrical behaviour, which are used.

A smart structure, or intelligent material system, contains a network of sensors and actuators, real-time control capabilities, computational capabilities and a host structural material. The structure is able to inspect its own health condition automatically and continuously. Structural health monitoring forms a complex activity that requires the interaction of concurrent factors. The actuator induces actuation into the structure, such as vibration through strain or displacement. The sensors recognize and measure the signal that results from this actuation, such as the resultant vibrational response. The control/processor unit acquires information from the sensors, and determines if corrective measures need to be taken.

On November 15, 2001, American Airlines Flight 587 crashed into the borough of Queens in New York. Investigators and experts familiar with composite materials like the one that broke on the jet cautioned in USA Today (Arlington, VA; Nov 19, 2001) that it was too early then to say whether the cracks were on the tail before the crash or resulted from the tail being wrenched from the jet, but if the cracks were present before the accident, it could help explain why the vertical tail fin fell off. It is insidious and potentially catastrophic and it could also have the same consequences as the other aircraft composite components. The goals of developing smart structures for damage detection are that the structure could, through the damage identification process, be able to detect the damage like those above as it is incurred by the structure, to determine the location and extent of the damage, to predict if and when catastrophic failure of the structure will occur, and to alert the operator as to how the performance of the structure is affected so that appropriate steps can be taken to remedy the situation (Gandhi, 1992; Culshaw, 1996).

Smart structure may be developed for composite repair patch so that constant monitoring can be carried out to ensure structural integrity. Currently, composite repair patching of metallic aircraft structures is becoming an important technology in the maintenance and repair of ageing aircraft. When compared to conventional Structural Repair Manual (S.R.M.) or Technical Order (T.O.) repair, composite repair provides several advantages including substantial repair cost savings, shorter aircraft downtime and better structural integrity. Composite repairs are performed on military aircraft both internally and externally. However, when a repair is performed internally, access to the repair location for in-service non-destructive evaluation is either rather limited or unavailable. In such cases, disassembly of the aircraft structure is required for inspections to determine flight worthiness and such inspections are thus expensive and time consuming. Thus an in-situ method for condition monitoring of the composite patch integrity is highly desirable.

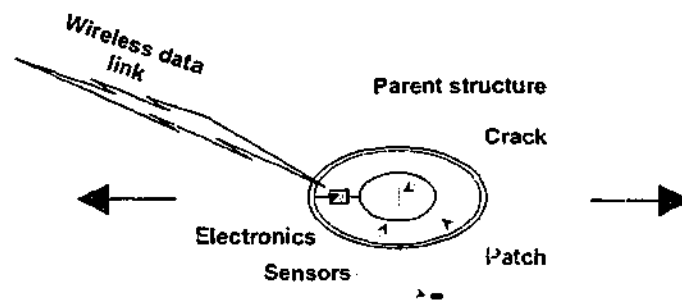


Figure 1.1 Schematic of the smart patch

One very exciting possible application of such a non-destructive structural health monitoring system would be a 'Smart Patch'. The 'Smart Patch' approach may be acceptable from the airworthiness perspective and be cost effective for the operator and may even allow some relaxation of the certification requirements. The most basic form of the "Smart Patch", as shown in Figure 1.1, involves the incorporation of an in-situ health monitoring system, i.e. the incorporation of sensors as the nerve system, to monitor in service the structural condition of the patch system and the status of the remaining damage in the parent structure. In order for these systems to be accepted in well-established and relatively rigid logistic schedules, associated with ageing aircraft, these systems need to be virtually maintenance free (i.e. autonomous, self-powered or externally powered and platform independent) with wireless interrogation capability.

The concept has been demonstrated in the laboratory (Baker et al, 1998; Moss et al, 2000) with a flight demonstration of a smart patch system on an F/A-18 aileron hinge repair planned in the near future (Galea et al, 2001). Although much has been done to date, more studies need to be conducted to ascertain a methodology for reliable detection of disbond growth in composite repair patch and impact damage of composite structure.

Critical to the success of composite repair of metallic aircraft structures is the integrity of the adhesive between the base aluminium panel and the reinforcing high strength composite patch. Constant monitoring of the adhesive layer is important to ensure composite patch integrity throughout the service life of the structure in order to prevent failure. If damage can be detected at an early stage, corrective measures can be taken and catastrophic failure can be prevented.

However, early damage detection is not easily achieved. The principal impediment to achieving early detection of incipient damage is the size of the damage. A disbond growth under a composite repair patch or a delaminated composite patch may be very small and difficult to detect using existing methods. Currently the only failure detection methods are either periodic inspection or in-situ monitoring. The composite patch can be subjected to periodic minute in-depth inspection but periodic inspection, which is both a time consuming and a labour intensive activity, is also not foolproof against failures of the composite patch between inspection intervals. A better method of monitoring is needed and in-situ structural health monitoring appears to be a promising alternative.

The aim of this research is to develop several structural health-monitoring methods for in-situ applications. Enabling technologies associated with the in-situ monitoring to be developed are the electromechanical impedance, the system transfer function and the stress wave actuator-sensor pairs.

In the first stage of the project a suitable testing scheme will be identified to be used with the enabling technologies with surface bonded piezoelectric transducers on composite repair patches. This will be carried out statically with artificial disbond sizes created by inserting foreign material under the composite repair patch. The

methods, namely transfer function, impedance and stress wave method, will be studied in detail within this preliminary investigation.

Comparison between the methods will be made to determine the sensitivity and robustness of methods and the number of PZT needed. The changes in the structure's integrity have an effect on the frequency response spectra, wave dispersion and attenuation of energy transmission; hence this stated measurements should be useful in damage characterisation. In addition signal-to-noise ratio will be taken into consideration during the initial testing phase, since a piezoelectric transducer has high capacitive property.

The optimal locations where the piezoelectric transducers will be bonded for the detection of incipient damage will be identified. Emphasis will be placed on formulating a methodology that allows practical in-service application. Optimisation of PZT placements will also include transducer configurations that will allow the application of all three methods in a synergistic manner. A numerical study will be conducted to examine the signal and an experimental study will be conducted to confirm the numerical findings.

The second stage of the project is to employ the methods developed for the detection of incipient damage with the optimal sensor/actuator pair locations to develop a network of sensors/actuators to improve the practical applicability aspect of in-situ monitoring. Employing only a pair of sensor and actuator to relate the condition of the repair patch has limitations since both sensors and actuators can be damaged during service, or the sensors or actuators can return values that can be misinterpreted due to various factors including mechanically degraded sensors or actuators, and different locations of damage relative to the sensor and actuator location.

In the process of achieving these aims, the project also aims to investigate mechanical degradation of piezoceramics when mounted during service, a problem that has never been examined before. There is no literature reporting any work in this area. However mechanical degradation has to be quantified, to isolate the different signals from a degraded sensor/actuator over a damaged zone. This can be a function considering the varying loads applied as well as the number of cycles experienced. The impedance

method and transfer function method will also be applied to the specimens, to determine the changes to the methods that are caused by the degraded signal. A methodology will be developed for incorporating this degradation into the health monitoring procedure to account for sensor/actuator degradation.

In aeronautical and aerospace applications, smart composite patches sometimes encounter impact damage. In order to assess the residual strength of a composite structure subjected to low velocity impact damage, the monitoring system proposed in this thesis must also be able to locate the damage, determine the extent of the damage and to determine the stress field in the vicinity of the damage. In order to test whether the damage detection method has this capability, the following research will be conducted.

A numerical simulation and experimental investigation will be first carried out to examine whether surface waves excited by the stress wave method can be used with surface mounted piezoelectrics to detect the extent of impact damage. This will provide a new understanding of the effect of damage on composite repair and composite structure towards the propagation of surface waves. In the numerical study, a flat plate will be used with simulated impact damage in the between two far field sensor/actuator. Two types of damage will be simulated, namely barely visible impact damage, which causes change in the Young's modulus of the local damaged area and delamination between plies. Damage of varying sizes will be simulated with changes in Young's modulus and the results analysed in the frequency domain and the spatial domain. An effective method for assessing the damage will thus be determined.

The experimental investigation will first determine the phase velocity and excitation frequency. The determined phase velocity and excitation frequency will be applied to a thin plate of boron/epoxy composite on which PZTs will be used as both sensor and actuator. The results obtained will be used to substantiate the numerical findings.

This thesis reports the experimental and numerical work done in this research and discusses the findings. An outline of the thesis is presented as follows.

Chapter 2 contains a review of the literature relevant to the study. The sources of this review are quite varied.

Chapter 3 describes the experimental method used in the experiments. Results from the evaluation of the effect mechanical degradation on the proposed methods are presented.

Chapter 4 describes the numerical models used. Validation of the numerical models is presented in this chapter.

Chapter 5 and 6 present and discuss the numerical analysis and experimental evaluation on the application the impedance method.

Chapter 7 and 8 present and discuss the numerical analysis and experimental evaluation on the application the transfer function method.

Chapter 9 and 10 present and discuss the numerical analysis and experimental evaluation on the application the stress wave method.

Chapter 11 contains the conclusions and recommendations for further work.

CHAPTER 2

LITERATURE REVIEW

2.1 INTRODUCTION

There is considerable research interest in structural health monitoring, including a particular interest in composite aircraft components, because failures of these components can have dire consequences. For example, catastrophic failure of composite aircraft components, which are sudden compared to metallic components, may lead to crashes with high casualties. This is also true in the case of composite repairs to composite or metallic aircraft structures.

In order to develop a suitable monitoring scheme, the properties of these composite repairs must be understood in detail. In section 2.2 a brief summary of the history of composite repair patches is given and then adhesive joints properties and the mechanical properties of the composite repair patches are outlined. Several case studies are examined that outline the environmental factors affecting the performance of composite repairs.

Research into problems with composite repair patches is also reviewed. In section 2.3 previous researches into disbonding of composite repairs, and, in section 2.4, studies of impact damage, which normally exhibit inter-ply delamination, are reviewed

In Section 2.5, previous experimental studies of conventional non-destructive inspection methods summarised for the detection of damage in both metals and composite materials. Due to the vast number of non-destructive evaluation methods, this section primarily concentrates on methods that are commonly used for composites and composite structures. In section 2.6, a critical review of the non-destructive evaluation methods most suited to detect disbond and impact damage is presented and a detailed description of the material used with these non-destructive methods is given in section 2.7.

This critical review of the relevant literature provides a clear understanding of the existing knowledge in this field and provides the rationale for the current research. The aims of this research are stated in section 2.8.

2.2 COMPOSITE REPAIR PATCHES

Composites are being increasingly used in many engineering applications due to their high specific stiffness and strength. Bonded composite repairs have proved to be an excellent option because their relatively small size means that the critically important spar stresses are largely unaffected by their presence, while crack growth in the wing-skin is slowed or stopped. The anisotropic material properties of the patches locally stiffen the structure only in the direction perpendicular to the crack path (along the fibre direction). The alternative of a mechanically fastened, isotropic and thicker metallic patch would most likely have changed load transfer for example around the spar cap making life assessment for this critical structure very difficult.

2.2.1 GENERAL BACKGROUND

Composite patches are used in civil infrastructures and aeronautical structures. In civil infrastructures, the use of composite overlays to reinforce masonry wall specimens by the US Army Construction Engineering Research Laboratory has been reported by Berman et al (1998). The specimens had dimensions 4-ft by 4-ft and were built from standard concrete masonry units. The masonry wall was strengthened with overlays of fibres reinforced polymeric (FRP) composite sheets applied on one face. The FRP composite overlays were generally thin (approximately 1/8-in), but were able to provide up to 94% increase in the load-carrying capacity of the wall. Several tests were performed with different composite-overlay fabrication solutions. One fabrication solution was to have the composite overlay cured separately in the form of rigid sheets. These sheets were applied on the masonry walls using contact pressure and room temperature adhesive. The other fabrication solution was to apply the composite overlay as a wet lay-up directly on the wall. In this situation, the polymeric resin had a double role, as matrix for the composite fibres in the overlay and as adhesive for the joint between the composite overlay and the wall.

In this study, during testing of the composite-reinforced masonry in the wall, three distinct stages of behaviour were observed.

- (i) Due to the composite overlay, the wall still kept together and additional loading could be applied.
- (ii) As high load levels were attained, disbonding of the composite overlay from the wall started to occur.
- (iii) Final failure of the specimen was accompanied by extensive disbonding between the masonry wall and the composite overlay. The failure load recorded during these tests was up to 94% higher than the failure load of an unreinforced wall. These tests showed the benefits of strengthening masonry walls with composite overlay. They also identified the adhesive interface between the wall and the composite as a critical area for structural safety.

For aeronautical structures, composite repair has extensive application in modern aircraft in which increasing consideration is being given to composite constructions

for various components. There are two main criteria for composite repair. First, the repair must function in the mission environment of the aircraft. In other words, thermal stability and strength are critical for operation. Secondly, the repair environment must be suitable with sufficient equipment availability and space.

Two general approaches can be taken to the problem of composite repair, namely bolted and bonded repair procedures. Both have their place in the repair of aircraft composite components. The factors that determine a particular approach include the specific component, the laminate thickness, the damage size, the accessibility, the load requirements and the repair capability.

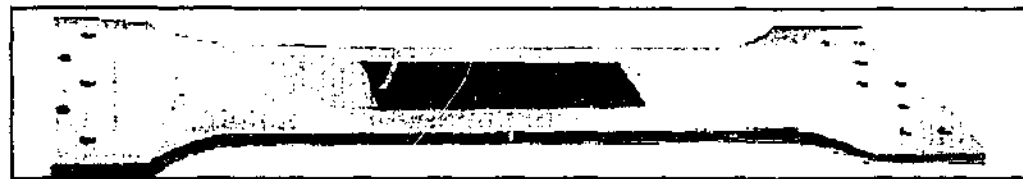


Figure 2.1 Aluminium dog-bone specimen repaired with boron/epoxy composite repair patch

Bonded repairs provide a far more effective reinforcement than mechanical repairs so that 'live' cracks can be left in the structure (Figure 2.1). Mechanical repairs require the removal of the cracked region and also the introduction of extra fastener holes. Both of these requirements are costly, highly intrusive, and potentially damaging to the structure and substructure.

2.2.2 PROPERTIES OF BONDED COMPOSITE REPAIRS

With bonded repairs, it is crucial to be confident that no catastrophic disbonding of the repair can occur due to environmental degradation or to service loading. To guard against failure in the patch system due to service loading the design approach is to ensure that shear and peel strains in the adhesive and composite patch, particularly the ends of the repair, shown in Figure 2.2, are maintained below the damage initiation threshold since disbond growth in this region has been found to be rapid (Baker, 1997; Hart-Smith, 1991).

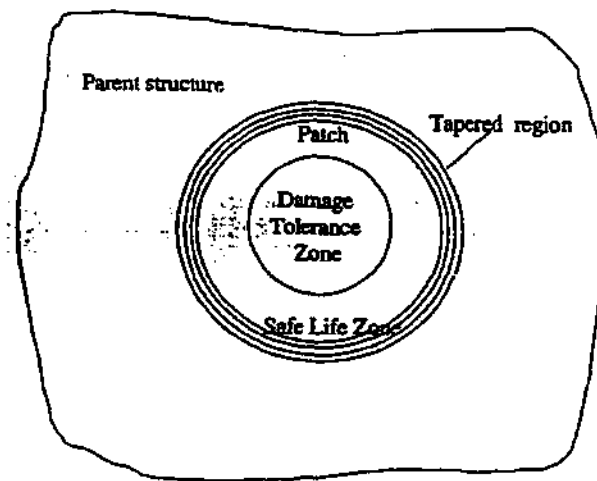


Figure 2.2 Schematic of a generic external bonded repair showing safe-life zone and damage tolerant zone (Baker, 1997).

Critical to the success of composite repairs of metallic aircraft structures is the integrity of the adhesive bonding between the base aluminium panel and the reinforcing high strength composite patch. For a certification process, a good understanding must be gained about the properties of the adhesive layer and the composite material. Monitoring of the bonding of a repair is important to ensure the composite patch integrity throughout the service life of the structure. Ideally, a non-destructive test would predict the strength of the bond. As found in previous investigations, this is very difficult to achieve, partly because a direct measurement of strength cannot be non-destructively made, so it is necessary to correlate strength with other properties such as bond area, stiffness or damping (Guyott et al, 1986).

Properties of the adhesive layer

Bonded repairs are achieved by bonding a repair patch on the aluminium parent structure with an appropriate adhesive. Adhesives have been used to connect materials for many centuries but the stresses in the adherends involved were usually very small. Modern adhesives have been used for less than 50 years. One of the first applications was in the Mosquito aircraft used in World War 2, and adhesive development has long been associated with advances in aviation. However structural adhesive joints are increasingly becoming a feature of general modern engineering construction. A number of adhesive joint types are shown in Figure 2.3.

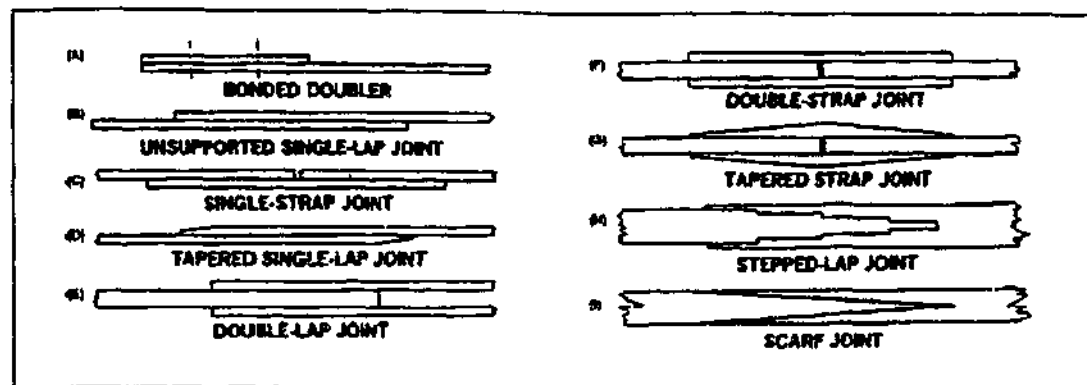


Figure 2.3 Adhesive joint types (Hart-Smith, 1974)

The most common form of adhesive joint is the overlap. Tapering of the adherends of the adhesive layer is often used to aid diffusion of loads through the structure, thus minimising the stress concentrations and maximising the joint strength. The joint strength depends on how the loads are carried by each part, and a weak link will lead to premature failure.

Adhesive joints offer advantages over bolts, rivets and other forms of localised connections. For instance, the stresses across the joint are more uniform, joint stresses are increased, sealing is achieved at the same time, machining is reduced and smoother external surfaces are attained. The low transverse and bearing strengths of composites often preclude the use of bolts and rivets unless load-spreading inserts have been bonded into the composite. In principle, adhesive joints are structurally more efficient than mechanically fastened joints because they provide better opportunities for eliminating stress concentrations; for example, advantage can be taken of the ductile response of the adhesive to reduce stress peaks. Mechanically fastened joints tend to use the available material inefficiently, while certain types of adhesive joints, namely scarf joints between components of similar stiffness, can achieve a nearly uniform stress state throughout the region of the joint.

Adhesive joints are capable of high structural efficiency and constitute a resource for structural weight saving because of the potential for elimination of stress concentrations, which cannot be achieved with mechanically fastened joints. Unfortunately, because of a lack of reliable inspection methods and a requirement for close dimensional tolerances in fabrication, aircraft designers have generally avoided

bonded construction in the primary structure of an airplane. Some notable exceptions include bonded step lap joints used in attachments for the F-14 and F-15 horizontal stabilizers as well as the F/A-18 wing root fitting (Hart-Smith, 1986). However bonded construction is used widely in repair patches.

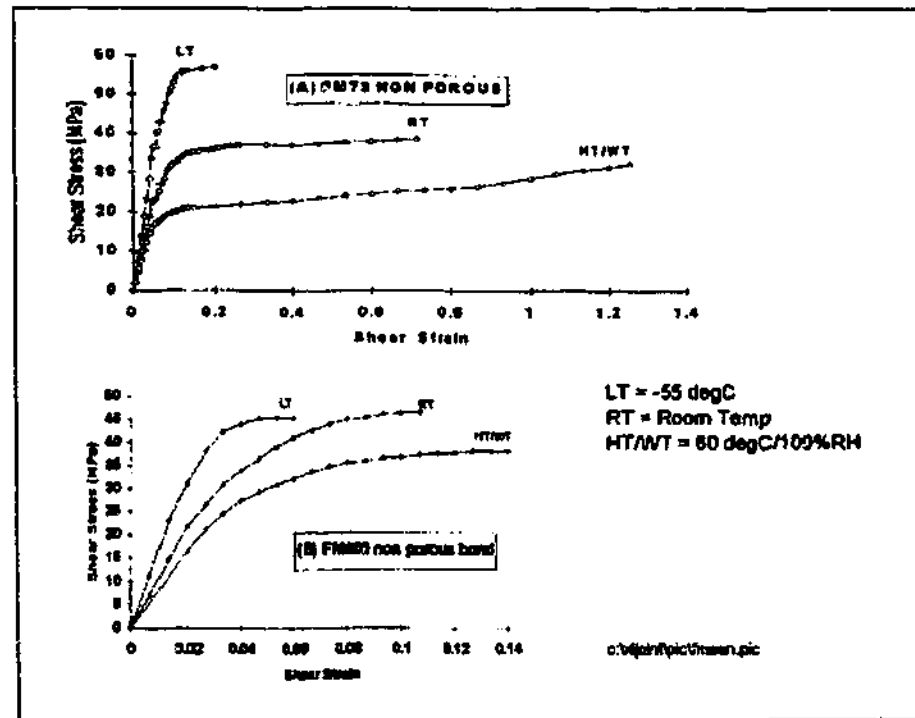


Figure 2.4 Typical characteristics of aerospace adhesives (Hart-Smith, 1978)

Adhesive ductility is an important factor in minimizing the adverse effects of shear and peel stress peaks in the bond layer. Figure 2.4 reproduced from Hart-Smith (1978) shows the shear stress-strain response characteristics of typical adhesives used in the aerospace industry as obtained from thick adherend tests. Figure 2.4, part (A) shows the characteristics of a relatively ductile film adhesive, FM73, under various environmental conditions, while Figure 2.4, part (B) shows the characteristics of a more brittle adhesive, FM400 under the same conditions. Even for the less ductile material FM400 it is clear from Figure 2.4 that ductility has a significant influence on the mechanical response of bonded joints, and restricting the design to elastic response deprives the application of a significant amount of additional structural capability. In addition to temperature and moisture, effects of porosity in the bond layer can have an influence on ductile response. Porosity effects are also illustrated in Figure 2.4, which compares the response of FM73 for porous and non-porous bond layers for various environmental conditions.

Properties of the composite patch

Some of the advantages of unidirectional boron/epoxy and graphite/epoxy composites for patch materials follow from their mechanical and physical properties given in Table 2.1, where they are compared with typical aircraft grade aluminium and titanium alloy.

Table 2.1 Relevant material mechanical and physical properties (Baker, 1988)

Material	Modulus GPa	Shear Modulus GPa	Critical Strain	Specific Gravity	Thermal Expansion Coefficient
Boron/epoxy (Unidirectional)	208 max 20 min	7	7.3	2.0	4.5 min 23 max
Graphite/epoxy (Unidirectional)	130 max 12 min	5	13-15	1.6	0.4 min 28 max
Aluminium Alloy (7075 T6)	72	27	6.5	2.8	23
Aluminium Alloy (7075 T6)	72	27	4.5	2.8	23
Titanium Alloy (6 Al/4V)	110	41	8.0	4.5	9

According to Baker (1988) the advantages of composite patches include

- (i) high directional stiffness, which allows use of the comparatively thin patches (important of external repairs) and allows reinforcement to be applied specifically in desired directions
- (ii) high failure strain and durability under cyclic loading, which minimises the danger of patch failure,
- (iii) low density, an important advantage where changes in the balance of a component must be avoided, as for example in the repair of control surfaces, and

- (iv) excellent formability, allowing low-cost manufacture of patches with complex contours.

Surface treatment of composite patches for durable adhesive bonding is much less of a problem than for metals, since surface abrasion is all that is required. Alternatively, composite patches can be co-cured on the cracked component with the adhesive, simplifying the patch fabrication procedure and also avoiding the need for any surface preparation of the patch.

In most repair applications the use of unidirectional patches (all 0° plies) will provide the highest reinforcement efficiency. The unidirectional composite generally has sufficient strain capacity to survive biaxial straining of the metal substrate without splitting. However, in some applications with high biaxial tension, it may be desirable to provide shear and transverse reinforcements. This can be achieved by incorporating a small proportion of plies oriented at $\pm 45^\circ$ and 90° .

The main disadvantage in employing composite patches results from the mismatch in thermal expansion coefficient between the composite and the metal, Table 2.1. When adhesives curing at elevated temperature are used to bond the patch, the metal can suffer a tensile residual stress that may adversely influence its performance in several ways.

Both boron/epoxy and graphite/epoxy have the above advantages and disadvantages for use as composite patch materials. However, boron/epoxy is considered to be the better choice because of its superior combination of strength and stiffness, higher expansion coefficient, which reduces the severity of the residual stress problem and low electrical conductivity, which avoids the danger associated with graphite/epoxy of inducing galvanic corrosion of the metal. The low conductivity of boron/epoxy allows use of simple eddy current procedures to detect and monitor cracks under the patch. However, graphite/epoxy would be preferable if patches with low radii of curvature were required (less than 30mm) or if boron/epoxy availability or cost was an important consideration.

2.2.3 RECENT SUCCESSFUL APPLICATIONS OF COMPOSITE REPAIRS

Composite repair patching of metallic aircraft structures is becoming an important technology in the maintenance and repair of ageing aircraft. When it is compared to the conventional Structural Repair Manual (S.R.M.) or Technical Order (T.O.) repair, a composite repair provides several advantages over conventional repairs including substantial repair cost savings, shorter aircraft downtime and better structural integrity (Chung, 1991). The composite repair is currently being performed on military aircraft externally and internally on an ad-hoc basis (Chung, 1993). When a repair is performed internally, access to the repair location for in-service non-destructive evaluation is rather limited or unavailable. In such cases, disassembly of the aircraft structure is required for inspections. These inspections are necessary during the service time of the aircraft for flight worthiness.

The use of bonded composites to repair cracking and other defects in aluminium airframe structures has been pioneered and extensively developed in Australia. Applications to primary structure, mostly in Royal Australia Air Force (RAAF) aircraft are included in Table 2.2 (Baker, 1999).

Table 2.2 Bonded applications on aircraft primary structures

Aircraft	Problem
C130	Stress corrosion cracked stiffeners in wing, aluminium alloy 7075
Mirage III	Fatigue cracking in lower wing skin, aluminium alloy AU4SG
F111-C	Secondary bending in wing pivot fittings leading to a fatigue problem, steel D6ac fastened to aluminium alloy wing skin
F111-C	Stress corrosion cracking in weapon bay longeron flange, aluminium alloy 7075-T6
F111-C	Stress corrosion cracking in longeron adjacent to refuel receptacle, 7049-T6
F111-C	Metal-to-metal and sandwich structure repairs. RAAF adopted GB + S and changed to FM 300 adhesive in 1992
F111-C	Pork-chop panel (lower fuselage). Panels rebuilt after repeated in-service failures
C141 (USAF)	Fatigue cracking in wing riser weep holes, 7075-T6
P-3C	Full depth corrosion damage in horizontal tail, aluminium alloy 7075-T6
Boeing 747	Simulated repairs to several regions including fuselage lap-joint, wing leading edge, trailing edge flap and engine thrust reverser cowl
Sea King helicopter	Fatigue crack in frame
F-111-C	Fatigue cracking in lower wing skin at fuel flow hole under forward auxiliary spar

The Aeronautical and Maritime Research Laboratory (AMRL) undertook a full-scale fatigue test of a Pilatus PC9/A aircraft with the aim of providing RAAF with data to enable the through-life structural fatigue management of RAAF's fleet of PC9/A aircraft. To enable the fatigue test to attain its goal of achieving greater than 50,000 simulated flight hours, AMRL-designed bonded boron/epoxy repairs were applied to these and other crack locations. Rapid application of these repairs ensured a quick restart of the fatigue test (Bartholomeusz et al, 2000).

The application of bonded boron/epoxy repairs to the PC9/A fatigue test article was successful in enabling the test to continue once significant cracking had occurred at several locations. Bonded repairs were probably the only option that could stop crack growth in the wing-skin, yet not significantly change the stresses in the tension spar boom. With just one exception, the patches applied to the PC9/A fatigue test article stopped the growth of cracks to which they were applied. The one exception was the original set of patches applied to the port uplock mechanism where the crack grew past one edge of the external patch within 1,500 simulated flight hours. These patches were tailored to meet the fatigue test constraints of not damaging nearby strain gauges and of not changing the spar cap stresses. Consequently thin patches were bonded to the uplock mechanism with a room temperature curing adhesive. The repair applied to the uplock mechanism at 38,000 simulated flight hours was applied without these constraints and consequently used a thicker patch bonded using FM73 at 80°C which was successful in stopping crack growth.

Figure 2.5 and Figure 2.6 show a PC9/A fatigue test article in its test rig. Common aeronautical defects include the disbond of repair patches as shown in Figure 2.1 and delamination due to impact damage. The use of adhesive bonding in primary structures has been limited by a lack of adequate non-destructive testing procedures. Without such procedures, the reliability of a structure cannot be guaranteed. Non-destructive inspection will usually be performed after manufacture or at stages during the manufacture; however in more stringent applications, continuous inspection during service may also be required. No reliable non-destructive testing method for the adhesion strength of a bond has been developed. Current standard practice in the aerospace industry is limited to test of the adherend surface prior to bonding.

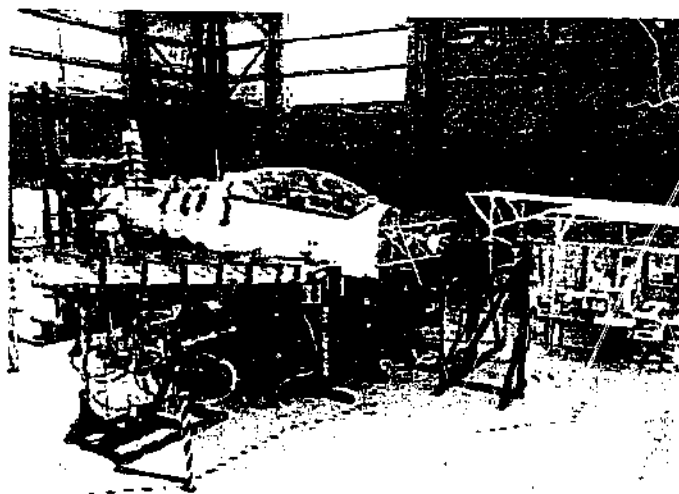


Figure 2.5 The PC-9/A fatigue test article (Bartholomeusz et al, 2000)



Figure 2.6 Photograph of the centre section of the lower wing-skin showing repairs (Bartholomeusz et al, 2000)

2.3 DISBOND OF COMPOSITE REPAIR PATCHES

Any structural health monitoring method must be able to detect a disbond in a composite repair. In this section, the background information on disbond of composite repair detected during service and typical causes for the initiation of disbond are presented. Useful information regarding the types and locations of disbond are also presented.

2.3.1 HISTORY OF COMPOSITE PATCH DISBOND

Disbond-type damage gives great cause for concern since large areas of this form of fracture can initiate under improper procedure of bonding, fatigue and stress. There exists, therefore, a clear need to identify and characterise damage in engineering composites at the earliest possible opportunity. The ideal damage detection method should be simple to use and be capable of identifying the initiation of disbonds.

Damage and general material degradation normally occur during the in-service operation of composite applications. Typical causes of such damage are continuous cyclic loading, rapid changes in local temperature, and impact loading such as that resulting from dropped tools or runway debris. Often, damage develops over a period of months or years, and it is not immediately visible even to the trained eye. However, once the size of the defect or stress-raiser reaches a critical value, failure can be catastrophic and the consequences severe.

Table 2.3 Composite patch fitment and disbond detection history (Chalkley and Geddes, 1998)

Wing number	Composite repair install date	AFHRS at install	AFHRS when disbond found
A15-3	28-Nov-91	3824.7	4584
A15-5	16-Apr-91	3983.2	4906.6
A15-10	31-May-90	3221.2	4286.2
A15-14	13-Jul-92	4414.8	5449
A15-19	9-Mar-92	4387.6	5620.8
A15-20	9-Mar-92	4387.6	5620.8
A15-284	29-Jul-92	5064.7	6068.7

There have been seven RAAF documented cases (Table 2.3) of F-111 wings with boron/epoxy composite patch disbonds including the wing intended for teardown inspection. The disbonds were detected between 759 and 1233 airframe hours (AFHRS) of service. However, many other wings have seen AFHRS of service within this range and greater without reports of disbonds. This, however, may be because of infrequent inspections. The first disbond was detected during repair of a fuel leak on

airframe wing in February of 1996. This wing had seen 759 hours of service before the disbond was discovered. A fractographic inspection of this wing performed at AMRL identified fatigue of the adhesive as a possible cause of the disbond. This wing has a plate thickness (Chalkley and Geddes, 1998) near the aft composite patch of only 0.225 inches compared to a fleet average of about 0.3 inches. Three wings with disbonds have been fitted to RF-111C airframes. Chalkley and Geddes (1998) consultation with the RAAF has shown that the RF variants typically carry large external fuel tanks on the outboard pivoting pylons more often than the standard F-111C's. Each of these fuel tanks carried 600 gallons of fuel and is over 2.5 meters long. The total weight of a pylon, tank and fuel is 4770lbs. This could have a marked effect on the torsion and bending loading of the wing and the measured strains at the wing pivot-fitting region.

2.3.2 TYPES AND LOCATION OF DISBONDS

Two types of disbonds generally occur (Pell, 1996): disbonding in the adhesive bondline caused by cohesive fatigue of the adhesive and inter-ply delamination of the layer of the boron/epoxy composite patch adjacent to the bondline. Earlier fractographic studies (Pell, 1996) and recent visual inspection of fracture surfaces from other wings suggest that disbonds initiate by fatigue of the adhesive at the doubler outboard edge and then after some inboard growth move into the first ply of the boron/epoxy doubler. Evidence of fibre failure, probably occurring during CPLT, has been found in wings A15-5 and A15-35 and is shown later in this section.

Peel stresses, i.e., through the thickness extensional stresses in the bond, are present because the load path in most adhesive joint geometries is eccentric. It is useful to compare the effect of peel stresses in single and double lap joints with uniform adherend thickness, since peel stresses are most severe for joints with uniform adherend thickness. The load path eccentricity in the single lap joint is relatively obvious due to the offset of the two adherends, which leads to bending deflection. In the case of double lap joints, the load path eccentricity is not as obvious, and there may be a tendency to assume that peel stresses are not present for this type of joint because, as a result of the lateral symmetry of such configurations, there is no overall bending deflection. However, a little reflection brings to mind the fact that while the

load in the symmetric lap joint flows axially through the central adherend prior to reaching the overlap region, there it splits in two directions, flowing laterally through the action of bond shear stresses to the two outer adherends.

On the other hand, the adherends tend to prevent lateral contraction in the in-plane direction when the bond is strained in the thickness direction, which minimizes the availability of ductility effects that could provide the same reduction of adverse effects for the peel stresses. This is what happens in the butt-tensile test in which the two-adherend surfaces adjacent to the bond are pulled away from each other uniformly. Here the shear stresses associated with yielding are restricted to a small region whose width is about equal to the thickness of the bond layer, near the outer edges of the system; in most of the bond, relatively little yielding can take place. For polymer matrix composite adherends, the adherends may fail at a lower peel stress level than that at which the bond fails, which makes the peel stresses even more undesirable.

It has been identified that composite repair patches disbond under fatigue conditions. Therefore this brings to light that the monitoring method must itself be functioning at high load cycles.

2.4 IMPACT DAMAGE OF COMPOSITE REPAIR PATCHES

Sensitivity to impact damage is one of the requirements of the certification process for composite structures in aeronautical applications (Baker, 1997). During impact on a flexible composite structure, matrix cracking initiates at the lower surface of the target and propagates upwards through the laminate forming planes of delamination. Matrix cracking frequently deflects planes of delamination from one-ply interface to another, and is in part responsible for the large areas of fracture observed following transverse impact loading. The fracture process of composite structure involves both macroscopic as well as microscopic failure mechanisms. Intralaminar cracking is a very common mode of failure in polymer composites. Although matrix cracking is frequently very localised and often extremely difficult to detect, it can, under

conditions such as fatigue loading, act as a precursor to delamination, a more detrimental form of damage.

Disbonded regions of the joint are essentially delaminations between the two adherends so the detection of disbond in adhesive joints is a very similar problem to the detection of delaminations in composite materials. If the adherends are of equal thickness, the defect is at midplane of the structure, which considerably simplifies the analysis. Disbonds or zero-volume unbonds can occur during manufacture due to the presence of a contaminant on an adherend or after manufacture as a result of impact or environmental degradation.

Delamination is one of the most frequently discussed modes of failure between plies of a laminated composite. It is a critical failure mechanism due to interlaminar stresses. The service environment of such composite structure gives static, fluctuating and impact stresses that can lead to defects. Local change in fracture characteristics causes the composite to dissipate its energy via delamination. Delamination has serious consequences on the compressive properties of long fibre composites. Interlaminar fracture reduces the stability of the load-bearing fibres resulting in a localised buckling-type of failure mode at low loads. In delaminations, the plane between two laminates is often a weak layer due to air entrapment during stacking and to excess resin. In unidirectional loading, interlaminar stress singularities have been shown to exist at free edges, which may cause delamination and other kinds of damage (Yin et al, 1996).

The vast majority research in the area of impact damage has considered unstressed coupons of particular composites laminates subjected to a range of impact energies. A few of previous studies have considered the effects of uniaxial pre-stress on the damage tolerance of composite structures (Butcher, 1979; Sandhu, 1985 and Kelkar et al, 1998). The only previously work which included the effects of biaxial pre-stress is Arnold et al (1995). Different coupon geometries have been employed in past experimental programs, e.g. square, rectangular and circular plan forms. Edge support conditions have generally been either simply supported or fully fixed. The particular choice of coupon geometry and support conditions has to a large extent been driven by either geographical or commercial preferences. Whilst limited use has been made

of the experimental evidence produced it is not possible to accurately correlate the various findings except in a general way.

A further and more serious difficulty facing those charged with assessing impact damaged composite structures, or incorporating appropriate allowable at the design stage, is translating the results of tests carried out on stress-free coupons to real composite structures, which invariably are under some form of applied stress when the impact loading occurs. With a few exceptions the initial stress state of the impacted structure dramatically changes the magnitude and form of resulting damage thereby rendering evidence from stress free coupon testing misleading at best.

Such difficulties have, over the years, necessarily led to a degree of pragmatism when assessing the damage tolerance of composite structures. For example, the US Air Force has recognised the aforementioned deficiencies and applied the inspection rule that "only visible indentations of greater than one tenth of an inch in composite airframes shall be worthy of detailed non destructive evaluation". Although easy to apply and without taking into account the real stress situation at the time of impact, this approach clearly points to a gap in knowledge. Moreover, it necessarily leads to concerns regarding the consequences of Barely Visible Impact Damage (BVID).

The "damage tolerance" of a structure can be considered as the inherent ability of a structure to continue to safely operate within design guidelines after some form of damage has been suffered. Although occasionally applied to processing faults such as inclusions or voids the term is generally understood to apply to the effects of impact damage. This in turn can be subdivided into hyper velocity (orbital space structures), ballistic (military or any full penetration of the structure) and low velocity impact damage (LVID). This latter category encompasses the vast majority of damage occurrences and generally is limited to impact energies of less than 12 Joules.

2.5 EXISTING NDE METHODS FOR DAMAGE DETECTION

There are a variety of non-destructive evaluation methods that can be used to determine the size and the location of damage in composite materials (Cantwell, 1992). These methods include ultrasonic, radiography, thermography, acoustic emission, eddy current, fibre optics, holography, Moiré interferometry, electromechanical impedance, system transfer function and the use of Lamb waves. These methods have different advantages and disadvantages and they are critically reviewed in this section. Since the last three methods listed offer greater potential for in-situ structural health monitoring, they are reviewed in more detail in section 2.6.

2.5.1 NON STRUCTURAL PARAMETER BASED ANALYSIS FOR NON DESTRUCTIVE EVALUATION

The thermography method depends upon the differential absorption and dissipation of heat in a damaged composite component. Two types of analysis are used, namely passive and active thermography. The former relies on an external heating source where normally uniform isotherms are distorted, and the latter on the internal heat generation from friction and fretting of fracture surfaces as a consequence of cyclic loading. The latter method is suited only to fatigue-loaded structures where a continuous heat generation process occurs. In the passive method, the surface of the component is subjected to a rapid temperature rise and the subsequent heat flow monitored. Since the flow of heat across a damage zone is reduced, defects such as impact damage result in the accumulation of heat, which can be detected by an infrared sensitive camera.

The effectiveness of the method depends upon the thermal conductivity of the material under investigation. Plastics and composite materials possess a relatively low thermal conductivity and thus are well suited to the use of thermographic methods. In the case of carbon fibre composites, the thermal conductivity in the plane of the laminate is approximately nine times higher than that in the through thickness direction (Stone, 1987). Thus the thermography method is best suited to the detection of gross delamination. It has the potential advantage of being able to monitor the

response of large areas when exciting at only one location. The degree of resolution depends, to a large extent, upon the thermal properties of the component as well as upon its thickness.

An alternative to the method discussed is radiography, which uses X- or γ -rays to inspect the cross section of a component. Radiography depends upon the differential absorption of radiation by the specimen or component under examination. The level of unabsorbed radiation that has passed through the coupon is monitored on a fluorescent screen, film or photosensitive paper. In order to improve the level of contrast between defects and the base material, a penetrant is usually applied to the coupon before examination. The choice of penetrant depends upon the level and type of damage within the composite. However, zinc iodide is frequently used since it is readily available, does not influence the mechanical properties of the laminate, and is not toxic.

X-ray radiography is an extremely useful method for identifying damage such as matrix cracking, delamination and extensive fibre fracture. If a fine grain X-ray film and a relatively high voltage are used, defects considerably less than 1 mm in size can be detected (Jones, 1988). However, in regions where damage is severe, the resolution of the method is limited, and differentiating between the various failure modes becomes difficult, if not impossible.

One of the difficulties of using radiography is the training required for radiographers to achieve proficiency. Medical radiographers spend years training to enable them to observe fine fractures in an otherwise healthy human body. In a similar fashion to the bones of the human body, each composite repair and adhesive layer differs by a small amount at least in thickness and width so it is very difficult to differentiate the damage condition. Furthermore, the method does not lend itself to inspection of large specimens, but is more suited to high-resolution damage characterisation. Large specimens like aircraft wings and fuselage would require X-ray equipments the size of a hangar and thus is clearly not practical for in-situ detection.

A Fibre Bragg grating (FBG) sensor is one of many optical fibre types used in the integration of sensors into smart composite structures allowing in situ process monitoring and continuous structural health check. It has attracted considerable attention since their development as strain and temperature sensors in the late 1980s. The use of FBGs as embedded sensors in fibre composite materials to provide in-situ measurements of strain, temperature, corrosion, vibration and state of cure has been reported in a number of studies (Morey et al, 1989; Kuang et al, 2001; Sivanesan et al, 1999). Kuang et al (2001) studied the post-fabrication FBG to examine the influence of manufacturing variables (such as composite stacking sequence and resin flow during processing) on the final profile of the spectrum and the functionality of the FBG sensor. This method is suitable for the application of detecting disbond growth under a composite repair patch. However the sensitivity of the method is questionable when the composite repair patch is of orthotropic type or quasi-isotropic type. Composite with plies orientation of $\pm 45^\circ$ and 90° are designed for applications with high biaxial tension. The fibre optics embedded in such composite patches tends to exhibit multiple peak spectra. Such spectra have been found to lead to strain measurement anomalies (Kuang et al, 2001).

2.5.2 WAVE BASED ANALYSIS FOR NON DESTRUCTIVE EVALUATION

Wave-based methods include the coin tap test, ultrasonic, acoustic emission and acousto-ultrasonic which depends on wave propagation. The coin tap test is one of the oldest methods of non-destructive inspection. It is regularly used in the inspection of laminates and honeycomb constructions. Until recently, however, the method has remained largely subjective and there has been considerable uncertainty about the physical principles behind it. The sound produced when a structure is tapped is mainly at the frequencies of the major structural modes of the vibration. These modes are structural properties, which are independent of the position of excitation. When a structure is struck with a hammer, the characteristics of the impact are dependent on the local impedance of the structure and the hammer used. The differences between the force pulses of the hammer can be quantified by the frequency content, which is achieved by carrying out a Fourier transform of the force-time record.

Time of flight inspection with ultrasonic waves is one of the most commonly used methods for detecting defects and damage in laminated composites. Damage is estimated using time histories of the input and vibration responses of the structure. Both the amplitude and the velocity of the ultrasonic signal received in the time domain is monitored. Attenuation of the ultrasonic signal occurs as a result of visco-elastic effects in the composite matrix, geometric dispersion due to the heterogeneity of the laminate as well as the dispersion due to damage or defects within the material. Increased attenuation also arises from an increase in vibration damping of the material due to miscuring (O'Donnell, 1978).

The ultrasonic velocity in a material may readily be obtained from the transit time of a pulse through the test component. The velocity of ultrasonic waves in the fibre plane is a function of fibre-volume fraction and orientation, and measurements of in-plane velocity can also be used to distinguish between fibre types of significantly different moduli. However, it is usually most convenient to perform the test in a direction perpendicular to the plane of the fibres. Speake et al (1974) have found that the state of cure of a polymer affects the modulus of the material and hence the ultrasonic velocity. The state of cure can therefore be checked by velocity measurement.

The usual method to monitor the amplitude and the quality of a composite plate is assessed by either the through-transmission method or by the pulse-echo method. Through-transmission uses two transducers while the pulse-echo method uses only one transducer. In both cases, it is essential that the transducers be coupled to the structure via a liquid or solid medium because of the severe impedance mismatch between air and solid materials. This is usually achieved by immersion testing or, for large components, by the use of water jet probes (Guyott et al, 1986). Immersion is often impractical for the large components and buoyant honeycombs that can be tested from the aircraft structure. Probes for the method can also induce contact pressure towards the test specimen.

Other methods of displaying ultrasonic reflections available are the A-, B- and C-scans, which can be chosen to show the defect required. The simplest presentation is an A-scan that gives information concerning the quality of a component at a single point. The amplitude of the arriving signal as a function of time, and its position

relative to those of the signals corresponding to the upper and lower surface of the target, give an indication of the severity and the through thickness location of the damage and defect.

The B-scan is essentially a linear collection of A-scans and is, therefore, equivalent to taking a slice through the sample. The time axis of the A-scan becomes the vertical axis in the B-scan. The third, a perhaps the most useful, type of ultrasonic method is the C-scan method in which the component is placed above a glass plate immersed in a bath of water, and the transducer sweeps back and forth across the component, receiving and analysing the signal reflected from the upper surface of the glass plate. The data are analysed by time gate, which converts the amplitude of the largest signal into a voltage, and the information presented on a current sensitive recording paper. The C-scan data are generally presented as a function of shade or colour. In one mode of data presentation, sound areas of the composite laminate are presented as black, severely damaged as white, and intermediate levels as varying shades of grey.

The ultrasonic C-scan method is ideally suited to the detection of delamination-type fracture between composite plies. However, the C-scan method suffers from several limitations for in-situ monitoring, such as the fact that the tank may have to be large in order to accommodate certain structural components, which in this case can be the aircraft wings. Further, the water/composite impedance ratio is much smaller than that of air/composite, so care has to be taken in order to ensure that water does not enter damage zones.

The ultrasonic backscattering method involves inclining the ultrasonic transducer at an acute angle normal to the test surface and then monitoring the echoes received by the transducer in pulse-echo mode as the component or the transducer is rotated about an axis normal to the component surface. When the angle of rotation is such that the transducer is normal to the fibre direction in any of the layers of the structure, the backscattered signal reaches a maximum. A plot of the signal intensity versus the angle of rotation may then be used to check structural integrity. If porosity is present, the backscattered signal is higher at all angles of rotation between the fibre directions than in a good structure (Bar-Cohen et al, 1982).

Acoustic emission relates to the generation, propagation and detection of stress waves in materials as they undergo deformation and fracture. These waves propagate to the surface of the material where they are detected by a transducer. In general, applying a moderate stress to the component precipitates acoustic events. The method is capable of detecting most of the failure modes associated with composite materials but suffers the disadvantage that it is not easy to differentiate between them. Cohen et al (1988) concluded that the emissions caused by the friction and rubbing of fracture surfaces within the composite exceeds, and therefore, may conceal emission activities associated with the actual fracture process. Acoustic emission is also hindered by the fact that composite materials tend to attenuate and disperse propagating stress waves. As a result, it is usually necessary to use a number of transducers on large or complex structures.

Further limitation of this acoustic emission monitoring is the need for damage to occur, whilst observation occurs. This may be achieved with a sophisticated analysis and acquisition package. An alternative to waiting for damage to occur is to deliberately load the structure and listen to the response obtained (Bennett, 1999). In this process, the applied loads may damage the structure further. The acoustic emission method is perhaps best suited to the proof testing of composite structures or long term monitoring of structural health via repeated testing over a period of time.

A modification was made to the acoustic emission method by Srivastava et al (1987) and Dokun et al (2000) to improve the actuation signal. Srivastava et al (1987) showed that fatigue life could be determined from a combination of acoustic emission and ultrasonic. It was shown that fatigue life could be determined from the parameter known as stress wave factor. Flexural fatigue tests on a cross-ply glass fibre-reinforced plastic (GRP) composite indicate that, for specimens with maximum values of stress wave factor, the required number of cycles to failure is maximised. In this work, a higher value of stress wave factor indicates good quality composites. In this respect, the stress wave factor can be an aid in predicting the fatigue life of such materials.

An alternative to applying a large low frequency load to the structure is to apply a small high frequency load at one point and observe the response obtained, either at

that point or at another. The principle of this is to determine a characteristic of the component's ability to transfer energy, which may be related to the response. Vary (1977) describes this technique as acousto-ultrasonic, since it uses principles of ultrasonic excitation and analysis techniques from acoustic emission. In a study on the ultimate performance of composite materials, Vary et al, (1977) reported that the acousto-ultrasonic approach provides a potential alternative to the widely used acoustic emission and ultrasonic methods for verification of composite integrity and strength, as well as degradation due to service condition. In this acousto-ultrasonic method, an ultrasonic pulser is used to inject discrete ultrasonic pulses into the material under test and the ultrasound is allowed to interact with the internal features of the material i.e. the micro structural environment within the material. The resultant waveform provides a modulated signal, which is picked up by an acoustic emission sensor. The acoustic emission signal thus obtained is then suitably processed and digitised to provide a measure of the quality of the material under test. Since the sensor used is similar to the acoustic emission, it will also encounter difficulty in separating the emissions caused by the friction and rubbing of fracture surfaces from the actual fracture process.

2.5.3 VIBRATION BASED ANALYSIS FOR NON DESTRUCTIVE EVALUATION

All vibration-based methods are related. The basic idea of these methods is that modal parameters are functions of the physical properties of the structure. Therefore, changes in the physical properties, for example, delamination of composite plies, will cause changes in the modal properties. Usually, damage will locally decrease the mass and stiffness of the structure and increase the damping ratio. Among the three structural property parameters, mass is less sensitive to damage while damping is the most sensitive to damage. Due to its complex physical nature, proportional damping is often adapted in damage detection methods.

Modal analysis is a common analytical method for the detection of damage between composite plies. Researchers have proved the existence of the 'delamination modes' in composite beams theoretically and experimentally (Hanagud et al, 1994; Nagesh Babu et al, 1990). The model-based methods undertake analysis of structural models

under vibration and are usually implemented by Finite Element Analysis (FEA). Damage growth is simulated in FEA by modifying the models by including predetermined damage sizes. Experimental data can then be compared with the analytical data to determine damage location and its extent. With the model, various response characteristics of the structure such as modal analysis and transient response can be extracted and analysed.

Modal analysis methods utilise the information for all modal parameters or combinations of some of them to detect damage. The methods can be categorised into global methods, in which the integrity of the whole structure is assessed using the excitation and measurement at a single point of the structure and local methods, in which measurements are taken at each point of the structure. Global methods offer the possibility of very rapid testing, but unfortunately they are not very sensitive. The local methods may be further divided into those requiring only a single excitation at each measurement point (Adam et al, 1985). The effectiveness of the whole group of model-based methods, however, is dependent on the accuracy of the structural model and these methods may have difficulties when applied to complex structures (Tappet, 1995; Sato, 1993).

Damage may also be detected by using the frequency response of the structure. Islam and Craig (1994) analysed the frequency-response of a structural member and determined the type of damage and its location on the basis of the shift in natural frequencies. The findings of these authors are consistent with Adams et al (1978) who showed that damage is usually accompanied by a local reduction in stiffness and an increase in damping. Increasing damage sizes leads to decreasing structural stiffness, which in turn causes decreases in natural frequency (Salawu, 1997). Natural frequency measurements have been used to quickly check the volume fraction and winding angle of filament-wound components; changes of around $1 - 1.5^\circ$ in winding angle or 4% in volume fraction are detectable (Cawley et al, 1985). Therefore the extent of damage can be estimated from the degree of change in natural frequency since it depends on the position of the defect for a particular mode of vibration (Rytter, 1994). Further, Adams et al (1978) found that local and distributed changes in

stiffness, produced changes in natural frequencies that varied depending on the damage location.

A formulation of a composite beam was developed based on Timoshenko beam theory and the Galerkin method to analyse a delamination effect on natural frequency and vibration mode shape of composite laminated beam (Shen, 1992). This model was extended by Zou et al (2000) to account for the effects of delaminations on the higher modes. The coupling effect between longitudinal vibration and transverse bending motion was considered and their results showed that it affected frequency response significantly. Barbero (1991) developed a finite element model using layer-wise theory in which it was assumed that the same displacement distribution in the individual layers was capable of representing displacement discontinuity conditions at interfaces between layers. The model can be used to study multiple delaminations through the thickness of the plate.

In general, delaminations decrease stiffness and increase damping of the structure. These changes in turn decrease the frequencies and increase modal damping in delaminated structures. In the study by Shen et al (1992), they concluded that the extent of frequency shifts in a particular mode of vibration caused by a delamination depends on the size and location of the delamination in the structure. It was also found that local delaminations do not have a noticeable effect on the global mode shape of vibrations of composite beams. Frequency shifts occurred in the modes where the wavelength was approximately the same size as the disbonded area. From these studies it is clear that damping is normally more sensitive to delamination as compared to stiffness. Therefore it is a better indicator for small crack lengths on a composite.

As only frequency information is required, these approaches can provide cost effective structural assessment techniques. However, natural frequency changes alone may not be sufficient for a unique identification of the location of structural damage (Sanders et al, 1992, Ceravolo and Stefano, 1995). Current frequency domain methods either uses lower frequencies for providing global information of structures or uses higher frequencies for providing local information of structures. It has been

found that none of these can provide sufficient information for the detection of both small and large defects.

Apart from the frequency domain, damage detection can be conducted in the temporal domain. Banks (1996) used transient response over a long period, while at the same time taking into account the information in several modes so that the damage evaluation is not dependent on any particular mode. The advantage of this method is that they can detect damage situations both globally and locally by changing the input frequencies.

Most of these temporal dependant methods require the flaw to be perpendicular to the direction of propagation of the wave. However when the flaw is horizontal to the direction of propagation of the wave, the flaw may not be detectable. This is because these methods rely on the reflection of waves by the flaw, a method known as the pulse-echo method. In addition some of these methods might not be suitable for in-situ monitoring because they involve the requirement for bulky instrumentation.

In summary, thermography, Moiré interferometer, Fibre Bragg's grating and modal analysis are only able to detect gross disbond. Other methods like x-ray and radiography are not suited for in-situ structural health monitoring, but is more suited for high-resolution damage characterisation. Eddy current and acoustic emission is not suited for the composite applications due to attenuation and dispersion of stress waves. However the electromechanical impedance method, system transfer function method and Lamb waves can potentially be used for the in-situ structural health monitoring.

2.6 THREE POSSIBLE EXISTING METHODS FOR MONITORING THE STATED PROBLEMS

Stiffness-based monitoring approach is found to be an effective means for the detection of incipient disbond growth and delamination of composite patches. The practical excitation and measurement of each method is reviewed in this section for the possibility of functioning in conjunction for the detection of damage.

2.6.1 THE PRACTICAL EXCITATION AND MEASUREMENT OF ELECTROMECHANICAL IMPEDANCE METHOD

A fourth possible analytical domain apart from those mentioned in the previous section is the impedance domain. The basis of this method is that each part of the structure contributes to the impedance of the structure to some extent. Any variation in the structural integrity will generally result in changes in the impedance.

The first non-destructive method of interest is based on mechanical vibration. The use of vibration analysis for the detection of delamination of thick composites has been attempted previously (Sanders et al, 1992). Penn et al (1999) explored the use of polyvinylidene fluoride (PVDF) films for the detection of delamination of both thin and thick composites. The specimens were investigated both in clamped and unsupported configuration and excitation was done using a hammer tap. It was concluded that the free vibration method using PVDF elements as sensors was able to detect in thin plates delaminations as small as 0.34% of the plate area. The authors observed dramatic shifts in natural frequency with varying delamination sizes. One of the major shortcomings of these methods is that they do not allow for the determination of the stress field in the vicinity of impact-damaged zone. This is an acute problem when composite repair is performed internally of an ageing aircraft; there is rather limited or unavailable access.

It has received much attention for damage detection in thin walled composites (Shen, 1992). A variety of low-frequency vibration methods are used in non-destructive testing (Adams and Cawley, 1985). These methods exploit the fact that the vibrational

characteristics of a structure are determined by its geometry, boundary conditions and viscoelastic properties. In composites, internal damage can have consequences to all of these. This approach is attractive because of its simplicity and properties can be measured at a single point on a structure, hence access is not required to the whole structure. Free vibration is initiated by a single mechanical input and is sensed by transducers. In composites, internal damage can have consequences to all these dramatic decreases in natural vibrational frequencies and significant increases in damping have been found to occur as a result of the introduction of delaminations or other damage in the composite.

The mechanical impedance method is also a form of vibration method and can be used to detect delaminations through measuring the changes of impedance in the structure (Cawley, 1984; Giurgiutiu and Rogers, 1998). It has been used for many years in the former Soviet Union (Lange and Moskovenko, 1978). This method models the defect as a spring and assumes that it is clamped around the edges of the defect. The basis of this method is that each part of the structure contributes to the change in impedance of structure. The point impedance at a disbond or delamination is lower than that in good areas of structure so impedance measurement can be used to detect these defects. The point impedance, Z , of a structure, can be defined as

$$Z = F/v \quad \text{Equation 2.1}$$

where F is the harmonic force input to structure and v is the resultant velocity of the structure.

Any global or local changes in the structure will result in changes in the impedance due to the changes in the stiffness of the overall structure. The impedance change produced by a given defect size reduces as the defect depth increases, so the test is most sensitive to defects close to the surface. The impedance method is most suitable for detecting planar defects such as delamination of composite layers (Cawley, 1984; Adam and Cawley, 1988) as shown in Figure 2.7.

Rogers and Lalande (1996) used the impedance method and real-admittance measurements to determine the presence of a reduction in tension in the bolts connecting the vertical tail to the rear fuselage. Admittance of the piezoceramics was

recorded between 100- and 150-kHz. They found that changes in the natural frequencies, of the piezoceramic-tailplane system, could be used to detect local, relatively small changes in the tension of the connecting bolts. It was also found that the response of the piezoceramics was insensitive to remote damage.

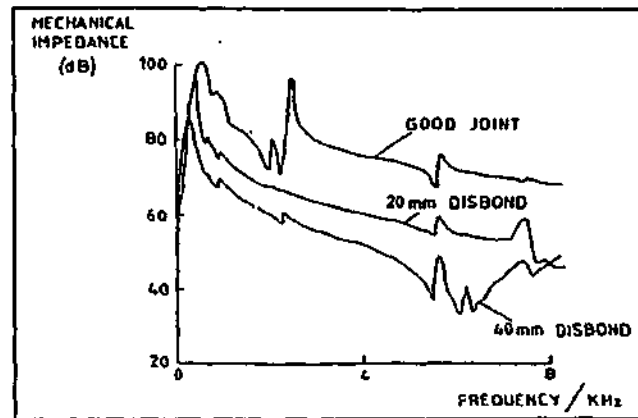


Figure 2.7 Mechanical impedance against frequency for a thick beam with an adhesively bonded skin 3.3-mm thick (Cawley, 1984)

Experimental investigations by Pohl et al (2001) with strip-shaped specimens show close connection between mechanical properties and impedance. They found that damage caused by low-speed impact could be experimentally and theoretically detected by changes in the impedance resonance peaks. In their study, disturbing factors such as ageing effects, mechanical loading and different electrical contacting has an influence on the structural impedance. Electrical impedance is defined as the voltage drop across an element divided by the current through the element. The presence of electrical resonance and anti-resonance make the piezoelectric impedance unique. The resonance results from the electrical input signal exciting a mechanical resonance in the piezoelectric element. For each mechanical resonance in the piezoelectric element, a resonance/anti-resonance pair will exist in the impedance.

Figure 2.8 gives an estimate of the minimum detectable defect diameter versus depth in aluminium and carbon fibre reinforced plastic structures. These curves assume a stiff base structure and that the impedance of the defective zone must be at least 3-dB lower than that of the sound zone for the defect to be reliably predicted. The method is less sensitive with the carbon fibre composite owing to the reduced contact stiffness obtained from the material.

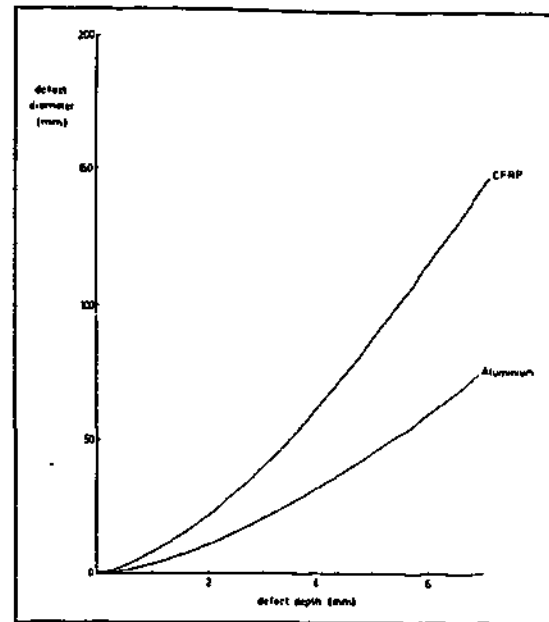


Figure 2.8 Minimum detectable defect diameter against depth in aluminium and carbon fibre composite assuming 3-dB reliability in impedance measurements (Cawley, 1984)

Chaudhry et al, (1995) used a vibration signature-based method to qualitatively identify a disbond. They found that this method is sensitive towards very minor disbands as small as 1/4 inch slit as shown in Figure 2.9 as well as crack growth on the base structure. The vibration signature is obtained as a variation in electrical impedance of the piezoelectric patch, while driven by a fixed alternating electric field over a frequency range.

It has little in common with the traditional modal-analysis based methods. The fundamental difference lies in the frequency range used to interrogate, i.e., excite and sense the vibration pattern of the structure. The frequencies used are typically in the high kHz range which are much more conducive to finding incipient damage like small cracks, loose connections, and delaminations. The other difference lies in the manner in which the structure is excited and the vibration signature acquired, i.e., through non-intrusive surface-bonded PZTs.

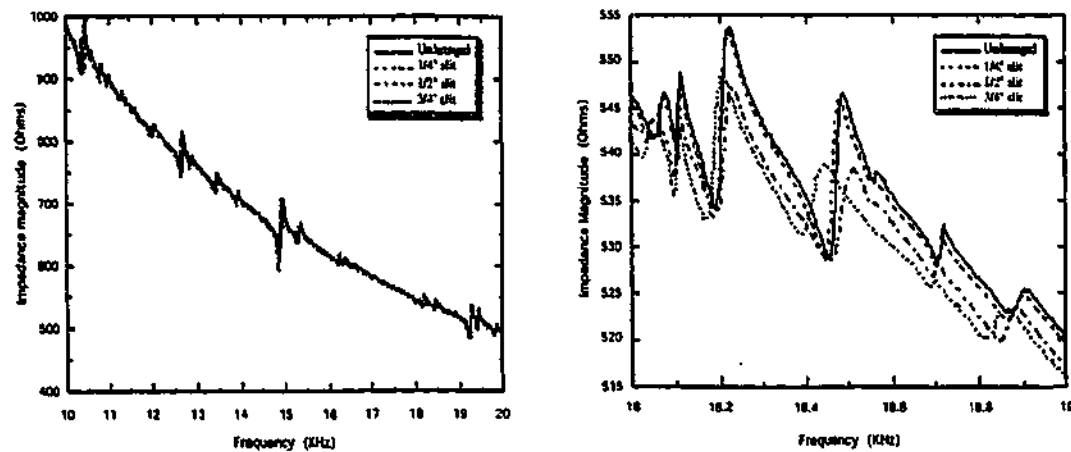


Figure 2.9 Effect of the disbonding on impedance magnitude from Chaudry et al (1995)

In this experiment by Chaudry et al the disbond damage was created by forcing a flat screwdriver to depths of 0.25 in., 0.50 in., and 0.75 in. between the composite repair patch and the substrate. The resulting impedance measurements are shown in Figure 2.9. It can be observed that the progressively deeper disbonds produced clear variations in electrical impedance. However there are limitations in their experiments where the results did not reflect a quantifiable progressive change in parameter measured with the severity of damage. It is difficult to see from the graphs shown in Figure 2.9 how the claims were made on damage detection index. At high frequency, impedance measurements are also found to band together. Therefore taking measurements at high frequency to detect incipient damage can be a self-defeating process.

2.6.2 THE PRACTICAL EXCITATION AND MEASUREMENT OF TRANSFER FUNCTION METHOD

Another frequency-based method, which is similar in principle to frequency response, is an approach called system transfer function. It is finite element model independent, and actively interrogates the structure though broadband excitation across the desired frequency. The potential advantages of this approach include simplicity since it is model independent, sensitivity and low cost implementation.

The ADI system developed by Lichtenwalner et al (1997) utilises measurement of the system transfer function between pairs of PZT transducers for damage detection and localisation. The system transfer function provides essentially the same information as that of the cross-electromechanical impedance function, but can be computed with less costly equipment. They developed algorithms using MATLAB software from The MathWorks, Inc. to compute transfer functions via Fast Fourier Transform (FFT) and to perform the statistical process necessary for damage detection and localisation. The severity of damage is quantified by means of statistical analysis of the changes in transfer functions between the actuator/sensor pairs.

This was an extension of an earlier work done by Castanien and Liang (1996). Castanien and Liang (1996) used cross-electromechanical impedance between pairs of PZT transducers to aid in monitoring a larger area of structure while still providing some localisation capability. They detected and localised rivet line failure in a section of metallic aircraft fuselage using a spectrum of 0- to 2-kHz. Lichtenwalner et al (1997) varied from Castanien and Liang (1996) in terms of their statistical process. They compared each transfer function magnitude spectrum, for all actuator and sensor pairs to a baseline transfer function computed by averaging several sets of data in the undamaged state. The difference between the current transfer function and the baseline is normalised by the standard deviation associated with the baseline. Consequently, the transfer function deviation was represented in terms of the number of standard deviations from the baseline. The statistic, which hence was known as TF Delta, was further processed by a windowed local averaging function to reduce minor variations due to random noise. The Windowed Delta was then integrated over the entire frequency spectrum to produce the Cumulative Average Delta, which provided them with a single metric assessing the magnitude of change in a particular transfer function. The statistical process that was used by them is similar to the 'Sumdelta' statistic used by Mitrovic et al (1995) for detecting delamination in a composite panel.

They conducted their damage assessment studies on a composite structural component of the MD-900 Explorer Flexbeam from the helicopter rotor system. Damage was initiated at the wide portion in the offal region of the flexbeam using a cutting blade and a Dremel tool. The first notch was about 0.25 of an inch at the base end of the wide offal region and extended at the rate 0.25 of an inch each time until 26

successive notches has been made. Their results show a general trend of increasing delta with successive damage. The ADI system was able to detect those notches assess its severity as shown in following Figure 2.10.

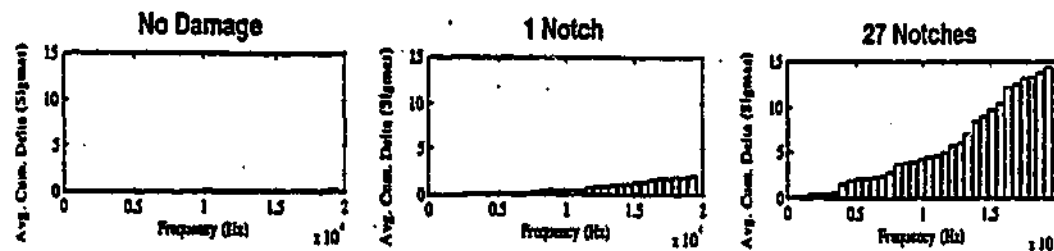


Figure 2.10 Cumulative average delta spectrums with successive damage (Lichtenwalner et al, 1997).

2.6.3 THE PRACTICAL EXCITATION AND MEASUREMENT OF STRESS WAVE METHOD

There has been a considerable amount of work in the development of inspection methods that can be used in-situ. Two methods are of interest in this research, one, which involves a vibration signature obtained from low frequency excitation of mechanical vibrations, and the other, which involves the generation and detection of ultrasonic waves using piezoelectric transducers in a plate-like structure. At high frequency, apart from the previously mentioned ultrasonic methods, Rayleigh waves and Lamb waves are also alternatives. The main idea behind the second method of interest is the generation of a single Lamb mode over a controlled frequency bandwidth.

The fundamental behaviour of Lamb waves in plate structures has been reported widely (Lamb, 1917; Worlton, 1957; Viktorov, 1970; Auld, 1990). Lamb waves refer to elastic perturbations propagating in a solid plate with free boundaries, for which displacements occur both in the direction of wave propagation and perpendicularly to the plane of the plate (Viktorov, 1967). Lamb waves represent one of the types of normal or plate modes in an elastic wave-guides, in this case a plate with free boundaries. For this reason, Lamb waves are sometimes simply called normal modes in a plate.

Many researchers have investigated the use of Lamb waves to inspect plate-like structures, the first of whom was Worlton (1957). Over the past 40 years those researchers have recognised the potential of Lamb waves in the NDE of metal structures and the use of Lamb waves for the NDE of composites has also been extensively investigated. Guo and Cawley (1993) and Guo and Cawley (1994) reported on the use of this method for the non-destructive evaluation of delamination in composite laminates and large composite laminates.

The advantages of using Lamb waves for fast inspection has been recognised, where some reduction in sensitivity and resolution compared with that of obtained standard, high-frequency ultrasonic inspection can be tolerated. Mansfield (1975), Ball et al (1973), Chimenti and Martin (1991) and Cheng and Berthelot (1996) have studied the application of Lamb waves to detect defects in composite plates. The use of Lamb waves is potentially a very attractive solution to this problem since they can be excited at one point of the composite laminate and can be propagated over considerable distances along the laminate. A large region can therefore be interrogated for each transducer position.

Lamb waves are also used in localised non-destructive testing applications as an alternative to conventional ultrasonic testing using bulk waves. In this localised application, the dispersive nature of Lamb waves is not so problematic, as the propagation distances are relatively small and reasonable signal-to-noise ratios may be maintained in most frequency-thickness region. Nayfeh et al (1988) and Mal et al (1991) have used Lamb waves to determine the elastic properties of materials. Beard and Chang (1997) demonstrated the feasibility of using piezoelectric transducers to generate and detect Lamb waves for the purpose of damage detection in a filament wound composite tube.

Bork and Challis (1995), Rokhlin (1991) and Todd and Challis (1999) have investigated the propagation of Lamb waves through bonded joints. Rokhlin (1991) studied the interaction of different Lamb modes with disbonds in adhesive joints in which plates of equal thickness are joined by a layer of adhesive. Rokhlin and Bendec (1994) investigated the transmission of Lamb waves through a welded joint connecting two elastic layers. The transmission coefficient was used as for estimating

the dimension of the contact region, which is an important parameter for evaluating the strength of a welded joint.

Excitation of Lamb wave

Lamb wave testing is complicated by the existence of at least two modes at any given frequency. In Lamb wave propagation, the vibration pattern through the thickness of the plate are quite different for different Lamb modes and are different even for the same mode at different frequencies. It is difficult to generate a single, pure mode, particularly above the cut off frequency-thickness of the a_1 mode. More than one mode is always possible and its through thickness deflected shape is a function of the frequency-thickness. The modes are also generally dispersive, which means that the shape of a propagating wave changes with distance along the propagation path (Alleyne and Cawley, 1992).

Propagation in composite materials is even more complicated due to the anisotropy, the complex attenuation mechanisms, and the inhomogeneous nature of the materials through the thickness of the laminate. These difficulties have tended to reduce the attractiveness of Lamb wave testing.

Numerical analysis of Lamb wave propagation

Due to the predominantly analytical nature of the previously mentioned work, the number of different cases investigated is rather limited. In using finite element methods, a variety of boundary conditions can be analysed with careful processing of transmitted Lamb wave signals. Explicit finite difference schemes were the first numerical methods to be applied to investigate the propagation and scattering stress waves. Temple (1988) has used finite difference schemes to model bulk wave propagation in inhomogeneous media and Bond et al (1984) have used finite difference schemes to model the scattering of stress waves from surface features.

Figure 2.11 shows the predicted phase velocity dispersion curves in the frequency-thickness product range from zero to 4 MHz-mm for a unidirectional laminate, in which the wave is assumed to propagate along the fibre direction. It can be seen from the above figure that apart from the fundamental asymmetrical mode, all the curves

have a flat region around 8800 m/s where it is relatively non-dispersive which makes them suitable for long range testing.

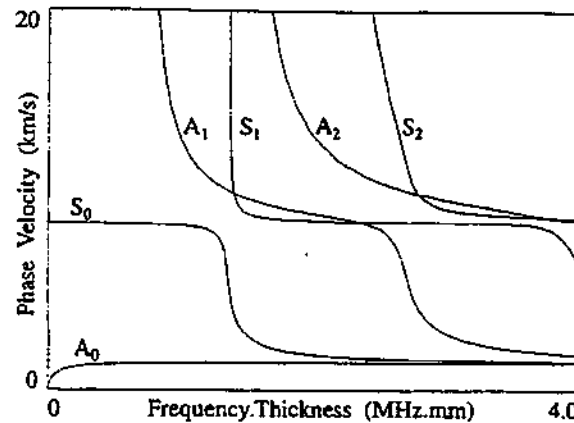


Figure 2.11 The calculated dispersion curves of a unidirectional laminate from Guo and Cawley (1993)

2.7 PIEZOELECTRIC TRANSDUCERS

Studies have been done on in-situ structural health monitoring using different types of sensors and actuators. Commonly used ones are piezoelectric materials, electro-rheological fluids, shape memory materials, magnetostrictive materials, electrostrictive materials and thermal materials. Piezoelectricity is an electro-deformation phenomenon derived from a Greek word, which is similar to electrostriction. It is a property of all dielectrics. A material is said to be piezoelectric if it has a high degree of piezoelectricity in which when the material deforms it produces a significant electrical change.

Electrostriction phenomenon can be described as a small change of geometry of a body when it is subjected to an electrical field. If the direction of electrical field is reversed, the direction of the small change in geometry of the body will remain unchanged. In contrast to this, piezoelectric materials exhibit a reversal in the direction of geometrical change when the direction of the electrical field is reversed. They can be regarded as a unique class of non-conducting class of materials (Gandhi, 1992). These piezoelectric sensors offer an excellent choice in a simple, low cost detection system.

2.7.1 MECHANICAL PROPERTIES OF PIEZOELECTRIC MATERIALS

The suitability of piezoelectric wafer elements for in-situ health monitoring is due to the controlled strain mechanism produced by an electrical charge that is governed by a linear constitutive relationship. Mathematically, piezoelectricity is described as a nominally linear relationship between the strain of the material and its electrical charge given by ANSI/IEEE Standard 176-1987, as shown in the following tensorial relation.

$$S_i = s_{ij}^E T_j + d_{mi} E_m \quad \text{Equation 2.2}$$

$$D_m = d_{mi} T_i + \varepsilon_{mk}^T E_k \quad \text{Equation 2.3}$$

The mechanical variables in the above equations are the stress T and the strain S , and the electrical variables are the electric field E and the electric displacement D . ε_{mk}^T is the dielectric permittivity measured at zero mechanical stress ($T=0$), d_{mi} is the piezoelectric coupling between the electrical and mechanical variables and s_{ij}^E is the mechanical compliance of the material measured at zero electric field ($E=0$). The first equation refers to the converse piezoelectric effect while the second equation reflects the direct piezoelectric effect. A piezoelectric sensor or actuator is made by metallising the upper and lower surfaces of flat sheets of the piezoelectric material, effectively producing a capacitor, which charges itself when deformed and deforms when charged. However the high leakage of these piezoelectric 'capacitors' makes them insensitive to slow variations in strain.

There are two particular types of piezoelectric materials that are of interest and they are the lead zirconate titanium (PZT), a ceramic material that is stiff and brittle, and piezopolymeric film polyvinylidene fluoride (PVDF). Penn et al (1999) pointed out several advantages in using piezoelectric polymeric material as sensors in place of strain gauges, namely that they require no external power source and they generate signals far stronger than those of traditional amplified strain gauges. PVDF operates over much wider ranges of voltage, stress, and frequency than do piezoceramic sensors. Since PVDF is a plastic it has properties like toughness, compliance, and

resistance to fatigue and abrasion. However it lacks the actuation authority of the piezoceramic device.

The high stiffness of piezoelectric ceramics gives them good actuation authority with much faster response than mechanical systems (Crawley et al, 1989; Eyraud et al, 1998). Due to its brittleness, piezoceramics are limited to very small strains and exhibit non-linear response and hysteresis (Crawley and Anderson, 1990). Rogers and Lalande (1996) used piezoceramics both as sensors and actuators to monitor the structural integrity of an aircraft fuselage.

Since the piezoelectric sensor's signal can only be outputted through the electrodes on it, the method of attaching the electrodes on the piezoelectric film is also very important. One way is to use a scanning probe, which can be regarded as a 'moving' electrode and a continuous curve of voltage distribution can be obtained, but it is not suitable for real time assessment. Another possible approach is to locate electrodes point by point, i.e. by recording voltage of each isolated point so that the distribution curve can be made, just like that carried out in the finite element approach. It is evident that the larger the number of electrodes, the more precise is the final results.

The piezoelectric transducers used in this project are thin piezoelectric transducers surface bonded to the host structure. In this configuration, mechanical stress and strain are applied in the x and y directions, i.e. in the plane of the surface, while the electric field acts in the z direction, i.e. normal to the surface. Hence the significant electro-mechanical couplings for this type of analysis are the z - x and z - y effects. The application of an electric field, E_z , induces surface strains in S_{xx} and S_{yy} directions and vice versa. For a piezoelectric transducer affixed to a 1-D, e.g. a beam along the x -direction, the analysis is mainly one-dimensional. In this case, the dominant electro-mechanical coupling constant is d_{zx} . If the transducer is placed on a 2-D the surface, the analysis is, in principle, two-dimensional. Since the coupling constants, d_{zx} and d_{zy} , have essentially same value, radial symmetry can be applied, and the analysis becomes one-dimensional in the radial coordinate, r .

2.7.2 APPLICATIONS OF PIEZOELECTRIC MATERIALS

Piezoelectric transducers are easily integrated into load bearing structures without significantly altering the passive static or dynamic stiffness characteristics of the structure. Due to the low structural impedance of piezoelectrics, a number of piezoelectric films or patches can be distributed along the structure with only minor effects on the structure's mechanical properties. The film or patches can be readily cut and shaped to conform to the given structure. It is important to note that there is an optimum size and an optimum placement or arrangement of piezoelectric sensors to give maximum sensitivity for the various damage cases and load conditions (Galea et al, 1993; Egusa and Iwasawa, 1996). These sensors are especially good for incorporating into a composite, usually attached or embedded into a structure, and thus are the ideal sensors to constitute an 'active' system for structure damage monitoring and on-line health monitoring.

Currently, piezoelectric materials are used in a variety of commercial applications including

- acoustics for noise cancellation (Clark and Fuller, 1992), with applications to reduce interior noise in aircraft;
- aerodynamics with applications to adjust wing surfaces (Barrett, 1992);
- ultrasonic scanning devices with applications to medical diagnosis (Liu, 1999);
- phonographic pickup cartridge where the vibrational motion of the phonograph stylus is converted into a time-varying electrical signal with applications to microphones where sound pressure waves are converted into voltages;
- devices for controlling the frequency of electrical signal, with applications to where only signals of a specific frequency can pass through (Gandhi, 1992);
- electronics for applications where they are used in the reading heads in video cassette recorders and in compact discs as positioning devices (Huber et al, 1997);
- shape control of beam under general loading with applications to minimize the maximum deflection of the beam (Bruch Jr, 2000); and

real-time qualitative health monitoring methods for application to local damage detection of civil infrastructures such as bridge joints, metallic structure bond lines, composite repair patches in metallic structures and aerospace structures (Chaudhry et al, 1995).

Attention has focused on the use of surface-mounted sensors (Penn et al, 1999; Chaudry et al, 1995; Lichtenwalner et al, 1997; Ayres et al, 1996; Rogers and Lalande, 1996, Bruch et al, 2000), embedded sensors and actuators (Weems et al, 1991; Pardo de Vera and Guemes, 1997) and combinations of embedded and surface mounted sensors and actuators (Islam and Craig, 1994). The two methods of placement offer different advantages. For instance, embedding the sensor provides some protection from surface impact as well as putting the sensor into intimate contact with the part. However piezopolymers have a limited temperature tolerance with the molecular orientation of piezopolymers and the piezoelectric properties disintegrating above 100°C. Hence they are restricted to external applications after part fabrication. An advantage of surface bonding is that it allows for the easy inspection, replacement and repair of piezoelectric transducers should they become damaged.

2.8 OBJECTIVES OF THE PRESENT INVESTIGATION

Based on the critical review of the relevant literature, it is clear that there needs to be a better non-destructive evaluation method for the monitoring of composite structural integrity for certification requirements as well as for management of critical repairs. This non-destructive method needs to be able to detect disbond growth in the safe life zone as shown in Figure 2.2 and monitor damage growth in the parent material below the damage tolerance zone.

The specific aims of this research are:

- Develop an approach for detecting disbond growth under bonded repair patches by means of surface-mounted lead zirconate titanate (PZT) as well as polyvinylidene fluoride (PVDF) and utilising local vibration-signature and surface waves.

- Develop a robust method using PZT and PVDF piezoelectric transducers to detect the size of disbond under the repair patch accurately and consistently.
- Examine the effectiveness of the impedance method, the transfer function method, and the stress wave method with multiple PZT and PVDF sensors and actuators for detection of disbond growth and the assessment of impact damage in composites.
- Develop a model of mechanical degradation occurrences to PZT. The issue of degradation is of importance since degradation could manifest itself as damage in the results.
- Develop a strategy for the distribution and the placement of the PZT/PVDF elements to increase the sensitivity for detecting disbond of repair patch and the assessment of impact damage in composite. Based on this strategy a set of guidelines to deduce the extent of damage from multiple sensors/actuators will be developed.
- Develop modelling and predictive tools for assessing the damage tolerance of composite structures under pre-stress subjected to low velocity impact forces.
- Develop a unified methodology for predicting the structural integrity of existing composite structures under pre-stress, which have suffered impact damage.

CHAPTER 3

EXPERIMENTAL METHODS

3.1 INTRODUCTION

The need to provide a method for in-situ health monitoring of composite repair using surface mounted piezoelectric transducers was discussed in the previous chapter. This method would contribute to the framework of the smart structure technology. For the in-situ structural health monitoring of composite repair patches three different methods were examined. Three experimental set-ups were used and two different specimen preparations made to acquire relevant data.

In section 3.2 to section 3.4, the set-up for the electro-mechanical impedance method is given followed by the description of the set-up for the transfer function method and the set-up for the stress wave method. The specimens used for the impedance method and for the transfer function method are the same. The specimen preparation for the application of the impedance method and of the transfer function method is given in section 3.5. In section 3.6, specimen preparation for the testing of stress wave method is presented.

In section 3.7 problems associated with the identification of signal from the surrounding noise signal. This includes a description of the effects of the degradation of the PZT on the signal detected.

3.2 SOURCE OF MATERIAL

The composite repair patches used in the experiments were either boron/epoxy or graphite/epoxy types obtained from the Defence Science Technology Organisation, Department of Defence, located at Fishermen's Bend, Melbourne (DSTO). The composite patches were designed on the basis of stiffness matching with the aluminium host. In the experiments, both five-ply unidirectional boron/epoxy lay-up and eleven-ply unidirectional graphite/epoxy were used. Each ply was 0.125-mm thick and the ends of the patches were stepped, at 4-mm per step, to reduce stresses at the patch ends. The 4-ply fibre-reinforced polymer was fabricated in the Department of Mechanical Engineering Workshop, Monash University in Clayton.

Aluminium of various grades was used during various stages of experimentation, depending on the application. For the preliminary experiments of prescribing artificial disbond growth by the insertion of Teflon, done to gain understanding and further experiments of prescribing artificial disbond growth by the insertion of blade, done for the visualisation of disbond growth, mild aluminium plate was used. For the experiment where the aluminium was required to undergo cyclical stress loading, aluminium of type 7075-T6 was the material of choice as it is be able to sustain high strain levels. This includes the experiment for the determination of the threshold of signal degradation due to the change in the constitutive relation of the PZT. Aluminium of this grade was obtained from H-Aircraft Spares near Mentone in Victoria, Australia.

Adhesive type FM73 was used to bond the composite patch to the aluminium. This adhesive was obtained from the DSTO and has the following material properties.

Table 3.1 Material properties of FM73 assumed at room temperature

Cytec FM73	Value
Shear Modulus	355 MPa
Thickness	0.2 mm
Shear Yield Strength	35.5 MPa
Elastic Strain Limit	0.1
Failure Strain	0.6
Plastic Strain Limit	0.5
Poisson's Ratio	0.33

Table 3.2 Material properties of PZT

Thickness	0.191 mm
Relative dielectric constant, K_3^T	1800
Piezoelectric strain coefficient, d_{33}	390 E-12 m/V
Piezoelectric strain coefficient, d_{31}	-190 E-12 m/V
Piezoelectric voltage coefficient, g_{33}	24 E-3 Vm/N
Piezoelectric voltage coefficient, g_{31}	-11.6 E-3 Vm/N
Coupling coefficient, k_{33}	0.72
Coupling coefficient, k_{31}	0.32
Polarisation field, E_p	2 E+6 V/m
Initial depolarisation field, E_c	5 E+5 V/m
Density	7800 kg/m ³
Mechanical Q	80
Elastic modulus, Y_3^E	5.2 E+10 N/m ²
Elastic modulus, Y_1^E	6.6 E+10 N/m ²
Thermal expansion coefficient	~ 4 E-6
Curie temperature	350°C

The piezoceramic used in the experiment were manufactured by Piezo Systems, Massachusetts and bought from Strategic Resources Industry, located at Melbourne, Victoria. The material properties of the PZT are as listed above.

3.3 SET-UP FOR THE ACQUISITION OF ELECTROMECHANICAL IMPEDANCE

In the experiments, the electromechanical impedance was obtained using two separate impedance analysers. Preliminary experiments were conducted with the Hewlett Packard LF Impedance Analyser model 4192A LF, which was on loan from DSTO, is as shown in Figure 3.1. Experiments conducted at the later stage of the project, which is the experiment to visualise disbond growth, was conducted using the impedance analyser purchased from Agilent Technologies, model 4284A Precision LCR Meter as shown in Figure 3.2. Both analysers allow 6-digit resolutions to an accuracy of 0.05%.

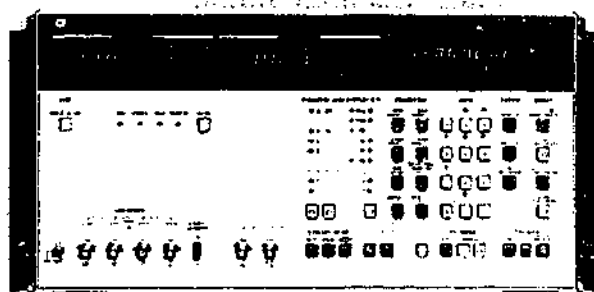


Figure 3.1 Impedance analyser model 4192A LF

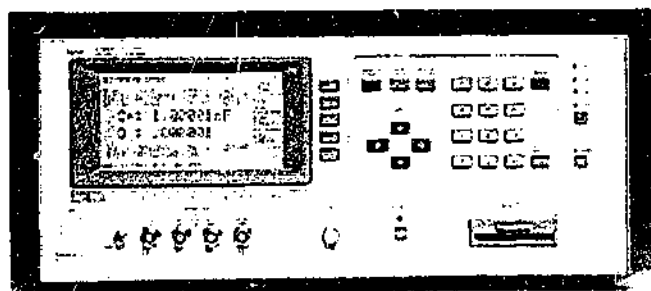


Figure 3.2 Impedance analyser model 4284A Precision LCR Meter

The first impedance analyser operates by generating a signal at a user-defined frequency in the range 5-Hz to 13-MHz, while the second operates from the range of 20-Hz to 1-MHz. This signal is introduced into the specimen through the actuator PZT element, and the resultant voltage and current from the sensor PZT element are sampled. The unit measures the magnitudes of the voltage and current, and the angle between them, and thus calculates the complex impedance of the load. From this value of impedance the reflection coefficient, R-L-C equivalent circuit and return loss can be determined. The impedance and phase angle measurements are selected from the menu list operated from the cursor keys. The impedance can be displayed in rectangular or polar format. The R-L-C equivalent circuit can be displayed as either a series or parallel circuit. The impedance meter can operate in 2 basic modes. In fixed frequency mode, interrogation is by means of a single frequency. In scan frequency mode, interrogation can scan sequentially through a range of frequencies. The scan mode is particularly useful for locating resonance such as in a quarter wave line or a crystal.

The impedance analyser can be controlled either via the keypads on the front panel or remotely from a PC using the RS232 serial line and the optional control software. The PC software can be used to log data from the TE1000 and store this in a format that is compatible with MS Excel.

The data output from the impedance analyser was acquired using a DT31EZ data acquisition card (manufactured by Data Translation in Massachusetts, USA). A software program called DTVee, running on a Pentium 133MHz desktop computer was used to acquire the data from the acquisition card. The relevant output data can be saved to a data file, and input directly into a Microsoft Excel spreadsheet via the Dynamic Data Exchange protocol (DDE).

3.4 SET-UP FOR THE ACQUISITION OF SYSTEM TRANSFER FUNCTION

The transfer function method presented in this project was based on the system transfer function between a pair of PZT transducers bonded in the repaired structure. This technique utilises both the converse and direct effect of the piezoelectric material for actuation and sensing respectively. Koh et al (1999) has previously shown that the transfer function method is particularly attractive because the actuating PZT can be located in a low stress region, whilst the sensor placed in the high stress region can be made from a more fatigue resistant PVDF.

To acquire the frequency response of the structure, the PZT transducer was excited through broadband random (white noise) vibration. In the project, the transfer function was computed using a Fast Fourier Transform (FFT) analyser. The Fast Fourier Transform maps any signal from temporal domain into the frequency domain. The transform of the input and output signal was calculated by the analyser and the frequency response for the structure was determined in that manner. The frequency response detected was used to indicate the structural integrity. Two different analysers were used for the acquisition of transfer function data. The first instrument used was the AND AD-3525 FFT analyser as shown in Figure 3.3. The AND AD-3525 FFT Analyser was manufactured by the A&D Company Limited, International Division.

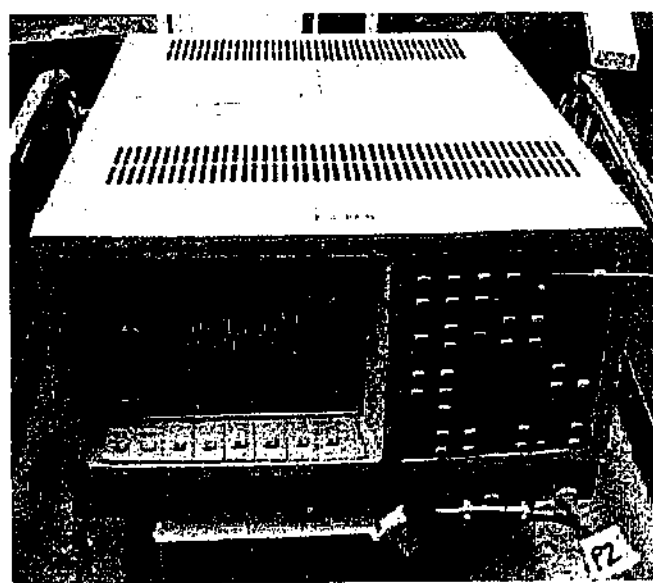


Figure 3.3 Photograph of the AND FFT Analyser

The acquisition of data done from the system transfer function between the sensor and actuator can be described as follows:

- A broadband signal using an AND AD-3525 FFT Analyser was used to evaluate the transfer function and to provide the broadband input signal to the actuator. The frequency bandwidth used was 250-Hz to 20-kHz and the RMS amplitude of signal input was set at 5-Volts.
- Above 100 averages were taken to obtain a single frequency response function. This is to eliminate errors associated to ensemble averaging.
- The real and imaginary transfer function of the sensor/actuator pairs is recorded and subsequently converted to amplitude and phase using Microsoft Excel.

The second Fast Fourier analyser used for data processing was SignalCalc ACE PCMCIA card-based as shown in Figure 3.4 and was purchased from Data Physics Corporation. The operation of the card is through software installed in a COMPAQ laptop. This second instrument was used for the experiments conducted at the later stage of the project to visualise disbond growth underneath a transparent 2-ply fibre-reinforced polymer.

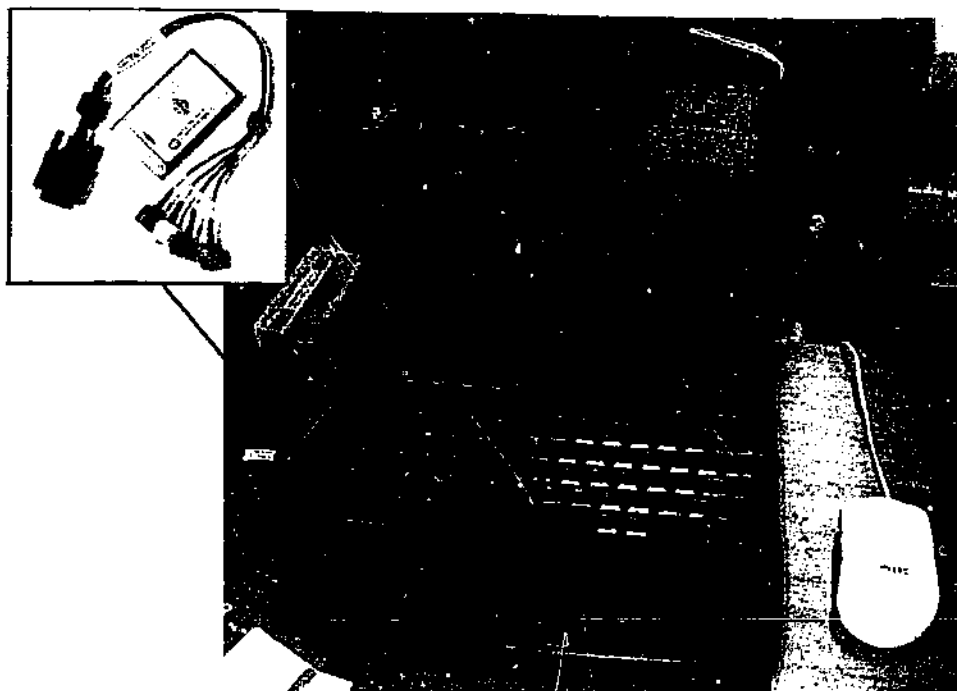


Figure 3.4 Photograph of the PCMCIA card based FFT analyser slotted into the laptop on the left

The acquisition of data done from the system transfer function between the sensor and actuator can be described as follows:

- A broadband signal was produced using HP Tektronix model TDS 210 waveform generator at 5-Volts.
- Using the SignalCalc ACE PCMCIA card-based FFT analyser to evaluate the transfer function and to provide the broadband input signal to the actuator. The frequency bandwidth used was 250-Hz to 10-kHz.
- Above 100 averages were taken to obtain a single frequency response function. This is to eliminate errors associated to ensemble averaging.
- The real and imaginary transfer function of the sensor/actuator pairs is recorded and exported as an ASCII test file, which was subsequently converted to amplitude and phase angle in MS-Excel.

3.5 SET-UP FOR THE ACQUISITION OF STRESS WAVE

In order to perform an ultrasonic inspection it was necessary to excite wave modes in the form of tone bursts in the laminate. When using Lamb (or stress) waves, one of the problems is that the wave will excite all modes and thus make the analysis of the response difficult. The tone burst waveform is important, and a Hanning window was applied in order to retrieve the appropriate frequencies or modes. The aim of the experimental investigation was to excite a single Lamb wave and to study its propagation.

When a Hanning window is applied the result is a characteristic waveform. However the waveform generator used in these experiments could not generate this particular waveform by itself, it was necessary to transfer the waveform from the PC-based software program, through a GPIB or General Purpose Interface Bus (Figure 3.5). This could not be done without a suitable application program. This was not readily available, and was therefore programmed using a graphical programming software called HP Vee Lab 5.0.

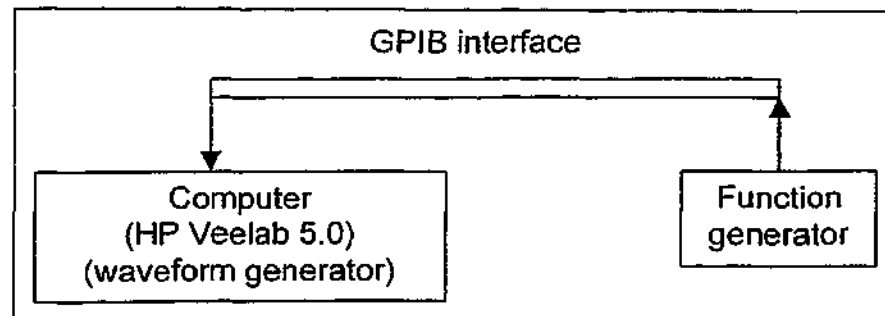


Figure 3.5 Waveform download set-up

The waveform consisted of a continuous sine wave (at approximately 1-MHz) enclosed by the Hanning window function $f(t) = 1/2 (1 - \cos t)$. The characteristic waveform were generated in HP Vee Lab Version 5.0 and then downloaded into the waveform generator (HP 33120a) volatile memory using the GPIB interface as shown in Figure 3.5.

This arbitrary waveform is finally copied into non-volatile memory and given a filename. It is now possible to excite this particular waveform using the waveform-

generator interface, by setting the waveform to 'user' and assigning the chosen file-name. The frequency, phase, amplitude and burst settings can then be altered individually to suit each particular experiment. If the need arises to change the basic shape of the waveform, it can be done by starting at HP Vee Lab 5.0, build a new waveform, re-activate the GPIB interface and repeat the rest of the above process.

In this particular case the aim was to excite a single burst of the waveform as shown in the experimental set-up in Figure 3.6. The total waveform burst consisted of a Hanning window enclosing five sine wavelengths with a carrier frequency of 1-MHz. The total duration of the burst waveform was now 5- μ s. The waveform was sent to an oscilloscope (Tektronix TDS 210) and then output, via channel 1, to the PZTs placed at certain locations on the surface of the plate to be investigated. Electric signals cause deformation in the transducers and this induces vibrations in the plates.

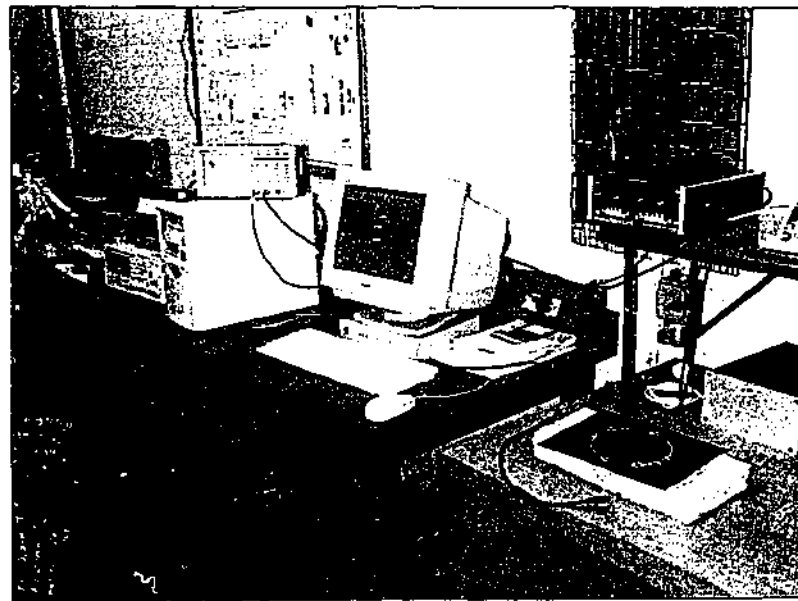


Figure 3.6 Photograph showing the complete experimental setup to excite Lamb waves as well as to acquire the response

On the opposite end of the plate we placed receiving transducers or sensors in a similar pattern as shown in Figure 3.7. These piezoelectric transducers are working in the opposite way, converting vibrations, carried through the plate from the exciting transducers, into electric signals. These signals are then sent back to the oscilloscope through Channel 2. After tuning, the response can be observed on the oscilloscope screen.

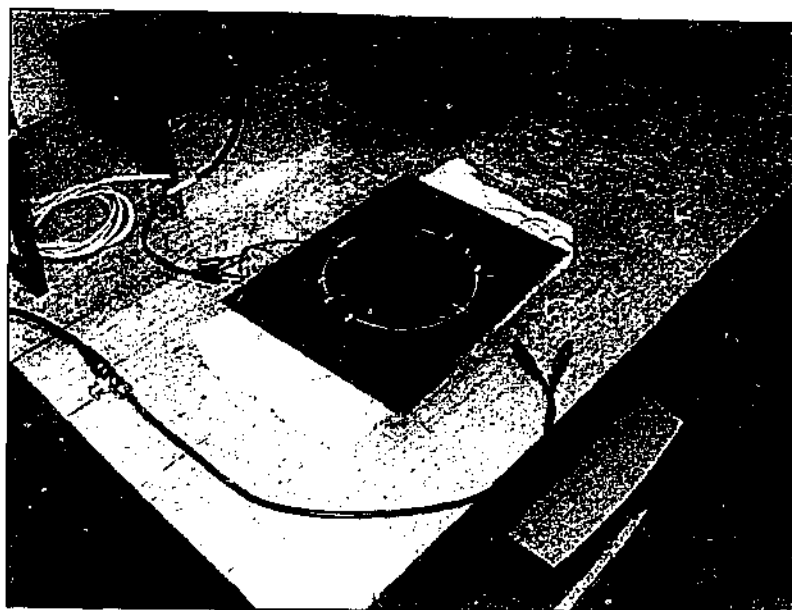


Figure 3.7 Photograph of the specimen with PZTs at various locations

To be able to capture images and other data from the oscilloscope, a connection to this instrument had to be established. Wavestar Lite Version 1.0 software was used to capture this data and because this version did not allow a GPIB connection, the data was downloaded using the RD-232 serial interface as shown in Figure 3.8.

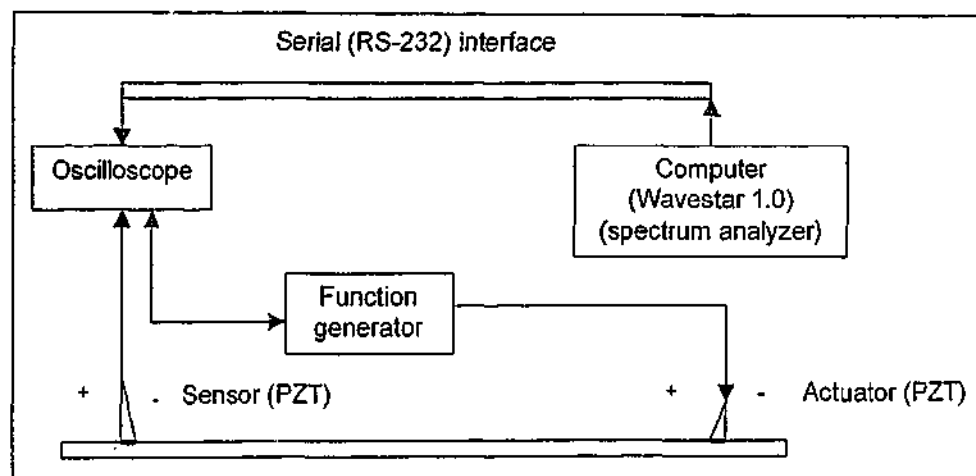


Figure 3.8 Experimental set-up

3.6 SPECIMEN PREPARATION FOR IMPEDANCE METHOD AND TRANSFER FUNCTION METHOD

The composite repair patches used for the evaluation of the impedance and the transfer function method are unidirectional boron/epoxy and unidirectional graphite/epoxy. The thickness of the patch was approximately one third that of the aluminium host as unidirectional boron/epoxy has a modulus approximately three times that of aluminium.

Figure 3.9 shows the PZT element before bonding on an aluminium foil, which later would be bonded together on a specimen. In the experiments the use of varying size of aluminium foil under the PZT element was investigated. The aluminium foil serves to earth the PZT element and it was found that the size of the aluminium foil does not have much influence on the sensitivity of the PZT elements.

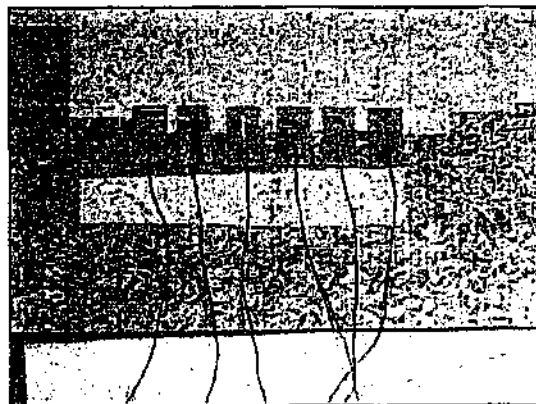


Figure 3.9 Piezoceramic transducers before bonding

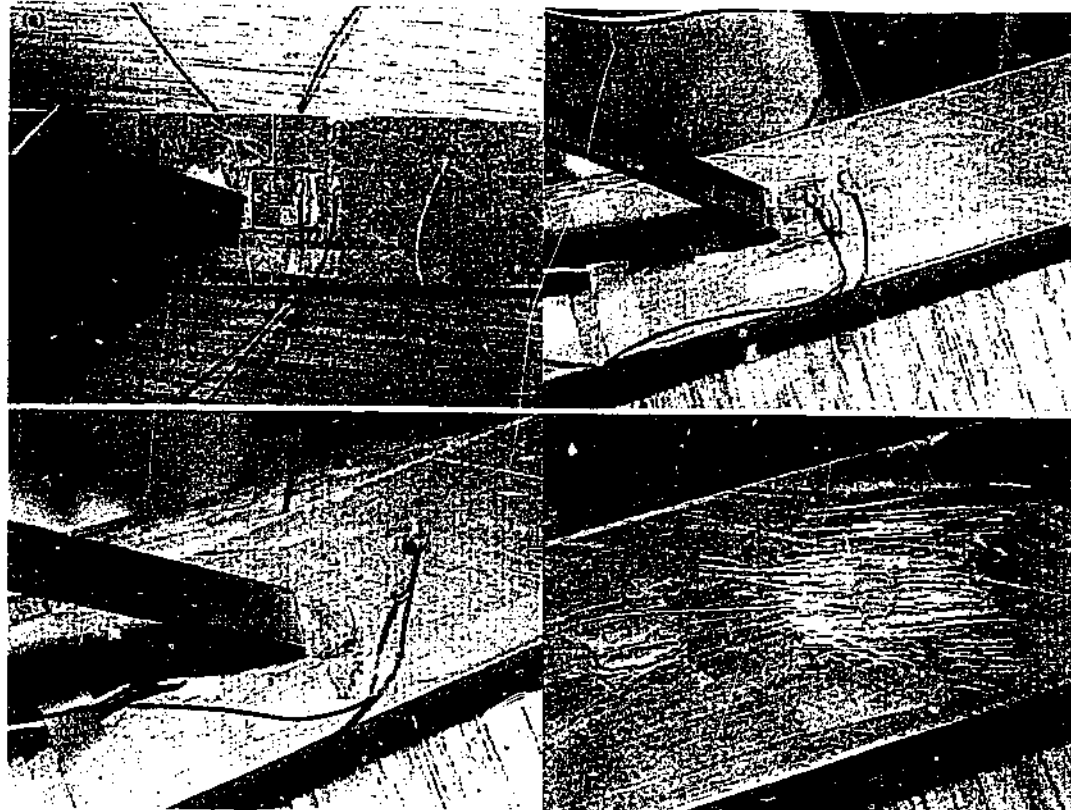


Figure 3.10 Removal of piezoceramic element for destructive evaluation of bonding condition from (a) to (d)

Evaluation of the bonding surface of the piezoceramic to the aluminium host as well as the composite patch was investigated by destructively removing a bonded element. The above diagram, Figure 3.10 shows the process where a chisel was used to forcefully remove the piezoceramic. The very well bonded element breaks into pieces as it is removed. Badly bonded element on the other hand can be removed as a single piece of wafer element.

The specimen shown in Figure 3.10 had undergone 100,000 loading cycles at 2000-microstrain, and it shows that the bonding between the element and the host structure did not degrade up that level stated. The grey zones in the middle of the specimen in Figure 3.10(d) shows the remaining adhesive after the full removal of the piezoelectric element.

3.6.1 STATIC EXPERIMENTS

Static evaluation with boron/epoxy composite repair

Figure 3.11 shows the schematic of the specimen used to gain preliminary understanding on the detection of disbond growth using both the electromechanical impedance and system transfer function. The specimens used for the transfer function method is similar to that used for the impedance method. Here a 5-ply unidirectional boron/epoxy composite patch was bonded on an aluminium plate to simulate bonded repairs on aircraft. Five of these specimens were prepared and four of the specimens were inserted with Teflon sheets in the bondline at 'A' during bonding of the composite repair. The size of the Teflon sheet bonded under the composite patch differs between the individual plates and they are of the following dimensions: 5×5-mm, 10×10-mm, 15×15-mm, and 20×20-mm. This is to simulate the development of disbond growth during active service.

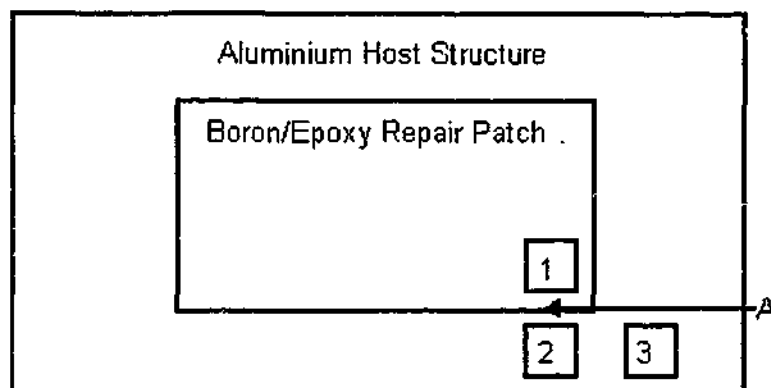


Figure 3.11 Schematic drawing of the specimen used for the detection of disbond growth by means of the transfer function method

Static evaluation with glass fibre reinforced plastic repair

Figure 3.12 shows the schematic of a corner of the specimen used to relate a visible disbond growth to the interpretation of results using the electromechanical impedance and system transfer function. The specimens used for the transfer function method were similar to that used for the impedance method. Here a 2-ply unidirectional glass fibre-reinforced plastic patch was bonded on an aluminium plate to simulate bonded repairs on aircraft. PZT transducers were bonded on two corners of the plate, where each corner had nine transducers as shown in Figure 3.12.

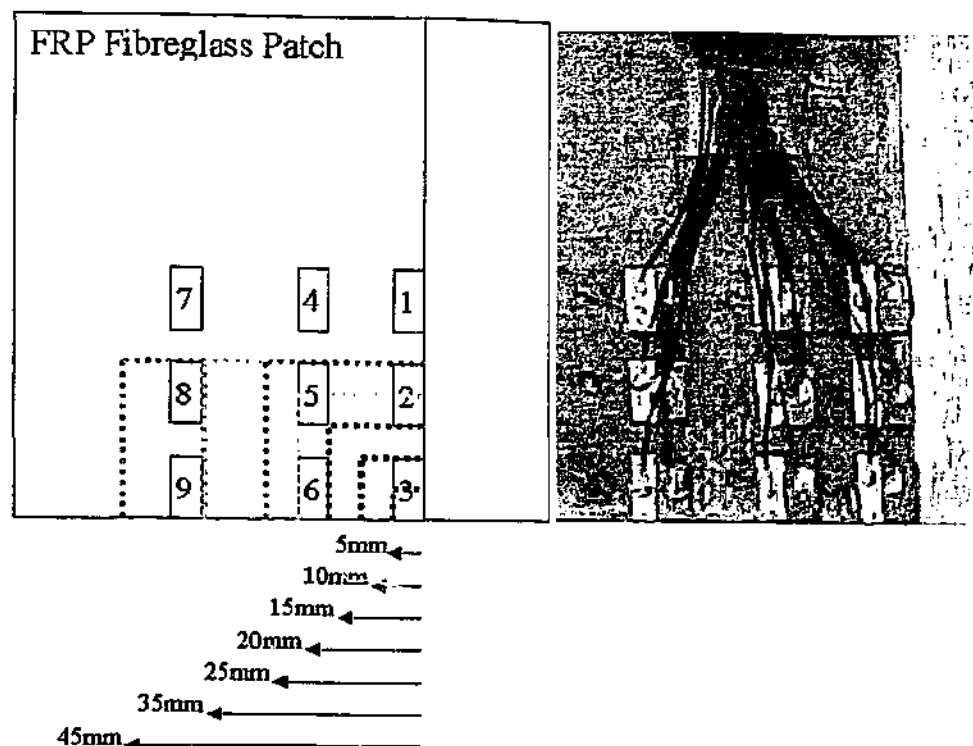


Figure 3.12 Schematic drawing of specimen (on the left) and the actual specimen (on the right) used for the visualisation of disbond growth

The aluminium specimen was prepared in a number of steps. First step was to prepare the glass fibre-reinforced plastic (GFRP) repair patch, 4-ply of woven fibreglass were used and a coat of resin was applied to laminate onto a sheet of Teflon. The vacuum bag method was used to fabricate the GFRP repair patch. When the GFRP patch was fully cured, it was then trimmed to $200 \times 200\text{-mm}^2$, the bonding surface of the aluminium plate and GFRP patch were then sand blasted to provide a better bonding surface. The bonding surfaces were cleaned with acetone; this effectively removes any sand and dust particles that will affect the bonding. Copper wires with cross-section diameter of 0.25mm were then positioned on the centre section of the aluminium plate before applying araldite as shown in Figure 3.13. This is to maintain a constant thickness of 0.25-mm between the GFRP patch and the aluminium plate when adhering both materials together. Adhesive was then spread evenly throughout the GFRP patch and patch carefully positioned in place. Weights were then place on the centre of the GFRP patch therefore it forces all the excess adhesive out on to the side and edges of the GFRP patch, maintaining even thickness throughout.

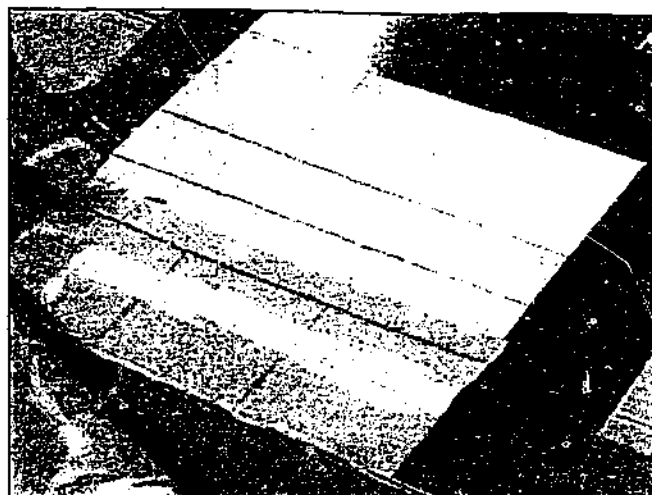


Figure 3.13 Aluminium plate with copper wires in the middle section

In this investigation the disbond was created at the corner of the GFRP patch, since this was the most likely location for a disbond to initiate under actual service conditions. To create this disbond growth, a thin blade with thickness of 0.2-mm was carefully driven into the adhesive at the edge of the GFRP patch. To provide better visual of the disbond, liquid penetrant was injected between the GFRP patch and aluminium plate. Eight different damage cases were considered to simulate the disbond growth under the repair patch for the specimen is tabulated in Table 3.3.

Table 3.3 Disbond sizes considered for the FRP composite patch

Damage Cases	Damage Dimension
0	No Damage
1	5×5-mm ²
2	10×10-mm ²
3	15×15-mm ²
4	20×20-mm ²
5	25×25-mm ²
6	35×25-mm ²
7	45×25-mm ²

These damage cases considered would illustrate three different situations. First situation was when disbond growth was far away from the sensor and actuator piezoelectric. Second situation was when disbond growth was approaching the sensor piezoelectric and third situation was when disbond growth had passed the sensor piezoelectric.

3.6.2 FOR FATIGUE EXPERIMENTS

Two separate fatigue experiments were conducted for the purpose of testing the applicability of the impedance and transfer function methods. The fatigue tests were done in a Materials Testing System (MTS) machine.

Location of Piezoelectric Transducers: Part I

Figure 3.14 shows the schematic drawing of the specimen discussed in the first section of the experimental results. This specimen was dynamically loaded in the MTS machine to simulate active service. In Figure 3.14, an 11-ply unidirectional Boron/Epoxy patch was bonded onto an aluminium plate to simulate bonded repairs. During the experiments the disbond on Side P was monitored using both the electromechanical impedance method and the transfer function method. The disbond on Side S was monitored using strain gauges. On Side P, PZT elements were bonded on three different locations. Whilst PZT element 1 (PP1) was bonded on the far field

of the aluminium substrate, PZT element 2 (PP2) was bonded on the edge of the repair patch and finally PZT element 3 (PP3) was bonded on the far field of the boron epoxy repair patch. PP1 and PP3 were each $10 \times 20\text{-mm}^2$ in size, while PP2 was $4 \times 20\text{-mm}^2$ in size. On the reverse Side S, only three PZT elements were bonded on to the specimen. They were labelled as SP1, SP2 and SP3 respectively. Strain gauges were attached on the edge of the repair patch taper. Transfer function method was carried out using all four PP1, PP2 and PP3. Impedance method was only conducted on PP2.

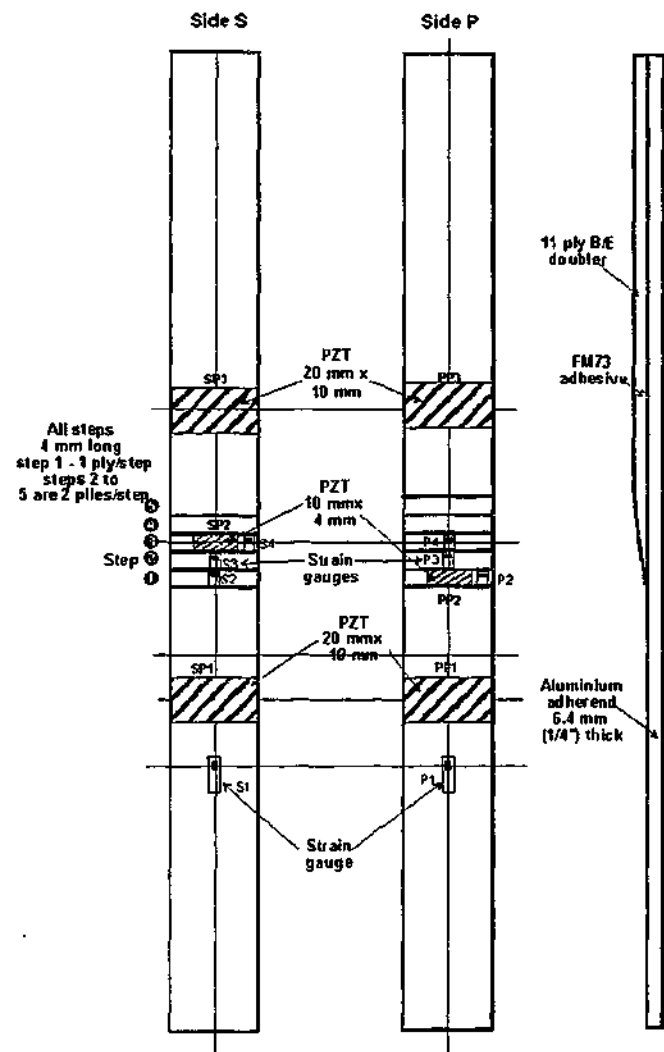


Figure 3.14 First specimen used for the verification of methods

Location of Piezoelectric Transducers: Part 2

Figure 3.15 shows the schematic drawing of the specimen discussed in the second section of the experimental results. Similar to the first specimen, the second specimen

Side A

Flow in adhesive extends half way along taper

Flow in between layers 2 and 3 extends half way along taper

Side B

13 piles graphite/epoxy with 3mm long steps at taper

Bragg OFB located between piles 9 and 10 2 mm parallel length

Roll strain gauges on surface 2 mm, normal length

AI inner adherend thickness 1/4"

PZT 5 mm x 10 mm

130 mm

36 mm

Agreed line of sensors

Location of additional internal sensors if required by testing laboratory (to stagger vertically)

Side B

40 mm

50 mm

BPZT2

BPZT3

BPZT1

10

10

10

10

140 mm

405 mm

Both specimens in the preceding sections were fatigued in the MTS machine belonging to the Fatigue and Fracture Laboratory, DSTO. The specimens used to

determine the degradation threshold of piezoceramics in later section were tested in the MTS machine belonging to the Department of Mechanical Engineering, Monash University (MTS2). MTS1 has a static load capacity of 100-kN and a dynamic load capacity of 50-kN, while MTS2 has a static load capacity of 1000-kN and a dynamic load capacity of 500-kN.

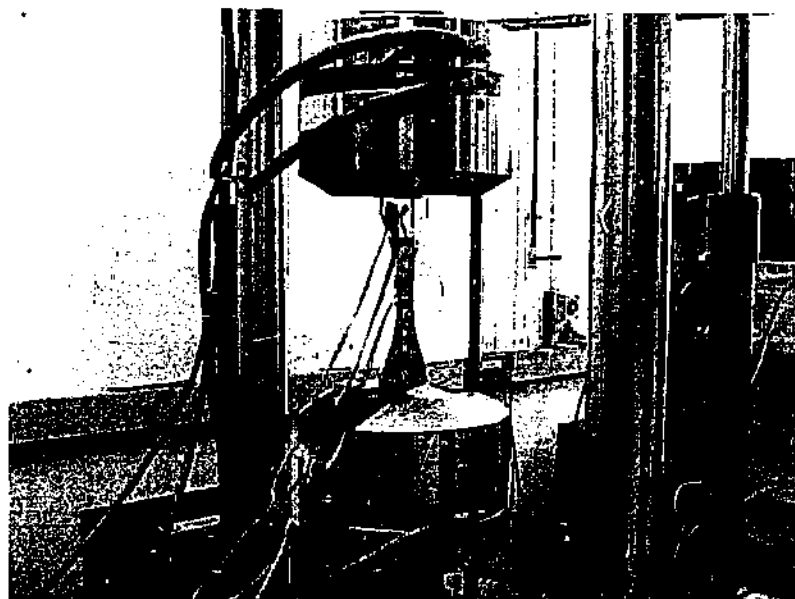


Figure 3.17 Specimen in the MTS of Department of Mechanical Engineering, Monash University test machine before the start of the fatiguing process

3.7 SPECIMEN PREPARATION FOR STRESS WAVE METHOD

This section describes the first impact test run performed on the graphite/epoxy composite plates. The plates were impact damaged and the stress wave method was used to quantify the extent of damage. These impact experiments were performed at Fatigue and Fracture Laboratory, DSTO.

3.7.1 TEST RIG

The rig at DSTO consisted basically of a base and an impactor unit attached to a tall guide rod using an approximately 5-m long slider joint (Figure 3.18). The impactor can be lifted to any chosen height, using a wire running around a cartwheel at the top

of the guide rod. The wire continues down almost to the height of the base table, runs under a second cartwheel, then over a third one and finally was attached to a manual winch. This winch was used to adjust the drop height corresponding to the respective impact energy. The releasing mechanism for the impactor, consisted of a hook penetrating an eyebolt. A cord was attached to the hook, and by pulling this cord the impactor was released, and this then dropped down onto the specimen. The drop height was measured using an electronic measuring tape device attached to the frame at the base plate. The end of the tape was hooked onto the impactor-carrying unit. The meter was reset to zero at the specimen surface for each test run.

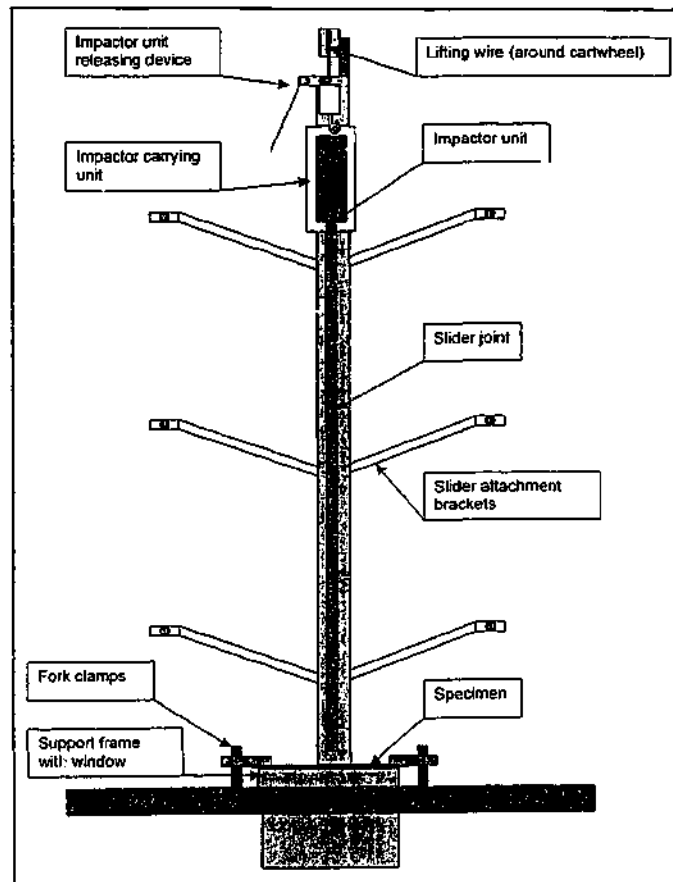


Figure 3.18 Schematic of impact test rig

The specimens were placed on top of a steel frame containing a circular window (Figure 3.19), and clamped to this frame by using fork clamps bolted to the base table (Figure 3.20). The specimens were hence restricted from moving in the horizontal plane. The circular frame window surrounding the point of impact allowed the specimen to deform in the direction normal to the surface.

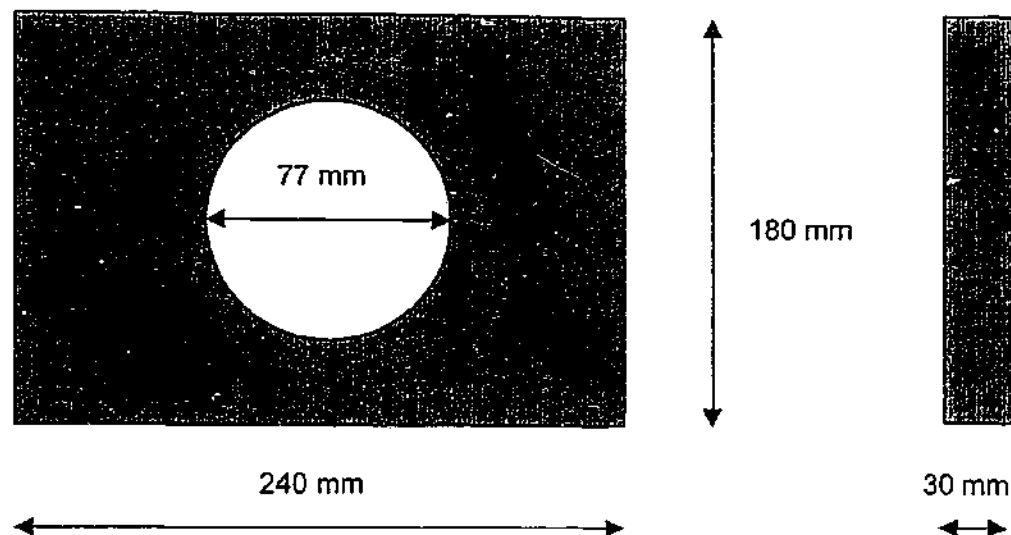


Figure 3.19 Schematic of support frame with window

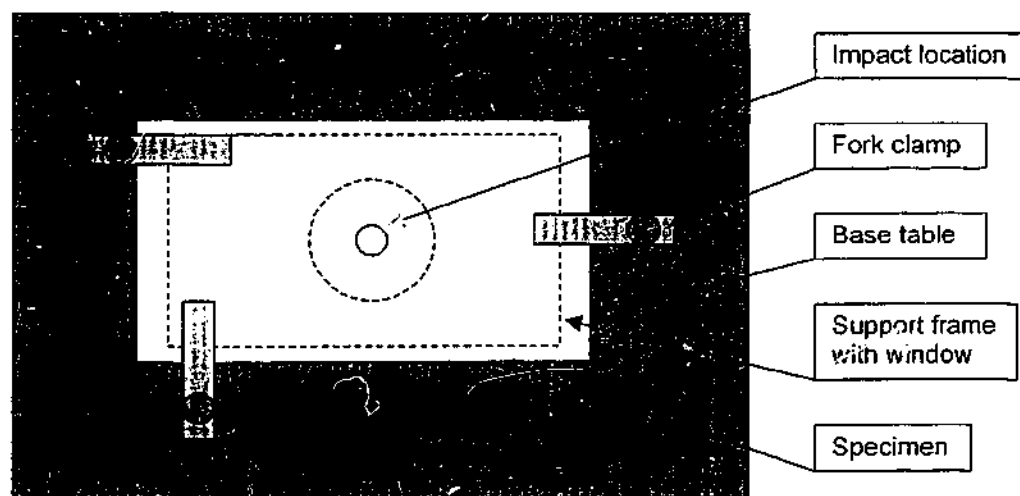


Figure 3.20 Schematic of the base table with frame, specimen and clamps

After impact, a mechanical brake mechanism was applied automatically to the impactor, thereby avoiding multiple impacting of the specimens. The acceleration forces induced at the time of the impact triggered this automatically.

Impactor

The rig was equipped with a modular impactor carrying unit, which is attached to the guide rod using a slider joint. The carrying unit allowed for variation of impactor size

and geometry by simply replacing the centre part containing the impactor module itself (Figure 3.21). The impactor module was attached to the carrying module using hex screws.

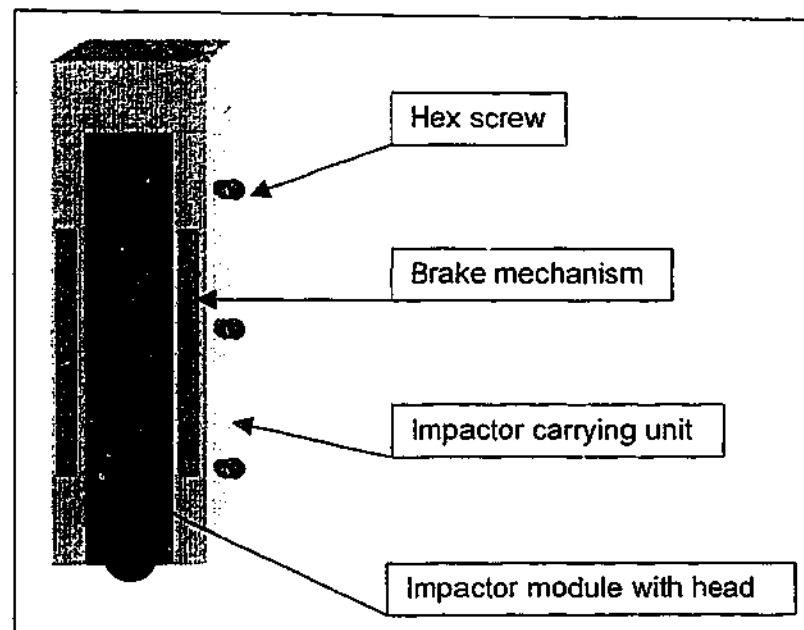


Figure 3.21 Schematic of impactor module attached to carrying unit

During the investigations, the characteristics of the impactor are as shown in Table 3.4. The weight shown was the total weight of the impactor including carrying unit. This was the weight that would determine the impact energy.

Table 3.4 Characteristics of the impactor

Weight (kg)	Geometry	Diameter (mm)	Material	Young's modulus
5.6	Hemispherical	16	Steel	210-GPa

Evaluating and compensating for the influence of friction forces

Friction in the system, and in the slider joint in particular, would have to be taken into consideration. This could be done by measuring the impact and rebound velocity, calibrate the rig according to this, and thereby avoid the problem of friction entirely. Alternatively, if photocell equipment was not available, the friction force can be calculated by measuring the time from drop to impact, and compare this with the theoretical values, based on the force of gravity.

Since equipment for velocity measurement was not available for this test rig, thus the alternative method was used to evaluate the influence of the friction forces. The time from drop to impact (Table 3.1) was measured using a manual stopwatch, and this together with the known drop height was used to find the true acceleration of the impactor during the drop. For this purpose, some basic energy and kinetic equations were applied. This is not as accurate as an automatic velocity measurement system, but should give reasonably good results. The calculations are shown below in Figure 3.5.

Table 3.5 Time from drop to impact

Drop height	Time delay in test no.			Average time from drop to impact
	1	2	3	
0.50 m	0.35 s	0.37 s	0.33 s	0.35 s

$$s = ut + \frac{1}{2}at^2 \quad \text{Equation 3.1}$$

The kinetic equation used is shown in Equation 3.1. From the basic kinetic equation the vertical acceleration of the impactor during the drop was determined to be 8.2-m/s²

The rather crude measurements of the time duration of the drop resulted in different values for impact velocity and acceleration than those provided merely by using the force of gravity. This difference is caused by friction. There will always be some friction in a mechanical system, and to account for the difference between acceleration in an ideal, frictionless system and the actual acceleration, the drop heights were increased for the respective impact energies.

3.7.2 SPECIMENS

Three new specimens were impacted using the drop test rig shown in Figure 3.9. They were made of 8-ply graphite/epoxy laminate. The plates have a length of 0.275-m, a width of 0.2-m and a thickness of 1.1-mm. The impact location in relation to the overall dimensions is shown in Figure 3.22.

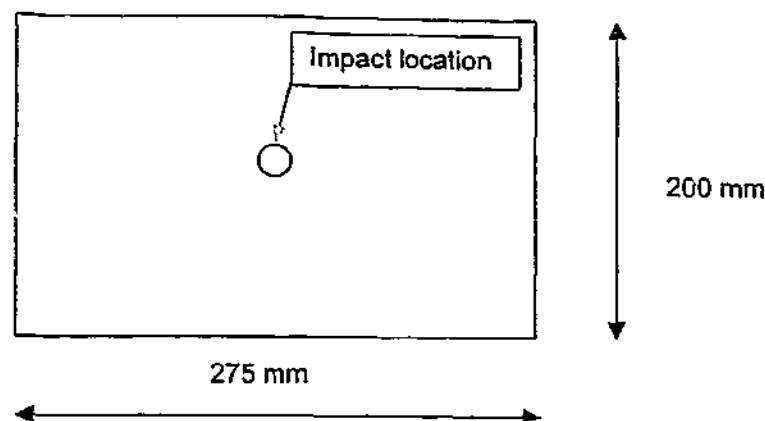


Figure 3.22 Schematic of the new specimens

The impact tests

In determining the drop heights the results from the calibration were used to calculate the impact velocity for impact energy of 6-J. Based on Equation 3.2, it was found that the impact velocity that corresponds to impact energy of 6-J is 1.46-m/s. This was assuming that the impactor had a mass of 5.6-kg. From this, the drop height for this impact energy can be found using a basic kinetic equation (Equation 3.3):

$$E_i = \frac{1}{2} m_i v_i^2 \quad \text{Equation 3.2}$$

$$2as = v_i^2 - v_0^2 \quad \text{Equation 3.3}$$

The drop heights for all other impact energies were determined using the same procedure. Because the potential energy of the impactor before impact is a linear function of drop height, the ratio between the impact energies was used to determine the new drop heights (Table 3.6).

Table 3.6 Impact heights for various impact energies

Test number	Specimen number	Impact energy (J)	Impact height (mm)
1	1	6	130
2	2	2	43
3	3	3	65

While the planned impact energies for this series of experiments were 4-J, 8-J and 12-J, an initial test using 6-J resulted in full penetration of the specimen. There was

therefore no need to go any higher, and since BVID (barely visible impact damage) was the main objective of the project here, the impact energy was reduced considerably. Impact energy of 2-J was chosen for the next test, which resulted in a BVID. The impact energy was then increased to 3-J for the third and final impact test in this series. This resulted in a small, but visible damage on the opposite side of the plate.

After the impacts have taken place, the impacted plates were inspected using the same method as for the existing plates. The impact damage in these new plates ranges from BVID in plate-2 to full penetration of plate-1.

Location of the piezoelectric transducers

PZT wafer elements were located onto the specimens to act as ultrasonic actuators and sensors. The dimension of each patch was $5 \times 5\text{-mm}^2$. The PZT elements were located in two $\frac{1}{4}$ -circles placed opposite each other. They were placed at 0° , 22.5° , 45° and 90° on each quarter circle, resulting in four opposing pairs of actuators and sensors, respectively.

In order to suppress any external noise, the specimens were placed on a piece of polymer foam damping material in the Acoustic Lab of the Department of Mechanical Engineering. Voltage was then applied to the PZT elements on the specimen plate, resulting in the emission of ultrasonic stress waves (or Lamb waves) into the material.

These waves were picked up by other PZT elements at the opposite end of the plate. The first arriving wave packet will by definition have followed the shortest path from actuator to sensor, forming a straight line with the impact location and major damage area lying directly in the middle of its path.

Schematic of the specimen with PZT transducers bonded is shown in Figure 3.23 below.

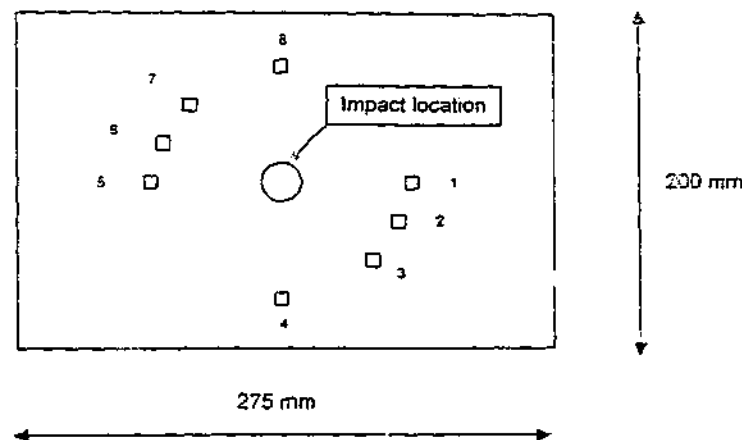


Figure 3.23 Schematic drawing of specimen-4 with location PZT transducers

3.8 DEGRADATION OF PIEZOCERAMIC TRANSDUCERS

Piezoceramic transducers experience degradation of signal at high strain levels. This is consistent with the properties of a ceramic material. Therefore in using PZT as actuators and sensors mounted *in-situ*, the threshold where the degradation of signal occurs had to be determined. While maintaining strain levels examined have to be suitable for aeronautical applications of the PZT. Three parameters are of importance if the PZT is to be used for in-situ structural health monitoring, viz. strain experienced by the host structure, the number of in-service loading cycles and finally the $[d_{31}]$ constant. Fatigue experiments were conducted to determine the relationship between the three parameters.

3.8.1 SPECIMEN PREPARATION

Two types of testing were done to quantify degradation of PZT. The first phase of testing involved single aluminium bars with PZTs bonded for constant strain fields. The second phase of testing involved a single dog bone shaped specimen with six PZTs bonded. Strain gauges were bonded onto the PZTs in both phases of testing to monitor the strain levels experienced by each PZT.

Constant strain fields

The PZTs were cut into squares of $10 \times 10\text{-mm}^2$ size. The first PZT was bonded to the centre of the aluminium grade 7075-T6 bars while the second PZT was bonded after the specimen had undergone cyclical loading. The bars were 31-mm in width, 244.5-mm in length and 6.5-mm in thickness. With a Young's modulus of 72-GPa, this material was most appropriate for these investigations given the ultimate and yield strength.

Two PZTs were bonded to a single aluminium 7075-T6 bar to obtain the impedance measurement, PZT voltage values when the bar had been strained and transfer function measurement after the cyclical loading. The adhesive used was araldite smeared along the perimeter of the piezoceramic square element surrounding a drop of silver-loaded epoxy as the conducting connection. The time required for this solution to cure was about 24 hours. A slight pressure was applied to secure the connection during curing.

Strain gauge was bonded to the PZT element to ensure that the strain experienced by the PZT element was accurate to a certain acceptable degree. By exerting a predetermined load on the aluminium 7075-T6, the piezoceramic underwent an amount of volumetric strain according to the constitutive relation (refer to the constitutive equation in Chapter 2).

The voltage outputs were taken at intervals of 50-cycles between 0- to 1-kcycles since the $[d_{31}]$ constant was expected to decay rapidly. The remainder intervals between the loading cycles are shown in Table 3.7. A total of one hundred thousand cycles were accumulated on each PZT bonded on the aluminium 7075-T6 specimens.

Table 3.7 Intervals between the loading cycles

From (cycles)	To (cycles)	Intervals (cycles)
0	1000	50
1001	5000	100
5001	10000	200
10001	50000	2000
50000	100000	5000

Dog bone specimen (varying strain fields)

The previous method of fatiguing the piezoceramic was applied on a dog-bone shaped aluminium 7075-T6 bar. With the varying cross-section along the length of the bar, different strain levels were created when the specimen was mechanically fatigued. To allow an even distribution of PZTs along the load spectrum from the non-degradable strain zone through to the degradable strain zone, a careful layout plan was made before the piezoceramics were bonded to the host structure. The respective zones corresponding to the strains were determined from the data acquired from the single aluminium bars.

In the first set of experiments, with aluminium bars, the PZTs were constantly strained uniformly with no load applied. Thus satisfying both criteria of (i) stress free, and (ii) uniform strain across the cross-section of the specimen; to determine the $[d_{31}]$ constant. In the second set of experiments, with a dog-bond specimen, the second criteria of uniform strain was not strictly adhered to. However, this investigation is necessary, as realistically, PZT mounted in-situ will not experience uniform strain. Thus, the $[d_{31}]$ constant referred to in this section is not strictly the piezoelectric constant but the ratio of voltage output/strain level experienced by PZT.

The schematic drawing of the locations of the PZT elements on the aluminium 7075-T6 dog-bone specimen is shown in the following Figure 3.24.

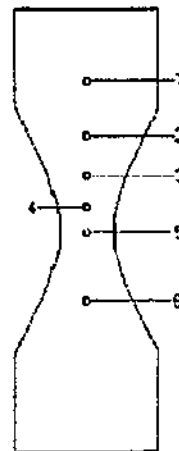


Figure 3.24 Dog bone shaped specimen

Table 3.8 Location of PZT on the aluminium dog bone

PZT location	Specimen width	Cross section area
PZT No. 1	90-mm	$5.76 \times 10^{-4} \text{ m}^2$
PZT No. 2	60-mm	$3.84 \times 10^{-4} \text{ m}^2$
PZT No. 3	45-mm	$2.88 \times 10^{-4} \text{ m}^2$
PZT No. 4	36-mm	$2.30 \times 10^{-4} \text{ m}^2$
PZT No. 5	30-mm	$1.92 \times 10^{-4} \text{ m}^2$
PZT No. 6	55-mm	$3.52 \times 10^{-4} \text{ m}^2$

By choosing a specimen of such a construction, the PZT that experienced the greatest strain under any loading conditions, was PZT No. 5. Since this location had the smallest local cross-sectional area, hence the datum load was based on that location. By setting the datum load to be 500-microstrain and the maximum load to be 2750-microstrain (both exerted at PZT No. 5), the other PZTs experienced the strains presented in Table 3.9.

Table 3.9 Strain at each individual PZT on the dog bone

PZT	Load (microstrain)(Max)	Load (microstrain) (Min)
1	916.68	166.67
2	1375.00	250.00
3	1833.32	333.33
4	2291.19	416.67
5	2750.00	500.00
6	1499.96	272.72

A total number of 100-kcycles of fatigue testing was performed at the two different levels of load. The intervals of between the loading cycles used were the same as the intervals used for the specimens with constant strain fields.

Each PZT had a strain gauge attached to it to monitor the exact strain experienced. This allowed the monitoring of strain fluctuations, if any, among the PZTs due to construction flaws or inaccurate input of load by the excitation machine.

3.8.2 EXPERIMENTAL EQUIPMENT

In the following section the settings on the equipment used for the acquisition of data from the degraded sensors are presented. This includes the settings for the MTS machine, the impedance analyser and the FFT analyser.

Material testing system setup

The MTS machine was used to provide the necessary degree of fatigue strain on the dog bone specimen as shown in Figures 3.25 and 3.26. This machine was calibrated to deliver a maximum load of 500-kN at a maximum frequency of 10-Hz. In the investigations, the load spectrum was between 7.254-kN and 43.524-kN.

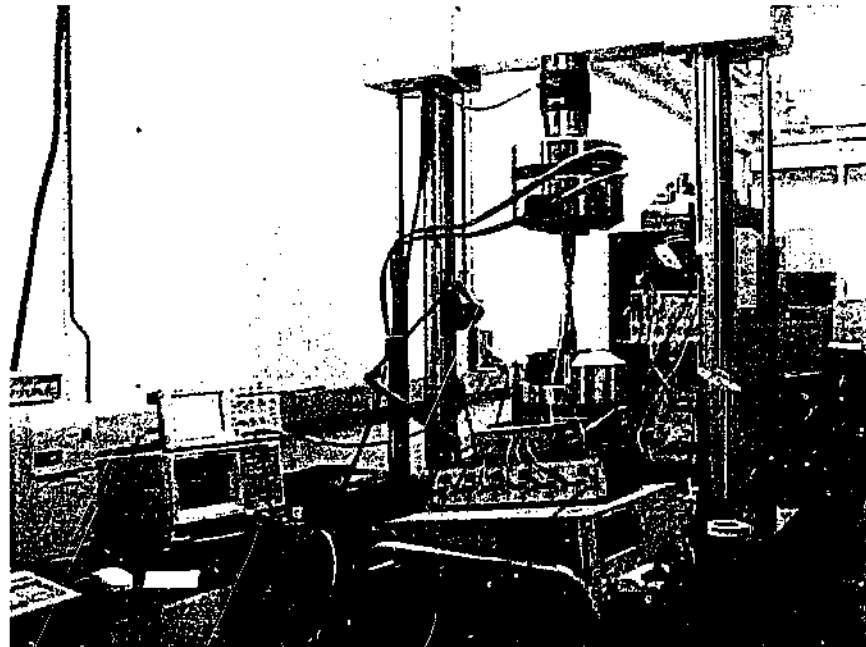


Figure 3.25 MTS machine located in the Department of Mechanical Engineering.

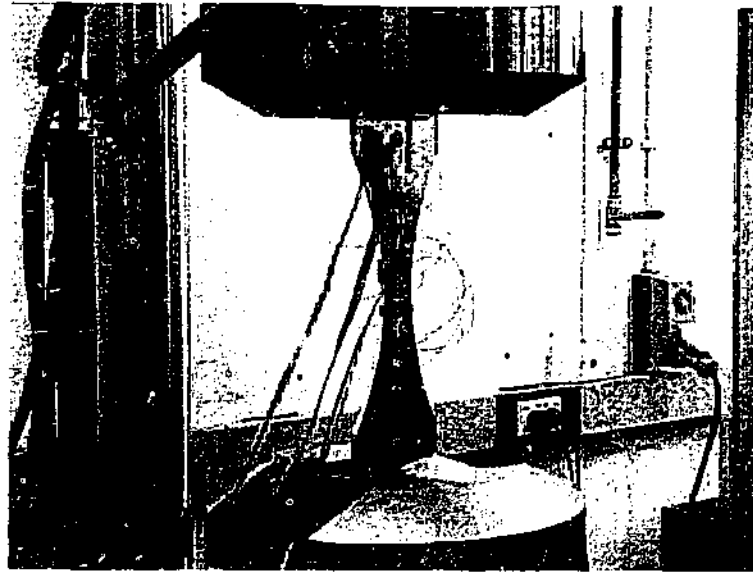


Figure 3.26 Dog bone clamped in position within the jaws

A Wheatstone bridge amplifier was used to amplify the signal from the strain gauges bonded to the piezoceramics. This allowed the recording of the actual strain experienced by each individual piezoceramic. The use of a dual-channel Tektronix TDS-210 oscilloscope shown in Figure 3.27 allowed the simultaneous reading of the strain gauge output through the Channel 1 input and the PZT voltage through the Channel 2 input. The input signal amplitudes were measured and recorded in the cursor mode. The true $[d_{31}]$ constant of each piezoceramic was obtained by relating the strain and voltage information recorded to the PZT constitutive relationship.

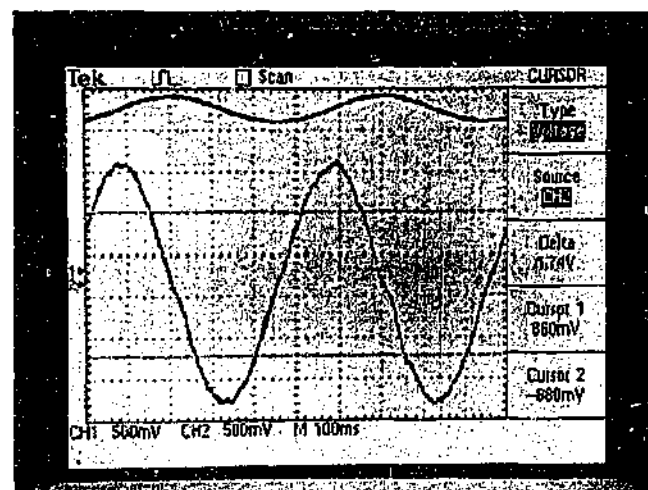


Figure 3.27 Tektronix oscilloscope model TDS 210

Impedance acquisition equipment setup

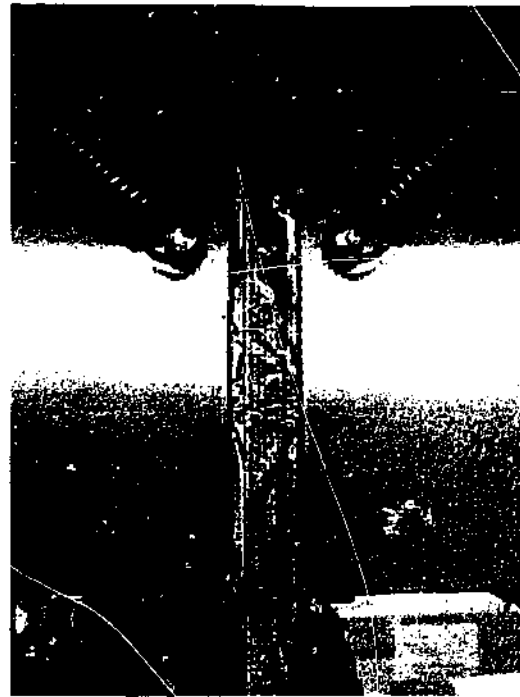


Figure 3.28 Aluminium tabs on the dog bone for electrical insulation

To overcome electrical leakage through the grips of the machine during testing of the aluminium dog bone, aluminium tabs were bonded to the parent aluminium structure as shown in Figure 3.28. The adhesive layer provided electrical insulation from earthing through the grips.

The impedance analyser was used to obtain the impedance of the piezoceramic during the loading cycles. By interrogating the PZT piezoceramic at different frequencies, a range of impedance values with respect to frequency was obtained. A frequency range of 1-kHz to 8-kHz was used to interrogate the piezoceramic. The excitation frequency was increased systematically between the range and the output recorded. This related the impedance measurements to changes in the structural integrity of the piezoceramic.

Transfer function acquisition equipment setup

An AND Fast Fourier Transform analyser was used to obtain the transfer function generated from the dog bone section of the experiments. A Hewlett-Packard wave

generator as shown in Figure 3.29 was used to generate the wave signal input. The waveform was a 5-Hz sine wave.

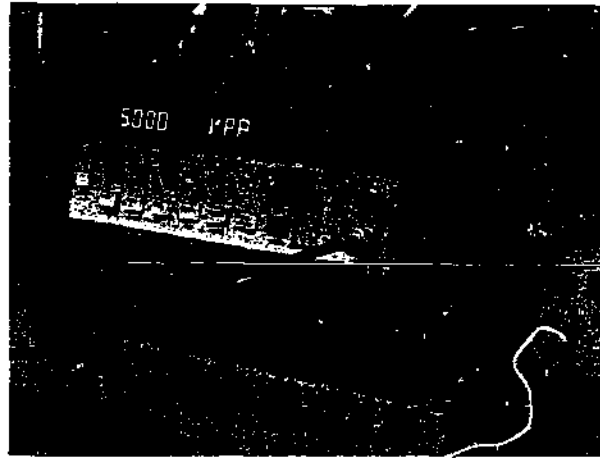


Figure 3.29 Hewlett-Packard waveform generator

To minimise systematic error, 100 successive response signals captured were averaged and the resultant set of data was filtered through the ADF Converter program before the data plots to be used in MS-Excel were obtained. The following graphs plotted show the transfer function of the wave propagated through the piezoceramic through the accumulated load cycles.

3.8.3 RESULTS AND DISCUSSION

The influences of PZT signal degradation on three important measurement parameters namely the PZT [d_{31}] constant; the impedance values and transfer function measurements are analysed in this sections. The results were acquired from both the aluminium bars with two piezoceramics bonded and the dog bone shaped specimen with multiple piezoceramics.

Change of voltage readings with [d_{31}]

The datum for recording voltage output from the individual PZT was established at the load of 500-microstrain. At this load no PZT material property changes were expected and it allowed comparison between the different specimens, which experienced different strain levels. In determining the threshold before the degradation of signal, the bisection method was applied to determine the level of strain to be applied.

By using one channel to measure the output voltage of the PZT due to mechanical excitation and the second channel to monitor the strain experienced by the PZT, an acceptable set of data points was obtained. The $[d_{31}]$ constant was determined as a function of both voltage output and strain output from the strain gauges. These points were then plotted in MS-Excel to produce a relationship between the $[d_{31}]$ PZT voltage and the strain levels as shown in Figure 3.30. The $[d_{31}]$ constants calculated were then normalized against the $[d_{31}]$ constant at 500-microstrain.

This was to regulate all voltages received because different PZT patches emit different voltage magnitude, depending on physical qualities of the bond and the production of the piezoceramic itself.

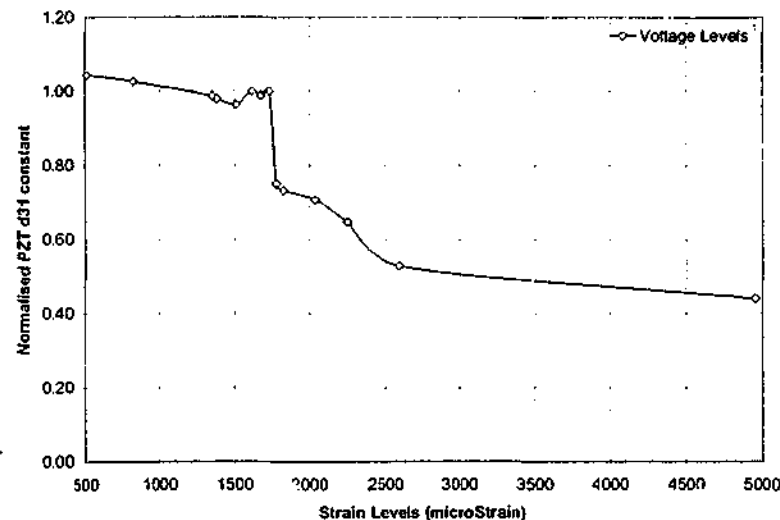


Figure 3.30 Change in $[d_{31}]$ constant with strain after 100-kcycles

In the investigations carried out over the different loading conditions, it was found that to prevent PZT sensors from degrading while in use, the load experienced by the them must not exceed 1850-microstrain.

When a piezoceramic experiences strain levels that exceed this limit, it is suggested that a formula be applied to obtain a rectified value of the voltage read from a PZT with degraded signal. A methodology must be formulated to analyse specimens with bonded PZTs experiencing strain level above 1850-microstrain, thus accommodating a wider range of strain levels during experiments. By also taking into account the

estimated number of cycles in the loading cycles graph, this formula may be able to establish an exact relationship between the strain at a given number of accumulated cycles and the voltage to be expected from the PZT's excitation.

Change in impedance measurements

In analysing the set of impedance values obtained from interrogating each piezoceramic after completing the whole fatigue testing, a high correlation was established. By plotting the impedance values for each specimen against the interrogation frequency used, in total 10 readings from 1-kHz to 8-kHz in Microsoft Excel, the resulting graphs easily fall within a 5% margin from each other. It is a small error considering the electrical noise of the surrounding lab and the differing bond conditions between the specimens.

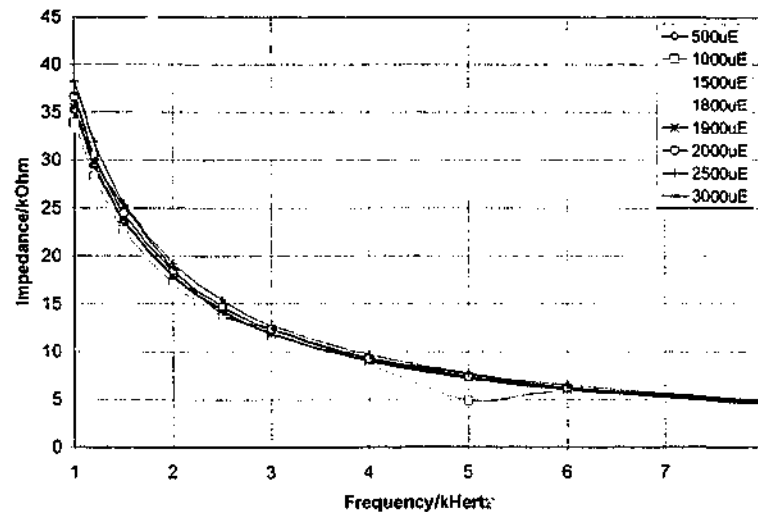


Figure 3.31 Change in impedance measurement with strain

These impedance values obtained from the PZT sensors band together at high frequency. Though the PZT sensors that experience strain loading above 1850-microstrain exhibit degraded voltage signal, however these specimens do not show much impedance value variation from those PZT sensors that experience strain loading below 1850-microstrain, which do not exhibit degraded signal.

Change in transfer function measurements

In analysing the set of transfer function measurements obtained from interrogating a pair of piezoceramic after completing the whole fatigue testing, a high correlation was

established. An additional PZT was bonded to the aluminium bar to be the actuator. The transfer function measurements for each completed specimen were plotted against the individual strain levels experienced by the examined PZT in Microsoft Excel. The results acquired are shown in Figure 3.32.

For low strain levels up to 1850-microstrain the transfer function measurement acquired remains at about the level of 14 (arbitrary unit). After 1850-microstrain there is an acute decrease in the transfer function measurement. Since the degraded PZT was used as the sensor in all the testing, this observation agrees with the voltage output reading shown previously. The ratio of the response displacement from a degraded sensor to the response displacement from a not degraded actuator will be similar to that of response displacement from a single PZT. This is in contrast to the observation made for the results using the impedance method.

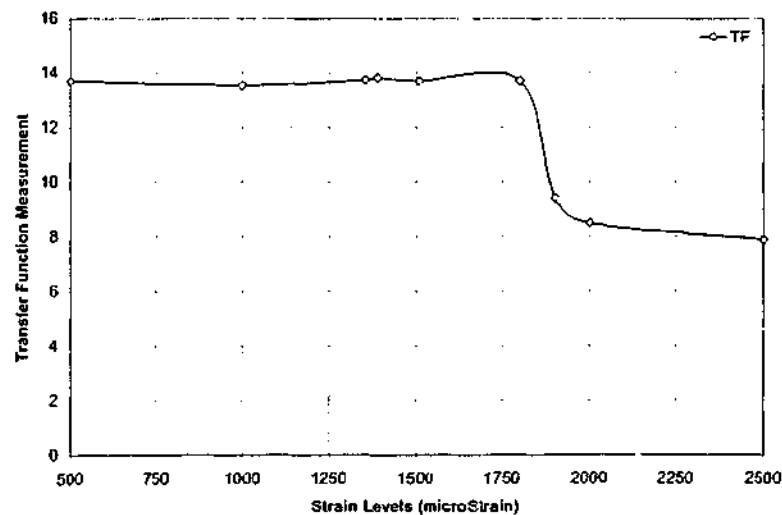


Figure 3.32 Transfer function measurement recorded with degraded sensors

These experiments show that degradation of PZT is a critical issue that needs to be addressed. The signal from the PZT output without identification of this problem could be misinterpreted. In summary, the voltage output from the PZT is depend upon the $[d_{31}]$ constant and when the $[d_{31}]$ reduces at a critical threshold the voltage output reduces in a proportional manner.

The change in $[d_{31}]$ has no impact upon the results obtained by the impedance method. This is expected as the impedance method acquires the ratio of the response velocity

to the force applied. When the $[d_{31}]$ constant changes the force applied as well as the response velocity detected through the PZT is proportional the change.

The change in $[d_{31}]$ constant has a similar impact on the transfer function method as the voltage does because the actuator used for this testing is newly bonded and thus does not record any degradation. The sensor has undergone the respective number of cycles. The ratio of response displacement between the sensor and the actuator will be similar to the voltage output.

PZTs surface mounted on a composite patch experience half the strain experienced by the host structure due to the patch thickness. Therefore in all the loading conditions used in the experiments, the host structure is able to sustain a strain level as high as 3,700 microstrain before the PZT degrades.

3.9 CONCLUDING REMARKS

It has been identified in this chapter that the equipments and the conditions are suitable for the investigation on the monitoring of composite repair patch. The settings required ensuring the repeatability the experiments, and the specimen preparation was clearly elaborated. The factors that will influence the effectiveness of the methods that will be used for the detection of disbond are as listed.

1. Equipments used for the acquisition of data from the respective methods are susceptible to electrical noise, thus during operation and the interpretation of data, a noise filter of certain 50-Hz harmonics is necessary.
2. The adhesive used to bond and the PZT to the host structure must be inspected to ensure good conditions. The connection of the PZT and the aluminium foil through the silver loaded epoxy can be tested using a multi-meter.
3. The MTS machine is able to deliver the load necessary to the specimen if proper calibration was made to the machine. Having a big load range will cause the machine to be not sensitive at delivering small loads.

4. Test rig to be used for impacting the composite plates must be calibrated to quantify the impact upon the composite plates. This is to ensure that the results acquired using the stress wave method can be related to the impact load.
5. Degradation of the PZT occurs above 1850-microstrain. Degradation of PZT has an impact on the voltage output, which affects the performance of the
6. Transfer function method. Since no methodology has been designed to solve the problem, the operating strain of the PZT in the experiments must be below 1850-microstrain.

CHAPTER 4

NUMERICAL MODELLING

4.1 INTRODUCTION

Many previous studies have been done, both experimental testing and numerical analysis, on wave propagation for the detection of damage in composite material and composite structures. In this chapter, for the validation of numerical models the results from the numerical analysis are presented and then compared to the results obtained by theoretical calculations or results previously published. Numerical analysis provides greater insight into the physics of the problem than possible through experiments due to physical limitations.

The numerical analysis uses the finite element analysis that is provided by the software PAFEC. This chapter will describe the temporal and spatial discretisation used in this study for the three different methods namely, low frequency impedance method, low frequency transfer function method and high frequency stress wave method. The boundary conditions used for the three separate models are also outlined. The results of the validation for the impedance and transfer function method are presented in section 4.2 while the results of the validation for the stress wave method are presented in section 4.3.

In order to validate the code and mesh density of the model for both the impedance method and transfer function method, the results were compared to theoretical calculations. For the purpose of investigation the frequency response of a plate was used to determine the resonant frequency. This is a reasonable idealisation of a PZT actuator being excited with a range of frequencies. Figure 4.1 show the mesh used in the model to represent a mild steel plate. The steady state response of the plate to an external sinusoidal excitation to the middle of the plate was used to determine the resonant frequency. Measurements were made at 1-Hz increment with the frequency range extending from 0- to 60-Hz.

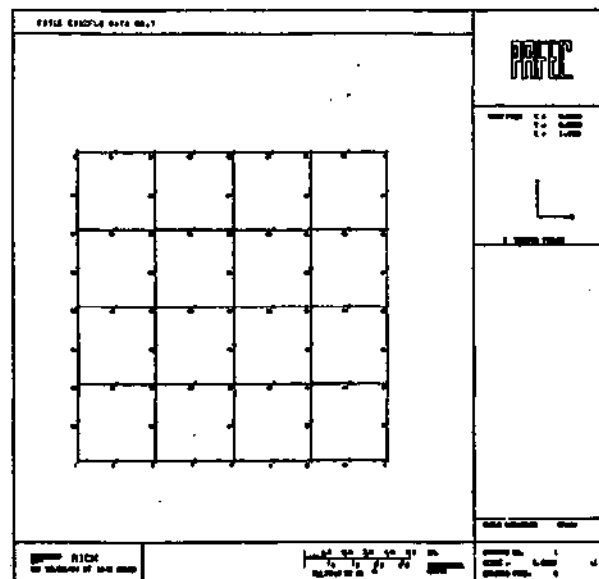


Figure 4.1 Initial mesh used for the validation

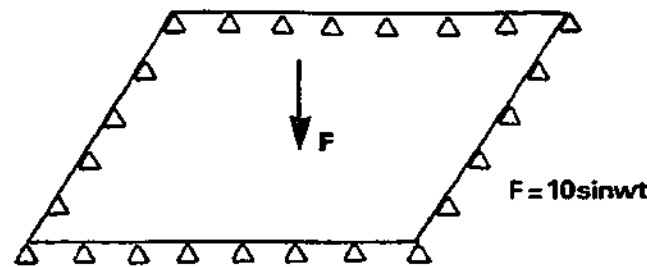


Figure 4.2 Sinusoidal excitation of the plate

All elements were of eight-node quadratic formulation and the initial simulated model was 0.001-m thick plate and had a mesh density of 0.125-m square. This was considered sufficient to support a wavelength of 0.5-m, if there are 5 nodes per wavelength. Based on the material properties for mild steel, the model was ascribed a Young's Modulus of 209-GPa, a density of 7800-kg/m³ and a Poisson's ratio of 0.3. The assumption that the fastest wave to be modelled is a longitudinal wave, which had a velocity of 6005-m/s, and this mesh density was predicted to support frequencies up to 12-kHz.

The element used for the model was a flat things isotropic or orthotropic shell element, which can carry bending, and membrane loads. Reasonable distortions from the basic square shape were permitted provided flatness was preserved. The sinusoidal excitation acted normally to the shell surface in the positive element z direction (from beneath the paper in the above Figure 4.2). Each node has five degrees of freedom at the element level but after transformation to a general shell the extra freedom is introduced. The element was based upon the thin plate bending theory and it should not therefore be used if the thickness of a plate is less than one fifth of typical plate sizes or radii of curvature.

The response of the plate at $x = 0.125\text{-m}$, $y = 0.125\text{-m}$ (denoted as Node 33) and $x = 0.25\text{-m}$, $y = 0.25\text{-m}$ (denoted as Node 34) in the z-direction (denoted as Direction 3) are shown in Figure 4.3. The first response was from the node located at the middle of the plate and the second response was from a node located at 0.125-m down and 0.125-m left from the middle. These results are presented in the form of amplitude versus frequency. The amplitude scale is linear and the units are arbitrary. The

amplitude reaches a maximum at a frequency of 19.744-Hz, which is the resonant frequency of the plate.

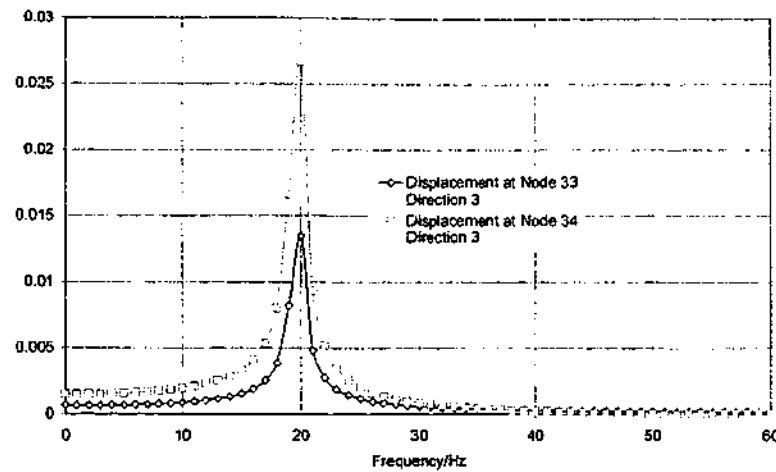


Figure 4.3 Output from PAFEC

The theoretical solution was obtained from Timoshenko et al (1974). The plate had a uniform thickness of h that was assumed to be small in comparison with its other dimensions. The x - y plane was the middle plane of the plate and that the deflections in the z direction were small in comparison with the thickness. In addition, the normals to the middle plane of the plate were assumed to remain normal to the deflected middle surface during the vibrations.

With the above assumptions they described the circular frequency of a square plate as shown in Figure 4.2 with simply supported edges using the following Equation 4.1.

$$p = \pi^2 \sqrt{\frac{D}{\rho h} \left(\frac{m^2}{a^2} + \frac{n^2}{b^2} \right)} \quad \text{Equation 4.1}$$

where

ρh the mass per unit area

D the flexural rigidity of the plate is described by the following Equation 4.2

$$D = \frac{Eh^3}{[12(1-\nu^2)]} \quad \text{Equation 4.2}$$

From the equation it was found that the frequency of vibration for the first mode to be 19.68-Hz. By refining the mesh density of the simulated model to 0.0625-m and increasing the automatic masters to 60, the frequency of vibration converged upon

19.68-Hz. Further refinement of the mesh density and increment of the automatic masters provided the same solution. The agreement with the theoretical result is seen to be very good.

4.3 VALIDATION OF FINITE-ELEMENT MODEL FOR SOLVING STRESS WAVE METHOD

Preparatory solutions using part of the model representing just one plate were used to confirm that the idealisation accurately predicted the expected propagation behaviour of the dispersion curves of Figure 4.4 and Figure 4.5. To validate the code and typical mesh size needed, this model of an aluminium plate was compared with two-dimensional Fourier transform technique results obtained by Alleyne and Cawley (1991). Simulations by Alleyne and Cawley (1991) are chosen as it overcomes the problems of multiple modes and dispersion by transforming the received amplitude-time record to amplitude-wave-number records at discrete frequencies. For further validation of the numerical simulation for the composite repair patch was done with the work by Lowe et al (2000). They investigated the transmission of Lamb waves across adhesively bonded lap joints.

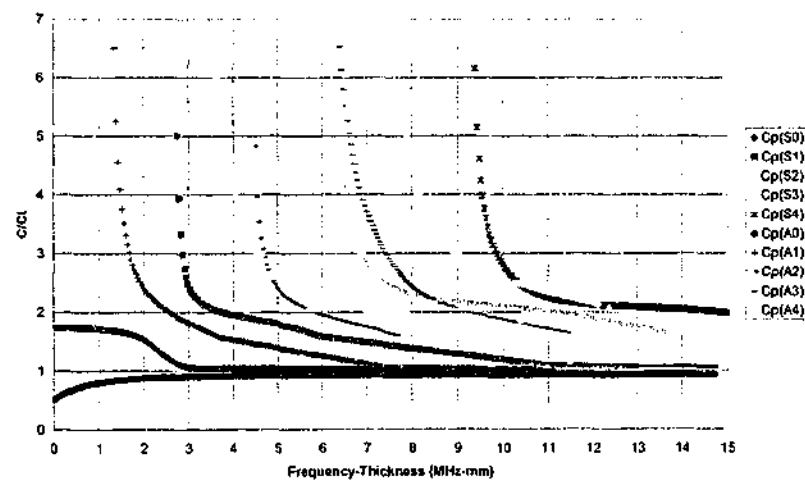


Figure 4.4 Dispersion curves of phase velocity at Poisson's ratio 0.34

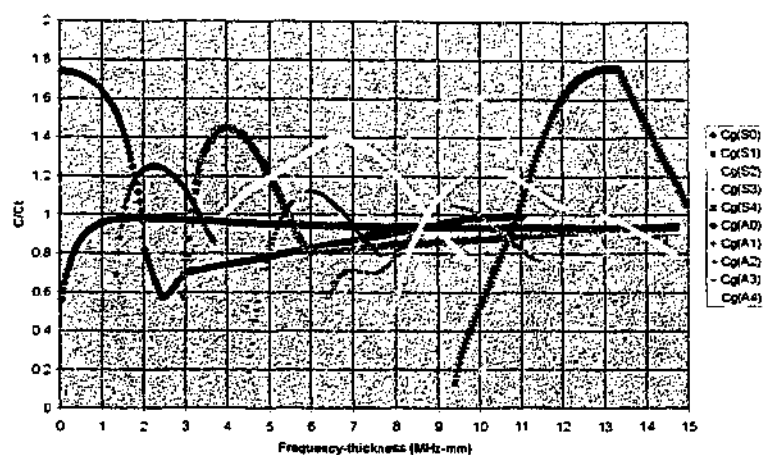


Figure 4.5 Dispersion curves of group velocity at Poisson's ratio 0.34

4.3.1 DISPERSION CURVE AND DEFLECTED SHAPES

Figure 4.4 and Figure 4.5 show the phase velocity and group velocity dispersion curves for the first ten Lamb modes in an aluminium plate with a Poisson ratio of 0.34. These, and all the other dispersion curves and mode shapes in this thesis, were calculated using a general purpose dispersion curve written in the C programming language developed to solve the following dimensionless transcendental equations from Viktorov (1967):

$$\frac{\tan \sqrt{1-\zeta^2} \bar{d}}{\tan \sqrt{\xi^2-\zeta^2} \bar{d}} = -\frac{4\zeta^2 \sqrt{1-\zeta^2} \sqrt{\xi^2-\zeta^2}}{(2\zeta^2-1)^2} \quad \text{Equation 4.3}$$

$$\frac{\tan \sqrt{1-\zeta^2} \bar{d}}{\tan \sqrt{\xi^2-\zeta^2} \bar{d}} = -\frac{(2\zeta^2-1)^2}{4\zeta^2 \sqrt{1-\zeta^2} \sqrt{\xi^2-\zeta^2}} \quad \text{Equation 4.4}$$

where,

$$\bar{d} = k_1 d \quad \text{Equation 4.5}$$

$$\zeta^2 = \frac{c_l^2}{c^2} \quad \text{Equation 4.6}$$

$$\xi^2 = \frac{c_t^2}{c_l^2} \quad \text{Equation 4.7}$$

The real roots of Equation 4.3 and Equation 4.4 correspond to propagating harmonic waves in the x-direction, while the imaginary roots relate to the non-propagating spatially varying vibrations, which are of importance in forced and transient wave motion. The group velocity, $c_g = \partial\omega / \partial k$, may be calculated once the phase velocity or wave number as function of the frequency-thickness product is known.

The amplitude of the x and z displacements at each node on the plate edge were given by the through thickness deflected shape calculated from the following equation (Alleyne and Cawley, 1991):

$$u_s = Ak_s i \left(\frac{\cosh q_s z}{\sinh q_s d} - \frac{2q_s s_s}{k_s^2 - s_s^2} \frac{\cosh s_s z}{\sinh s_s d} \right) e^{i(k_s x - \omega t)} \quad \text{Equation 4.8}$$

and

$$w_s = Aq_s \left(\frac{\sinh q_s z}{\sinh q_s d} - \frac{2k_s^2}{k_s^2 + s_s^2} \frac{\sinh s_s z}{\sinh s_s d} \right) e^{i(k_s x - \omega t)} \quad \text{Equation 4.9}$$

where u_s and w_s are the displacements in the x and z directions, respectively, k_s is the wave number of the symmetric Lamb modes, $q_s^2 = k_s^2 - k_1^2$, and $s_s^2 = k_s^2 - k_2^2$. Similar relations for the antisymmetric modes may be obtained by changing the subscript s to a and replacing sinh by cosh and vice versa.

In the next section the results of finite element modelling investigations on 0.5-mm steel plate will be presented. These results are used to show how the 2-D FFT method may be used to quantitatively analyse Lamb wave response signals before and after reflection from the free edge of the plate.

4.3.2 DESCRIPTION OF FINITE ELEMENT MODEL

The parameters for this problem are chosen so as to match the finite element model of 0.5-mm thick plate, 200-mm long and the spatial sampling interval of 1-mm by Alleyne and Cawley (1991). All the modelling was carried out assuming plane strain in the xz plane. The finite element package of PAFEC was used with uniform square mesh of eight-noded quadrilateral element. The elements representing the 1.6-mm thick aluminium plates were each 0.2-mm square, so there were 16 elements through

the thickness of the plate, and at least 12 elements per wavelength along the plate. This comfortably satisfies the threshold of eight elements per wavelength, which the authors have found from experience to be a good limit for accurate modelling. Sufficient lengths of plate were such that reverberations of the signals along the lengths of the plates can be avoided.

The following bulk material properties were assumed for steel. All models were ascribed a Young's Modulus of 209-GPa, the longitudinal velocity 5960-m/s, transverse velocity 3260-m/s, density 8000-kg/m³ and a Poisson's ratio of 0.34 for the steel component. All of the finite element analyses assume perfectly elastic materials, thus neglecting any damping properties. The steel has negligible damping properties and is therefore accurately modelled in this way. The piezoelectric patches were modelled as thin plates of material with the properties quoted by Piezo Systems for their Lead Zirconate Titanate (PZT) patches; That is, a Young's modulus of 66-GPa, a Poisson's ratio of 0.34 and a density of 7800-kg/m³.

Explicit time marching was employed, assuming a diagonal mass matrix. The time step was chosen to satisfy the stability limit L/C , where L is the element length and C is the wave speed of the fastest wave present. The time step was set at 10 nanoseconds for all models, which is one-sixteenth of the time that a longitudinal wave would take to propagate 1-mm.

In order to excite a pure Lamb wave, two conditions have to be simultaneously satisfied. Firstly, the frequency of the excitation must be appropriate for the desired mode and secondly, the variation of the excitation with the z at the excitation position ($x = 0$ in the tests reported here) must correspond to the exact mode shape of the Lamb wave being excited. Assuming a single frequency input, the required excitation $f(z, t)$ is of the form

$$f(z, t) = \Phi(z, \omega)e^{i\omega t} \quad \text{Equation 4.10}$$

where $\Phi(z, \omega)$ describes the displacement of the plate in the x and z directions in the mode of interest at the desired frequency as a function of z .

The excitation of each chosen input mode was achieved by prescribing the displacements at the nodes across the thickness of the remote end of the transmitter plate, over the time period of the signal. According to the earlier discussion, the signals that were used consisted of five cycles of the target frequency in a Hanning window. In order to excite the desired mode without exciting any other modes, which could exist at the same frequency, the amplitudes of the displacements (in both in-plane and out-of-plane directions) at each node across the thickness of the plate were scaled by the amplitudes of the displacement mode shapes at the appropriate depth in the plate. Furthermore, by performing this scaling in the frequency domain, it was possible to account for changes of the mode shape over the frequency bandwidth of the signal. This method ensures reliably that only the desired mode is excited. The input signal was the only boundary condition, which was applied to the models.

From the group velocity dispersion curves, it can be seen that dispersion of the s_0 and a_0 modes is relatively small at 0.5-MHz.mm, and that operation above 1.5-MHz.mm could result in the spurious excitation of other modes. Operation at very low frequency-thickness would result in propagation of signals that are temporally and spatially long and this could cause practical problems due to reverberation and interference. A frequency-thickness of 0.5-MHz.mm would therefore seem to be reasonable for the s_0 and a_0 modes. In this work this corresponds to an excitation centre frequency of 1.0-MHz for aluminium plates of 0.5-mm thickness.

It is convenient to excite the s_0 mode at its maximum group velocity because dispersion is kept to a minimum and also at this point it is the fastest of all possible modes. This means that it would be the first signal of a group of modes to be received when several modes are converted. However, the frequency at which this occurs is relatively close to the cut-off frequency for the a_0 mode, which has a wave number similar to that of the s_0 mode. This can be seen in the close proximity of their phase velocities in the region of this frequency in Figure 4.1. The implication of this is that it would be difficult to resolve the two modes in the wave number domain and hence it would be virtually impossible to obtain transmission coefficient results for the s_0 mode alone. Decreasing the frequency would reduce the excitation of the a_0 mode, so a frequency of 1.0-MHz was eventually chosen, corresponding to a frequency-

thickness of 0.5-MHz.mm; this gives a working compromise between the avoidance of the excitation of the a_0 mode whilst achieving relatively low dispersion.

The signals, which were used in the study, consisted of five cycles tone burst of the chosen centre frequency, windowed by a Hanning function to limit the bandwidth. This choice was made in order to give a good compromise between the needs for a narrow bandwidth, for mode selectivity, and short time duration to give temporal separation of multiple signals.

4.3.3 RESULTS AND DISCUSSION

Figure 4.6, Figure 4.7 and Figure 4.8 show the normalised time histories of the response of the top surface of the plate at $x = 0$ -mm, 100-mm and 163-mm, respectively, where the input at $x = 0$ -mm was appropriate to excite only s_0 . The response of the plate at $x = 100$ -mm shows that the propagating wave is essentially non-dispersive and the group velocity is 5430-m/s.

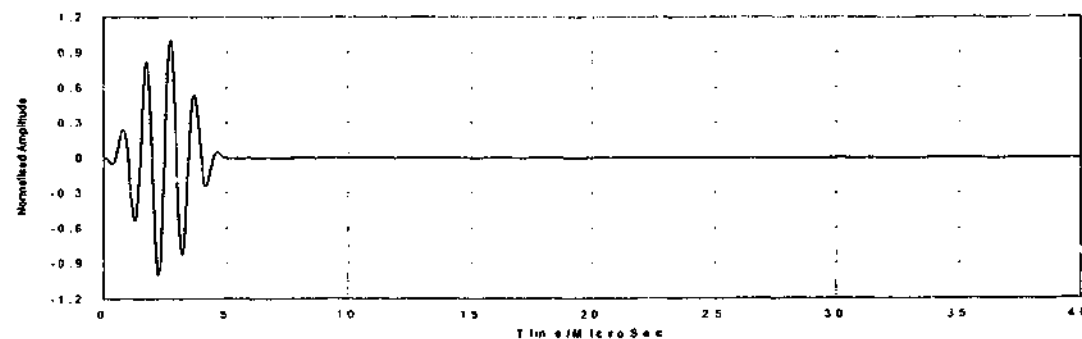


Figure 4.6 Normalised time history of the z displacement at $x = 0$ -mm used in all the numerical test

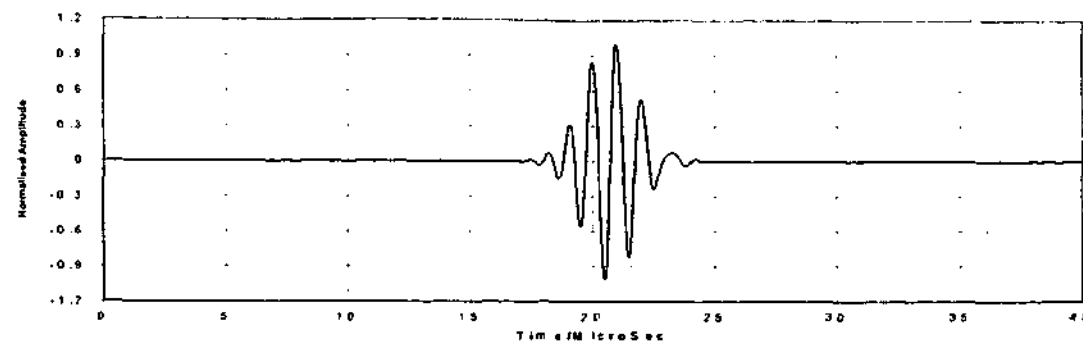


Figure 4.7 Normalised time history of the z displacement at $x = 100$ -mm in a 0.5-mm plate when the input at a is designed to excite only s_0

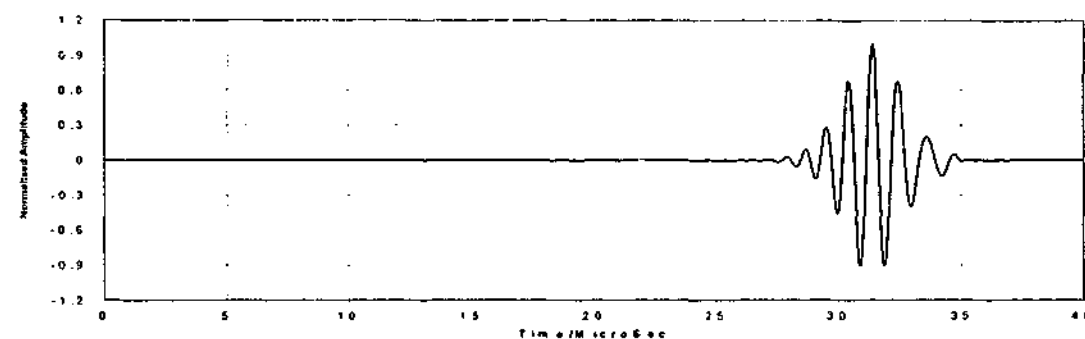


Figure 4.8 Normalised time history of the z displacement at $x = 164$ -mm in a 0.5-mm plate when the input at a is designed to excite only s_0

The agreement with the time history obtained from Alleyne and Cawley (1991) as shown in Figure 4.9 and Figure 4.10 is very good. A comparison of the time history from the finite element that predicted the arrival of the first wave at 1.8 microseconds agrees with the non-dispersive group velocity of 5430-m/s.

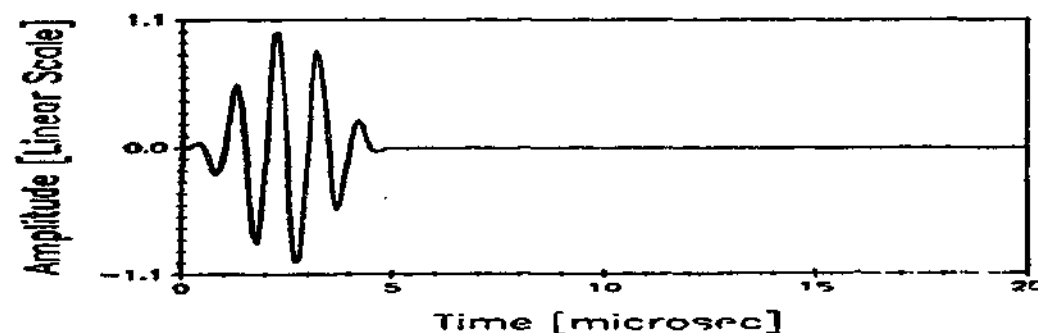


Figure 4.9 Normalised time history of the z displacement at $x = 0$ -mm from Alleyne and Cawley (1991).

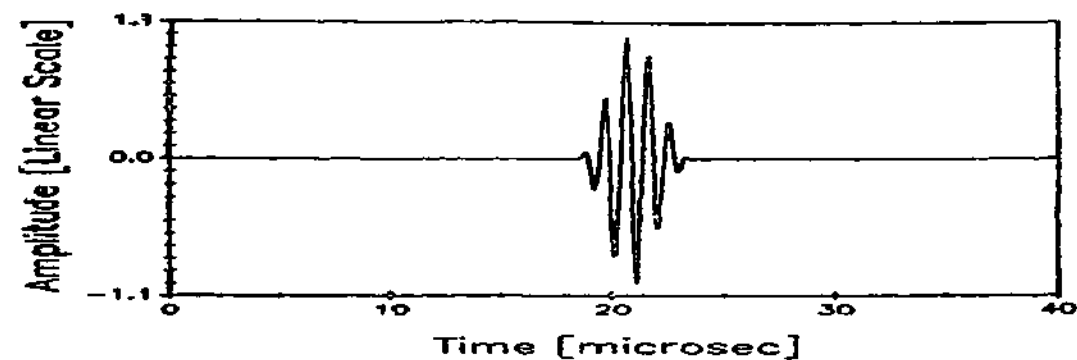


Figure 4.10 Normalised time history of the z displacement at $x = 100$ -mm in a 0.5-mm plate from Alleyne and Cawley (1991).

The finite element results were also post-processed using the 2D-FFT method prescribed by Alleyne and Cawley (1991) using MATLAB 6. From the following diagrams the results from the 2D-FFT is compared with the theoretically predicted wave-number dispersion curve. The agreement is seen to be very good.

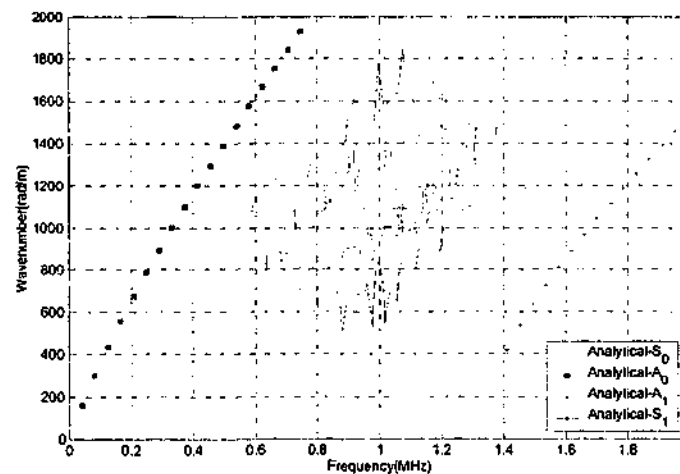


Figure 4.11 A comparison of the finite element predictions with the analytical solution of the dispersion curves

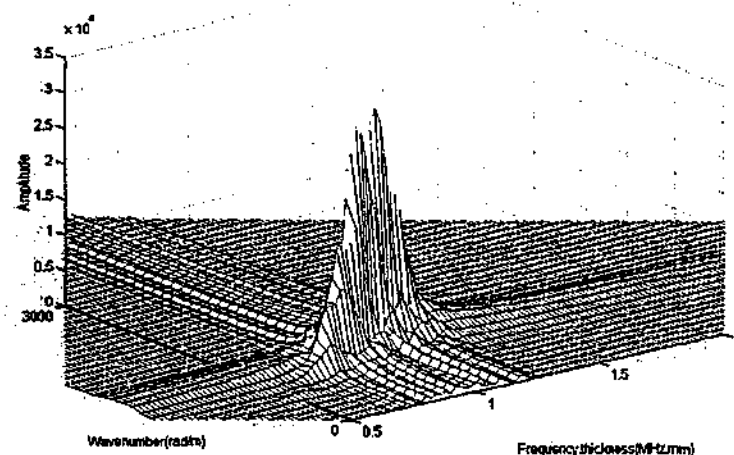


Figure 4.12 3-D plot of the 2-D FFT results of the case given in Figure 4.8, showing a single propagating mode, s_0

4.4 CONCLUSIONS

In this chapter it is established that the results from both the numerical model for impedance method and transfer function method and the numerical model for the stress wave method agree well with the respective comparisons. The results from the numerical model for the impedance method and transfer function method agree with the results from the theoretical formulation by Timoshenko et al (1974). The results from the numerical model used for the stress wave method agree with the published findings of Alleyne and Cawley (1990). Based on this validation of the two models, these models can be applied for the analysis of more complex problems.

CHAPTER 5

EVALUATION OF THE IMPEDANCE METHOD USING NUMERICAL ANALYSIS

5.1 INTRODUCTION

In this chapter, the detection of disbond growth by means of piezoelectric transducers using the electromechanical impedance method is analysed. The problem was simulated using a finite element analysis prior to experimental testing. Section 5.2 presents the background theory of the electromechanical impedance method in order to provide a good understanding of the response of this method to the existence of disbond.

Section 5.3 outlines the model development for the initial simulations conducted to gain understanding of the detection possibilities. The first model was a simple model with four bonded piezoelectric transducers. The results obtained using the impedance method are used to establish a relationship between impedance and the progress of the disbond growth.

In section 5.4, a more complex model is developed to simulate realistic shapes and sizes of disbond underneath a composite repair patch. Although these types of

disbond are not exhaustive they represent some of the most common damage recorded in practical application of composite repairs.

5.2 BACKGROUND THEORY

Mechanical impedance is defined as the ratio of the driving force acting on the support to the response velocity at the point of application of the force. The characteristic mechanical impedance is analogous to characteristic electrical impedance, which is defined as the ratio of the applied voltage to the resulting current. This property of the piezoceramic (PZT) allows the coupling of the mechanical impedance to the electrical impedance and hence provides both actuation and sensing when the impedance method is used in this research. On the other hand, a commonly used piezoelectric transducer polyvinylidene fluoride (PVDF), does not function as an actuator since it is a film, and thus has high compliance and low stiffness compared with that of PZT.

When a piezoelectric sensor/actuator is bonded to a structure and subjected to a given sinusoidal voltage it responds mechanically due to its constitutive piezoelectric property shown in Equation 2.7 and Equation 2.8, of the literature review in Chapter 2. However, its response is constrained by the structure to which it is bonded. When the structural condition in the vicinity of the PZT element changes (i.e. with disbond), the response of the PZT element is likely to change due to the change in local impedance. This change in impedance behaviour is consistent with the observation of Cawley (1984), whose findings are discussed in section 2.7.1 in Chapter 2. In this current research it is proposed to use the change in the PZT response as an indication of the presence of the disbond.

The impedance method utilises the electromechanical properties of the PZT material. Therefore the parameter measured for the experimental electromechanical impedance method is in the electrical unit of ohms. However, in the numerical simulation, mechanical impedance can be measured as the ratio of the applied force to the rate of

change of strain in the PZT as shown in the following equations. Therefore the measurement parameter is measured in the mechanical unit of Ns/m .

The velocity of response, v , can be written as:

$$v = \frac{d\xi}{dt} \quad \text{Equation 5.1}$$

where ξ is the average strain across each PZT or PVDF. The temporal behaviour of the vibrating material is described by a complex angular frequency, $\omega = \omega + j\beta$, whose real part is the angular frequency of vibration, ω . Therefore as postulated by Kinsler et al (1982), the strain for a given wave number, k , is as follows.

$$\xi(x, t) = (Ae^{jkx} + Be^{-jkx})e^{j\omega t} \quad \text{Equation 5.2}$$

Equation 5.2 can be simplified to:

$$\xi(x, t) = De^{j\omega t} \quad \text{Equation 5.3}$$

By substituting Equation 5.3 into Equation 5.1, v can be expressed as:

$$v = j\omega De^{j\omega t} \quad \text{Equation 5.4}$$

Impedance can thus be written as follows:

$$Z = \frac{F}{j\omega\xi} \quad \text{Equation 5.5}$$

where Z is the impedance of the structure, F the sinusoidal forcing and ω the angular frequency. The force due to sinusoidal loading is assumed to be analogous to the voltage input. Therefore the force is considered to be 10 units since the applied voltage is a constant voltage of 10-V. This assumption is valid because piezoelectric materials actively elongate when voltage is applied as related by the $[d_{31}]$ constant.

In the present investigation, the average strain, ξ , used above is calculated by taking into consideration five nodal positions along a simulated PZT strip as shown below. By using the auto meshing option contained in the numerical simulation software, each strip was divided into 9 nodes along the length and 2 nodes across the width.

Since the readings taken from each node did not differ much from one another on a single side it was sufficient to consider only five nodes on each side. The strain experienced by each sensor is calculated by taking the difference in the average displacement of the nodes along A and B, and subsequently dividing it by the distance between A and B as shown in Figure 5.1. Displacement is recorded for both the x- and y-direction and subsequently the strain measured includes both directions.

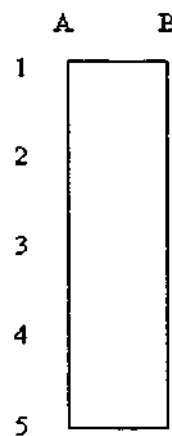


Figure 5.1 Schematic drawing of node positions on PZT- or PVDF- sensors and actuators

5.3 PRELIMINARY SIMULATION STUDY

The model used here represents a preliminary investigation into the use of the impedance method in this thesis. The first numerical model developed for the detection of disbond growth was to replicate the experiments that would be done with artificial disbond growth through insertion of Teflon between the repair and structural component. The aim was to identify the possibility of damage detection using impedance method by means of piezoceramic elements. The results were to be compared to the experimental evidence for verification.

5.3.1 MODEL DEVELOPMENT

Figure 5.2 illustrates in detail a specimen with the repair configuration considered in this investigation. It shows an 11-ply unidirectional boron/epoxy doubler with a

tapered edge bonded onto an aluminium plate. In the numerical analysis of this specimen, seven models were developed, each with a disbond size of, 0-, 2-, 4-, 6-, 8-, 10- and 12-mm respectively. The series of disbonds simulated the progressive development of a disbond that may occur during active service. The disbond shape is assumed to be rectangular and spans the entire width of the specimen. The material used for all the piezoelectric transducers were made of PZT.

The two-millimetre damage was located directly beneath piezoelectric-3 while the four-millimetre damage was located up to the border of piezoelectric-3. Damage of 6-mm was between piezoelectric-3 and piezoelectric-2. The 8-mm and 12-mm damages were located up to the border of piezoelectric-2 while 10-mm damage was beneath piezoelectric-2.

In the simulation, four piezoelectric transducers were assumed to be bonded onto the specimen as shown in Figure 5.2. Piezoelectric-1 was bonded on the repair patch far from the disbond; piezoelectric-2 was bonded on the repair patch at the top-end of the taper; piezoelectric-3 was bonded above the disbond area at the bottom-end of the taper and finally piezoelectric-4 was bonded on the aluminium substrate. In order to provide an indication of the extent of simulated disbonding, we interrogated all the PZT transducers bonded. The width of piezoelectric-1 and piezoelectric-4 were 10-mm and piezoelectric-2 and piezoelectric-3 were 4-mm.

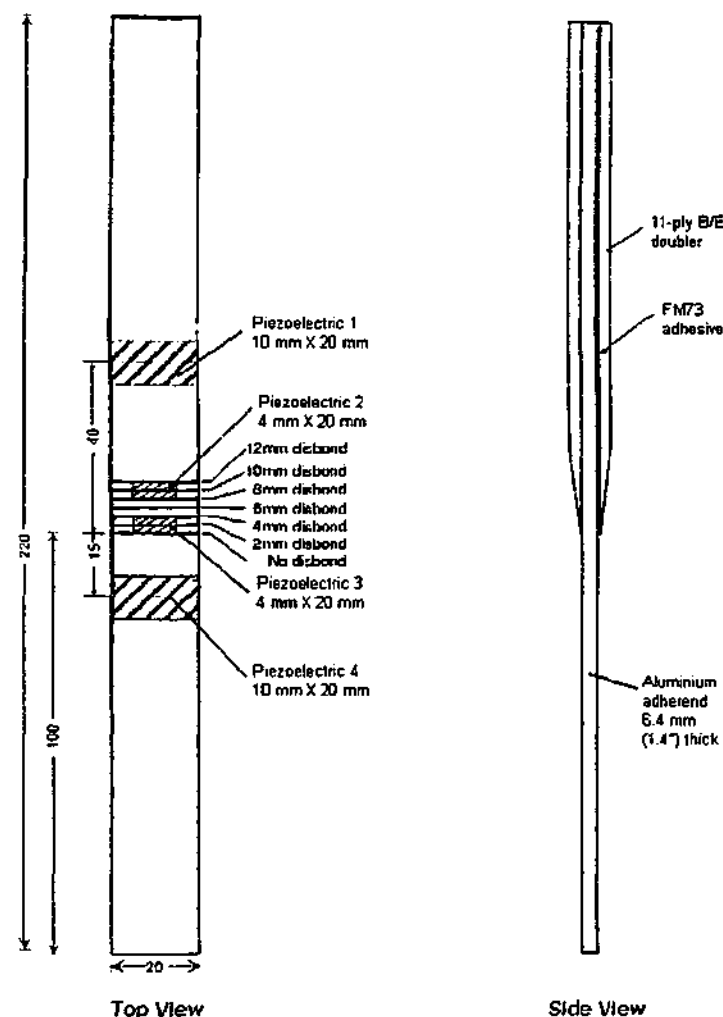


Figure 5.2 Schematic drawing of the specimen with sensor/actuator bonded

5.3.2 RESULTS AND DISCUSSION

Impedance measured at piezoelectric-1 (PZT1) is shown in Figure 5.3. The unit for impedance is Ns/m . The y-axis for the impedance graphs is measured in Ns/m and the x-axis is measured in hertz. The case shown in Figure 5.3 refers to that when the damage is far from the sensor/actuator (PZT1). The impedance curves tend to band together. These results shows that a PZT located on the far field on the composite patch is not expected to yield any measurable indication of the disbond.

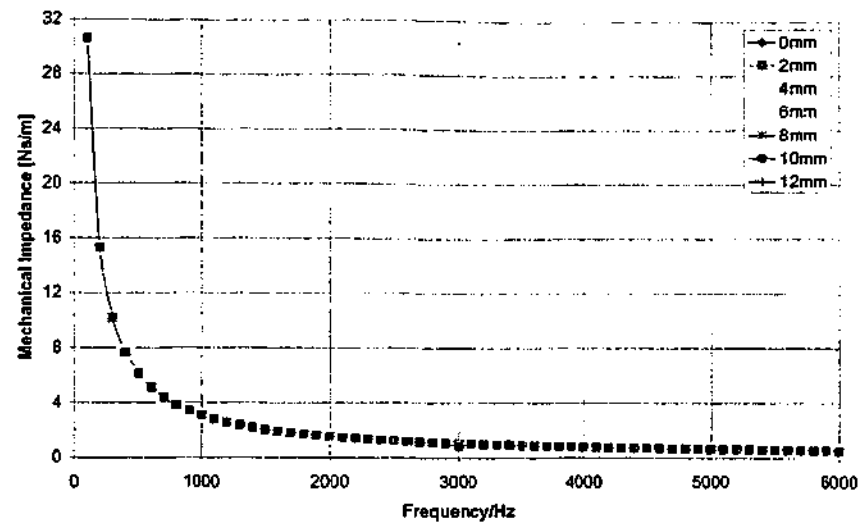


Figure 5.3 Impedance measurement recorded at piezoceramic location PZT1

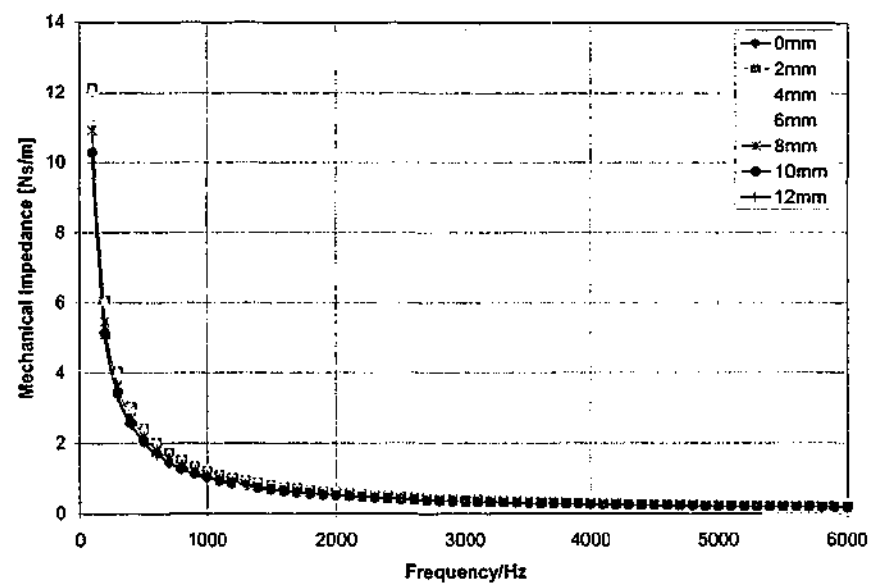


Figure 5.4 Impedance measurement recorded at piezoceramic location PZT2

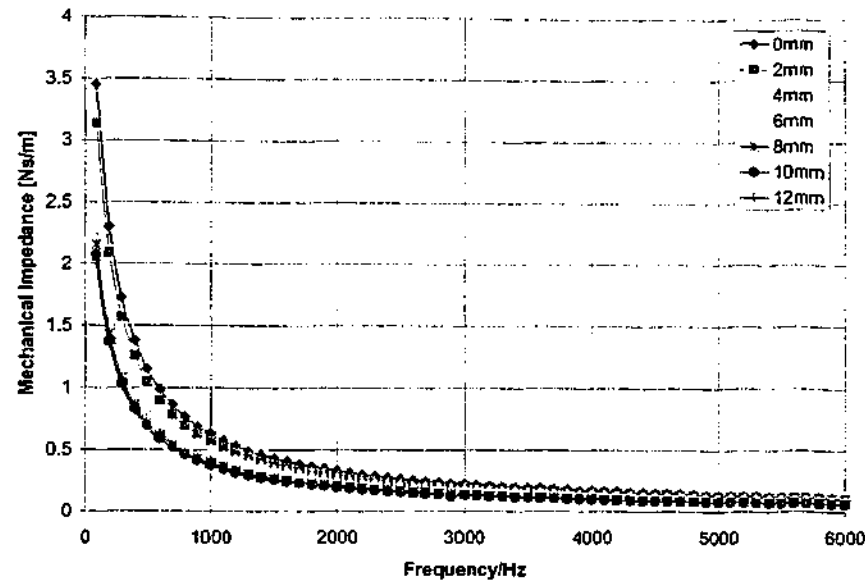


Figure 5.5 Impedance measurement recorded at piezoceramic location PZT3

Figure 5.4 and Figure 5.5 show the response of the impedance as a function of the damage sizes when PZT2 and PZT3 were used. In Figure 5.4, as the initial damage was located at a distance from PZT2, the impedance graphs tend to band together, and as the disbond growth approaches PZT2 the impedance starts to decrease. Figure 5.5 shows that when the damage under PZT3 was allowed to grow, a reduction in the impedance was recorded. The impedance reaches an asymptote when the damage develops past PZT3. It can also be seen from this figure that there is a significant decrease in the impedance when the size of the damage is similar to the size of the individual sensor/actuator PZT. In this respect the size of a PZT needs to be governed by the size of the given disbond to be detected under the patch.

Finally in Figure 5.6, the graphs remain close together from 50-Hz up to 6000-Hz when PZT4 is located far from the damage area as it is bonded on the aluminium substrate. The results shown in Figure 5.6 closely resemble those in Figure 5.3 since both graphs are for the PZTs located far from the disbond area. It is difficult to deduce the existence of a disbond from these sets of results, as they show no measurable indication of damage. It is worth noting that the results shown in Figure 5.6 have the highest value of mechanical impedance compared to the other three results. Since the impedance method is a stiffness-based method, it is expected that the absolute value acquired using the method will be dependent on the location of the PZT. Piezoelectric

element PZT3 that is located on the taper where the composite is the thinnest exhibits the lowest impedance values. This could lead to confusion if the impedance measurement is taken with these axes without knowledge of the sensor/actuator locations. Normalising the results with respect to their initial readings might overcome similar problems in future.

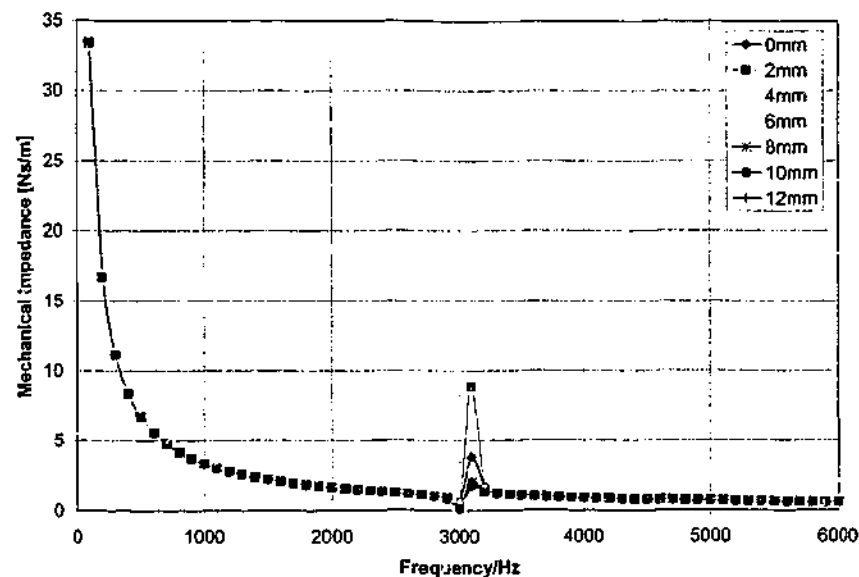


Figure 5.6 Impedance measurement recorded at piezoceramic location PZT4

It is evident that the impedance method is particularly effective when the PZT is located directly over the damaged area. In addition since this method is only able to detect disbond growth within the fixed sensing limits of the PZT, this method can be used to monitor the disbond growth. In summary, the individual sensor/actuator PZT has to be located in the vicinity of the disbond. The impedance will reach an asymptote when the disbond growth passes the individual sensor/actuator PZT. To help in the interpretation of the size of the disbonds, the size of the PZT must not be greater than the amount of disbond allowed.

This preliminary numerical analysis has demonstrated that the impedance method can be used to detect disbond within fixed sensing limits. In the next section, an extension of this method using an array of PZT sensors is reported. This impedance method was used to detect more realistic disbond types. The result of this extension of the method will be compared with the results from the fatigue experiments and will be reported in Chapter 8.

5.4 MODELLING COMPLEX DISBOND TYPES

In this section, an extension of the preliminary study described above is presented. Here three different types of disbond developments were considered. Multiple sensors and actuators were also used. Attempts were made to formulate a methodology to be used in conjunction with the impedance analysis, for the prediction of type, location and severity of damage. The damage types are the same as those recorded by the RAAF in their composite patch applications.

5.4.1 DATA ANALYSIS

In the preliminary investigation conducted, it was found that for each size of disbond simulated there was a plot of impedance varying with respect to frequency. This would make the interpretation of the results difficult for an ongoing acquisition of data during the online monitoring of the structure, where a huge number of tests would be done. Condensation of the data acquired for each disbond size was necessary to simplify the process. Therefore to enable reliable real time analysis with progressive disbonds, the impedance readings were integrated with respect to frequency in the impedance-frequency graph. The variation in the signal energy over time was used as the basis for assessing structural integrity over time. It was suggested by Vary (1977) that the mean square response is an appropriate measure of energy for stationary random signals. The expected value of the mean square response can be written as:

$$E[x^2] = \int_{-\infty}^{\infty} S_x(\omega) d\omega \quad \text{Equation 5.6}$$

where S_x is the spectral density of the response.

For the comparison of the various damage cases, the area under each impedance spectral-density curve was obtained following the approach in Newland (1993). Specifically, the impedance spectrum is condensed into a single measure, defined as,

$$IM = \int_{f_l}^{f_u} Z(f)df \quad \text{Equation 5.7}$$

where f is the frequency, Z the impedance, f_u the upper frequency limit and f_l the lower frequency limit chosen to exclude the first structural resonance. In the results presented in the following sections, the IM-parameter was normalised with respect to the value obtained prior to the application of cyclic loading. This was to enable the comparison of results recorded from sensors/actuators bonded on material with different stiffness.

In the analysis that follows, the impedance was calculated over a frequency range from 0-Hz to approximately 3000-Hz.

5.4.2 MODEL DEVELOPMENT

Models were developed based on three different types of damage conditions in order to investigate the applicability of the impedance method in detecting the conventional type of damage shapes. All three models involved simulating disbond developing from a point instead of across the entire width of the test specimen. This is because in experiments conducted to dynamically grow disbond under the repair patch, it was found that disbond generally initiated from either the corner of the patch or a point along the side of the repair patch (Koh et al, 2002).

The first model considered a disbond initiating from the corner of a repair patch denoted as COR (see Figure 5.7). The top view of the simulated specimen is shown in Figure 5.7, and the side view in Figure 5.8. In this model, the size of the PZTs labelled PZT1 and PZT4 was 10mm × 20mm while PZT2 and PZT3 were 4mm × 20mm. The PZTs spanned the entire width of the repair patch.

The second model considered a disbond located along the side of the repair patch denoted as BLP (see Figure 5.9). The top view of the simulated specimen is shown in Figure 5.9, and the side view in Figure 5.10. In this model, the size of the PZTs was 4mm × 10mm each. The damage was allowed to develop under PZT1b (see Figure

2a). The damage initiated from a point under PZT1b and along the side of the repair patch.

The third model considered a disbond when the damage also initiated from a point as shown in Figure 5.11 with side view in Figure 5.12 denoted as MID. The damage is between the PZTs and therefore the damage is growing into the area under the PZTs. In the models, the different damage conditions provided a range of realistic disbond development that can occur to a repair patch. These damage types will be used to evaluate the sensitivities of the impedance method.

The simulated disbond under the repair patch had dimensions as listed in Table 5.1.

Table 5.1 Disbond sizes simulated

Cases	COR	MID	Cases	BLP
0	No Damage	No Damage	0	No Damage
1	2.5mm × 2.0mm	4.0mm × 2.0mm	1	2.0mm × 2.0mm
2	5.0mm × 4.0mm	8.0mm × 4.0mm	2	6.0mm × 2.0mm
3	7.5mm × 6.0mm	12.0mm × 6.0mm	3	10.0mm × 4.0mm
4	10.0mm × 8.0mm	16.0mm × 8.0mm	4	14.0mm × 6.0mm
5	12.5mm × 10.0mm	20.0mm × 10.0mm	5	18.0mm × 8.0mm
6	15.0mm × 12.0mm	24.0mm × 12.0mm	6	22.0mm × 10.0mm
			7	26.0mm × 12.0mm

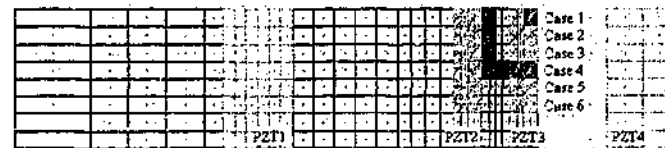


Figure 5.7 Top view for disbond initiating from corner of repair patch (COR)

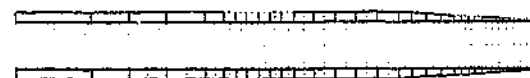


Figure 5.8 Side view for disbond initiating from corner of repair patch (COR)

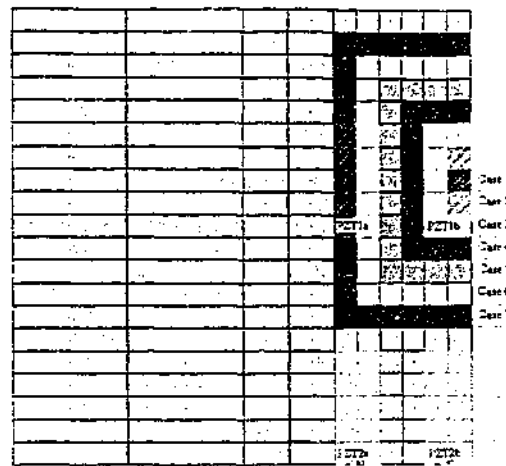


Figure 5.9 Top View for Disbond Under the PZT and the Repair Patch (BLP)

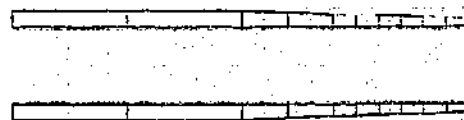


Figure 5.10 Side View for Disbond Under the PZT and the Repair Patch (BLP)

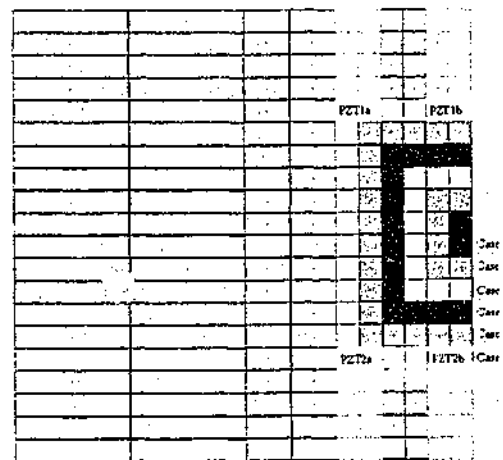
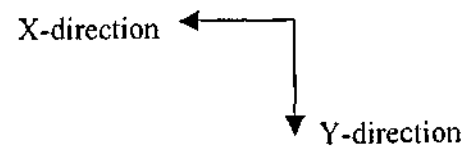


Figure 5.11 Top View for Disbond Between PZT (MID)



Figure 5.12 Side View for Disbond Between PZT (MID)



5.4.3 RESULTS AND DISCUSSION

Disbond from corner of the repair patch

The model for the simulation of corner disbond schematically drawn in Figure 5.7 and Figure 5.8 was used to estimate the sensitivity of the impedance method when the damage developed in a "seashell" shaped manner. The results shown in Figure 5.13 were obtained from an impedance simulation when PZT3 in Figure 5.7 was used. They show that if the damage was under the PZT, the disbond can be detected by using the impedance method. Impedance readings show that the method was dependent on the area that had been disbanded. This is because the measured impedance is a function of the compliance of the disbanded composite repair patch.

The impedance readings obtained showed that the greater the area underneath the PZT that was disbanded the greater the change in the impedance readings. At least 25% of the area within the sensing region of the PZT must be disbanded to have a significant change in readings. The damage started to cause a decrease in the IM-parameter in damage case 2 as shown in Figure 5.13 in damage case 2 (COR) when damage size was $5.0 \times 4.0 \text{ mm}^2$. This decrease was 7%. The damage continued to cause a decrease in the IM-parameter with damage size resulting in larger deviations.

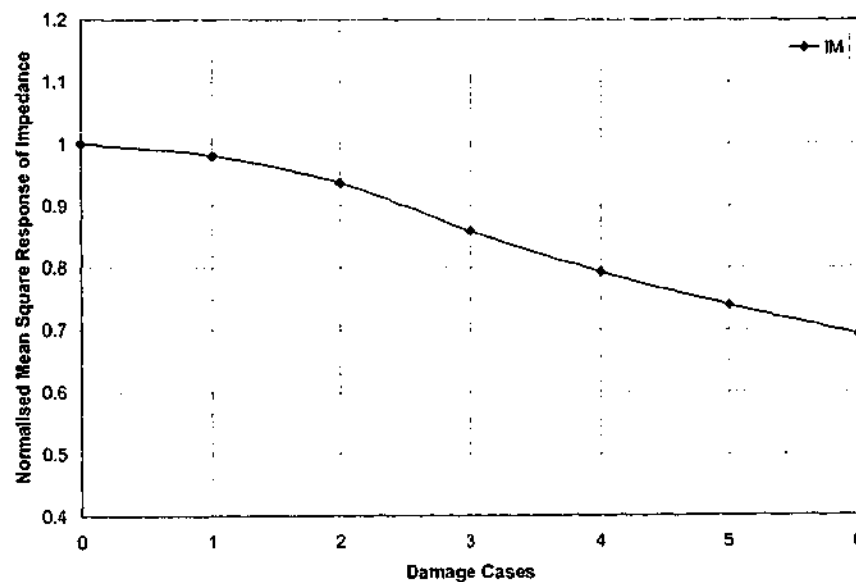


Figure 5.13 Results obtained from PZT bonded on the edge of repair patch taper (see Figure 5.7, PZT3)

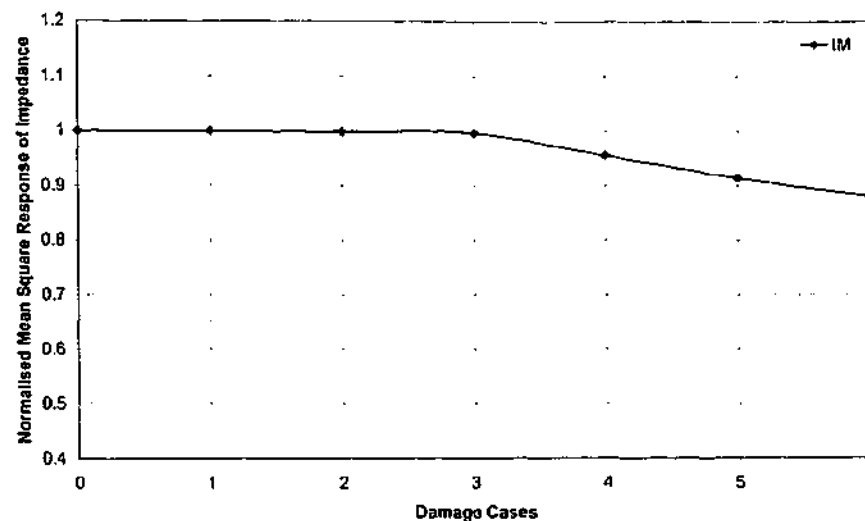


Figure 5.14 Results obtained from PZT element bonded on the top end of the repair patch taper (see Figure 5.7, PZT2)

In Figure 5.14, the data presented confirm the sensitivity of the method when the PZT element bonded on the top end of the repair patch taper was used (see Figure 5.7, PZT2). The piezoceramic sensor/actuator was located between 8-mm and 12-mm from the edge of the taper. No decrease of IM-parameter was recorded up to 6-mm disbond, which in the graph above is represented as damage case-3, and for disbond greater than 6-mm the IM-parameter started to decrease. This shows that the PZT is sensitive to changes when the damage approaches the PZT. This is consistent with the preliminary model that was shown in Section 5.3.2 in Figure 5.4, where impedance was measured across PZT2. The sizes of disbond between both cases are different. In the preliminary study the disbond spans the entire width of the specimen, while in this case it is only half the specimen width.

Disbond initiating from a point below the PZT

Simulation for disbond initiating from a point below the PZT confirmed earlier findings from the simulation of the corner disbond discussed in the previous section. In Figure 5.15, the results do not show any change in the IM-parameter when there was a small damage size of $2 \times 2 \text{ mm}^2$ under PZT1b (see Figure 5.9). As the disbond grew to $2.0 \times 6.0 \text{ mm}^2$ damage, which is 30% of the adhesive layer encompassed by

the PZT area, the change in readings reflected the damage condition. Progressive disbond was detected with further decrease in recorded readings.

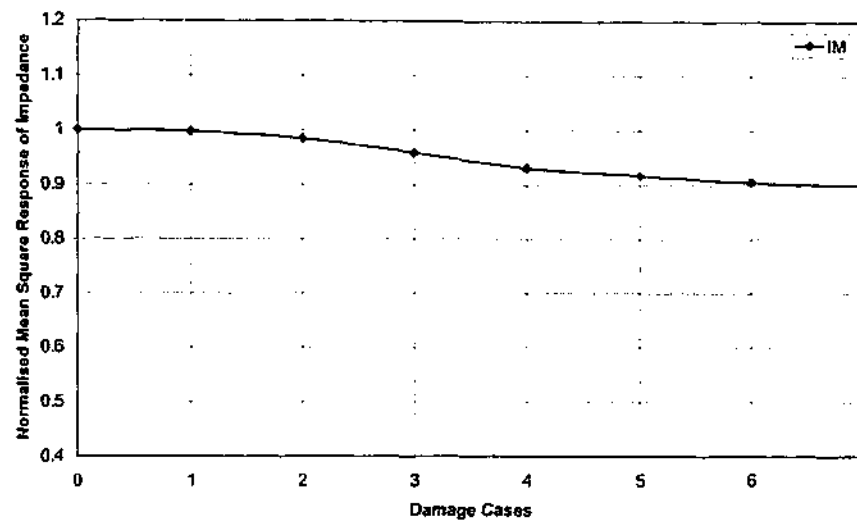


Figure 5.15 Results obtained from PZT element located directly above the disbond (see Figure 5.9, PZT1b)

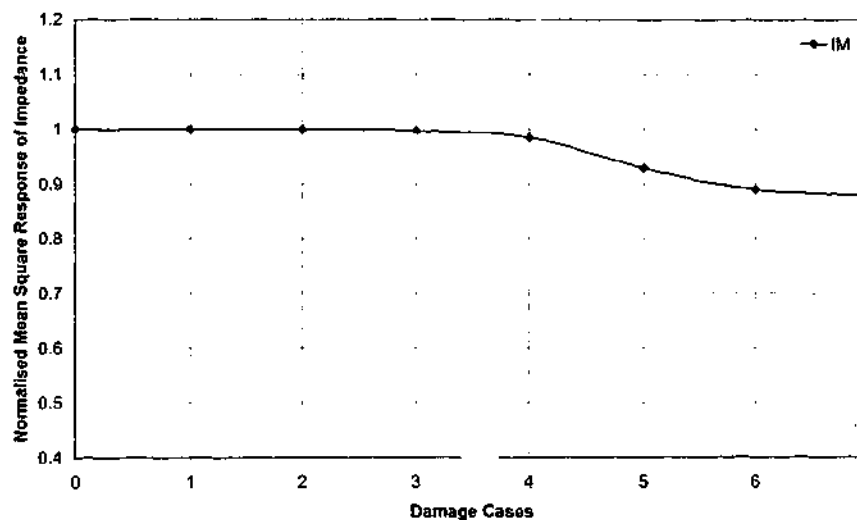


Figure 5.16 Results obtained from PZT element located to detect approaching disbond (see Figure 5.9, PZT1a)

The result shown in Figure 5.16 was taken from PZT1a to monitor further disbond growth. PZT1a was located at a distant that only detects advanced disbond sizes. The IM-parameter decreased by 8.6% when the damage approached the PZT. Increasing disbond size under the repair patch resulted in further decrease in the IM-parameter.

These findings were consistent with the preliminary model that was shown in Figure 5.4 and COR model shown in Figure 5.14. Both sets of results were obtained from PZT2. Comparing the results when the disbond approached each PZT (Case-4 for the COR model, refer to Figure 5.7; Case-5 for this BLP model, refer to Figure 5.9), it was found that the decrease is greater for the BLP model. These results imply that the method was sensitive towards disbond growth propagating from both the x - and the y -direction. When the disbond developed beyond the PZT, the mean square response of the impedance continued to decrease but at a slower rate.

To determine the extent of the sensitivity in the y -direction, PZT2b (see Figure 5.9) was used since the PZT element was located at right angles to the direction of growth propagation. The graph shown in Figure 5.17 does not show any discernible change with the disbond growth. The detection capability of the impedance method was limited to a sensing zone when the disbond was approaching in the y -direction. This is similar to that of disbond growth approaching in the x -direction. In this simulation, it was determined from the results that the sensing zone will not be greater than 2-mm from the top edge of PZT2b.

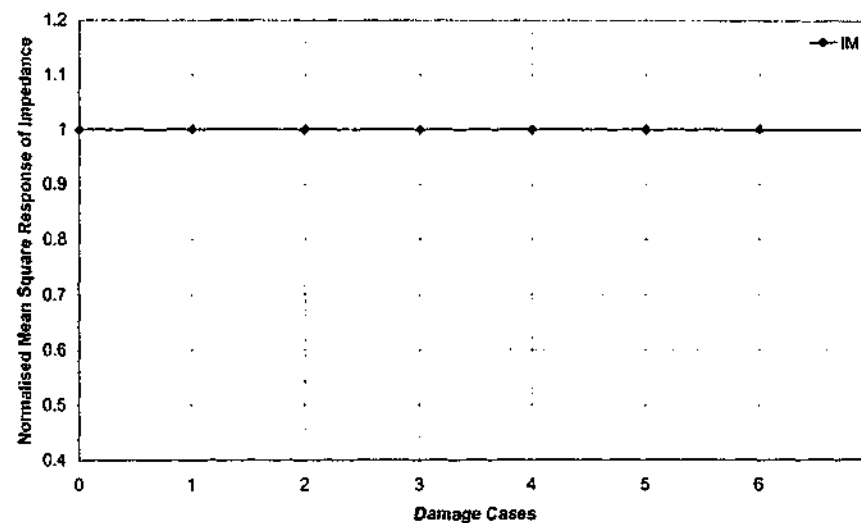


Figure 5.17 Results obtained from PZT element located far from the disbond (see Figure 5.9, PZT2b)

Disbond initiating between PZT sensors

The results presented in the previous sections, indicates that there exist a 'damage detectable zone'. The simulation for disbond initiating from a point between two pairs

of PZT shows that this damage can only be detected when it penetrates into the 'damage detectable zone' of the sensing PZT. In most of the damage cases simulated for disbond initiating between PZT sensor/actuator (Figure 5.11 and Figure 5.12), the disbond was outside the zone hence there is no effect on the IM-parameter readings. Figure 5.18 shows the impedance results obtained when PZT1b in Figure 5.11 was used. Here it was found that as the damage advanced to within 2-mm from PZT1b, the disbond could be detected. Thus the zone was limited to a distance of 50% of the PZT width from all the four edges of the PZT. Beyond the perimeter of the zone, no changes can be detected by the impedance method using PZT elements.

Figure 5.18 shows the result of an immediate drop of 3.98% in impedance reading from damage case-4 to damage case-5 followed by a further 5.75%. Damage case-5 is at the threshold of the 'damage detectable zone' of the sensing PZT. From the distance between the upper row bonded PZT elements and the lower row bonded PZT elements one can deduce the severity of the disbond in the y-direction.

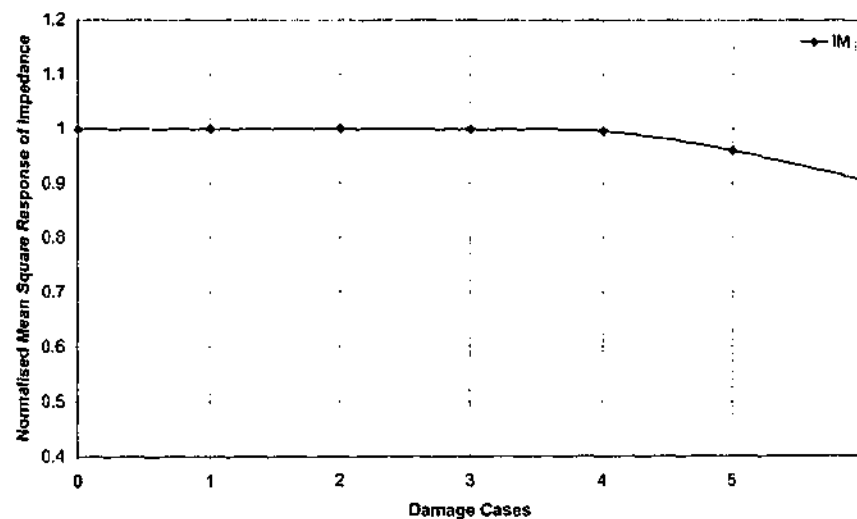


Figure 5.18 Results obtained from PZT element located above the initial disbond (see Figure 5.11, PZT1b)

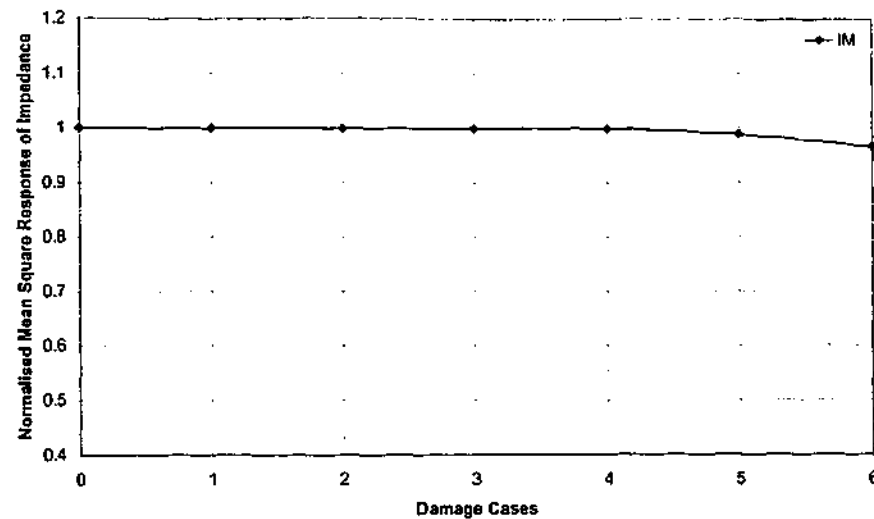


Figure 5.19 Results obtained from PZT element located diagonally above the initial point of disbond (see Figure 5.11, PZT1a)

Figure 5.19 shows a result, which is consistent with the findings when the PZT elements are located far from the damage zone. Damage grew beneath the composite patch directly below PZT1a at damage case-6. The decrease in the measured parameter is proportional to the extent of damage. For the damage to be detected the damage must penetrate the 'damage detectable zone' of the PZT in the y -direction as well.

5.5 CONCLUSIONS

The impedance method based on numerical simulation has been found to be sensitive towards disbond growing in both the x - and y -directions. However, based on the evidence shown in this numerical simulation, the width and the length of the PZT element seem to determine the sensitivity of the sensor to a particular disbond growth direction. The decrease in IM-parameter is greater for the growth in the x -direction as well as the disbond size required for a significant decrease in the measured IM-parameter is smaller. With the COR model, a disbond size of 25% of the PZT length due to the disbond growth in the x -direction resulted in a decrease of approximately 9%. While in the MID model, a disbond size of 50% of the PZT width resulted in no significant change in IM-parameter due to the disbond growth in the y -direction.

Thus, for optimum sensitivity the sensor should be square or approximately equal PZT length and width.

The PZT is able to detect the disbond when the disbond comes within the damage detectable zone of the PZT element. The method is not able to detect a disbond that is beyond the sensing zone of the sensor. Therefore for future practical application more than one sensor will be required to determine the underlying condition. A network of sensors and actuators will allow the visualisation of the disbond type apart from determining the perimeter of the disbond growth. This method therefore provides a viable alternative method of determining the extent of disbond growth by condition monitoring. Condition monitoring is vital in the event that the damage occurred during the manufacturing phase and not during active service. The electromechanical impedance method will not record any further changes in impedance at the individual PZT if the PZT is bonded over a damage region. Those surrounding sensors will function as point monitors that will allow the monitoring of the surrounding region of the damage.

The size of the piezoelectric sensor has to be the same as the minimum extent of disbond to be detected. This is because when the disbond grows past the PZT, the impedance reading will reach an asymptote. In addition using multiple smaller PZTs will improve the sensitivity of the network.

In the next chapter, a numerical investigation for the transfer function method will be presented. Both methods, when utilised together, will reinforce any conclusions to be drawn. Assumptions made by either can be verified, especially resonant frequencies that affect the statistical methods.

CHAPTER 6

EXPERIMENTAL EVALUATION OF THE IMPEDANCE METHOD

6.1 INTRODUCTION

The primary aim of the experimental investigation was to substantiate the set of numerical results reported in the previous Chapter 5 Numerical Results: Impedance Method, which demonstrated using synthetic data that a simple signal processing method could be applied to piezotransducer data to detect disbond growth in a bonded composite patch.

In order to understand the experiments, the theory behind the piezoelectric element and the stiffness-based impedance method must be understood in detail. In section 6.2, the background theory is presented and a general description of the effects on the impedance method of the change in stiffness of the composite patch with disbond growth through the piezoelectric sensor/actuator.

In section 6.3, the first experiment conducted with prescribed disbond sizes is presented. The experimental procedures describe the specimen and settings for the experimental equipments used. The result from this simple experiment provides in-

depth knowledge of method sensitivity and requirements for the detection of disbond using a piezoelectric element.

In section 6.4, the second experiment conducted with prescribed disbond sizes is presented. The composite repair patch used was made of clear fibre-reinforced polymer. This experiment allowed the comparison of the results obtained by means of the impedance method and the visual inspection of the disbond size.

To establish the practical efficacy of the method under real loading conditions, two different specimens were used in realistic rather than artificial loading experiments and these specimens are described in Section 6.5. The composite patch in one specimen was made of boron/epoxy and in the other was made of graphite/epoxy.

6.2 BACKGROUND THEORY

The key attraction of the impedance-based method is the electromechanical coupling of the piezoelectric actuator/sensor patch. The electromechanical property of piezoelectric material has a direct and a converse effect. The direct effect is defined as the generation of an electrical charge in the material when it is subjected to a mechanical stress, and the converse effect is described as the generation of a mechanical strain in response to an applied electric field. The linear interaction between electrical and mechanical variables can be described by linear relations of the form

$$S_i = s_{ij}^E T_j + d_{mi} E_m \quad \text{Equation 6.1}$$

$$D_m = d_{mi} T_i + \varepsilon_{mk}^T E_k \quad \text{Equation 6.2}$$

The mechanical variables in the above equations are the stress T and the strain S , and the electrical variables are the electric field E and the electric displacement D .

The impedance method utilises a single piezoelectric wafer element in both the direct and converse sense. It relies on the relationship between the mechanical impedance, defined as the ratio of the applied force and the resulting velocity, and the electrical

impedance, which is defined as the ratio of the applied voltage and the resulting current. The vibrational response to the forced broadband excitation is characteristic of the particular structure. This allows the extraction of structural information from electrical impedance measurements.

A unique property of this vibration analysis technique is that it utilises simultaneous actuation and sensing of the structural response. This means that a single piezoelectric is used to fulfil the task of the direct as well as the converse effect, as mentioned previously. In order to understand how piezoelectric materials can be used to obtain a vibrational structural response, it is necessary to have clear understanding of how they affect the structure. The piezo transducers operate as an actuator using a fixed alternating electric field, which provides the induced vibration, as well as operating as a sensor, obtaining the frequency response. This response is characteristic of the structure, modulating the current flowing through the PZT. The PZTs are actuated at varying frequencies. The response obtained provides vital information regarding the mechanical interaction between the PZT actuator/sensor and the structure.

Similarly, in relation to electrical terms, the PZT provides details about the electrical impedance. The information provided using such a method is similar to that obtained using a transfer function, as it relates force and velocity. Electromechanics is defined as the interactions between a piezoelectric material and the host structure, interactions that are the mechanical and electrical impedance. The following sections, report the static and fatigue evaluation of the method was conducted. A typical application where the impedance method is suitable can be described using a structure with the presence of a disbond reported by Summerscales (1987).

6.3 STATIC TESTING WITH BORON/EPOXY REPAIR PATCH

To ascertain whether it was feasible to use the impedance method to detect disbond growth under a composite patch, the static testing was carried out. The selection of static evaluation was due to its simplicity and ease of testing methods as found in the experimental procedures. The limitations of the method are that, in simulating

multiple plates with different disbond sizes, it introduces unique boundary conditions and physical variables of each individual plate which are assumed to be negligible during the initial stage of investigations.

6.3.1 EXPERIMENTAL PROCEDURES

In this investigation, we seek to use changes in local stiffness to determine the severity of the disbond. When there is a change in local stiffness, it is envisaged that a given force over the damaged region will result in a change in the displacement or strain response. To this end, we are seeking to use PZT to enable us to relate this change to damage sizes.

In this experiment, a disbond was created at the corner of the patch, since this was the most likely location for a disbond to initiate under actual service conditions. It is known that a flaw such as this described in Figure 6.1 has been demonstrated to have minimal effect on the global dynamic properties of the structure (Summerscales, 1987), however it compromises the local stiffness. Preparation of the specimens was described in Chapter 3, Experimental Methods. Five specimens were prepared and four of the specimens were inserted with Teflon sheets in the bondline at 'A' during bonding of the composite repair. The Teflon sheet bonded under the composite patch and they were of the following dimensions: 5×5-mm, 10×10-mm, 15×15-mm, and 20×20-mm. This was to simulate the development of disbond growth during active service.

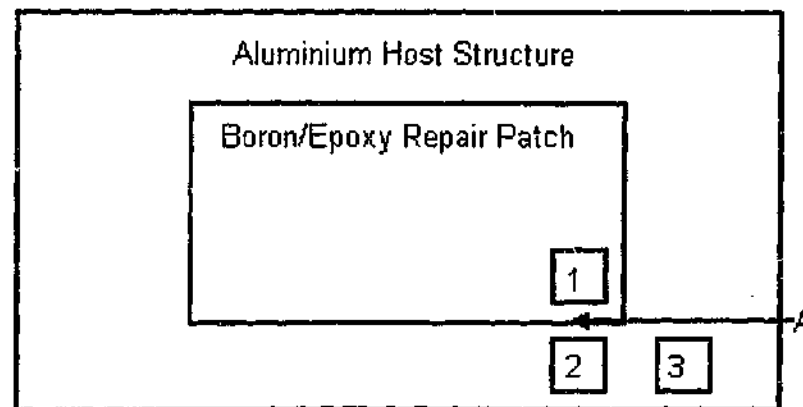


Figure 6.1 Schematic drawing of the specimen used for the detection of disbond growth by means of the transfer function method

The electrical impedance was measured at discrete frequencies in the range 400-Hz to 25-kHz, using an impedance analyser. The large range used with increments of 10-Hz was to determine the most suitable experimental testing range. Data was acquired using a Data Translation Visual Programming Interface (DTVPI) system. For further analysis of the results, the measured amplitude and phase data obtained from the electromechanical impedance were plotted against frequency.

6.3.2 RESULTS AND DISCUSSION

The degree of disbond of the composite patch was successfully monitored with microprocessor-based electrical impedance analysers on the specimen (Figure 6.1). Amplitude and phase measurements were made in the 400-Hz to 1-kHz and 1-kHz to 25-kHz frequency bands. The experimental results for the repair patch are presented in Figure 6.2 and Figure 6.3 when impedance was taken from PZT sensor/actuator located at position 1.

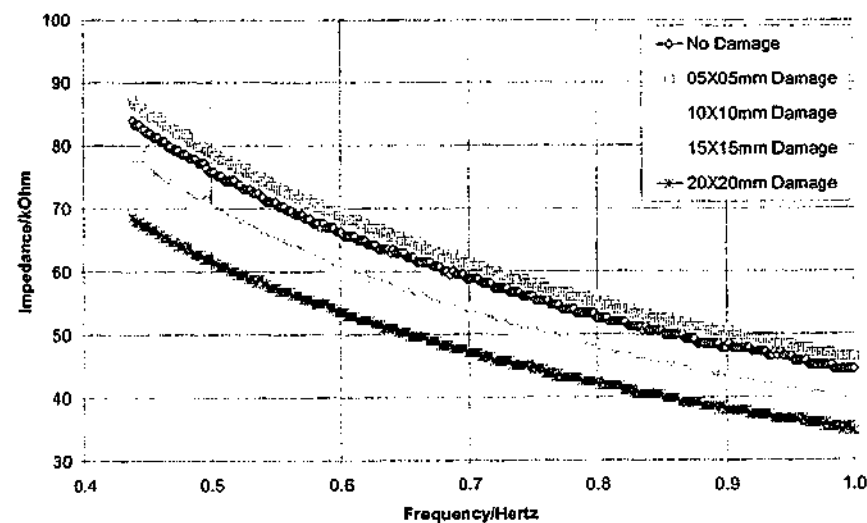


Figure 6.2 Impedance measurement interrogated at low frequency taken at PZT location 1

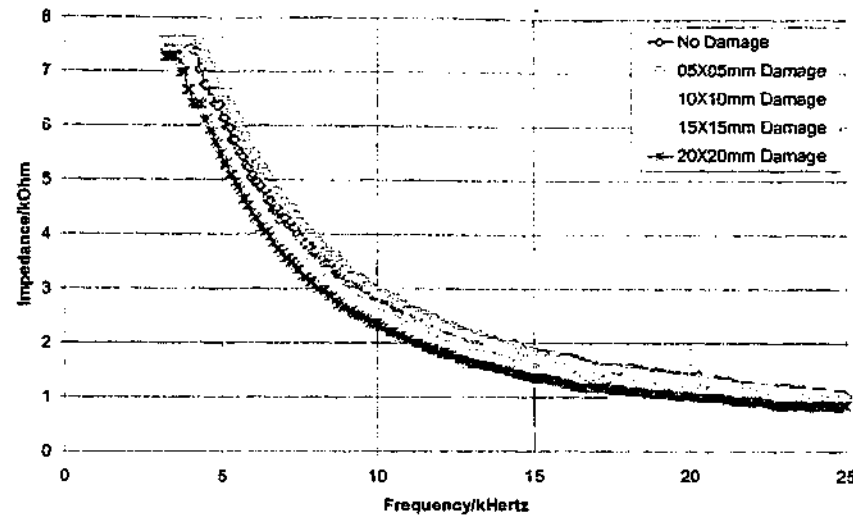


Figure 6.3 Impedance measurement interrogated at high frequency taken at PZT location 1

As can be seen in Figure 6.2, as the disbond grew, the downward translation of the impedance response in the y-direction increased. The degree of downward translation depends on the location of damage relative to the PZT sensor/actuator location. The frequency range used to obtain the results in Figure 6.2 is between 400-Hz to 1000-Hz. When a higher frequency range was used, the impedance curve tends to band together as shown in Figure 6.3. It is obvious from these results that the choice of frequency range is important.

It was also found that in order to detect a disbond the PZT needs to be located on the patch. Placing the element on the host structure for example yields no measurable indication of the disbond. The impedance responses for the case where the PZT was located on the aluminium structure that is when PZT sensor/actuator location 2 was used are shown in Figure 6.4 and Figure 6.5. It is clear from these figures that the impedance method was particularly effective when the sensor/actuator was located directly over the damage area.

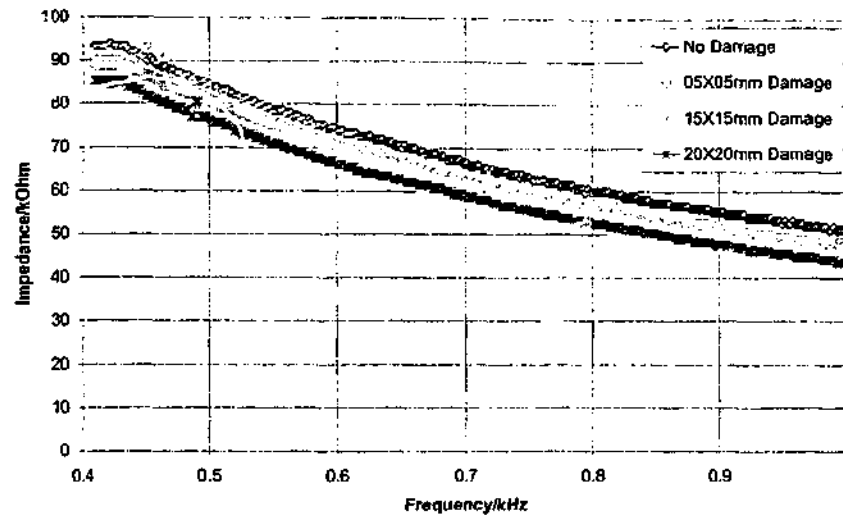


Figure 6.4 Impedance measurement interrogated at low frequency taken at PZT location 2

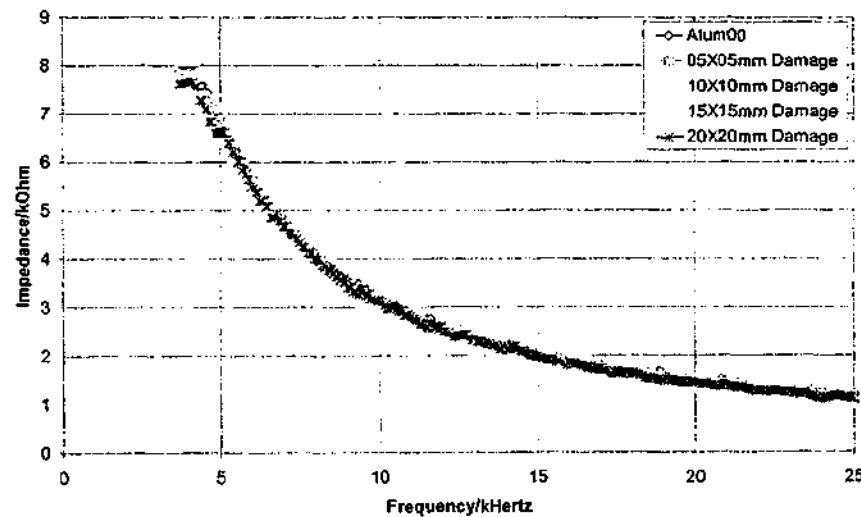


Figure 6.5 Impedance measurement interrogated at high frequency taken at PZT location 2

6.4 STATIC TESTING WITH GLASS FIBRE-REINFORCED PLASTIC REPAIR PATCH

To enable visualisation of the underlying damage the second static evaluation was undertaken using glass fibre-reinforced plastic (GFRP) as the repair patch. The PZT

was located at various locations in order to verify the damage with the impedance measurements taken in experimental testing in the prior section.

6.4.1 EXPERIMENTAL PROCEDURES

The specimens were prepared as described in Chapter 3, Experimental Methods. Nine PZT elements were mounted on the GFRP composite patch as shown in Figure 6.6. The simulated disbond was created by inserting a blade from the corner of the composite patch below the location of PZT3. The disbond was later highlighted with black colour liquid penetrant. This allowed the photography of the disbond underneath the composite patch. The various disbond sizes are illustrated in Figure 6.6 with faint dotted lines. Several stages of disbond in both x- and y-direction were simulated, to the limit of 45-mm and 25-mm respectively and impedance measurements were taken at each disbond level. The specimen was interrogated with a frequency range between 100-Hz to 10-kHz at a frequency interval of 20-Hz.

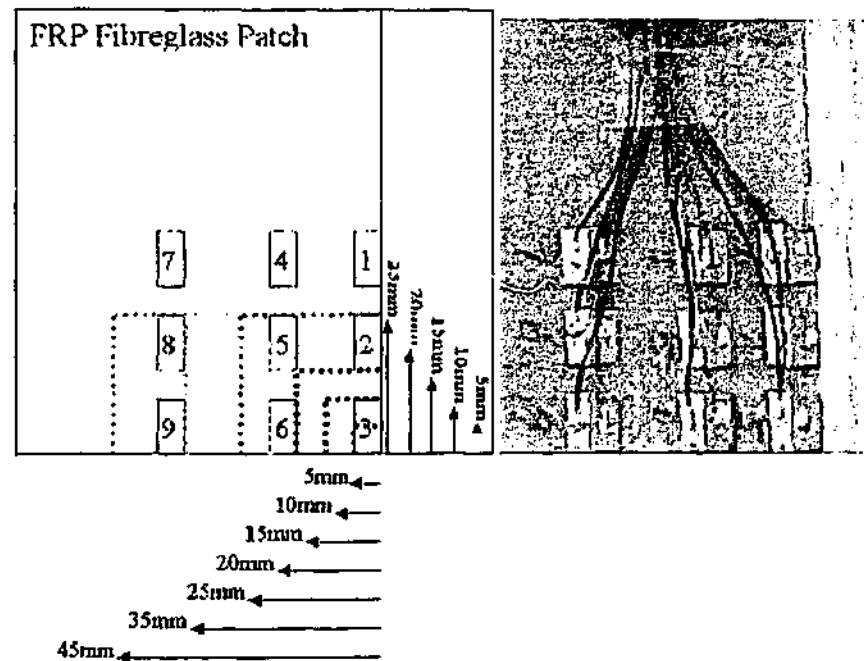


Figure 6.6 Schematic drawing of specimen (on the left) and the actual specimen (on the right) used for the visualisation of disbond growth

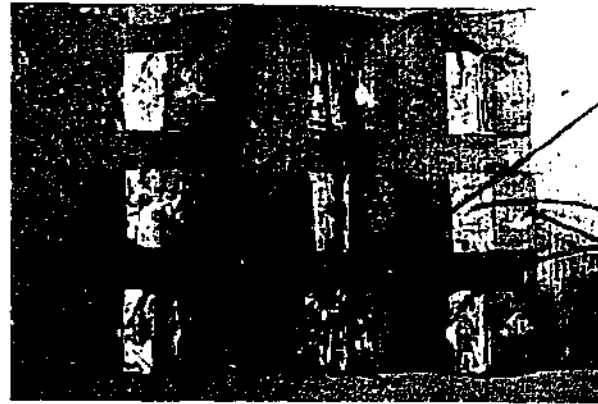


Figure 6.7 Specimen with dye-penetrant showing damage size of $45 \times 25\text{mm}^2$

6.4.2 DATA ANALYSIS

This method of analysis used to interpret the results obtained was described in detail in Chapter 5. The variation in the power signal over time was used as the basis for assessing structural integrity over time. It was suggested by Vary (1988) that the mean square response is an appropriate measure of power for stationary random signals. The expected value of the mean square response can be written as:

$$E[x^2] = \int_{-\infty}^{\infty} S_x(\omega) d\omega \quad \text{Equation 6.3}$$

where S_x is the spectral density of the response.

For the comparison between the various damage cases, the area under each impedance spectral-density curve was obtained following the approach in Newland (1993). Using this approach, the impedance spectrum was condensed into a single measure, defined as,

$$IM = \int_0^{3000} Z(f) df \quad \text{Equation 6.4}$$

where f is the frequency, Z is the impedance and the upper frequency limit of 3.0-kHz is chosen to exclude the first structural resonance. In the results presented in the following sections, the IM-parameter was normalised with respect to the value obtained prior to the application of cyclic loading.

6.4.3 RESULTS AND DISCUSSION

The impedance measurement is a function of the composite patch velocity response. It varies according to the size of disbond. Greater disbond under the composite repair patch leads to a decrease in the impedance measurements. Thus it was expected that the IM-parameter would progressively decline with the increase in disbond growth.

The following Figure 6.8 shows the insertion of the blade into the specimen resulting in a disbond size of $5 \times 5\text{-mm}^2$. This was case where the disbond was located far from PZT1. It was not within detectable range of this PZT and the impedance measurement was not expected to vary. This measurement allowed the determination of errors associated with signal to noise ratio. Any variation would have been a systematic error due to the surrounding electrical equipments.

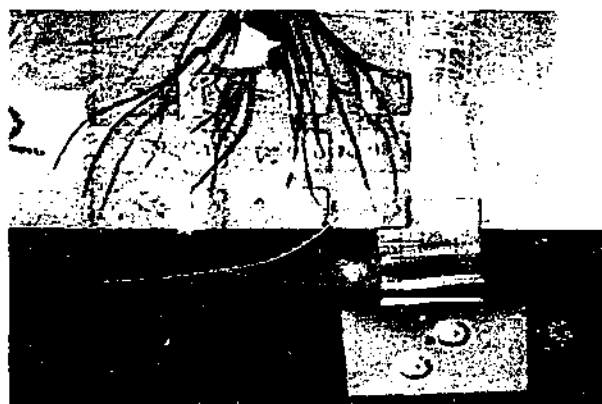


Figure 6.8 Blade inserted to create a damage size of $5 \times 5\text{-mm}^2$

The IM-parameter shown in Figure 6.9 is constant up to $5 \times 5\text{-mm}^2$ damage, then decrease 2% at $10 \times 10\text{-mm}^2$ damage and finally remain constant with further disbond growth. There is no great variation as the damage increases. This result was expected since the piezoelectric was located at a distance from the disbond and not within the detectable range of the sensors. It is possible that the 2% decrease was due to the thinner composite i.e. 4-ply and less stiff fibre reinforced polymer as compared to the previous boron/epoxy composite patch. The location of PZT1 at the edge of the composite compounded this effect. Thus this would have introduced a systematic error impedance measurement after $10 \times 10\text{-mm}^2$ disbond. This error is negligible when a stiffer composite patch is used.

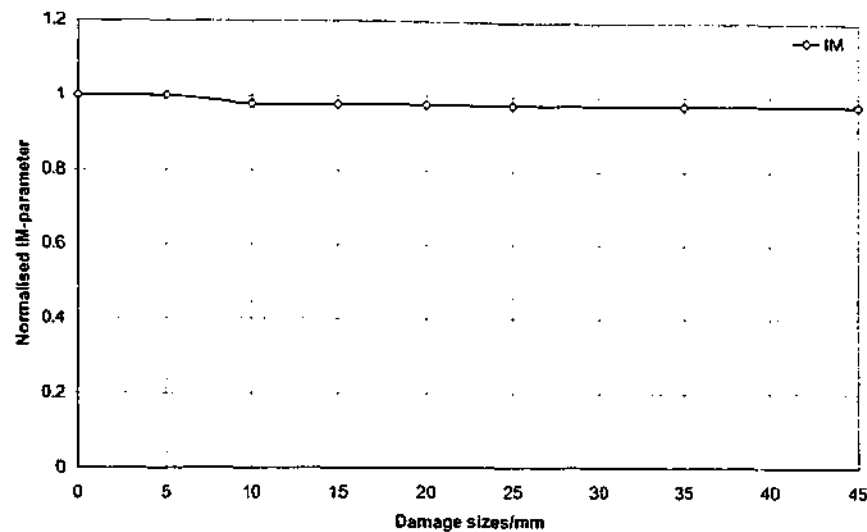


Figure 6.9 IM-parameter obtained from PZT1 (see Figure 6.6)

The IM-parameter shown in Figure 6.10 decreases immediately from the no disbond case to a lower IM value as the damage grows. After $5 \times 5\text{-mm}^2$ damage there is no great variation as the damage increases. This result was expected since the piezoelectric was located directly above the initiation point of damage. Damage beyond $10 \times 10\text{-mm}^2$ was not within the detectable range of the PZT sensor/actuator.

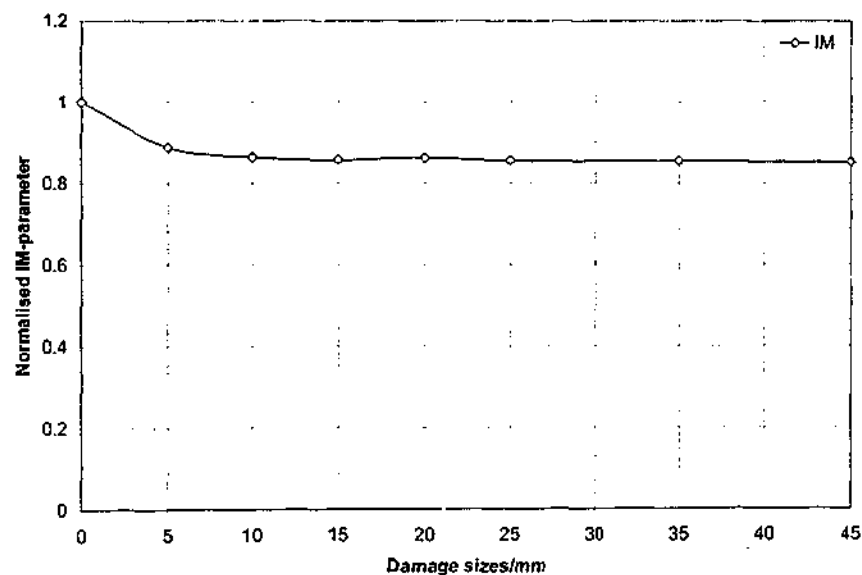


Figure 6.10 IM-parameter obtained from PZT3 (see Figure 6.6)

The results obtained from PZT5 located in the middle of the PZT matrix shows the condition of the disbond approaching PZT5 from undamaged condition until the

damage had passed the sensor/actuator. This case allowed determination of the concept of "damage detectable zone" first mentioned in chapter 5.

The normalised IM-parameter shown in Figure 6.11 is as expected for a sensor/actuator at location PZT5. Initial disbond growths were not reflected in any changes in the IM-parameter, however with further growth beyond $10 \times 10\text{-mm}^2$ disbond size the response progressively decreases up to a disbond size of $25 \times 25\text{-mm}^2$. For disbond growth beyond the size of $25 \times 25\text{-mm}^2$, the IM-parameter remains constant. This observation agrees with the numerical results where the "damage detectable zone" was determined to be at a distance of 50% PZT element width from all edges of the PZT element.

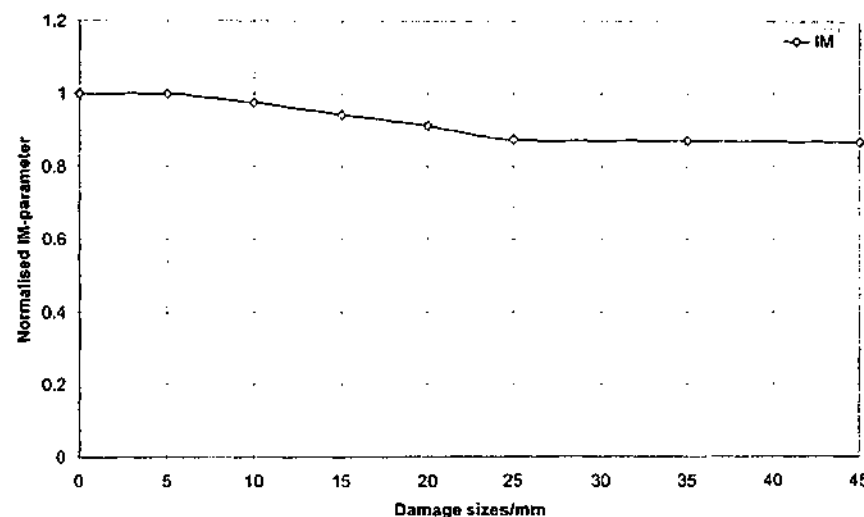


Figure 6.11 IM-parameter obtained from PZT5 (see Figure 6.6)

The results obtained from PZT6 located to the left of PZT3 show the case of disbond approaching PZT6 from the no disbond case until the damage had passed the sensor/actuator. The normalised IM-parameter shown in Figure 6.12 is as expected for a sensor/actuator at location PZT6. Initial disbond growths were not reflected in any changes in the IM-parameter. However with further growth beyond $10 \times 10\text{-mm}^2$ disbond size the response progressively decreases up to a disbond size of $25 \times 25\text{-mm}^2$. For disbond growth beyond the size of $25 \times 25\text{-mm}^2$, the IM-parameter remains constant. This observation agrees with the numerical results where the "damage detectable zone" was determined to be at a distance of 50% PZT element width from all edges of the PZT element.

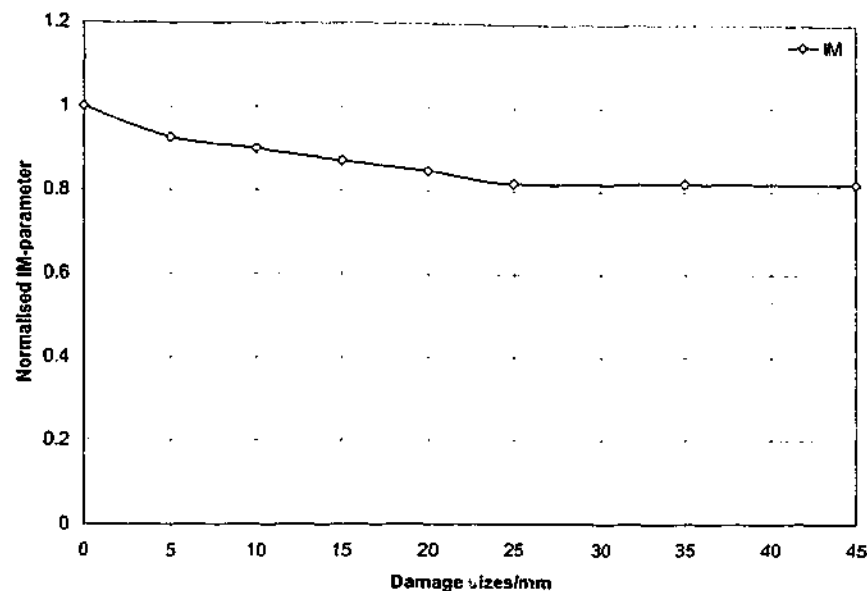


Figure 6.12 Mean square impedance response for PZT6 (see Figure 6.6)

The results obtained from PZT9 shows the condition of the disbond approaching PZT9 from no damage until the damage had past the sensor/actuator. The damage condition of the specimen was shown previously with coloured liquid penetrant in Figure 6.7 where the specimen had a disbond growth up to $45 \times 25\text{-mm}^2$. It attempts to confirm the results observed at PZT5 regarding the determination of the concept of "damage detectable zone" first mentioned in chapter 5.

The impedance measurements shown in Figure 6.13 do not show any changes for small disbond sizes since PZT9 was located a distance from the initiation of the disbond. When the disbond grew to a size of $35 \times 25\text{-mm}^2$ the damage was detected by the PZT and was reflected with a decrease in the IM-parameter. The decrease stopped at the disbond size of $45 \times 25\text{-mm}^2$ when the disbond had grown beyond the "damage detectable zone".

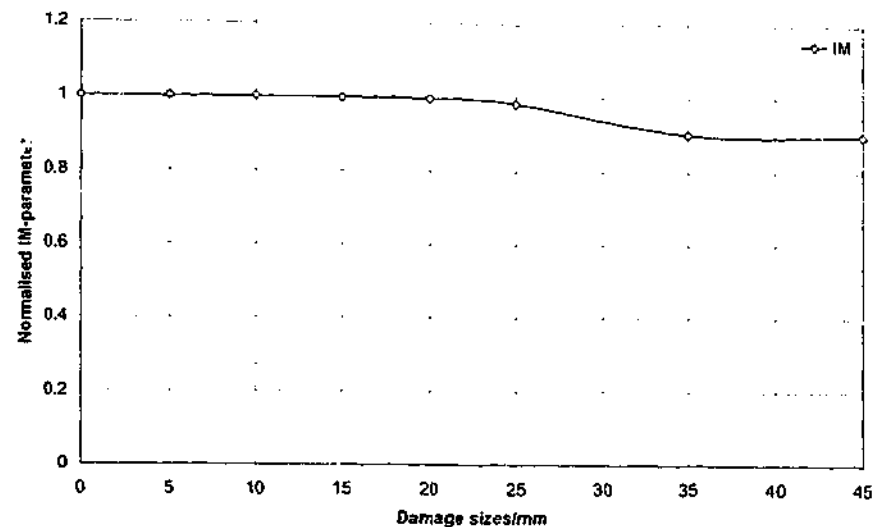


Figure 6.13 Mean square impedance response for PZT9 (see Figure 6.6)

6.5 FATIGUE TESTING

Fatigue testing of the specimen in an attempt to grow a disbond and detecting the disbond with the impedance method allows useful insight to practical efficacy of the method in detecting irregular disbond shapes and sizes. The experimental procedure used also allows the investigation on the suitability of the PZT and the prescribed method in during cyclical loading of the specimen. Examining the results obtained by means of the impedance method for the specimen while undergoing cyclical loading enable the identification of potential problems during realistic applications.

6.5.1 EXPERIMENTAL PROCEDURES

The specimens used for the fatigue testing were prepared as described in Chapter 3, Experimental Methods. Figure 6.14 shows a schematic drawing of the first of two specimens considered in this fatigue testing investigation. This specimen, referred to as DD2, was dynamically loaded to simulate active service. As shown in Figure 6.14, the specimen comprised an aluminium plate with a bonded 11-ply unidirectional Boron/Epoxy patch to simulate a bonded repair. On Side P, PZT elements were bonded at three different locations, PP1, PP2 and PP3. On Side S, another three PZT elements were bonded on to the specimen and they were labelled as SP1, SP2 and SP3

respectively. Strain gauges were attached at six different locations. On Side S, they were labelled as S1, S2 and S3; while on Side P, they were labelled as P1, P2 and P3. The impedance method was applied only to PP2. During the experiments the disbond on Side P was monitored using the electromechanical impedance. In addition, the disbond on Side P and Side S was both monitored using strain gauges.

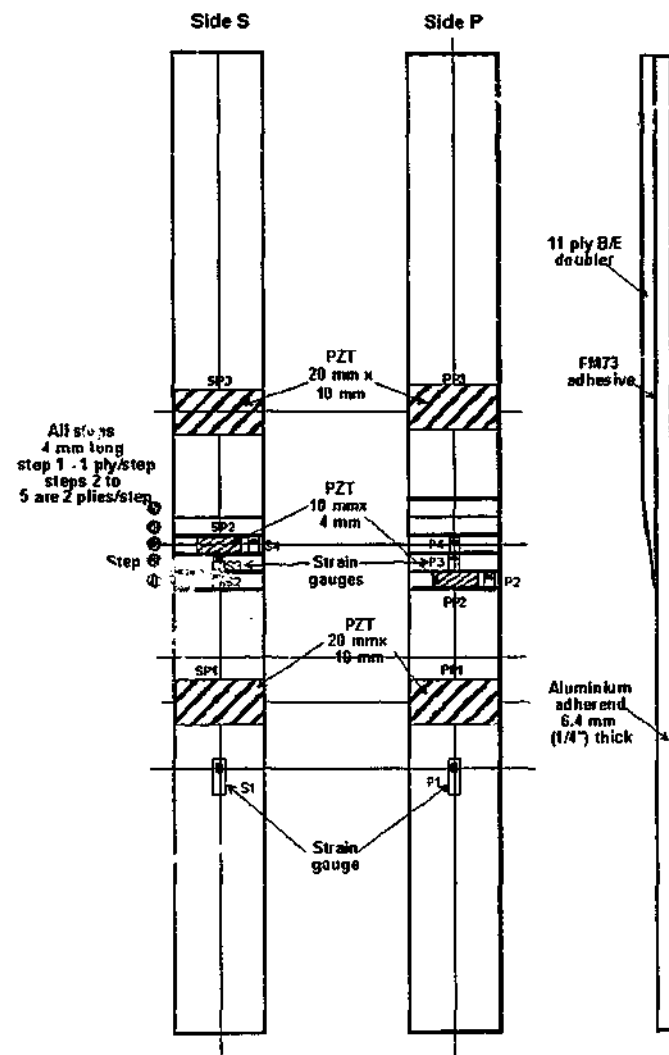


Figure 6.14 Schematic drawing of DD2 specimen used for the impedance method

Figure 6.15 and Figure 6.16 show the schematic drawing of specimen TTCP2. Similar to specimen DD2, TTCP2 was also dynamically loaded to simulate active service. As shown in Figure 6.15 and Figure 6.16, the specimen comprises an aluminium plate with a bonded 13-ply unidirectional graphite/epoxy patch to simulate a bonded repair. Seven PZT elements (each 5mm x 10mm in size) are bonded on seven different locations however only three of the PZT elements were used in the experiments. The

three used are BPZT1, BPZT2 and BPZT3. Strain gauges are attached at four different locations and are labelled as B1, B2, B3 and B4. The impedance method was applied to BPZT2. During the experiments the disbond on Side B was monitored using the electromechanical impedance as well as four strain gauges, labelled B1-B4.

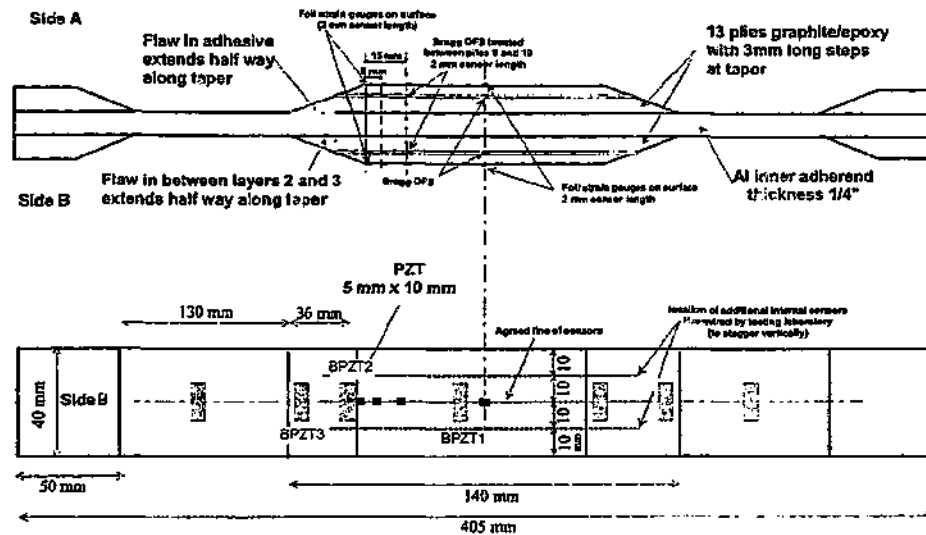


Figure 6.15 Schematic drawing of TTCP2 specimen used for the impedance method

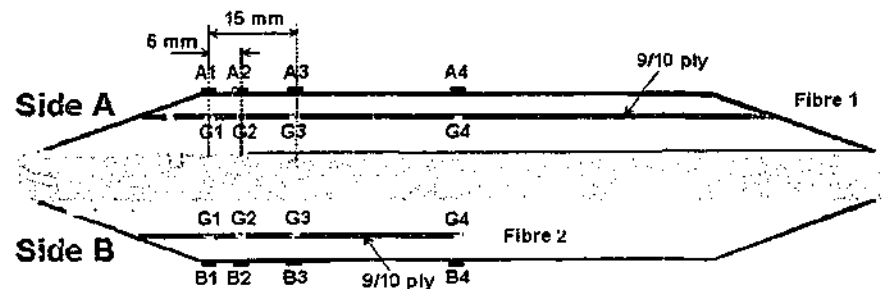


Figure 6.16 Locations of strain gauges on the TTCP2 specimen

The electrical impedance in these experiments was measured using the HP Impedance Analyser and data acquired using the DTVEE Data Acquisition.

The acquisition of the electromechanical impedance can be described as follows:

- The impedance analyser provides a constant voltage signal of 5-V rms.
- Frequency is incremented a low frequency range of 400-Hz to 5-kHz range.

Amplitude and phase measurements were obtained from the electromechanical impedance and were plotted against frequency.

6.5.2 RESULTS AND DISCUSSION

Two specimens with the different composite patch materials were tested with actual loading. This section reports on the experimental investigation in which an array of surface mounted lead zirconate titanate elements (PZT) were used for the in-situ detection of disbond growth in a bonded composite repair patch. The impedance method was used to track the evolution of disbond growth. The method was found to provide a reliable and robust basis for the detection of disbond growth in artificial loading arrangements. The results also demonstrate the importance of transducer placement relative to the disbond location as a factor in the sensitivity to disbond growth.

Previous numerical studies in Chapter 5 and Chiu et al (2000) have shown that disbond growth under a repair patch results in a decrease of the mean square response. In the present application, where there is progressive growth of a disbond due to fatigue failure of the adhesive during cyclical loading of the specimen we would expect to observe a similar declining trend in the mean square response. The evolution of the IM-parameter shown in Figure 6.17 indicates no significant change up to 190,000 cycles at 19-kN, implying no disbond growth in this phase of testing.

Evidence of disbond growth appears at the beginning of 200,000th cycle at 20-kN, in the form of a decrease in the IM-parameter, consistent with the trends reported in the earlier numerical results in Chapter 5. The systematic decline in the IM-parameter appears to end at about the 230th keycycle stage. It is likely that at this point the disbond has grown beyond the PZT sensor footprint, with subsequent testing revealing no further systematic change in response, again, behaviour consistent with that reported in Chapter 5.

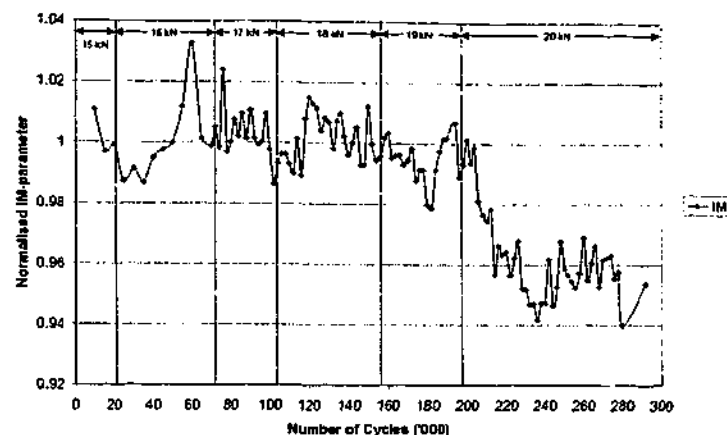


Figure 6.17 Impedance readings from sensor on edge of repair patch taper (PP2)

It is noted that the change in mean level associated with disbond growth is approximately 4%, the coefficient of variation, or the ratio of systematic change to the level of noise of 5-dB as shown in Figure 6.18. This decrease of 4% is due to the disbond growth occurring in close proximity to sensor PP2 that represents a favourable condition for the impedance approach.

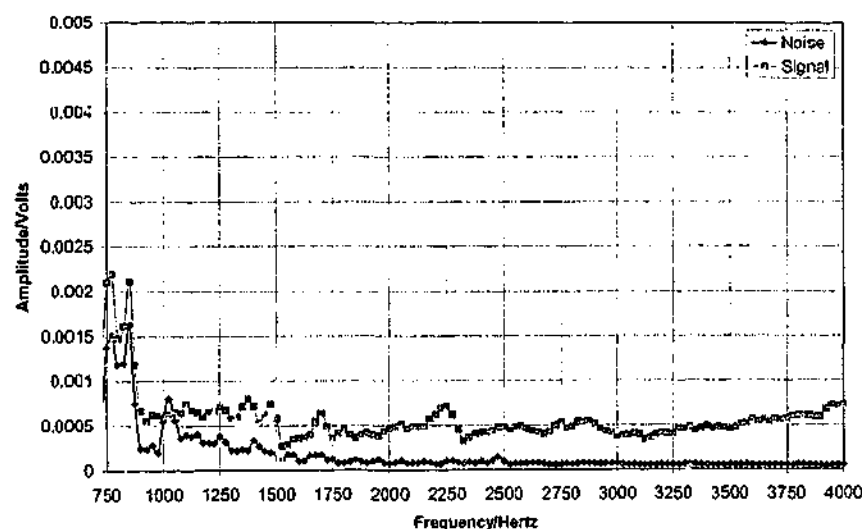


Figure 6.18 Signal to noise ratio determined for the experiment

The progression of disbond growth inferred from the impedance measurements is broadly consistent with the strain gauge readings shown in Figure 6.19. Figure 6.19 shows a decrease in the strain amplitude, which is expected to correspond to initial growth of the disbond. It will be noted that this initial change occurs at the 205th keycycle, some 25 keycycles earlier than for the opposing patch. A possible reason for this

is that the strain gauge is, in relation to the PZT element, located slightly closer to the patch edge, meaning that disbond growth should be detected earlier.

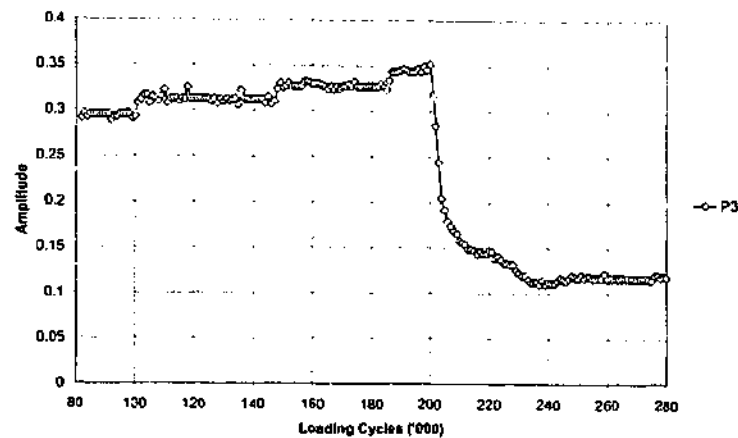


Figure 6.19 Strain gauge reading taken from edge of repair patch taper, P3

The impedance response for specimen TTCP2 is broadly similar to that recorded for DD2. For the case at hand, a systematic decline in the IM-parameter for BPZT3 is recorded after approximately 680 kcycles at 24-kN, as shown in Figure 6.20. This decline tapers off at about the 735th kcycle stage and is likely to be due to disbond growth beyond the sensor footprint. Subsequent testing revealed no further systematic change in response.

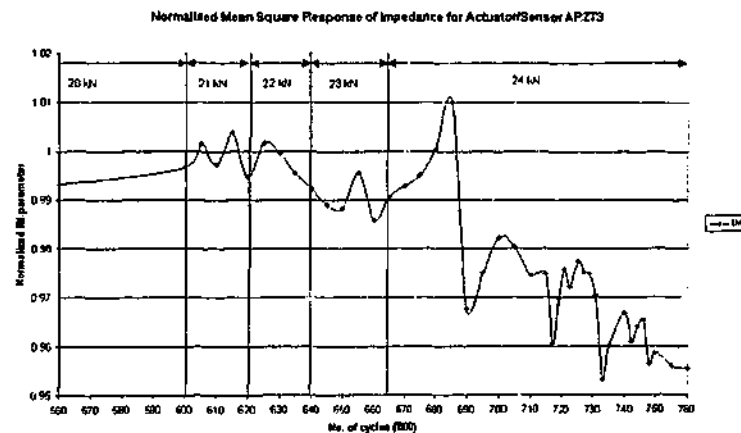


Figure 6.20 Results using the impedance method in the second experiment on BPZT3

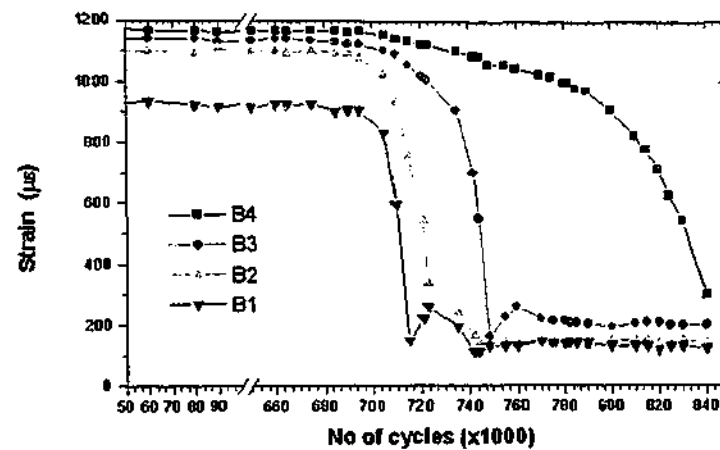


Figure 6.21 Strain gauge results for the second specimen of study

The strain gauge results shown in Figure 6.21 show reasonable agreement with the impedance measurements. Gauges B1-B4 exhibit a noticeable change in response marginally later than that observed for the impedance measurements - 710 keycles compared to 690 keycles. The difference is probably explained by the fact the PZT transducer was located ahead of the strain gauge sensor, and would thus detect disbond growth at an earlier stage.

A closer comparison of the impedance measurements for specimens TTCP2 and DD2 reveals a difference in the extent of signal reduction caused by disbond growth; 4% for TTCP2, compared to 6% for DD2, under nominally similar loading conditions. This is could partly be due to the greater thickness of the graphite/epoxy composite repair patch on TTCP2, since a thicker patch is expected to exhibit a lower change in overall stiffness for a given disbond length. The difference could have been attributed to a difference in patch thickness as well as to a different reference level. It is not possible to compare the effects of the thickness, given that the second specimen, TTCP2 started off from a different reference level (larger initial flaw size). The extent of disbond growth/structural change is presumably greater for DD2 than for TTCP2, so a difference in percentage change can be expected with that alone.

6.6 CONCLUSIONS

The static experiments conducted show that to locate disbond, the sensor/actuator PZT has to be located within the vicinity of the damage region. The observation of the reduction in the impedance measurements in the first specimen agrees with the results from the second specimen. The disbond size predicted by using the impedance method on the first specimen agrees with the disbond visible in the second specimen. In addition the range of the PZT element when excited using the impedance method was found to be limited. The experimental results described above shows that surface mounted PZT elements can be used to predict the type and extent of disbond under the repair patch.

The fatigue experiments conducted show that the impedance method is consistent and robust when undergoing cyclical loading, and therefore practical for real-time application. However the sensitivity of the method could be dependent on the thickness of the composite, a limitation that reduces its attractiveness. This limitation affects the impedance method, as the systematic change with the introduction of damage is less than 10%. On the other hand, the impedance method remains attractive, as it requires only one single piezoelectric transducer. In any case the method is highly reliant on the placement of the PZT elements within the likely disbond initiation area. That said the approach has advantage over strain gauges as it continuously monitors the growth of disbond within the sensitivity footprint of the PZT element.

CHAPTER 7

EVALUATION OF THE TRANSFER FUNCTION METHOD USING NUMERICAL ANALYSIS

7.1 INTRODUCTION

Chapters 5 and 6 evaluated the use of the impedance method for the detection of disbond growth. Another possible method for the detection of disbond growth is the transfer function method. In this chapter the application of the transfer function method is evaluated using numerical analysis. The numerical analysis was carried out using PAFEC, a finite element analysis software package.

Section 7.2 presents the background theory required to understand the transfer function method for disbond detection. The transfer function method utilises both direct and converse effect of the piezoelectric material for actuation and sensing. A stiffness-based mathematical model of the repair patch is then derived.

Section 7.3 presents a model of a given specimen for the preliminary simulation study. This model is the same as that used for the impedance method because it

enables the use of one set of sensors and actuators to acquire data sets for both methods in practical applications. It also allows for the comparison of the methods and the damage detected. The results obtained using the transfer function method are presented and the application of the method to monitor the progress of disbond growth is discussed.

In section 7.4, three more complex numerical models of different specimens are presented. These models are used to anticipate various shapes and sizes of disbond underneath a composite repair patch. These various models are not exhaustive but represent the most common damage recorded in experimental and actual applications of composite repairs. The results obtained using the transfer function method are presented and the application of the method to monitor the progress of disbond growth is discussed.

7.2 BACKGROUND THEORY AND ANALYSIS

To evaluate the transfer function method, a known force was applied to the elements simulating the PZT actuator. The response of the PZT sensors was simulated by the elemental strains calculated during the excitation of the PZT actuators on the repair patch. For this investigation, the transfer function obtained is the amplitude ratio of the response strain to the excitation strain, which is thus dimensionless. Using this method, the PZTs were used to detect the response to a series of closely spaced excitation frequencies, and the amplitude ratio from the transfer function was plotted as a function of frequency.

In theory, if the excitation frequency extends from zero to infinity then the dynamic characteristics of the system are completely defined (Newland, 1993). The results obtained are analysed in order to understand how the statistical characteristics of the repair patch response depend on the statistics of the excitation, and the dynamic properties of the composite patch.

To assist in explaining the results obtained from the numerical analysis, a mathematical model representing the repair patch was developed. In this model the system (repair patch bonded on an aluminium host) was simulated using a five-degree freedom spring-mass system as shown in Figure 7.1. Damping was not included in the development of the model, as the numerical analysis was stiffness-based.

7.2.1 DATA ANALYSIS

The results were analysed using two different approaches. The first approach presented was a variation of the ADI method proposed by Lichtenwalner et al (1997). In Lichtenwalner et al's (1997) case, the integral of the transfer function spectral density is obtained at every discrete frequency. The transfer function spectral density at a discrete frequency is expressed as

$$T.F. = \frac{y_0}{x_0} \quad \text{Equation 7.1}$$

where y_0 is the amplitude of the response strain and x_0 is amplitude of the excitation strain. Excitation used for this method is in the low frequency range up to 20-kHz. The transfer function gives the steady state response of the system to each discrete frequency excitation. This provides the information of the transmission characteristics for the range of fixed frequencies. The transmission characteristics of the different damage conditions were compared with the baseline of the undamaged state to determine its severity.

The second approach was the mean square transfer function method. The mean square was determined for each damage case. This approach was used to condense the results obtained. Each transfer function spectrum was consolidated into a single mean square transfer function defined as

$$MTF = \int_0^{f_u} T.F.(f)df \quad \text{Equation 7.2}$$

where f is the frequency, T.F. is the amplitude ratio from the transfer function and f_u the upper frequency.

The mean square transfer function is the statistical expectation of square of the amplitude ratio of the response strain to the excitation strain. For a given mode and frequency, the power flow of the mode is proportional to the square of its amplitude (Auld, 1990), the constant of proportionality being a function of the mode, the properties of the plate and the frequency. Since power varies proportionally to amplitude squared, the mean square transfer function is indicative of the average power transmitted between the PZT actuator and PZT sensor. The mean square transfer function will also experience an increase if there is a resonant frequency within the analytical range. As the power transmitted is the parameter of interest, the transfer function spectral density, T.F., obtained at frequent intervals throughout the course of the fatigue test, was calculated over a frequency range up to an upper limit. The upper limit was just below the measured first structural resonance of the specimen.

In the following sections, the parameter MTF was used to measure the severity of damage in the structure. For all cases presented the MTF-parameter was normalised to the MTF-parameter for the undamaged case.

7.2.2 MATHEMATICAL MODEL

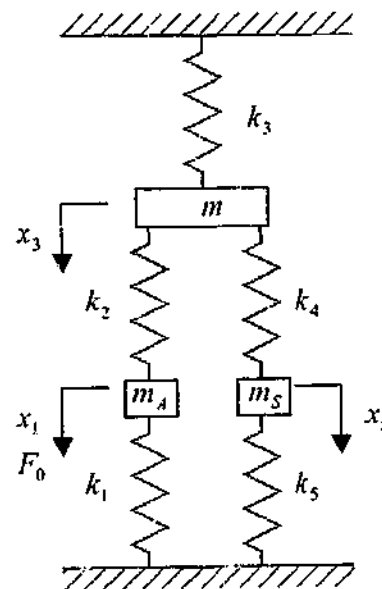


Figure 7.1 Mathematical Model with Spring Mass System

The mathematical model is a development based on the defect for coin-tap model by Cawley (1990). In the model developed shown in Figure 7.1, the system was simulated using the following discrete quantities:

- m - mass of aluminium host
- m_A - mass of PZT actuator
- m_s - mass of PZT sensor
- k_1 - stiffness of PZT actuator
- k_2 - stiffness of repair patch under the PZT actuator
- k_3 - stiffness of aluminium host
- k_4 - stiffness of repair patch under the PZT sensor
- k_5 - stiffness of PZT sensor
- F_0 - sinusoidal forcing function

Given a frequency dependent excitation at the mass, the displacement experienced by each mass, $x_1(t)$, $x_3(t)$ and $x_5(t)$ can be written as follows: -

$$x_1 = \frac{F_0(-k_2)(k_4 + k_5 + m_s\omega^2)}{Det} \quad \text{Equation 7.3}$$

$$x_5 = \frac{F_0(-k_4)(k_1 + k_2 - m_A\omega^2)}{Det} \quad \text{Equation 7.4}$$

$$Det = (k_2^2)(k_4 + k_5 - m_s\omega^2) - (k_2 + k_3 + k_4 - m\omega^2)(k_1 + k_2 - m_A\omega^2)(k_4 + k_5 - m_s\omega^2) + (k_4^2)(k_1 + k_2 - m_A\omega^2) \quad \text{Equation 7.5}$$

$$TransferFunction = \frac{x_5(t)}{x_1(t)} = \frac{(k_4)(k_1 + k_2 - m_A\omega^2)}{(k_2)(k_4 + k_5 - m_s\omega^2)} \quad \text{Equation 7.6}$$

Comparison between the results from the mathematical model and the numerical simulation are reported at the end of the next section. Substituting values of the material property used in the numerical simulation into the mathematical model provided a good means of comparison and the level of agreement between both provided useful insight into the stiffness-based problem.

7.3 PRELIMINARY SIMULATION STUDY

7.3.1 MODEL DEVELOPMENT

Figure 7.2 illustrates in detail a specimen with the repair configuration considered in this preliminary investigation, which has similar dimensions to the specimen used for the impedance method investigation. It has four piezoelectric elements bonded. In these experiments, two sets of simulations were carried out on seven specimens, each with a different disbond size of 0-, 2-, 4-, 6-, 8-, 10- and 12-mm. In one set of simulations, the material of Piezoelectric-3 was PZT and the other set of simulation the material of Piezoelectric-3 was PVDF. In both sets of investigation Piezoelectric-1, -2 and -4 have the material properties of PZT. The use of the transfer function method with a combination of PZT and PVDF sensors and actuators is of major interest when the critical location of the piezoelectric sensor or actuator is in a region of high stresses. It is particularly attractive because the actuating PZT can be located in a low stress region, whilst the sensor placed in the high stress region can be made from a more fatigue resistant PVDF. Since the sensor can be made of more fatigue resistant polymeric piezoelectric films when the transfer function method is used, the use of this method to a sensor and actuator pair has significant advantage over the impedance method.

In the simulation, four piezoelectric elements were assumed to be bonded onto the specimen as shown in Figure 7.2. Piezoelectric-1 was bonded on the repair patch far from the disbond; Piezoelectric-2 was bonded on the repair patch at the top-end of the taper; piezoelectric-3 was bonded above the disbond area at the bottom-end of the taper and finally Piezoelectric-4 was bonded on the aluminium substrate. In order to provide an indication of the extent of simulated disbonding, the PZT/PVDF elements bonded in such an arrangement were interrogated. Piezoelectric-1 and -4 were 10-mm wide, while Piezoelectric-2 and -3 were 4-mm wide.

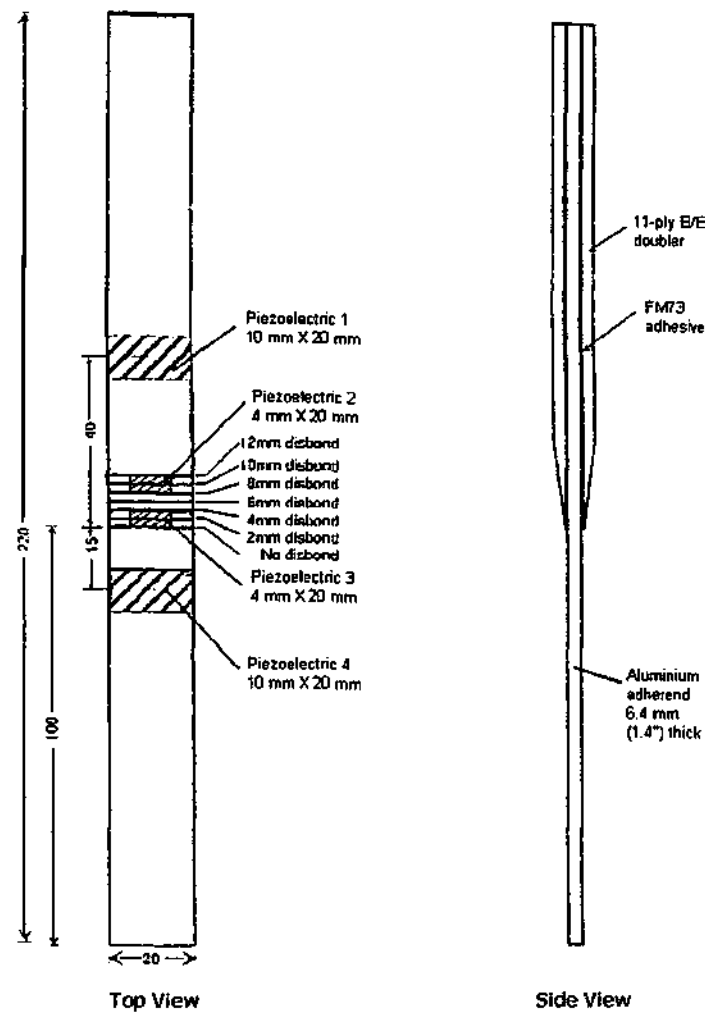


Figure 7.2 Schematic drawing of the specimen with bonded piezoelectric transducers

As two sets of simulations were done to investigate the use of PZTs or PVDFs as sensor, in total twenty-one possible combinations were examined in detail. The possible combinations are shown Table 7.1.

Table 7.1 Piezoelectric-3 with PZT material property

Sensor	Actuator	Transfer Function
PZT2	PZT1	Figure 7.4
PZT1	PZT2	Figure 7.5
PZT3	PZT1	Figure 7.8
PZT4	PZT1	Figure 7.11
PZT3	PZT2	Figure 7.9
PZT4	PZT2	Figure 7.10
PZT4	PZT3	Figure 7.12

Table 7.2 Piezoelectric-3 with PVDF material property

Sensor	Actuator	Transfer Function
PZT2	PZT1	Figure 7.13
PVDF3	PZT1	Figure 7.14
PZT4	PZT1	Figure 7.15
PVDF3	PZT2	Figure 7.16
PVDF3	PZT4	Figure 7.17

The various modes of natural frequency were determined from the post-processor. These modes caused structural resonance and in some cases resulted in maximal local displacements at the repair patch leading to an increase in transfer function. In this set of numerical simulations, the fundamental resonance frequency of the system was at 3000-Hz. This was determined by the case where PZT2 was used as a sensor and PZT1 was used as an actuator for which the transfer function obtained is shown in Figure 7.3. As can be seen in this figure, the fundamental resonance occurs at 3,000-kHz so it was decided that the upper limit of our frequency analysis should be 2900-Hz.

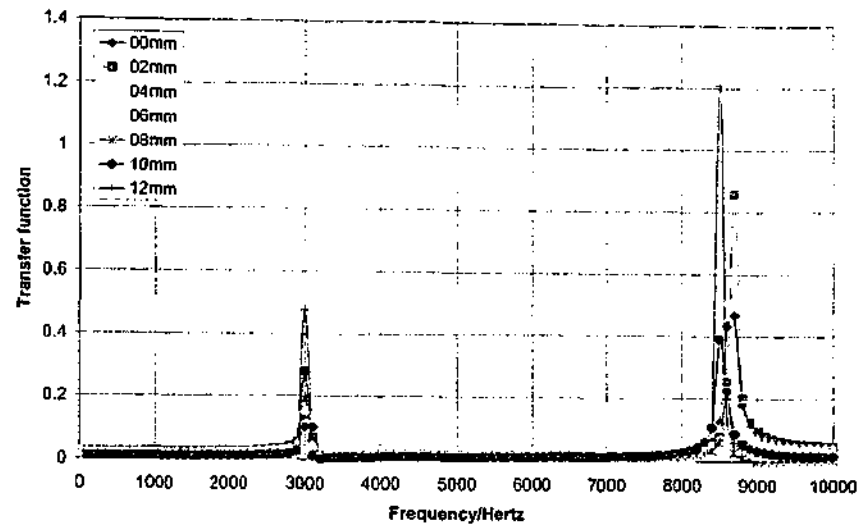


Figure 7.3 Variation of transfer function spectrum with respect to frequency for sensor PZT2 and actuator PZT1

7.3.2 RESULTS AND DISCUSSION

Piezoelectric-3 with PZT material property

Two analytical approaches were used to analyse the numerical simulation results. Each figure consists of two graphs, where the graph on the left was obtained by means of the transfer function integral (i.e. the area under the spectral density) analytical approach at each discrete frequency. The graph on the right was obtained by means of the mean square transfer function (MTF-parameter) approach at a fixed frequency before the first structural resonance for the same set of simulation and plotted with respect to progressive damage increment. The MTF-parameter is indicative of the power transmitted between the actuator and sensor.

Figure 7.4 shows the results obtained when PZT2 was used as a sensor and PZT1 was used as an actuator. The figure indicates that damage can be detected if it was located between the sensor and actuator pair. When PZT1 was used as sensor and PZT2 was used as an actuator, the results shown in Figure 7.5 have a similar trend to those in Figure 7.4. As the damage simulated approached PZT2 the transfer function integral plots shift downwards in the y-axis direction but as the damage passed PZT2, the corresponding transfer function integral plot increases from the 10-mm damage plot. The graphs on the right of both figures illustrate a result that has similar

characteristics to the results obtained using the impedance method. When the initial damage was located 0-, 2-, 4-, and 6-mm away from the sensor or the actuator PZT2, the corresponding plot has a small increasing negative slope, and as damage approached PZT2 the slope becomes increasingly negative.

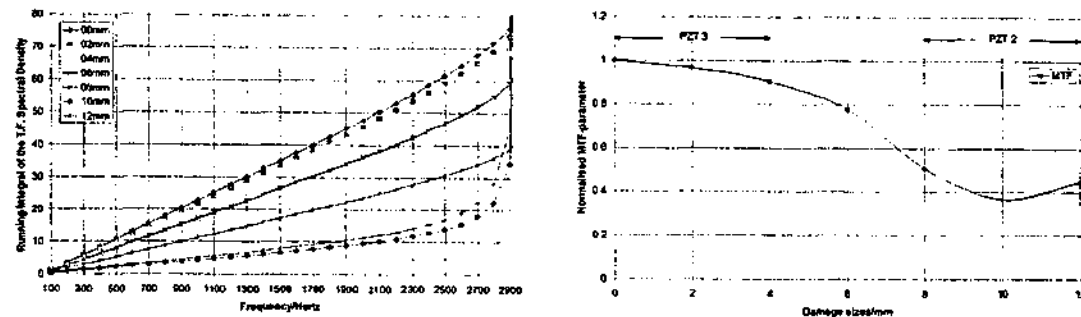


Figure 7.4 Transfer function integral between sensor PZT2 and actuator PZT1

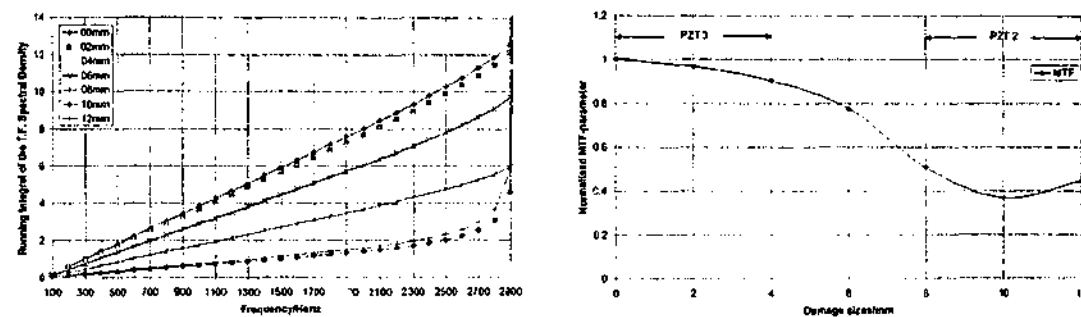


Figure 7.5 Transfer function integral between sensor PZT1 and actuator PZT2

The normalised MTF parameter is independent of the choice of sensor or actuator for a common pair. The trends are the same since system transfer function is a measure of signal transferred from the actuator to the sensor, and in this application, the transferred signal relative to the undamaged state is the same. However from Figure 7.6, it is noted that the magnitude of the transfer function in both cases discussed are not independent of the choice of sensor and actuator for a common pair. The difference in transfer function integral magnitude is due to the different stiffnesses of material to which the actuator was bonded whereby a higher stiffness of host substrate would have a higher magnitude in the transfer function integral.

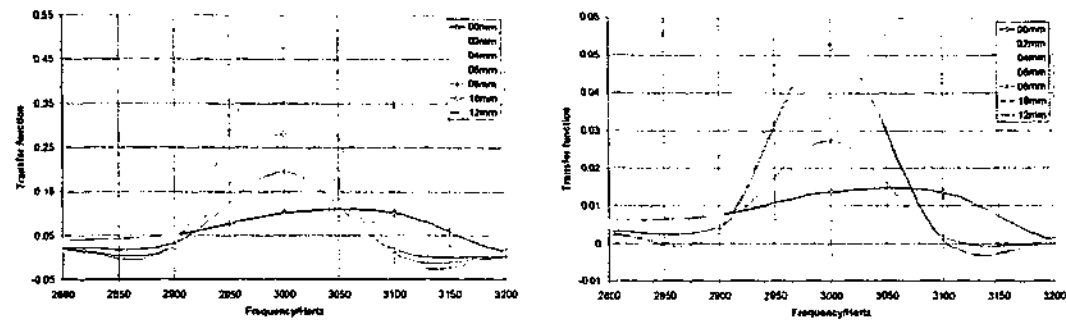


Figure 7.6 Spectral density of actuator PZT1, sensor PZT2 (on the left) and actuator PZT2, sensor PZT1 (on the right)

It is noted that the both figures show an increase from 10-mm to 12-mm disbond. Upon closer inspection of the transfer function plot of both sets of sensor and actuator as shown in Figure 7.6, the magnitude of the resonant frequency increased for disbond size of 10-mm and 12-mm. The increased magnitude affected the leakage within the frequency region of analysis i.e. up to 2,900-Hz. This increase in magnitude was caused by a change in local stiffness. The lower stiffness was a result of the composite patch at the disbonded region behaving like a cantilever.

The following observation of the y-direction displacement from the finite element analysis output in Figure 7.7 confirms the cantilever behaviour mentioned. In the finite element analysis adhesive, elements were removed to simulate disbond. With successive disbonds, the composite patch over the disbonded region was no longer constrained in the out-of-plane direction. In Figure 7.7, the different damage cases were plotted relative to the undamaged case, which was assumed to have zero out-of-plane displacement.

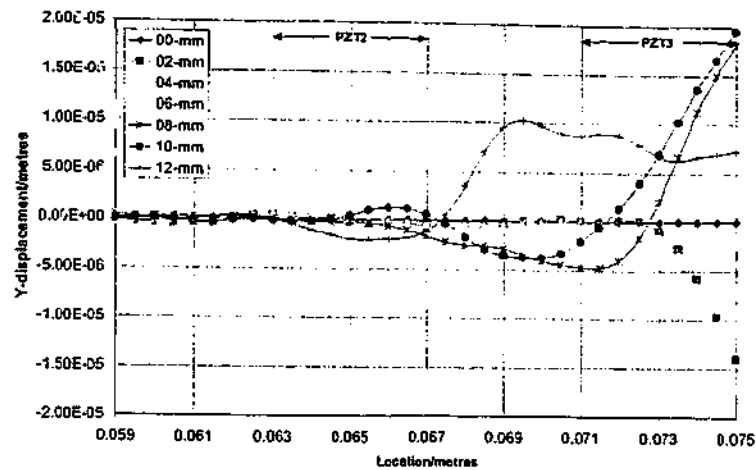


Figure 7.7 Y-direction displacement output from finite element analysis

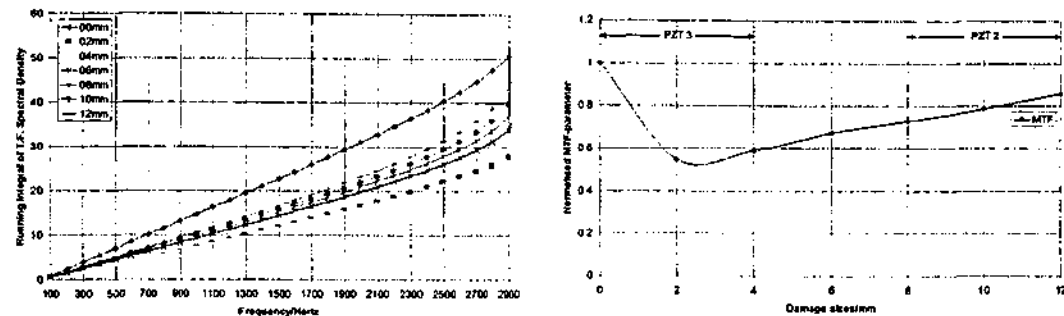


Figure 7.8 Transfer function integral between sensor PZT3 and actuator PZT1

Now, in Figure 7.8 the results shown were obtained when PZT1 was used as actuator and PZT3 was used as sensor. The sensor was located above the growing damage, it is noted that downward shifts of the plots occur when the damage was between the sensor and actuator pair. When the damage size increased to 4-mm a slow upward shift of the plot is recorded. Similarly for the MTF-parameter, at small disbond sizes when the extent of disbond growth was under PZT3, the plot slopes downward immediately after 0-mm damage. As the damage grew past the edge of PZT3, the plot increased gradually. The slow incremental change was due to the decrease in the local stiffness of the composite patch beyond PZT3.

It appears reasonable that the early stages of disbonding of a composite repair patch, occurring between two closely located sensor and actuator, can be detected before damage advances beyond the sensor footprint of both the sensor and actuator. Each

sensor or actuator can be considered a threshold whereby signal from each sensor or actuator located above damage can be used to determine the extent of damage.

In order to consider damage that grew beyond the sensor and the actuator, damage up to 12-mm disbond with PZT3 as the sensor and PZT2 as the actuator, was simulated and the results shown in Figure 7.9. It was previously observed from cases where the disbond that grew past only the sensor located at PZT3, the magnitude of plots decrease with introduced damage and continue to decrease up to a damage size of 10-mm size damage. From Figure 7.9 it can be seen that the plots stay at the same level after 6-mm damage, but in this new simulation with the damage size beyond the sensor and the actuator distance, the plots increase with further damage growth, which means the amount of transferred signal increased.

Since the composite patch behaved like a cantilever as previously described in Figure 7.7, the extent of the transfer function recorded would vary with the change in boundary conditions, which affects the stiffness of the system. The rigorous vibration of the disbonded repair patch beneath PZT2 with the change in composite patch stiffness could have caused this increase in the response strain. At 12-mm disbond, the rate of change in stiffness under PZT2 had slowed to the same rate of change in stiffness under PZT3; therefore the transfer function plot decreases from that of 10-mm. However on the whole the absolute response strain at 12-mm was relatively higher compared to smaller disbond sizes since the overall stiffness of a disbonded patch was lower and thus have an effect on the response.

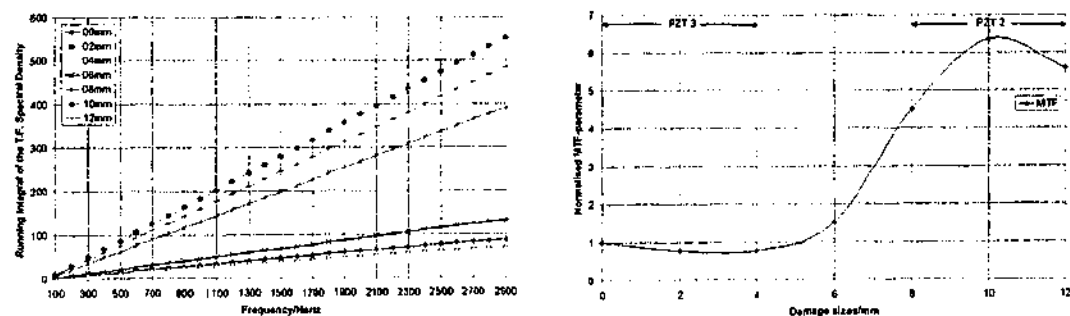


Figure 7.9 Transfer function integral between sensor PZT3 and actuator PZT2

In the previous three cases considered, both sensor and actuator were bonded on the composite repair patch. In the following three cases either a sensor or an actuator was

bonded on the aluminium host. When PZT2 was the sensor and PZT4 was the actuator the result shown in Figure 7.10 closely resembles the result shown in Figure 7.4. The increase of the normalised MTF-parameter at 12-mm disbond was observed. The transfer of signal required a medium, and between PZT2 and PZT4 this medium would have included the boron/epoxy, the adhesive layer and the aluminium host. With the adhesive layer elements removed to increase disbond size, it decreased the local stiffness thus the magnitude of the plots decrease gradually up to the disbond size of 10-mm. As with the case of sensor and actuator pair of PZT2 and PZT3, at 10-mm the repair patch where PZT2 was bonded the rate of change in stiffness under PZT2 had slowed, therefore at 12-mm disbond the transfer function plot increases from that of 10-mm. The increase in transferred signal is as shown in Figure 7.10. In summary so far, the characteristic of the normalised MTF-parameter was dependant on the stiffness of the system.

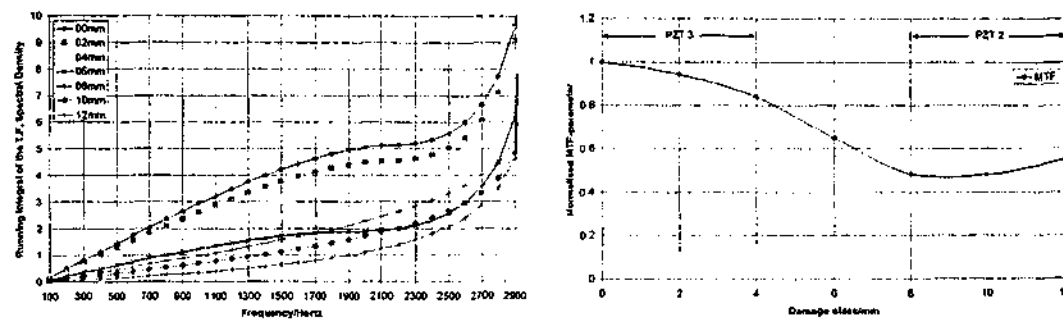


Figure 7.10 Transfer function integral between sensor PZT4 and actuator PZT2

The high stiffness of the material provided a good medium for signal transfer, but because of the long wavelength, the method was insensitive to damage if both the sensor and the actuator were located far from the damage region. This is proven by the results shown in Figure 7.11, where the sensor was located at PZT4 and the actuator was located at PZT1. The signal transmission could occur through either the boron/epoxy repair patch or the aluminium substrate. Hence, the damage would not noticeably affect the transmission of signal with the frequency range used in this study when the distance between the sensor and the actuator was great. The MTF-parameter does not reflect any damage due to the large distance between sensor and actuator and due to the high stiffness of host material.

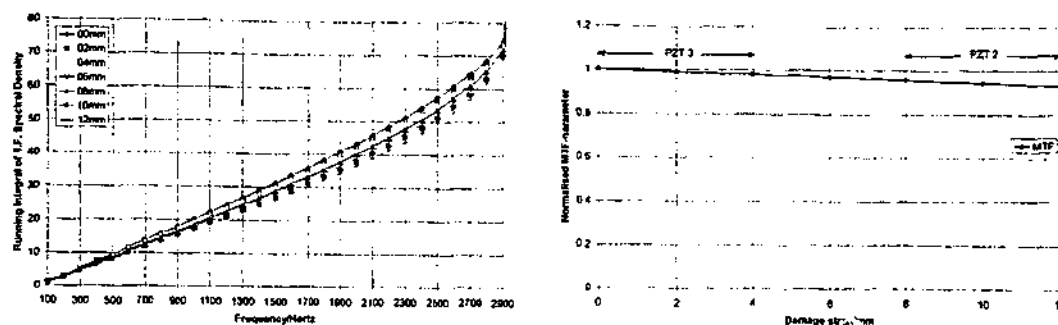


Figure 7.11 Transfer function measurement between sensor PZT4 and actuator PZT1

The case of the sensor at PZT4 and the actuator at PZT3 was next considered and the results are as shown in Figure 7.12. The transfer function plots decrease gradually in y-axis direction with increasing damage size. With PZT3 located directly above the damage, the signal transferred through reduced with each contraction of adhesive. The reduction is proportional to the change in the simulated stiffness of the composite patch that was gradually decreasing up to 12-mm damage.

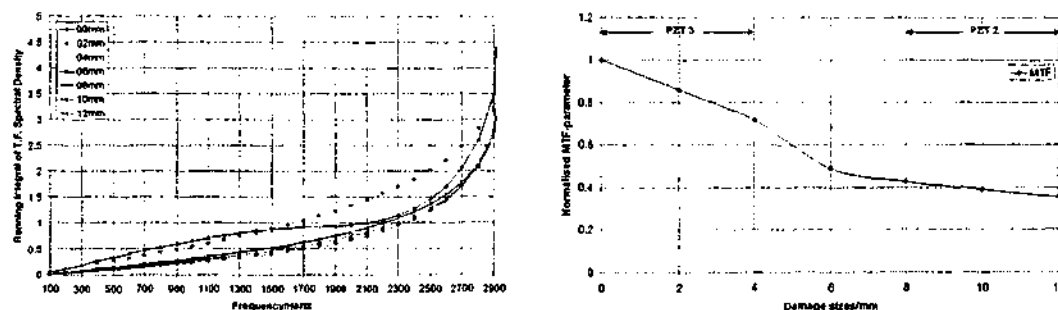


Figure 7.12 Transfer function integral between sensor PZT4 and actuator PZT3

In Figure 7.12, the trends when PZT3 was the actuator and PZT4 was the sensor are observed to be very similar to those in Figure 7.8 for small damage sizes. Downward slopes of the MTF-parameter represent initial damage sizes. The signal decreased gradually with increasing damage size. The signal transmission can only decrease, because the alternate path for power transmission is constantly decreasing. As the disbond increased in size the local stiffness surrounding the PZT decreased. The adhesive layer along the disbonded area is no longer an effective means of transferring the power to reach the repair patch and the aluminium or vice versa. As damage size grew further to the right, the slope decreased gradually.

As previously stated, the absolute power transmitted depended upon the location of the actuating piezoelectric. Excitation strain from the actuator on the tapered edge to any of the sensors had a smaller magnitude as compared to reversing the sensor or actuator role on other surface. The difference was by a factor of two can be attributed to the change in the local stiffness where the actuator was located. With lower local stiffness at the tapered edge, the power transmission is weaker when originating from the tapered edge. In Figure 7.4, it can be seen that the magnitude of all the points is about half in value of those in Figure 7.5. This is important as in real life applications; the location of disbond can be determined by interpreting the shape and the magnitude of the graphs.

Piezoelectric-3 with PVDF material property

The use of PVDF as sensor material for piezoelectric-3 was investigated. Interpretation of results was done using the established method of transfer function spectral density integral. The results were consistent to the use of PZT as material for piezoelectric-3 in terms of the trends with the actuator and sensor locations but differ in magnitude. The transfer function using PVDF had a higher magnitude therefore it shows that PVDF was more sensitive than PZT. At low frequency a well spread result was obtained using PVDF as compared to PZT as shown as comparison in Figure 7.13 and Figure 7.17.

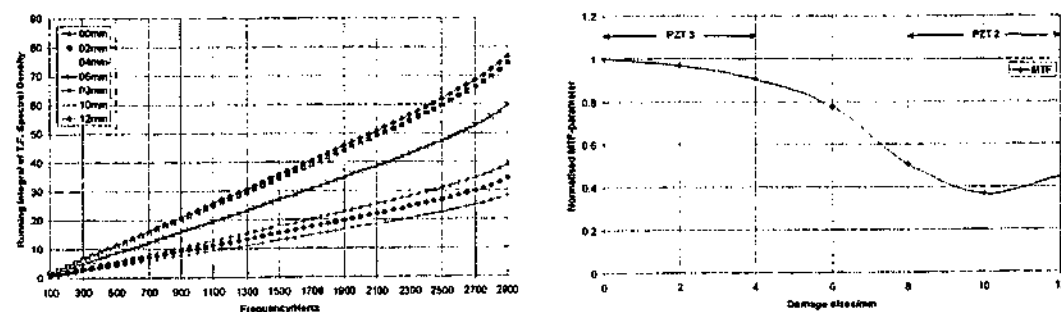


Figure 7.13 Transfer function measurement for sensor PZT2 and actuator PZT1

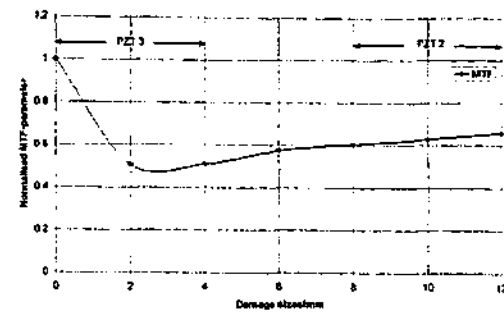
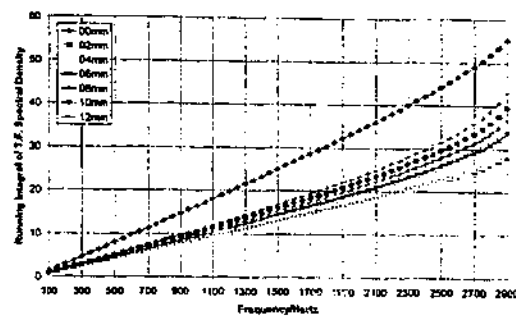


Figure 7.14 Transfer function measurement for sensor PVDF3 and actuator PZT1

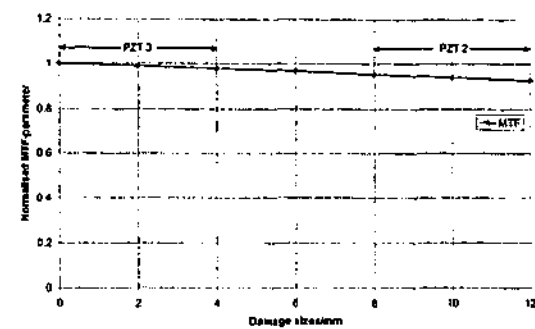
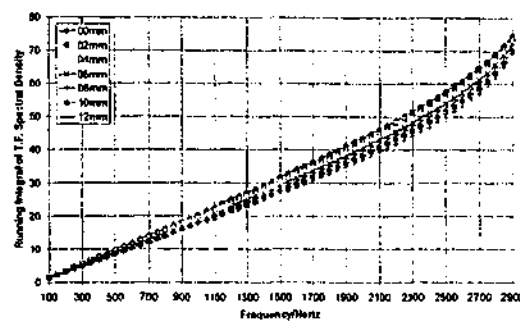


Figure 7.15 Transfer function measurement for sensor PZT4 and actuator PZT1

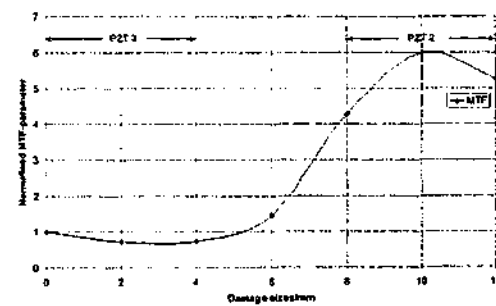
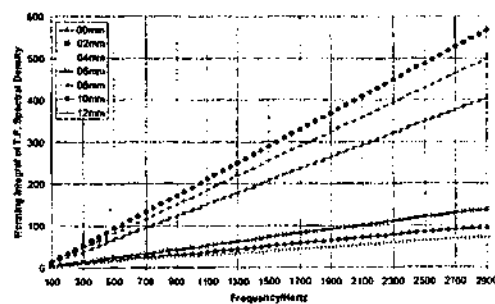


Figure 7.16 Transfer function measurement for sensor PVDF3 and actuator PZT2

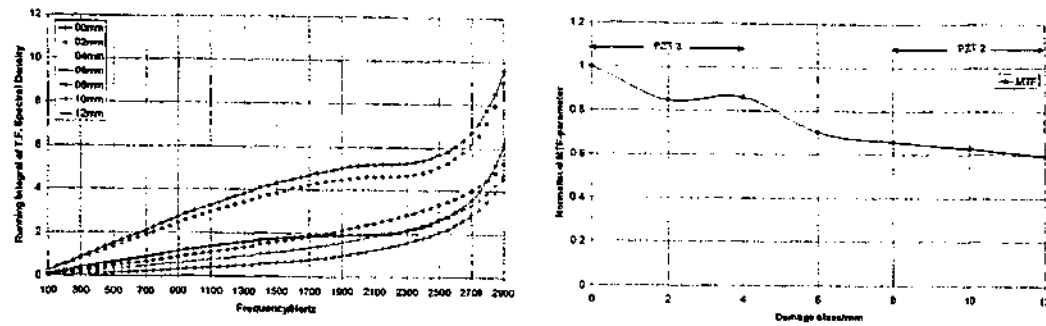


Figure 7.17 Transfer function measurement for sensor PVDF3 and actuator PZT4

It was found the PVDF was more sensitive and strain resistant as compared to PZT. However since the PVDF cannot be used as actuator therefore reduces one set of possible combination for transfer function method as well as the use impedance method on the PVDF. The transfer function for PVDF as sensor has double the absolute MTF-parameter implies that the response strain detected was greater. The amount of signal transferred between the sensor and actuator should be greater than using PZT over the range of frequencies. The shape of the graphs using PVDF is also similar to using PZT. Therefore from the comparison of results using the two different materials, is that PVDF was more sensitive but there will be limited information due to the inability of it to function as an actuator.

The results from the transfer function technique can be summarised as follows: -

- The frequency range should be limited to below the first natural frequency to reduce the effect of resonance on the results.
- The results above show that the sensor or actuator has to be in the vicinity of the disbond for detection and monitoring.
- The MTF-parameter revealed that an increase in the magnitude when the disbond extends past the sensor. In this respect, the size of the sensor will also determine the minimum size of the disbond that can be detected.

7.3.3 COMPARING NUMERICAL ANALYSIS TO THE MATHEMATICAL MODEL

Using the model shown in Section 6.2.1 with the heuristic development of the transfer function written as Equation 7.6, as well as the analytical method presented in Section 6.2.1, we can expect the following observations in the numerical results.

- (1) When the disbond begins to develop below the sensor PZT element (i.e. small initial damage), the stiffness k_4 will decrease; based on Equation 7.6 the MTF parameter should decrease. This decrement is not likely to be significant because the change in k_4 is not expected to be large.
- (2) When the damage has developed passed the sensor PZT element, k_4 would have decreased to a constant value and now k_2 should now decrease. This is because the disbond is larger and the overall stiffness represented by k_2 is now affected. According to Equation 7.6, the MTF value should now increase in magnitude since the change in k_2 is likely to be more significant, a larger increase in transfer function. This can only occur when the actuator and sensor were located close together (e.g. the pair PZT2 and PZT3 in Figure 7.2). When they are far apart, (e.g. the pair PZT1 and PZT3), the increase in transfer function is unlikely to occur.

Now, by substituting the above variables of the mathematical model with the material properties of the composite repair patch system as follows, the MTF-parameter can be calculated and compared with the numerical results.

$$\begin{aligned}m_A &= 7.8 \times 10^{-3} \text{ Kg} \\m_S &= 7.8 \times 10^{-3} \text{ Kg} \\k_1 &= 6.6 \times 10^6 \text{ N/m} \\k_5 &= 6.6 \times 10^6 \text{ N/m}\end{aligned}$$

The stiffness of k_2 and k_4 is dependant on each individual PZT location simulated by the mathematical model. The first calculated model was for the actuator located at PZT2 and the sensor located at PZT3. The stiffness used for k_2 was $2.8215 \times 10^8 \text{ N/m}$ and k_4 was $7.315 \times 10^7 \text{ N/m}$ and applying the above observation (1) and (2), the results are shown in the following Figure 7.18. The results from the reverse of the sensor and actuator pair above were also consistent with the numerical analysis. The second pair

of sensor and actuator calculated was for PZT1 and PZT3 respectively. The stiffness of the repair patch under the actuator PZT3, k_d and its change with damage is similar to that used in the previous calculated model, while k_d remains the same for all calculated cases at 5.225×10^8 N/m. The results are shown in Figure 7.19.

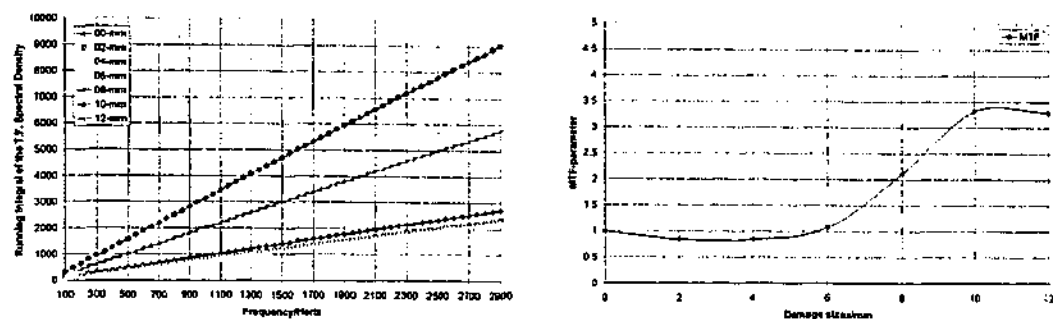


Figure 7.18 Calculated transfer function spectral density and MTF-parameter for sensor PZT3 and actuator PZT2

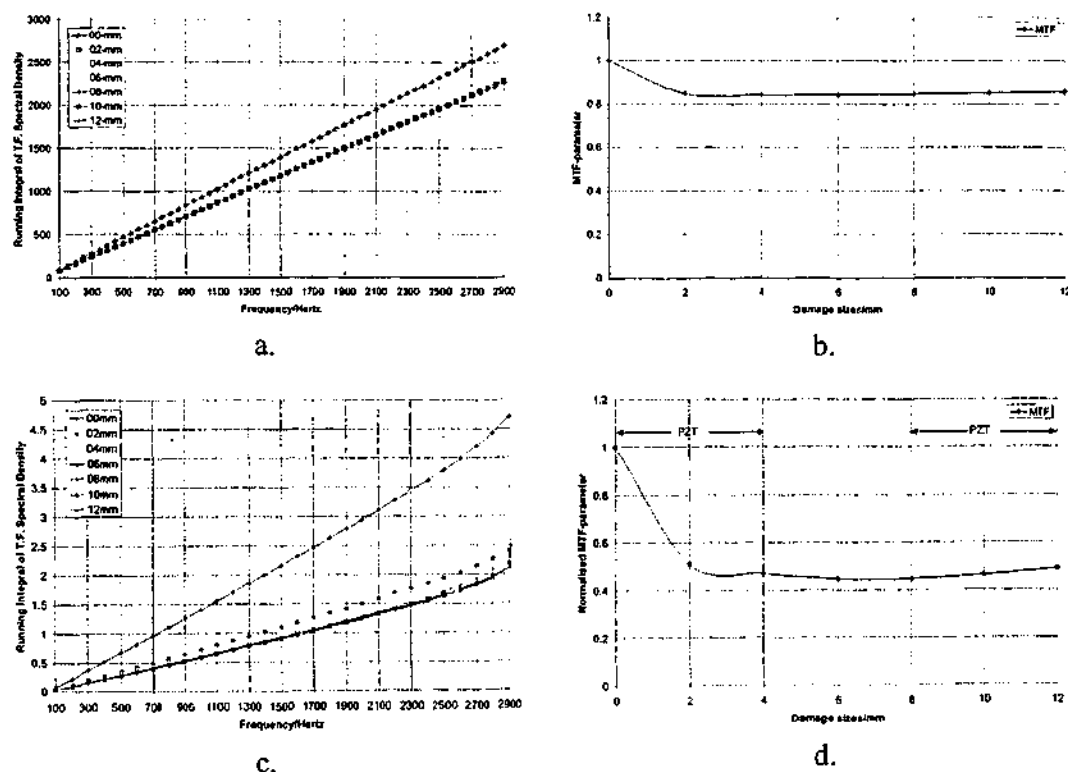


Figure 7.19 Calculated (a. and b.) and numerical analysis (c. and d.) transfer function spectral density and MTF-parameter for sensor PZT1 and actuator PZT3

These results in Figure 7.19 (a. and b.) show good agreement with the results of numerical analysis shown in Figure 7.19 (c. and d.) when PZT3 was used as the actuator and PZT1 was used the sensor. The third and final calculated model was the case considering PZT4 as actuator and PZT2 as sensor. The stiffness of the repair patch underneath PZT2 is the same as the first case while the stiffness of the aluminium underneath PZT4 was 1.136×10^8 -N/m.

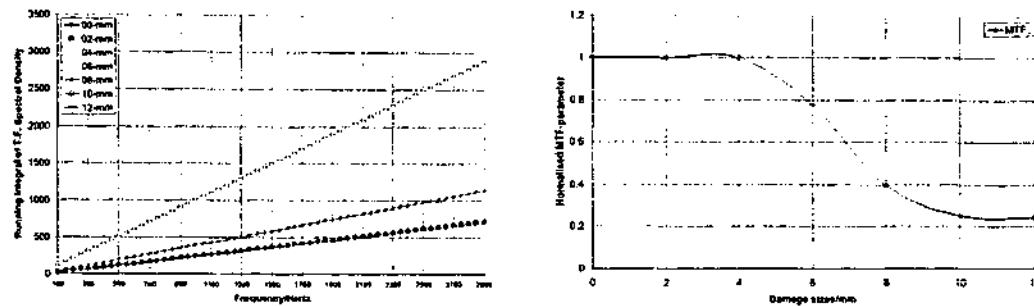


Figure 7.20 Calculated transfer function spectral density and MTF-parameter for sensor PZT4 and actuator PZT2

These calculation based on the mathematical model agrees with the numerical results shown in Figure 7.10. Thus the results show that the stiffness-based mathematical model is a good representation of the transfer function method.

With the successful representation of the finite element analysis with a mathematical model, the next task was to understand the effects of complex disbonds on the transfer function method. The results will be used for comparison with the experimental results from fatigue testing in Chapter 9.

7.4 MODELLING COMPLEX DISBOND TYPES

7.4.1 MODEL DEVELOPMENT

The work presented in the following investigation aims to show the sensitivity of the transfer function method for the detection of complex disbond types in a bonded repair. One of the aims is to determine the minimum detectable damage with respect to the PZT size. The results from this investigation will be used to characterise the response of this methodology when: -

- (i) The damage is located outside the bonded actuator/sensor pair, in using the transfer function method;
- (ii) The damage is located within the actuator/sensor pair, in using the transfer function.

The dimension of the specimens simulated and the damage types were similar to those used for the impedance method. The simulated disbond under the repair patch had dimensions as listed in Table 7.3. In addition, the analysis was done using the MTF-parameter as it allows comparison of numerous results collected over time.

Table 7.3 Disbond sizes simulated

Cases	COR	MID	Cases	BLP
0	No Damage	No Damage	0	No Damage
1	2.5mm X 2.0mm	4.0mm X 2.0mm	1	2.0mm X 2.0mm
2	5.0mm X 4.0mm	8.0mm X 4.0mm	2	6.0mm X 2.0mm
3	7.5mm X 6.0mm	12.0mm X 6.0mm	3	10.0mm X 4.0mm
4	10.0mm X 8.0mm	16.0mm X 8.0mm	4	14.0mm X 6.0mm
5	12.5mm X 10.0mm	20.0mm X 10.0mm	5	18.0mm X 8.0mm
6	15.0mm X 12.0mm	24.0mm X 12.0mm	6	22.0mm X 10.0mm
			7	26.0mm X 12.0mm

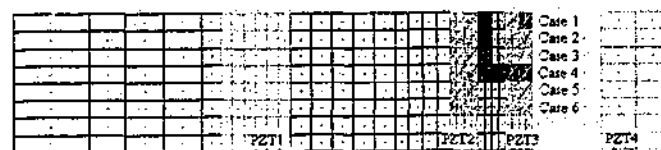


Figure 7.21 Top view for disbond initiating from corner of repair patch (COR)

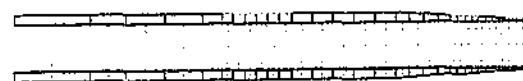


Figure 7.22 Side view for disbond initiating from corner of repair patch (COR)

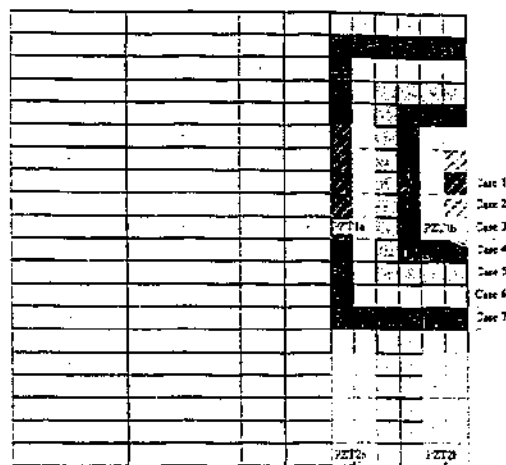


Figure 7.23 Top view for disbond under the PZT and the repair patch (BLP)

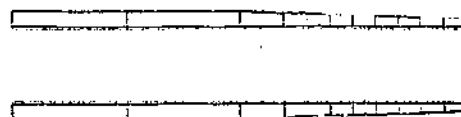


Figure 7.24 Side view for disbond under the PZT and the repair patch (BLP)

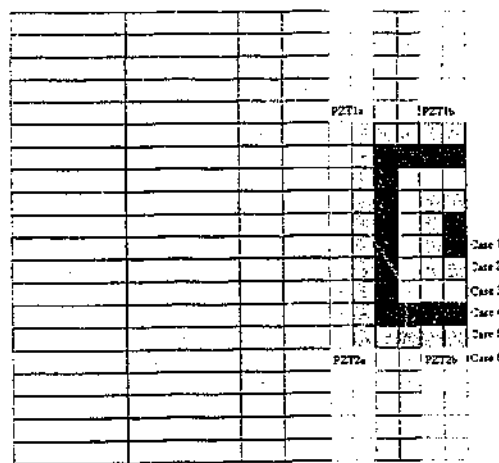


Figure 7.25 Top view for disbond between PZT (MID)

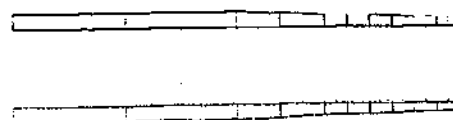
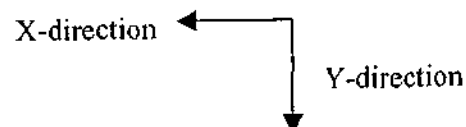


Figure 7.26 Side view for disbond between PZT (MID)



7.4.2 RESULTS AND DISCUSSION

Preliminary investigative experimental results showed that a transfer function between a sensor and an actuator pair located far away from the disbond was not sensitive to the disbond. Thus a 6% change in the mean square transfer function in the finite element analysis would not be detected in experimental situations as shown in Figure 7.27.

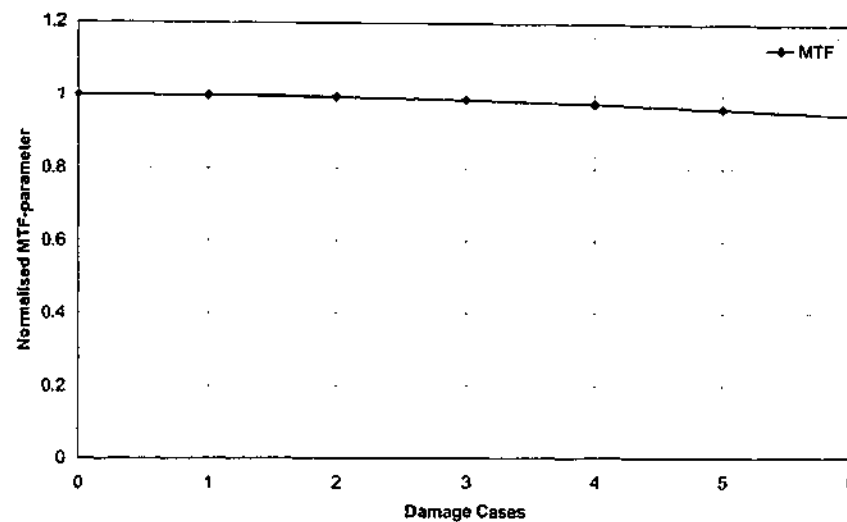


Figure 7.27 MTF-parameter between sensor on aluminium host far field (see Figure 7.21, PZT4) and actuator on repair patch far field (see Figure 7.22, PZT1)

The basis for such generalisation is the inclusion of experimental errors, electrical noise of the equipments and the physical nature of the problem. This error was quantified by using a pair of sensor and actuator placed on far field aluminium and far field repair patch as in Figure 7.21. Experimentally, there would not be a change in response strain, as the sensitivity of the method is limited. Numerically a decrease of 5% - 6% is recorded as damage progresses in damage case 6, Figure 7.21. Hence it was decided that up to 6% change is considered too small to be considered significant. With the range of significance decided, analysis of the graphs was done to predict the size and location of disbond.

Disbond from corner of repair patch

To demonstrate the sensitivity of the transfer function method to detect disbond developing under a repair patch, the model shown in Figure 7.21 was analysed. In simulating disbond initiating from a corner of the patch, the damage was statically grown both in x-direction and y-direction as shown in Figure 7.21, in a seashell manner. If PZT2 was used as an actuator and PZT3 was used as a sensor, it was expected that the MTF-parameter would decrease from the 'no damage' reading with increasing damage growth. When the damage develops beyond the sensing PZT3, the MTF-parameter would increase as explained in Equation 7.6. This will result in a large increase in the MTF-parameter.

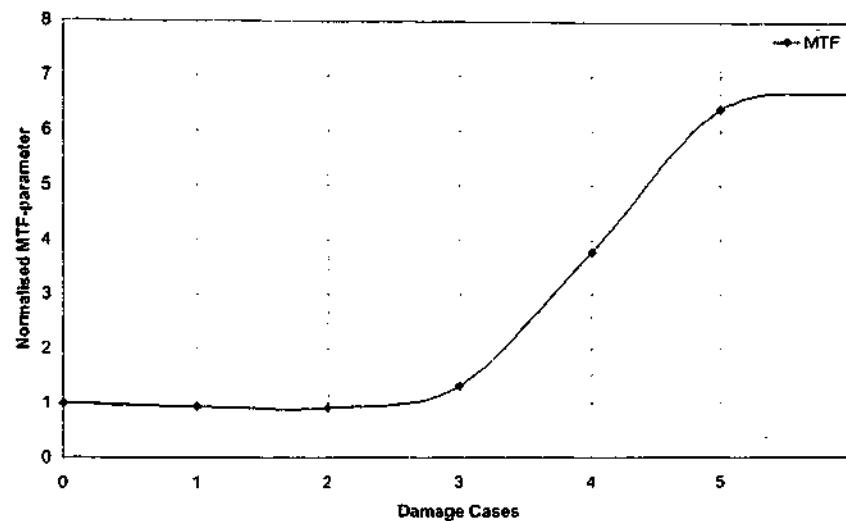


Figure 7.28 MTF-parameter between sensor on edge of repair taper (PZT3) and actuator on top end of repair patch taper (PZT2)

Figure 7.28 shows the mean square transfer function calculated for sensor located on the edge of the repair patch taper (PZT3) and actuator located on the top end of the repair patch taper (PZT2). The decrease in the MTF-parameter when a disbond is under the PZT is observed at damage case 1 and damage case 2. As discussed in the previous section, this disbond would result in a decrease in power transmitted. The decrease is approximately 9%, which would have been observable experimentally. The graph shows only a slight decline as it has been masked by the large increase in the transfer function when the disbond increased in size. The increase is 296.9%. This set of simulation shows that the big increase in mean square transfer function occurs

regardless of whether the disbond has fully disbanded across the entire width of the test specimen contrary to the results in the preliminary investigations above.

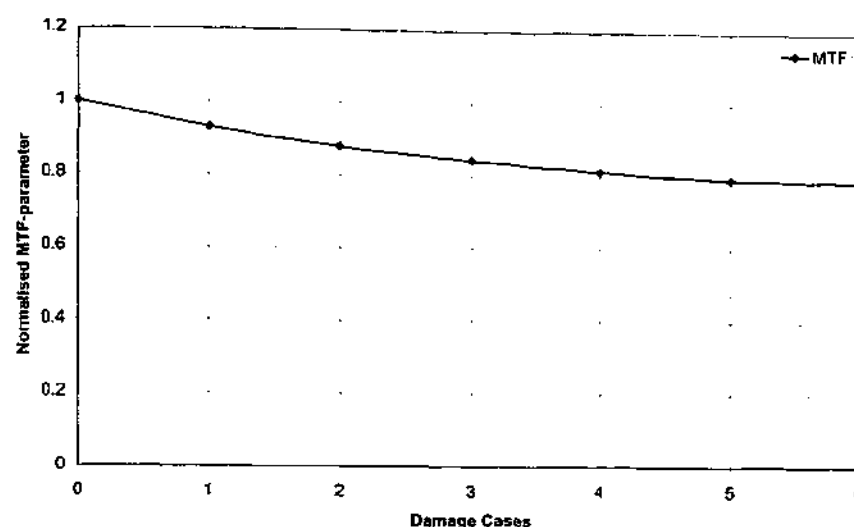


Figure 7.29 MTF-parameter between sensor on Edge of Repair Patch Taper (PZT3) and Actuator on Far Field Repair Patch (PZT1)

Data obtained when PZT1 in Figure 7.21 was used as an actuator and PZT3 was used as a sensor are presented in Figure 7.29. The results show that the magnitude of the transfer function decreases with increasing damage sizes. Since the actuator is located at a distance from the disbond, Equation 7.6 shows that this will only result in a decrease in the magnitude of the transfer function. The increase of the MTF-parameter observed in Figure 7.28 does not occur here since a decrease in stiffness k_2 is not likely to occur because the actuator PZT1 is located away from the disbond. By contrast, the results shown in Figure 7.29, both PZT2 and PZT3 were both located close to the disbond as can be deduced from the results shown in Figure 7.28.

A third sensor and actuator pair combination of interest comprised a sensor located on the top end of the repair patch taper (PZT2) and an actuator located on the far field of the repair patch (PZT1). The MTF-parameter plotted against damage cases is as shown in Figure 7.30. As discussed in an earlier section, a decrease in MTF-parameter of more than 6% can only be classified as significantly detectable, thus damage was only detected when it had developed to damage case 3 (i.e. with a 7.65% decrease). With damage case 3, the front of the advancing damage was located about 2-mm away from the sensing PZT2 (See Figure 7.21). Suppose a "damage detectable zone"

around the sensor exists as described in previous Chapter 5, when the damage has developed into this zone the MTF-parameter calculated would detect the advancing damage. Here the boundary of this zone appears to be approximately 2-mm in front of the sensor.

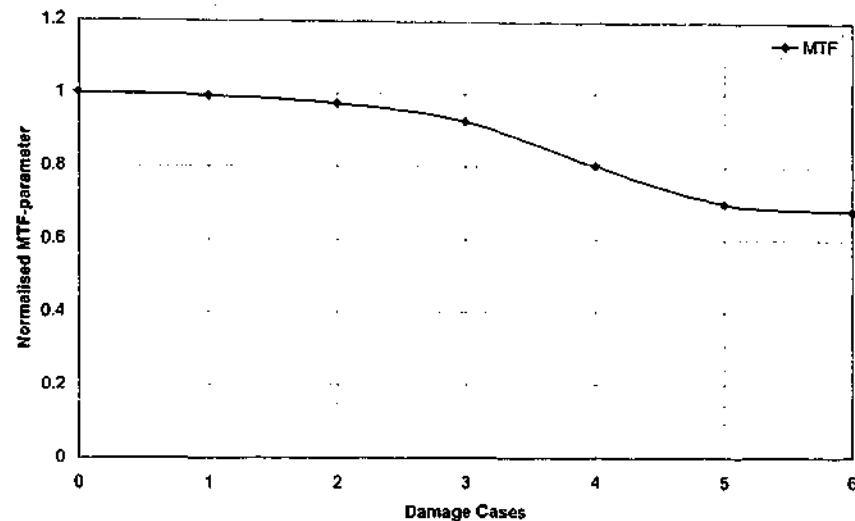


Figure 7.30 MTF-parameter between sensor on top end of repair patch Taper (PZT2) and actuator on far field repair patch (PZT1)

Disbond initiating from a point below the PZT

The results in this section relate to disbond initiating at a point under the PZT and the model simulated is schematically represented in Figure 7.23 and Figure 7.24. Figure 7.31 presents a set of result where PZT1b was used as a sensor and PZT1a was used as an actuator. The MTF-parameter extracted from this simulation exhibits a similar increase when damage developed passed the sensor. This result can be explained using Equation 7.6. When the disbond was confined to the vicinity of PZT1b (i.e. sensor), an increase in the size of disbond, which corresponded to decrease in stiffness k_4 led to a decrease in the power transmitted. When the disbond developed passed the PZT1b, the stiffness k_2 decreased.

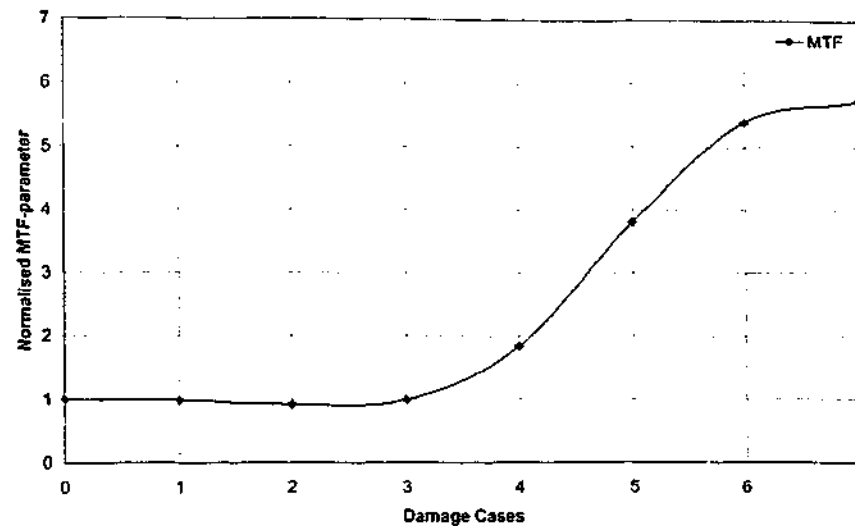


Figure 7.31 MTF-parameter between sensor on top right (PZT1b) and actuator on top left (PZT1a)

As Equation 7.6 suggested, a reduction of stiffness k_2 would lead to an increase power transmission. This is shown in the later part of Figure 7.31 and that a 250% increase in the power transmitted can be obtained when the damage has developed passed the sensor. The initial increase can be used as an indication of the size of the damage. This simulation showed that even when the disbond has grown beyond the size of the sensing PZT in all directions, the transfer function method is still able to monitor underlying changes beneath the repair patch.

When the sensor/actuator pair (PZT2a and PZT2b shown in Figure 7.23) located next to the damage area on the bottom row was used, the transfer function obtained is shown in Figure 14. There are no changes in the MTF value for all simulated damage cases. This result suggests that the front of the advancing damage may not have penetrated the 'damage detectable zone' of the sensor. Since the front of the damage is about 2-mm away from the sensor, it suggests that the damage detection zone in the y-direction of less than 2-mm can exist.

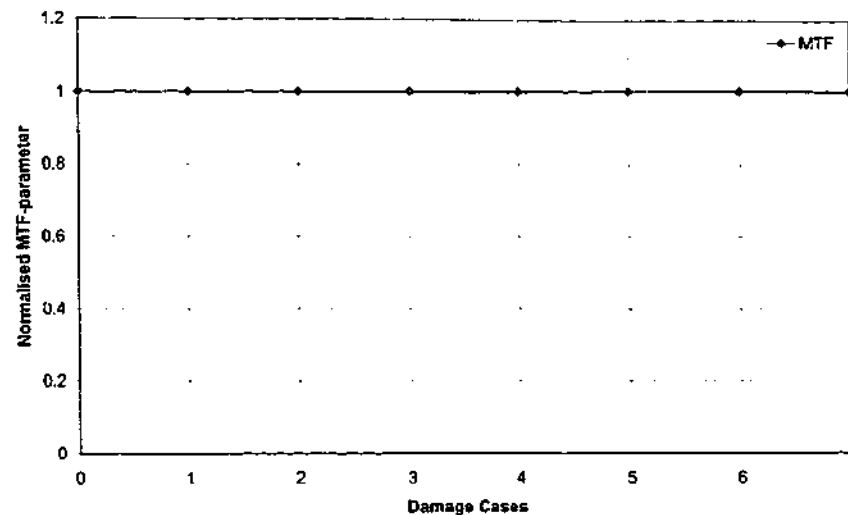


Figure 7.32 MTF-parameter between sensor on bottom right (PZT2b) and actuator on bottom left (PZT2a)

This simulation also shows the difference between the transfer function method and the impedance method. When a disbond develops beyond the PZT, the transfer function reading will increase, while the mean square response from the impedance method will continue to decrease but at a slower rate.

Disbond initiating between PZT sensors

In order to substantiate the statement postulated earlier in previous sections that a 'damage detectable zone' exists and is located at or within less than 2-mm from the top and bottom end of the PZT length in the y-direction, the model shown in Figure 7.25 and Figure 7.26 was simulated and the results are as follows. Figure 7.33 shows the results obtained when PZT1a and PZT1b were used as actuator and sensor respectively. Disbond was not detectable until damage case 5. Here the damage was 2-mm from both top and bottom of the sensors as seen in Figure 3a. In advanced stages of disbond, as described in damage case 5 and damage case 6, when the disbond had developed beneath the repair patch of the sensor and actuator, the MTF-parameter increased significantly. The increment recorded for damage case 5 is 18% and damage case 6 is 72% as shown in the normalised graph of Figure 7.33.

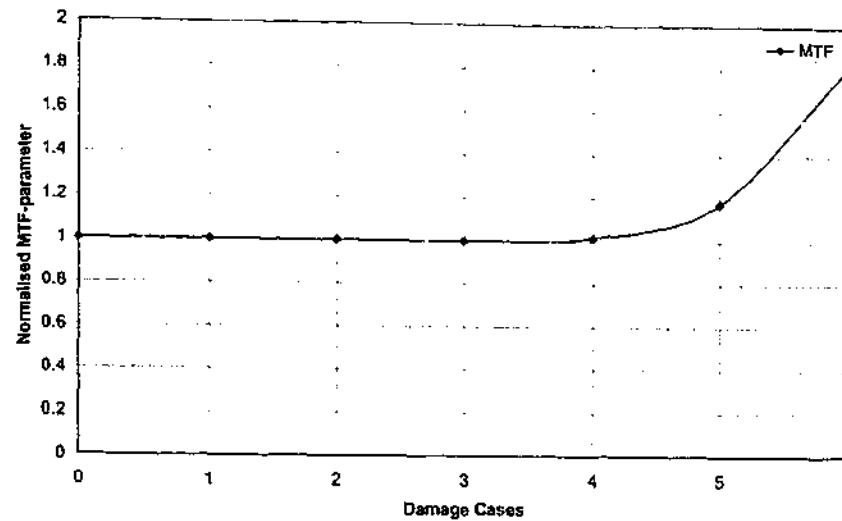


Figure 7.33 MTF-parameter between sensor on top right (PZT1b) and actuator on top left (PZT1a)

These results are consistent with the mathematical model and the results of the previous two sets of simulations. It also confirms a 'damage detectable zone' exists and the MTF-parameter can only be used to indicate the presence of the damage when the damage has penetrated this 'damage detectable zone' of the sensing PZT.

These results show that the transfer function method with strategic positioning of the PZT actuator and sensor is able to discern:

1. The extent of damage, from the trends of the graphs;
2. The location of damage, deducing it from the location of sensor/actuator pairs;
3. The type of damage, analysing the transfer function response from the different combinations of sensor/actuator pairs.

7.5 CONCLUSIONS

A series of numerical studies has been presented to show that the transfer function method can be used to identify typical disbond growth shapes and sizes underneath a composite repair patch. Simulation output was in displacement and from the mean square transfer function the transmission of power a very useful measurement parameter was determined. An increase in mean square transfer function within the

frequency range of analysis can be due to the two factors, the resonant frequency and the increase in the power transmitted. Resonant frequency is detected by both impedance method and transfer function method while increment in power transmitted is only detected by the transfer function method. Because the impedance method takes measurement of the ratio of excitation and response of the local area, it only detects changes in the local stiffness, while the transfer function method is dependent upon the local stiffness surrounding the actuator, the sensor and the medium of transmission.

It was found that a "damage detectable zone" exists whereby no changes in MTF-parameter calculated by means of the transfer function method until the damage has advanced into this zone. The results presented above show that by using some simple signal processing techniques and by strategically placing the PZT elements, the MTF-parameter described above can provide information on the location, type and severity of disbond. The findings obtained using the transfer function method agree with the findings obtained using the impedance method and the transfer function method can be employed without locating extra sensors on the composite patch or the aluminium host structure. Thus the transfer function method is both efficient and effective for the constant monitoring of the repair patch structural condition.

CHAPTER 8

EXPERIMENTAL EVALUATION OF THE TRANSFER FUNCTION METHOD

8.1 INTRODUCTION

The previous chapter evaluated the use of the transfer function method for the detection of disbond growth using numerical analysis. In this chapter the application of the transfer function method is evaluated using experimental analysis. The results obtained from the experimental analysis will be compared to those obtained from the numerical analysis.

Section 8.2 presents the background theory required to understand the transfer function method for disbond detection. This method will also be compared to the impedance method presented in Chapters 5 and 6 to enable identification of areas for synergistic development.

In section 8.3, a preliminary static evaluation of the application of transfer function method is reported. This evaluation was carried out to gain an understanding of the change in the system transfer function with impending damage and disbond growth. The transfer function method was applied to a specimen with boron/epoxy composite

patch. The scope of signal processing suitable for the analysis of the data acquired from the FFT analyser was studied.

In order to verify the findings of the preliminary study, the transfer function method was applied to another specimen with bonded a clear fibre-reinforced polymer composite patch, which was to enable visual inspection of the disbond growth. This application is reported in Section 8.4.

Finally the feasibility of the method undergoing a fatigue test is studied in Section 8.5. In order to evaluate the reliability of the transfer function method when applied to the detection of disbond growth as well as to monitor the progress of the damage underneath the boron/epoxy composite repair, traditional non-destructive methods of ultrasonic C-scan and strain gauges were also used. The results obtained using the transfer function method are presented and compared to the results obtained from these non-destructive methods.

8.2 BACKGROUND THEORY

In the previous chapters, the use of the impedance method for the detection of disbond growth was discussed and evidence was obtained by means of experimental and theoretical investigations. The impedance method reliably predicts damage when the damage was within the predefined damage detectable zone as mentioned in Chapter 5 and 6, however when the damage grows beyond the detection of a single piezo transducer, no further information can be provided. The transfer function method allows the constant monitoring of the disbond growth between the sensor and actuator pair. The present chapter will focus on fatigue testing of a composite repair patch with the aim of detecting disbond growth with the transfer function method. The results are also compared to a set of numerical results reported in Chapter 7.

The transfer function method presented here is based on the system transfer function between a pair of PZT transducers bonded to the repaired structure. This technique utilises both the converse and direct effect of the piezoelectric material for actuation

and sensing respectively. It was previously shown that the transfer function method is particularly attractive because the actuating PZT can be located in a low stress region, whilst the sensor placed in the high stress region can be made from a more fatigue resistant material, like PVDF. Penn et al (1999) pointed out several advantages in using piezoelectric polymeric material as sensors in place of strain gauges, namely that they require no external power source and they generate signals far stronger than those of traditional amplified strain gauges. They explored the use of polyvinylidene fluoride (PVDF) films for the detection of delamination of composites. The specimens were investigated both in clamped and unsupported configurations and excitation was done using a hammer tap. It was concluded that the free vibration method using PVDF elements as sensors was able to detect in thin plates delaminations as small as 0.34% of the plate area. The authors observed dramatic shifts in natural frequency with varying delamination sizes.

Islam and Craig (1994) used modal analysis techniques with piezoceramic sensors and actuators. They analysed the frequency-response of a structural member and determined the type of damage and its location on the basis of the shift in natural frequencies. The findings of these authors are consistent with Adams and Cawley (1985) who showed that damage is usually accompanied by a local reduction in stiffness and an increase in damping. Further, they found that local and distributed changes in stiffness, produced changes in natural frequencies that varied depending on the damage location.

Several different transfer functions are used in vibration measurement, depending on whether displacement, velocity or acceleration is measured (Boller and Dilger, 1992). The various system transfer functions are illustrated in Table 8.1.

Table 8.1 Transfer Functions Used in Vibration Measurement

Response Measurement	Transfer Function
Acceleration	Inertance
Velocity	Mobility
Displacement	Receptance

The receptance transfer function (also called the compliance or admittance) is of importance in this investigation, since the displacement is the response measured by the PZT transducer. The compliance given in Laplace domain for a single degree of freedom system is denoted by

$$H(s) = \frac{X(s)}{F(s)} = \frac{1}{ms^2 + cs + k} \quad \text{Equation 8.1}$$

The corresponding frequency response function is obtained by substituting $s = jw_{dr}$ into the equation. It is noted that the largest value of this magnitude occurs near $k - mw_{dr}^2 = 0$, or when the driving frequency is equal to the natural frequency of the system, $w_{dr} = \sqrt{k/m}$. A continuous structure (ie. a plate) has an infinite number of natural frequencies. The natural frequencies for a plate are a function of boundary conditions, material properties such as Young's modulus, density and Poisson ratio, along with plate dimensions; length, width, and thickness. Hence, in the frequency response of plate like structures it is expected to observe many resonant frequencies.

This background information reinforces the knowledge obtained from the literature review. It is followed with a preliminary investigation of the detection possibility with a square piezoceramic element.

8.3 STATIC EVALUATION WITH BORON/EPOXY REPAIR PATCH

This was the first experimental investigation of damage detection by means of the transfer function method. It is a preliminary investigation thus experimental procedures described are general in nature. The results and discussions are carried out to determine the fundamental principles of the method needed for the detection of disbond.

8.3.1 EXPERIMENTAL PROCEDURES

The specimen used for the preliminary investigation is similar to that of impedance method. Three piezoceramic (PZT) wafer elements were bonded on the specimen in the configuration as shown in Figure 8.1. These PZT elements were used as sensor or actuator during the experimentation of the detection of disbond growth by means of the transfer function method. The different pairs of PZT combinations being used as sensor and actuator were to identify the optimal sensor placement with a suitable frequency range for the identification of disbond growth. The possibility of detection of disbond when both the sensor and the actuator were located on the aluminium host structure (i.e. remote from disbond) was also investigated.

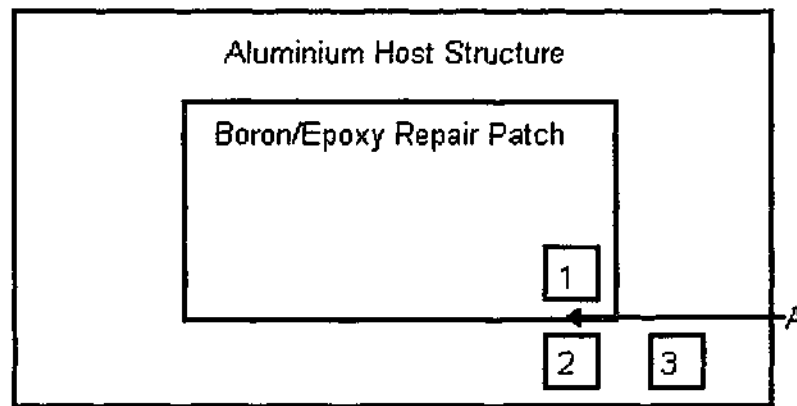


Figure 8.1 Schematic drawing of the preliminary investigation specimen

To define the dynamic characteristics of the system, the PZT transducer is excited through broadband random (white noise) excitation. The output is measured for a series of closely spaced frequencies; the ratio of the Laplace transform (Boller and Dilger, 1992) of the two signals then yields the transfer function (TF). In this investigation, the transfer function is computed via the Fast Fourier Transform (FFT) analyser. The FFT analyser determines the transfer function in the following way.

$$TF = \frac{\text{Sensor_Signal}}{\text{Actuator_Signal}} \quad \text{Equation 8.2}$$

The Fast Fourier Transform analyser maps any signal from time domain into the frequency domain. The transform of the input and output signal was calculated and the frequency response for the structure was determined. In this manner, the system

transfer function for each of the individual plate representing progressive damage state was acquired and disbond sizes can be easily interpreted from the spectrum obtained.

In the investigation on the feasibility of the detection of disbond growth statically using the transfer function method, three sets of experiments were conducted with the configuration in Figure 8.1. They were as follows:

1. When PZT element-1 was used as a sensor and PZT element-2 was used as an actuator.
2. When PZT element-2 was used as a sensor and PZT element-1 was used as an actuator.
3. When PZT element-2 was used as a sensor and PZT element-3 was used as an actuator.

A broadband signal was produced using an AND AD-3525 FFT Analyser, with a frequency bandwidth of 250-Hz to 100-kHz and RMS signal amplitude of 2-V. This broadband signal was supplied to the PZT serving as the actuator, whilst simultaneously acquiring the signal from the PZT sensor. In this manner, the transfer function of the various actuator/sensor combinations was obtained. When calculating the transfer function, a total of 100 spectral averages were taken.

8.3.2 RESULTS AND DISCUSSION

Figure 8.2 shows the transfer function obtained for the case where PZT element-1 was used as a sensor and PZT element-2 was used as an actuator. For clarity, Figure 8.2 only shows the results obtained from the no-damage case and from the $20 \times 20\text{-mm}^2$ case of disbond. Given this configuration, Chiu et al (1999) predicted that the magnitude of the transfer function would decrease with an increase in the size of the disbond. From Figure 8.2, the transfer function plot for the case with damage exhibits a downward translation in the y-axis direction. As a means of reducing the effects of experimental noise and thus improving the clarity of genuine trends, an accumulative integral of measured transfer function was performed. This is similar to the data analysis approach of Lichtenwalner et al (1997) reported in Chapter 6. Peaks in the

transfer function amplitude spectrum represent global structural modes at lower frequencies and local structural resonances at higher frequencies.

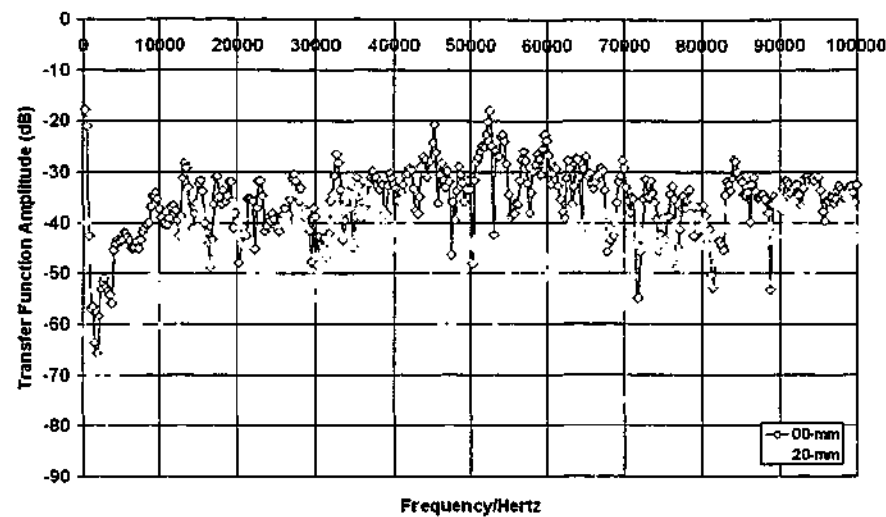


Figure 8.2 Transfer function spectrum for no damage and $10 \times 10\text{-mm}^2$ damage

Figure 8.3 provides a plot of this integration. It is clear from this figure that the magnitude of the transfer function decreases with the size of disbond under the patch, which is consistent with the earlier predictions. When PZT element-2 bonded on the aluminium host structure was used as sensor and PZT element-1 bonded on the composite patch with prescribed damage area was used as an actuator the results shown in Figure 8.3 shows a separation between the frequency response plots for the different disbond sizes under the composite patch. As disbond size increased, the integral of transfer function spectral density decreases.

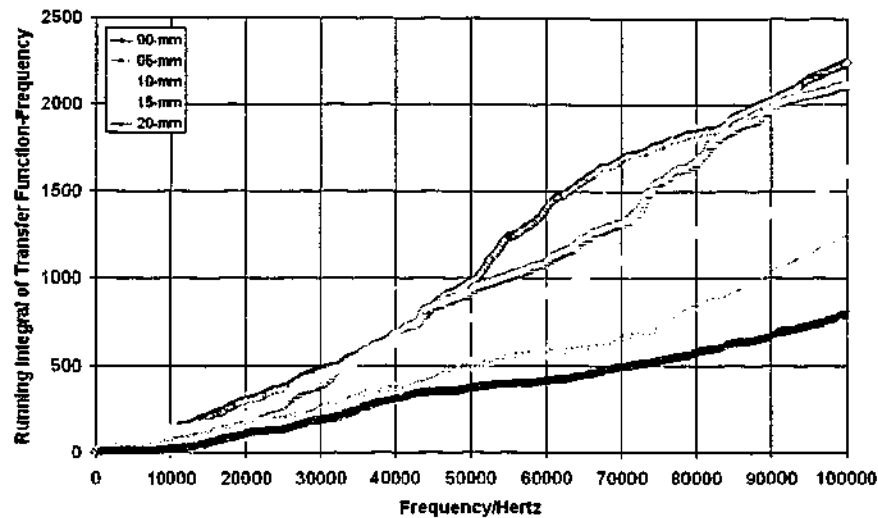


Figure 8.3 Transfer function between actuator on composite patch and sensor on aluminium

Similar plot decrement characteristics to that found in Figure 8.3 can also be observed in Figure 8.4. Figure 8.4 presents the results when PZT element-1, which was bonded on the aluminium host structure, was used as sensor and PZT element-2 bonded on the composite patch with prescribed damage area, was used as an actuator. The mean square response of the transfer function spectral density decreases with damage severity.

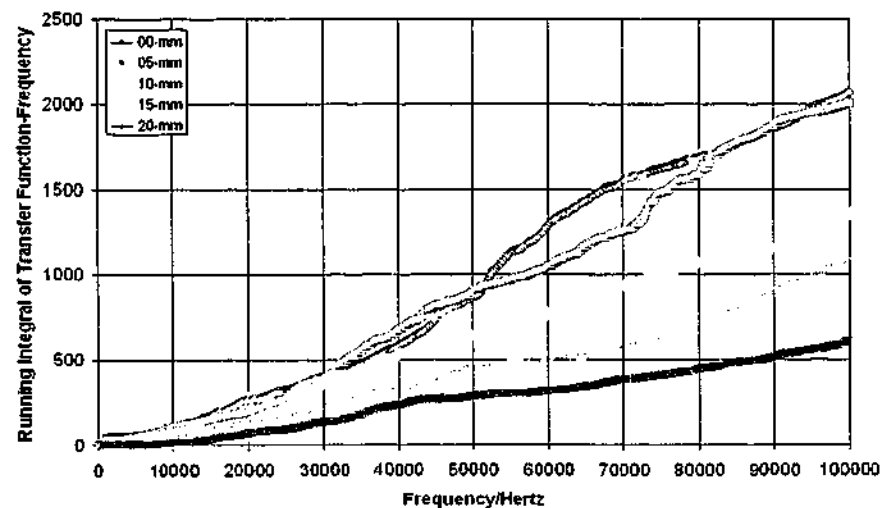


Figure 8.4. Transfer function between actuator on aluminium and sensor on composite patch

From the results obtained, this method was found to be very sensitive to the presence of disbond. Figure 8.5 shows the graph obtained when PZT element-2 was used as a sensor and PZT element-3 was used as an actuator. The frequency response plots representing the individual damage sizes remains close together within the range of interest.

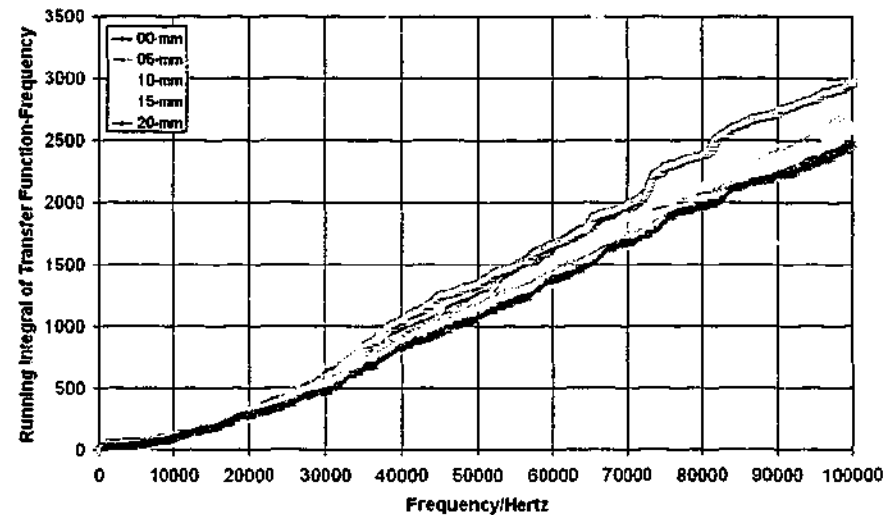


Figure 8.5 Transfer function between sensor on aluminium and actuator on aluminium

The results from the figures show that the method was capable of detecting the disbond growth as long as a sensor or an actuator was located over the damage area. The result from Figure 8.5 indicates that when both the sensor and the actuator were on the host substrate it would not detect the disbond growth under the composite patch, either the sensor or the actuator had to be located over the damage area for integrity assessment.

We can summarise the experimental results for the transfer function approach as follows:

- The transfer function of a pair of sensor and actuator decreases with an increase in the disbond size in the composite repair.
- This decrease in the transfer function is obtained as long as a sensor or an actuator was located on the damage zone.

- The results described above revealed that locating both the sensor and actuator on the aluminium substrate is not likely to provide any information on the size of the disbond.

The frequency range used for this preliminary investigation provided a good indication of the requirement needed for a clear resolution with the optimal placement of the sensors/actuator to achieve damage detection capability. Thus further validation of the transfer function method was conducted by using glass fibre-reinforced plastic repair patch. This allows the comparison of the damage predicted by means of the transfer function method and the damage made visible by the liquid penetrant.

8.4 STATIC EVALUATION WITH GLASS FIBRE-REINFORCED PLASTIC REPAIR PATCH

The aim of this stage of the experimental investigation was to confirm the results obtained in the experiment on boron/epoxy composite patch by viewing the underlying condition. A 4-ply [0,90]_s lay-up glass fibre-reinforced polymer (GFRP) was used as the orthotropic properties closely resembles that of the boron/epoxy composite repair. The specimen and the locations of the piezo transducer used for these experiments were described in section 3.6.1 of Chapter 3.

8.4.1 EXPERIMENTAL PROCEDURES

To acquire the frequency response of the specimen, the same broadband random excitation at a RMS voltage of 5-V was used as in the preliminary investigation to actuate the piezoelectric transducers. The broadband signal was produced using a TDS-210 wave generator. The vibration signature of the structure was then computed via the transfer function for each sensor. The real and imaginary transfer function of the current drawn by the sensor was recorded and converted to amplitude and run integral. For this investigation the transfer function was computed using a PCMCIA card based Fourier Transform analyser. Analysis was carried out between the frequency bandwidth of 0-Hz and 10-kHz. The transform of the input and output

signal was calculated and the frequency response for the structure was determined. As in the preliminary investigation when the transfer function was calculated, more than a total of 100 spectral averages were taken. The measured frequency response was used as the basis for inferring the structural condition of the component.

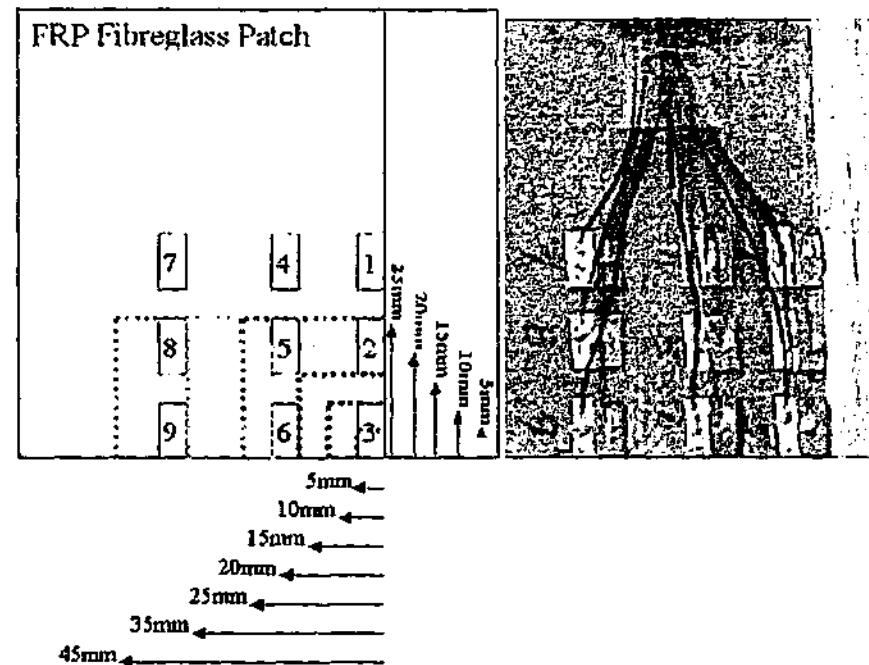


Figure 8.6 Schematic drawing of specimen (on the left) and the actual specimen (on the right) used for the visualisation of disbond growth

The transfer function method was applied to the six 'possible' different combinations of actuator/sensor combinations involving all the elements shown in Figure 8.6. Based on the assumption that the transfer function is not directional the combinations were as follows

1. TF17 (piezoelectric-7, actuator and piezoelectric-1, sensor).
2. TF47 (piezoelectric-7, actuator and piezoelectric-4, sensor).
3. TF28 (piezoelectric-8, actuator and piezoelectric-2, sensor).
4. TF58 (piezoelectric-8, actuator and piezoelectric-5, sensor).
5. TF39 (piezoelectric-9, actuator and piezoelectric-3, sensor).
6. TF69 (piezoelectric-9, actuator and piezoelectric-6, sensor).

8.4.2 DATA ANALYSIS

The transfer function spectrum (T.F.) obtained at frequent intervals throughout the course of the fatigue test was calculated over a frequency range up to an upper limit of 3.0-kHz, which was just below the measured first structural resonance of the specimen. Each transfer function spectrum was consolidated into a single mean square response defined as

$$MTF = \int_0^{3000} T.F.(f) df$$

where f is the frequency and T.F. is the transfer function spectrum.

In the following sections, the parameter, MTF, is used to relate the severity of damage in the structure to the undamaged structure. For all cases presented the MTF-parameter was normalised with the MTF value for the undamaged case.

8.4.3 RESULTS AND DISCUSSION



Figure 8.7 Specimen with the blade inserted for a damage size of $10 \times 10\text{-mm}^2$

Figure 8.7 shows the specimen with a damage size of $10 \times 10\text{-mm}^2$ made visible by the insertion of the blade. The transfer function results shown in Figure 8.8 were obtained using piezoelectric-4 as an actuator and piezoelectric-7 as a sensor. As shown in Figure 8.6, this actuator and sensor were located some distance from the disbond area. Figure 8.8 shows a slight decrease in the MTF trend by about 3%, however it would be considered too small to be considered significant. The MTF-parameter is expected to remain linear since the detection zone excludes the damage area.

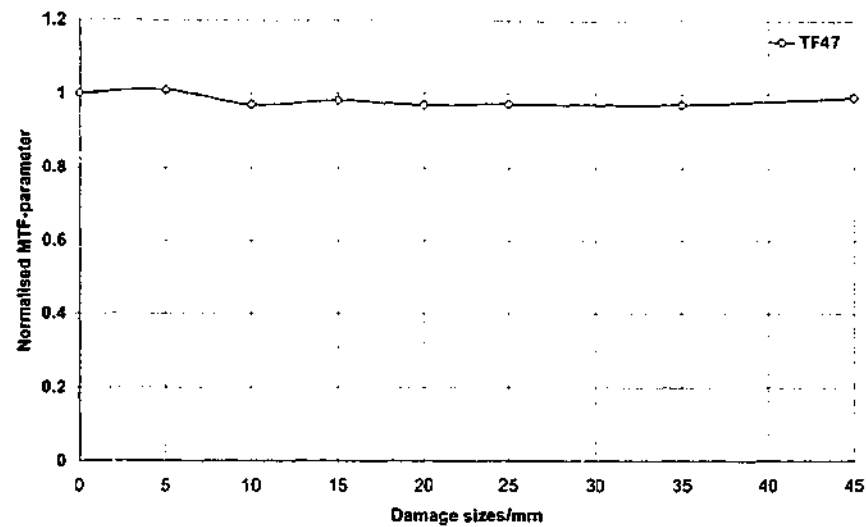


Figure 8.8 Transfer function of signal between sensor PZT 4 and actuator PZT 7 (see Figure 8.6)

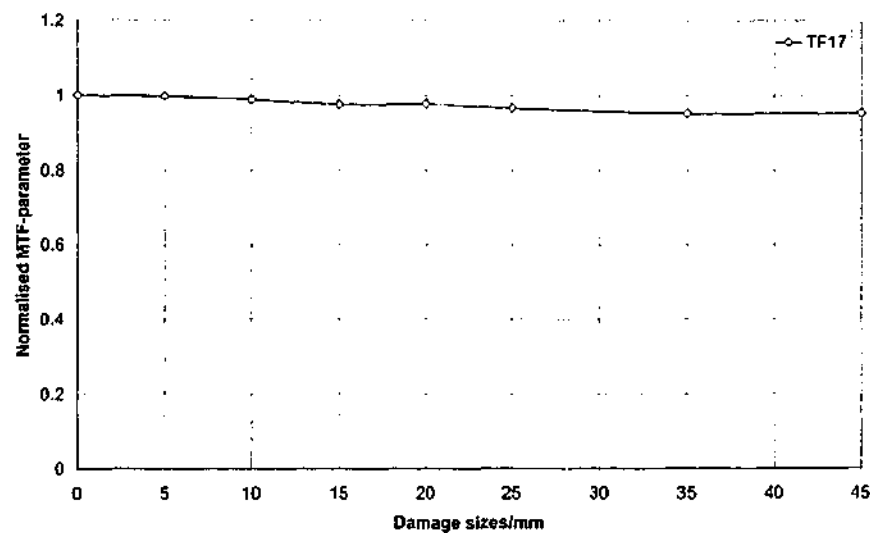


Figure 8.9 Transfer function signal between sensor PZT 1 and actuator PZT 7 (see Figure 8.6)

The graph of the transfer function for TF47 is similar to that for TF17. This is expected, as both transfer function combinations had piezoceramics that were located at a distance from the damage area. The slight increments or decrements in the MTF-parameter are largely random in nature and not indicative of any damage conditions.

Figure 8.10 shows a specimen with a damage size of $25 \times 25\text{-mm}^2$ highlighted by black colour liquid penetrant. The disbond was made to grow from the corner of the patch and the blade insertion was both in the x-direction and y-direction. Here piezoelectric-8 was used as an actuator and piezoelectric-2 was used as a sensor. The transfer function for TF28 is shown in Figure 8.11. As can be seen in the figure the MTF-parameter declines from the undamaged condition and continues to decrease with progressive damage up to the disbond size of $35 \times 25\text{-mm}^2$. With the final disbond area greater than the distance of the sensor and actuator, the MTF-parameter is 12% higher than the MTF-parameter for the undamaged condition.

The result of interest in this investigation is the change in the MTF-parameter as the disbond approaches the piezoelectric that is used as the sensor. It was expected that the MTF-parameter would progressively decrease from the undamaged condition with increasing damage growth until the damage had grown beyond the actuator as well. When the damage area developed beyond the distant of both the sensor piezoelectric-2 and the actuator piezoelectric-8, the MTF-parameter would increase above the MTF-parameter of the undamaged specimen. These expected results are based on the numerical analysis and the mathematical model reported in Chapter 6.

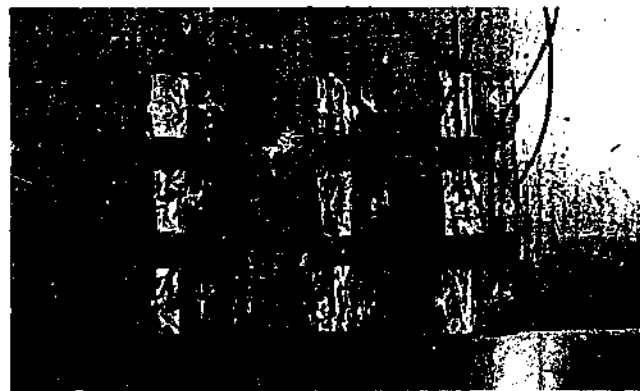


Figure 8.10 Specimen with the black colour liquid penetrant highlighting damage size of $25 \times 25\text{-mm}^2$

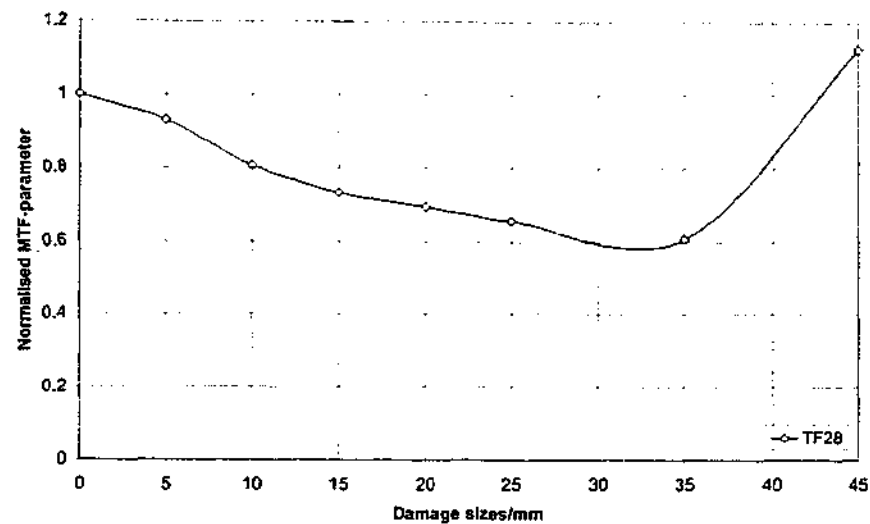


Figure 8.11 Transfer function between sensor PZT2 and actuator PZT8 (see Figure 8.6)

A similar trend to that noted for TF28 is observed for TF58 for advanced disbond sizes. A repetition of the increment in MTF-parameter occurs for the final disbond size in both cases. The decrement in MTF-parameter for the case of TF58 occurs when the damage penetrates the damage detectable zone, which in this case was $15 \times 15\text{-mm}^2$. This damage case was reflected by a decrease of 11% in the MTF-parameter.

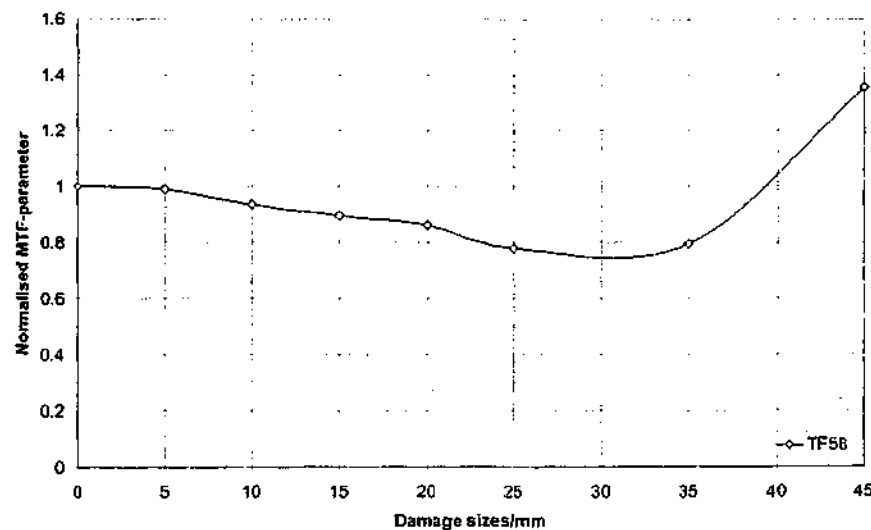


Figure 8.12 Transfer function between sensor PZT 5 and actuator PZT 8 (see Figure 8.6)

With results obtained from the PZTs located on the first and second rows of the matrix agreeing with the observations derived from the numerical results, for completeness, transfer function spectrums were obtained from sensors and actuators in the third row. Figure 8.13 shows a specimen with a damage size of $45 \times 25\text{-mm}^2$ highlighted by black colour liquid penetrant where the actuator piezoelectric-9 interrogated was located at a distance from the initial disbond.

Results obtained when piezoelectric-9 was used as an actuator and piezoelectric-6 was used as a sensor are presented in Figure 8.14. As can be seen, the magnitude of the transfer function integral decreased with increasing damage sizes. This gradual decrease is associated with the proportional decrease in stiffness of the composite patch with the propagating disbond growth. The decrease in the magnitude of the transfer function was observed up to the damage size of $35 \times 25\text{-mm}^2$. When the disbond size was $45 \times 25\text{-mm}^2$ the magnitude of the transfer function increased by 30%. This increase was caused by the decrease in the local area stiffness of the composite patch onto which the actuator was bonded.

Based on the mathematical model presented when the disbond had developed past both the sensor piezoelectric-6 and the actuator piezoelectric-9, it was expected that the MTF-parameter for the damage case would increase past the MTF-parameter of the undamaged case. This increase agrees with results from the numerical simulations presented in Chapter 6.

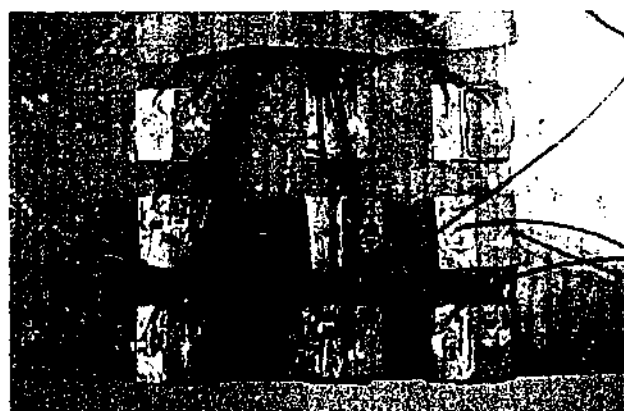


Figure 8.13 Specimen with the black colour liquid penetrant highlighting damage size of $45 \times 25\text{-mm}^2$

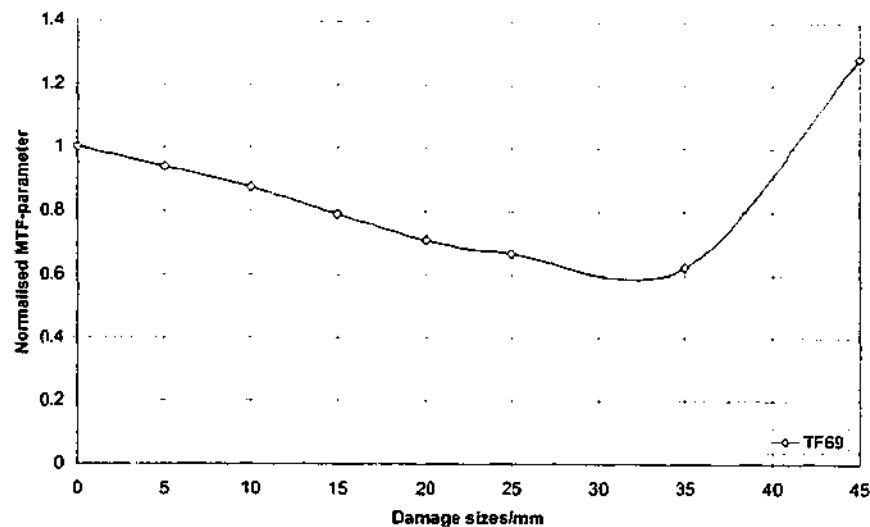


Figure 8.14 Transfer function between sensor PZT 6 and actuator PZT 9 (see Figure 8.6)

In summary, these results presented show excellent agreement with the mathematical model in section 7.2.2 of Chapter 7 and the findings made from the boron/epoxy composite patch static experiment reported in section 8.3. Those figures that show the specimens with the blade inserted and liquid penetrant provide clear indication of the disbond extent underneath the FRP composite patch. The following findings agree with those reported in section 8.3:

- The transfer function of a pair of sensor and actuator decreases with an increase in the disbond size in the composite repair.
- This decrease in the transfer function is obtained as long as a sensor or an actuator is located on the damage zone.
- The location of both the sensor and actuator on the aluminium substrate is not likely to provide any information on the size of the disbond.

Thus, the transfer function method is able to detect the location, type and extent of a prescribed damage when the piezoelectric actuator and sensor are strategically positioned.

8.5 FATIGUE TESTING

The experimental procedures used are similar to those in the static testing since the resolution and accuracy of the method had been established. The results will show the robustness of the transfer function method as well as the applicability of the sensors/actuators during active service.

8.5.1 EXPERIMENTAL PROCEDURES

Figure 8.15 shows a schematic drawing of the first of two specimens considered in this study. The detailed description on the preparation of the specimen can be found in section 3.6.2 of Chapter 3 Experimental method. This specimen, referred to as DD2, was dynamically loaded to simulate active service. On Side P, three PZT elements were bonded on to the specimen and they were labelled as PP1, PP2 and PP3 respectively. On Side S, another three PZT elements were bonded on to the specimen and they were labelled as SP1, SP2 and SP3 respectively. Strain gauges were attached at six different locations. On Side S, they were labelled as S1, S2 and S3; while on Side P, they were labelled as P1, P2 and P3. The transfer function method was applied to all three PZT elements on Side P: PP1, PP2 and PP3. During the experiments the disbond on Side P was monitored using the transfer function method. In addition, the disbond on Side P and Side S were both monitored using strain gauges.

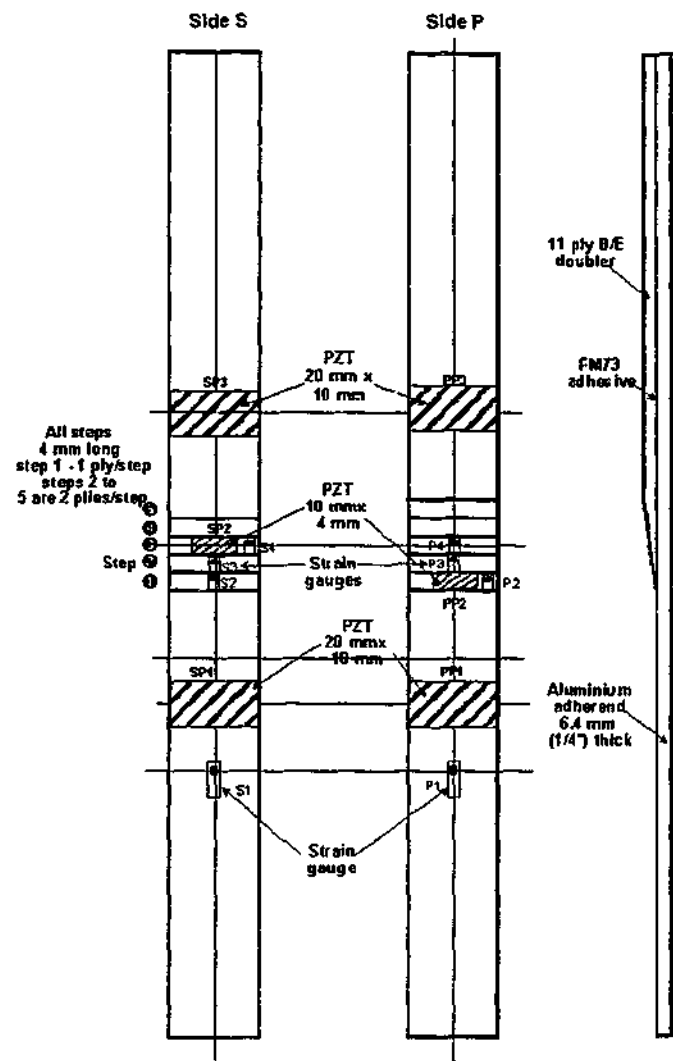


Figure 8.15 Schematic drawing of the DD2 specimen used for the transfer function method

Figures 8.16 and 8.17 show a schematic drawing of the second specimen, TTCP2. TTCP2 was also dynamically loaded in the same way as DD2, to simulate active service. Seven PZT elements (each $5 \times 10\text{-mm}^2$ in size) were bonded on seven different locations but only two of the PZT elements were used for the transfer function method in the experiments. The remainder PZT elements were used for other methods, which include the impedance method. The two used were BPZT1 and BPZT3. Strain gauges were attached at four different locations and were labelled B1, B2, B3 and B4. During the experiments the disbond on Side B was monitored using the transfer function method as well as four strain gauges.

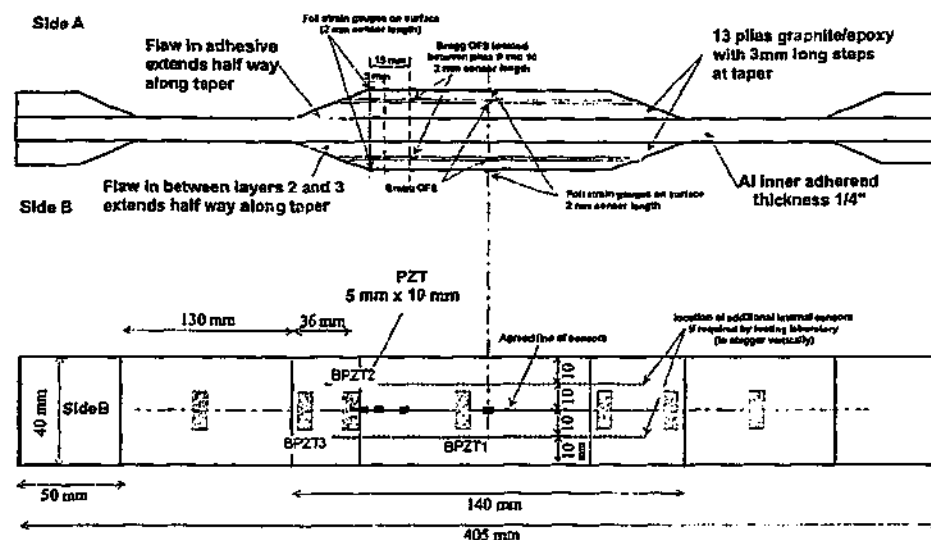


Figure 8.16 Specimen TTCP2 used for verification of both methods

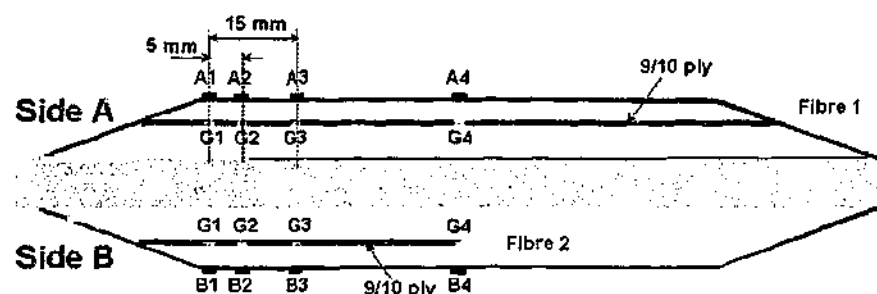


Figure 8.17 Location of strain gauges on the TTCP2 specimen

8.5.2 RESULTS AND DISCUSSION

The transfer function method was applied to the six 'possible' different combinations of actuator/sensor combinations involving elements PP1, PP2 and PP3. However only three combinations were considered as it was assumed that the transfer function is not directional. These combinations are TF12 (PP1 actuator, PP2 sensor), TF32 (PP3 actuator, PP2 sensor) and TF31 (PP3 actuator, PP1 sensor).

Figure 8.18 shows a decrease in MTF-parameter with the onset of disbond. As can be seen in the figure, the number of cycles to the predicted disbond is similar to that shown in Figure 6.16 of Chapter 6 that was obtained by using the impedance measurements over sensor PP2. There is a relatively steady phase up to 200-kcycles

and then in response to an increase in the applied load to 20-kN, there is a systematic reduction in signal with further loading cycles. It is interesting to note that although the change in mean level associated with disbond growth is much higher in the case of the transfer function measurement (about 40% compared to 4% for the impedance measurement), the coefficient of variation, or the ratio of systematic change to the level of noise of 5-dB as shown in Figure 8.19, is similar. This suggests that the transfer function method has no real advantage in terms of sensitivity to damage compared to the impedance method despite the use of an additional piezotransducer element. This is not unexpected, however, as disbond growth occurred in close proximity to sensor PP2 which represents a favourable condition for the impedance approach. It is expected that if damage growth occurred further away from PP2 it is likely that the transfer function approach would outperform the impedance method.

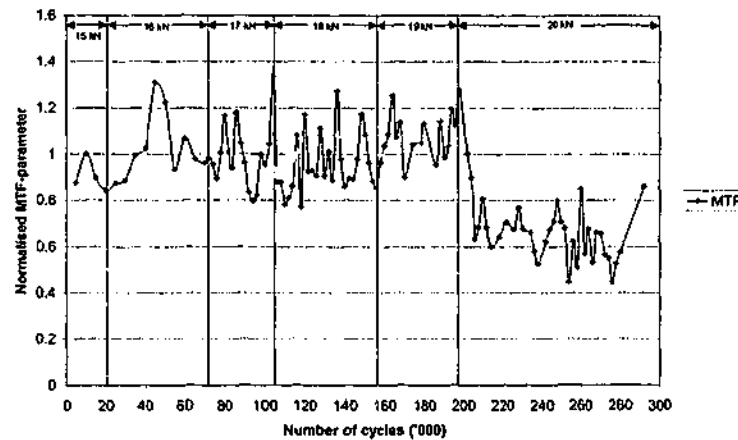


Figure 8.18 Transfer function between actuator PP3 and sensor PP2

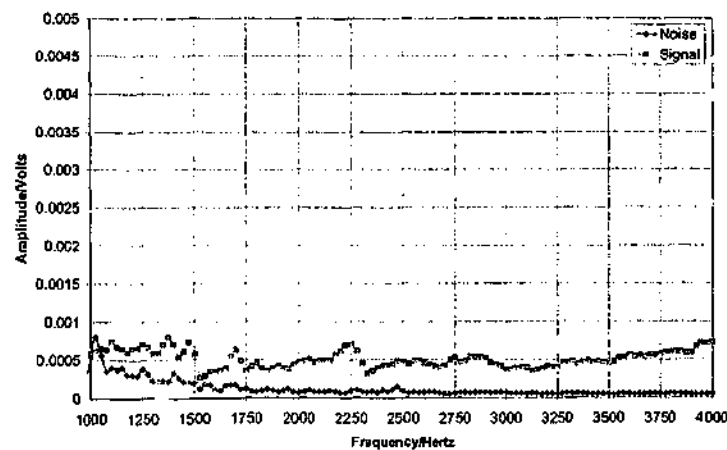


Figure 8.19 Signal-to-noise graph

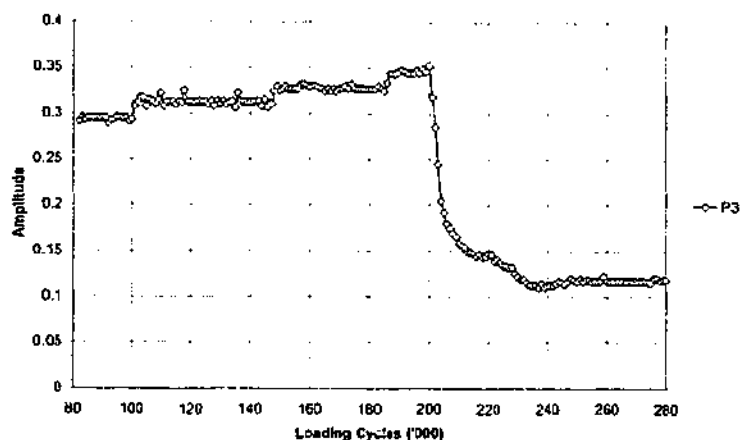


Figure 8.20 Strain gauge reading taken from edge of repair patch taper, P3

The progression of disbond growth inferred from the transfer function measurements is broadly consistent with the strain gauge readings shown in Figure 8.20. The strain gauge readings in Figure 8.20 show a decrease in the strain amplitude, which is expected to correspond to initial growth of the disbond.

The response shown in Figure 8.21 is for case TF12. At around the 200th kcycle, a similar decline to that noted for TF32 is observed. Beyond this initial decline, the behaviour is noticeably different. At about the 230th kcycle, the MTF-parameter increases. The rather high levels of noise evident in the response means that it is possible the increase is an artefact rather than a result of changed structural dynamics. However, subsequent finite element analysis indicates the likelihood that this increase could be attributed to a shift in the frequency spectrum caused by disbond growth.

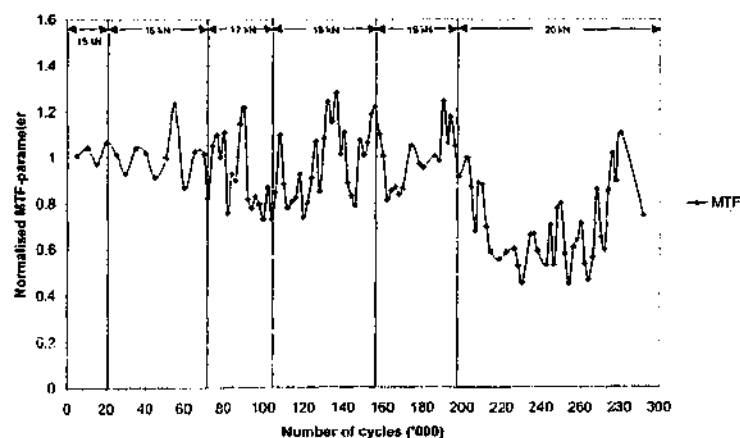


Figure 8.21 Transfer function of actuator PP1 and sensor PP2

Specifically, a finite element analysis was performed to identify changes in the transfer function with disbond growth that might explain the increase in the MTF-parameter. A schematic of the modelled geometry showing placement of the piezoelectric transducers in relation to the disbond is shown in Figures 8.22 and 8.23. As indicated, the disbond was located at the top right corner, in close proximity to sensor PP2. Seven disbond lengths were considered, ranging from 0-mm to 12-mm in 2-mm increments. The MTF-parameter can increase either due to resonant frequency shifting into the region of analysis or an increase in the overall strain energy in the response. Figure 8.24 shows the effect of disbond growth on the transfer function across the range of frequencies. It indicates a downward shift in the resonant frequency (to 3,050 Hz) at a disbond length of 12-mm, which causes an increase in response amplitude over a narrow range of frequencies below resonance. Given that the experimental work encompasses part of the affected frequency range, this shift provides at least a part explanation for the increase in response shown in Figure 8.21.

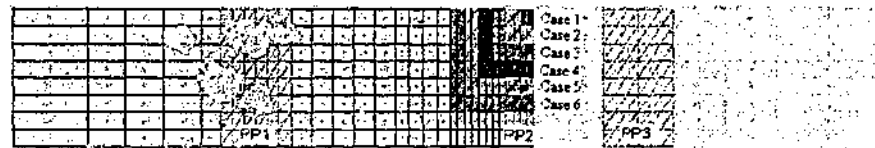


Figure 8.22 Top view schematic of the finite element modelled specimen



Figure 8.23 Side view schematic of the finite element modelled specimen

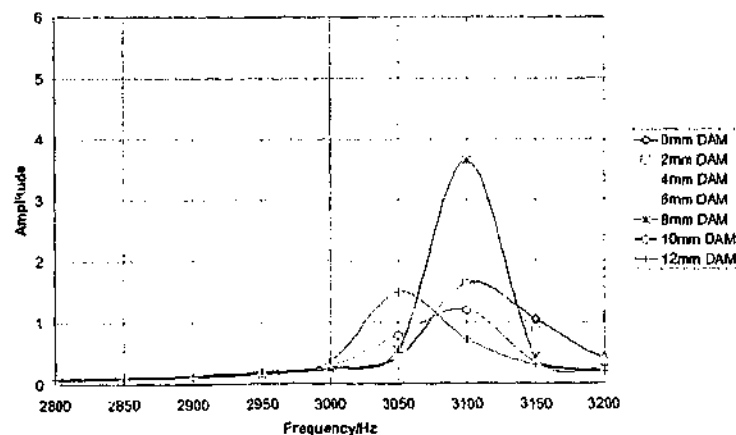


Figure 8.24 Transfer function between actuator PP1 and PP2

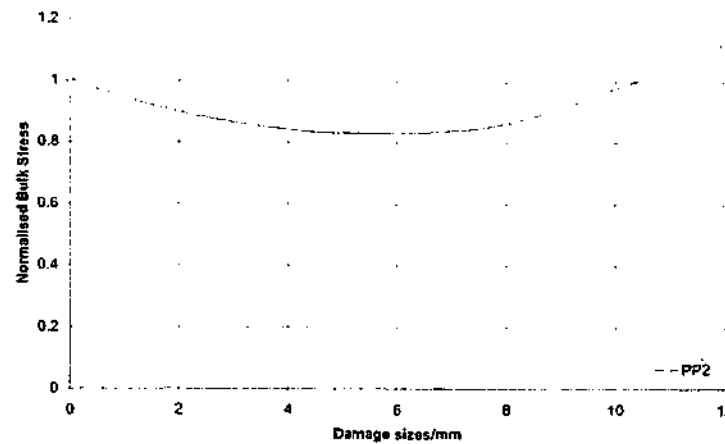


Figure 8.25 Variation of integrated bulk stress with damage

To verify if the increase in the MTF-parameter could also be partly due to the increase in volumetric strain in the response, the integrated bulk stress across PP2 was obtained with varying damage sizes and the results are shown in Figure 8.25. The integrated bulk stress was calculated from the sum of the principal stresses at each piezoelectric node under PP2. The increase in the volumetric strain is indicative of the change in mode shape as the resonant frequency shifted to the left of the frequency x -axis. Therefore in summary, the increase in the MTF-parameter is due to the effect of the leakage from the downward frequency shift.

Another possibility discounted with the increase in MTF-parameter with damage growth, was the degradation of the PZT. As observed in Chapter 3 Experimental methods, degradation of the PZT led to the decrease of the transfer function measurement. In this experiment, the MTF-parameter increases with damage growth.

Figure 8.26 shows the response for configuration TF31, which as indicated by Figure 8.15, excludes the zone of disbond growth. As expected the response is comprised of largely random fluctuations. Interestingly, the SNR level for the signal is similar to that recorded in the pre-disbond growth phase for configurations TF12 and TF32, which suggests a common noise source, possibly in the instrumentation.

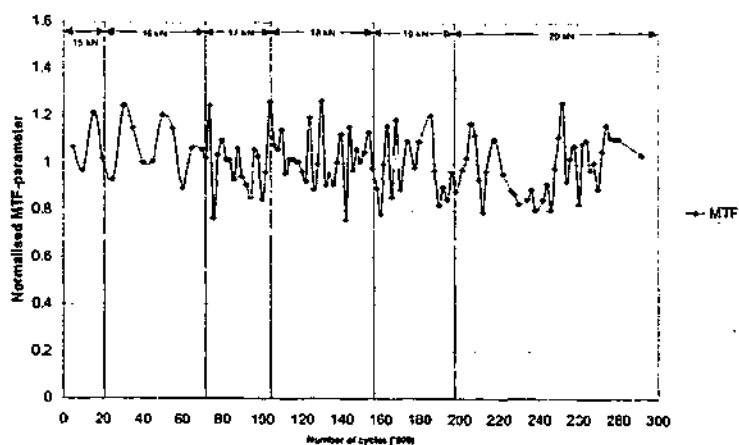


Figure 8.26 Transfer Function of Control Group Actuator PP3 and Sensor PP1

The findings from the transfer function experiment that were also made in the complimentary numerical analysis in Chapter 7: -

- For the particular specimen configuration considered, a disbond growing under either the sensor or actuator lead to a systematic decline in the MTF-parameter,
- Disbond growth beyond either sensor or actuator but between the sensor and actuator pair leads to a slight incline in the MTF-parameter,
- Growth beyond both sensor and actuator leads to an increase in the MTF-parameter greater than the initial MTF-parameter recorded.

Results from the TTCP2 specimen also exhibit this behaviour. Figure 8.27 shows the evolution of the MTF-parameter obtained from sensor BPZT3 located on the edge of the repair patch taper with actuation supplied in the far field of the repair patch by BPZT1. Unlike DD2, TTCP2 was manufactured with a Teflon strip in the adhesive bond extending half the length of the taper (see Figure 8.16), to promote disbond growth below BPZT3. It is interesting to compare the MTF-parameter response with the equivalent for DD2 (Figure 8.18). These appear distinctly different, which probably stems from the much larger initial flaw size in TTCP2, which precludes a stage of disbond growth beneath the sensor footprint, which in the case of DD2 led to a reduction in the MTF. It is notable that a change in the MTF-parameter is observed at around 700 keycycles, which roughly accords with the change in strain readings

shown in Figure 8.28 as well as the change in the ultrasonic A-scans shown in Figure 8.29.

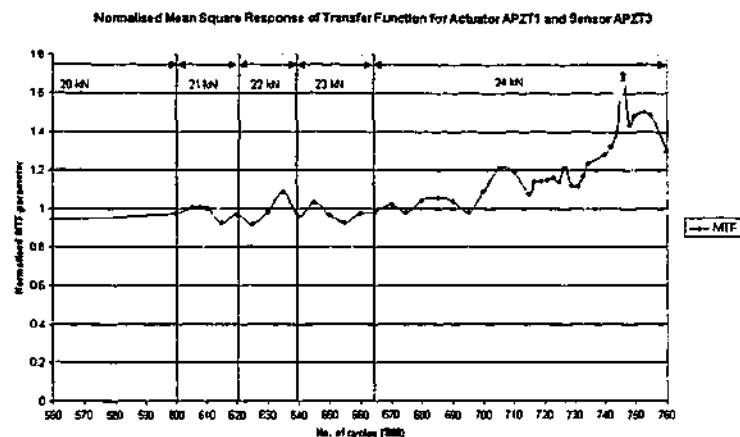


Figure 8.27 Second Specimen, Actuator on BPZT1 and Sensor BPZT3

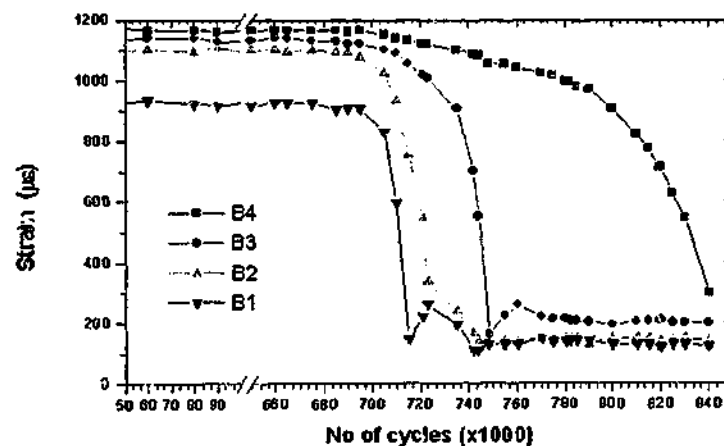


Figure 8.28 Variation of surface strains (side B) with loading cycles

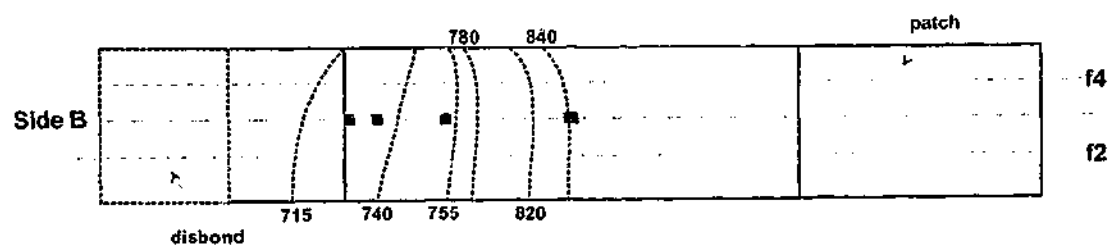


Figure 8.29 Ultrasonic A-scans of disbond on side B

Another interesting aspect of the comparison between Figures 8.27 and 8.18 is that the absolute change in response observed for TTCP2 is about 50% smaller than that for DD2. It is not possible to relate the difference in measurement to the thickness of the composite patch thickness given that the TTCP2 specimen had started off from a different reference level due to the Teflon insert. The extent of disbond growth/structural change is presumably greater for the DD2 specimen than for the TTCP2, so a difference is expected from that itself. However from Table 8.2 it can be seen that the transfer function method is more sensitive by approximately 6.5 times. With both specimens the percentage change is about the same by using the same PZT transducer as the sensor.

Table 8.2 Relationship between composite thickness and sensitivity

	13-ply G/E Composite		11-ply B/E Composite	
	Impedance Method	Transfer Function Method	Impedance Method	Transfer Function Method
Percentage Change with Damage	-3.9%	-25.33%	-5.5%	-38.46%

Negative percentage change is due to a decrease in the MTF-parameter as the disbond grows. To obtain the results shown in Table 8.2, the actuator was located on the far field boron/epoxy repair patch (PP3 or BPZT1) and the sensor was located on the edge of the repair patch taper (PP2 or BPZT3).

It is instructive to consider the possible sources of noise in the experiments.

- The interval between readings, which is 2,000 cycles, might lead to a large systematic change in response. Progressive disbond growth might be reflected as a drastic change in the measured parameter.
- The existence of a spew fillet of the adhesive at the edge of the repair patch taper is a systematic error. This error is synchronous with the loading frequency before the onset of disbond.

- The high capacitive nature of the PZT elements makes them susceptible to electrical noise and surrounding environmental noise. The length of the leads and wirings also introduce systematic error to the impedance measurements.
- The 50-Hz mains noise is the main source of noise. Effects of the leakage can be felt up to 750-Hz. In analysing the mean square response, the leakage will have an impact on the large fluctuations.

8.6 CONCLUSIONS

The transfer function approach offers an effective non-destructive technique for locating disbonds in a layered structure. Some of the advantages of this technique are:

- It provides cost-effective distributed actuation/sensing technology towards the development of smart composites;
- It enhances the inspectability of composites and provides a new technology for improved material diagnostics;
- It can be implemented for real-time in-situ health monitoring or for in-production quality control.

The experimental results described above show that surface mounted PZT elements can be used to predict the type and extent of disbond under the repair patches. This set of experiments shows that the transfer function method is consistent and robust when the specimen is undergoing cyclical loading, and therefore this method is practical for real-time application on board aircrafts. However the sensitivity of the method is dependent on the thickness of the composite, which reduces their attractiveness. In addition the method is highly reliant on the placement of the PZT elements within the likely disbond initiation area. That said the transfer function method has the advantage over strain gauges as it continuously monitors the growth of disbond within the sensitivity footprint of the PZT element and the sensor and actuator combination.

CHAPTER 9

EVALUATION OF THE STRESS WAVE METHOD USING NUMERICAL ANALYSIS

9.1 INTRODUCTION

The preceding four chapters have evaluated the potential of two low frequency methods for the detection of disbond in a bonded repair. This chapter will present the evaluation of the stress wave method as a high frequency method for the inspection of adhesively bonded composite joint. Bonded composite joints are in ever increasing use in critical applications such as those found in the aeronautical and aerospace industries. Elastic stress waves, which could be transmitted from one location to another on a plate, appear to offer the potential for cheap and convenient in-situ inspection.

The background theory and analytical procedures required by the stress wave method are presented in Section 9.2. A comparison is made between the high frequency method and the low frequency methods. The broader sensitivity range of the stress wave method may provide a better basis than the low frequency methods for the quantitative assessment of disbond growth.

Two distinct applications of the stress wave method are evaluated using numerical analysis. The first preliminary simulation study was to evaluate the suitability of stress wave method for the detection of impact damage on a composite plate of constant thickness and it is presented in Section 9.3. The preliminary study was necessary to provide the understanding for the more complex composite bonded aluminium structure. The type of impact damage considered in this investigation is delamination between plies and barely visible impact damage (BVID). The results obtained using the stress wave method are presented and the application of the method to monitor the damage size is discussed.

In Section 9.4, the second study presents an evaluation on the suitability of stress wave method for the detection of disbond growth under a composite repair patch. This problem is considered more complex, as the structure has varying thickness at the repair patch taper. The results obtained using the stress wave method are presented and the application of the method to monitor the disbond growth is discussed.

9.2 BACKGROUND THEORY AND ANALYSIS

Sir Horace Lamb (1916) proposed the existence of Lamb waves and these waves are now known to be able to travel in plate sections that are so thin that it is difficult to resolve the waves by the more conventional testing procedures. The velocity with which each mode propagates in a given plate can be calculated from Lamb's equations as a function of frequency, plate thickness and material. Lamb wave methods are attractive because the substrate with a composite bonded can be used as wave-guides along which ultrasonic waves can be propagated between interrogating transducers.

Many studies over the years have recognised the potential of Lamb waves in the NDE of metallic structures (Workton, 1957; Alleyne and Cawley, 1992; Rokhlin and Bendec, 1983). Most work has focused on the use of the 'null zone' technique, which enables the Lamb wave dispersion behaviour in a localised region of the structure to be measured. A large region can be interrogated for each transducer position. In Lamb

wave propagation, the vibration patterns through the thickness of the plate are quite different for different Lamb wave modes and are different even for the same mode at different frequencies. Conventional time domain methods of measuring amplitudes and velocities of transient response generally require minimal signal processing and are often the easiest to apply. If the time history of a wave packet consisting of a single mode can be resolved separately from other wave packets then attenuation can be used as a form of measurement.

There have been many studies done on the propagation of Lamb waves on composites and composite structures including the following studies, which are closely related to the present topic. Chimenti and Martin (1991) and Cheng and Berthelot (1996) studied the application of Lamb waves to detect defects in composite plates. Bork and Challis (1995), Rokhlin (1991) and Todd and Challis (1999) investigated the propagation of Lamb waves through bonded joints. Bork and Challis (1995) found that broadband excitation of Lamb waves is the best approach for the evaluation of the adhesive fillet size in a T-peel joint. Rokhlin (1991) studied the interaction of different Lamb modes with disbonds in adhesive joints in which plates of equal thickness are joined by a layer of adhesive. Rokhlin and Bendec (1983) investigated the transmission of Lamb waves through a welded joint connecting two elastic layers. The transmission coefficient was used to estimate the dimension of the contact region, which is an important parameter for evaluating the strength of a welded joint.

Lamb waves can be excited by a variety of methods just like bulk waves, though it is preferable to excite only the modes that are likely to be most informative in from a NDE standpoint. In Alleyne and Cawley's (1994) experiment, they excited a particular mode of Lamb wave using piezoelectric transducers by employing a variable angle probe. The variable angle, the constant emission point and the broadband transducer used during the experimental investigation are shown in Figure 9.1. The experimental set-up incorporates a damping wedge at the front of the probe body to attenuate the face reflection from the base of the transducer body. These probes are bulky and can only be used on structures that are easily accessible.

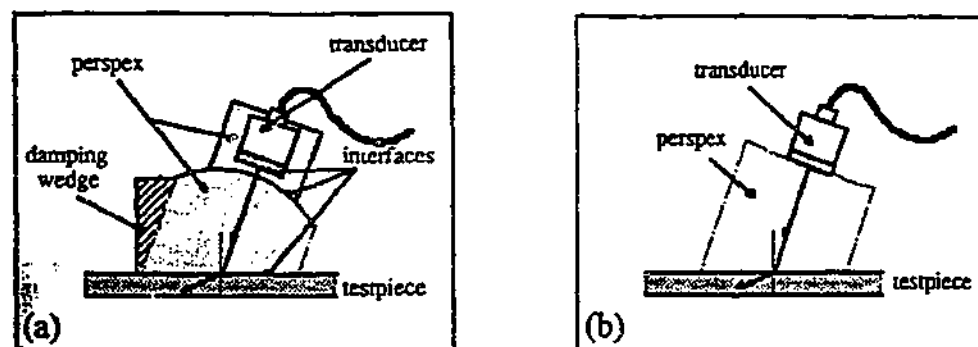


Figure 9.1 Probes used in experiments to excite Lamb waves

9.2.1 DATA ANALYSIS

The main focus of the investigation was to determine whether surface-mounted piezoelectric sensors, comprising monolithic lead-zirconate-titanate (PZT) wafers, could be used for in-situ monitoring of structural condition since it is not easy to use these PZT elements to excite and receive the pure modes reported by Alleyne and Cawley (1994). Alleyne and Cawley (1994) used a variety of probes to detect the existence of various modes in their test plates.

The excitation of elastic stress waves is relatively straightforward given the broadband frequency response characteristic of piezoelectric materials. In this investigation, the approach was to excite elastic stress waves in the host by applying a modulated sine wave toneburst to a piezoelectric element surface mounted to the metal substrate some distance from the damage zone. Excitation of stress waves using side nodes of the plate was also used and the different waveforms were compared.

The first task with any technique involving Lamb waves is to decide on appropriate regimes on the dispersion curves for exciting the required Lamb modes. Two ideal regimes are:

1. a single mode should be excited, in order to limit the complexity of the received signals;
2. the choice of frequency should be such that the wave is relatively non-dispersive, so that signal shapes are retained as the wave packet propagates.

Alleyne and Cawley (1991) showed that the frequencies and wave numbers of positions on the ridge of a mode in the two-dimensional Fourier transformation (2D-FFT) plot corresponds to locations on the dispersion curve for the mode, and that the amplitude of the plot at any of these positions may be used to determine transmission or reflection coefficients at the given frequency-wave number. Provided that the 2D-FFT is applied in the same manner to both the received and the incident modes, the coefficient is thus given by the ratio of the 2D-FFT amplitudes in the two signals. The conditions of validity require that certain aspects are identical for both the measured and the reference signals, including the thickness and material of the plates, the component which is monitored, the mode, and the processing parameters and windows which are used for the 2D-FFT. For a given mode and frequency, the power flow of the mode is proportional to the square of its amplitude (Auld, 1990), the constant of proportionality being a function of the mode, the properties of the plate, the frequency, and the choice of the component which is used to define its amplitude. Given the above conditions, which are placed on the 2D-FFT calculations, the constant of proportionality is the same for both the incident and the received signal at any chosen frequency. In this case the square of the transmission coefficient at that frequency may therefore be identified as the power transmission coefficient.

A conventional approach for determining a transmission coefficient for a mode is to measure the amplitude of a particular component of displacement in the receiver plate, at a particular frequency, and then divide this by the amplitude of the corresponding component in the transmitter plate. Such an approach yields a transmission coefficient for any chosen frequency within the bandwidth of the signal. However, as seen in the 2D-FFT plot, the received amplitude of a mode varies dramatically with frequency because of the interference between the directly transmitted signal and the reverberating signal. The frequency values associated with the interference extrema in the spectrum may in fact be useful for the characterisation of the joint, and indeed Todd and Challis (1999) found that these features are particularly important in the successful operation of an artificial neural network scheme for estimating the bond dimensions from Lamb wave signals that have transversed a joint. However in the present work we are interested in determining a single scalar measure of the strength of transmission, without sensitivity to a precise chosen value of the frequency. We

therefore prefer a measure that depends on the whole spectrum of the signal rather than a single frequency.

A simple procedure for calculating a scalar measure of transmission over the full spectrum of the signal is the sum values over the area of the 2D-FFT plot, which represents the received signal. Results of one the simulations taken from a report by Lowe et al (2000), for the s_0 mode and a joint with 2-mm bond length and 0.2-mm bond thickness, are shown in Figure 9.2. The figure shows a signal received after the modulated sine wave has propagated across the joint. Specifically, the plot is a time record of the displacement component in the direction normal to the plate, at one of the finite element nodes on the top surface of the receiver plate.

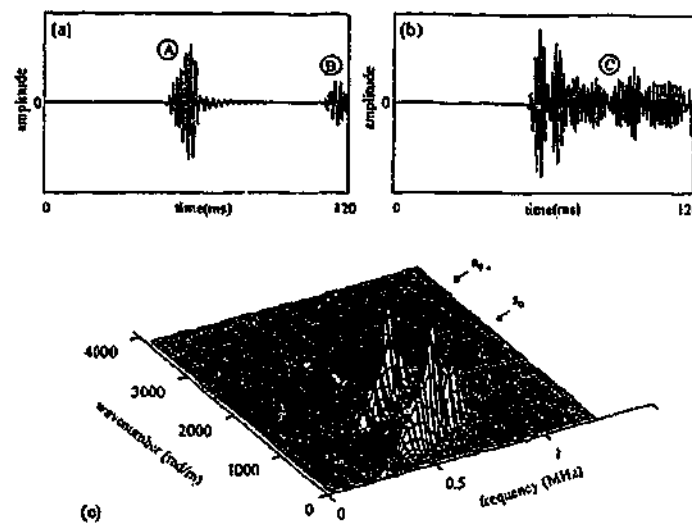


Figure 9.2 Output from Lowe et al (2000)

This received signal is clearly different in shape from the incident windowed tone burst. Lowe et al (2000) identified three phenomena, which could be responsible for this:

1. in general, several possible modes can propagate within the overlap region, interfering with each other and each transmitting power at a different velocity;
2. the modes within the overlap region can reflect as well as transmit at the ends of the overlap at the ends of the overlap, so that they reverberate over the length of the overlap region, emitting power into the receiver plate at each reverberation;
3. both s_0 and a_0 modes can be transmitted into the receiver plate by mode conversion from the modes in the overlap region.

9.3 PRELIMINARY SIMULATION STUDY

A preliminary study was conducted that includes a series of finite element simulations to study in some detail the effects of Lamb wave transmission across a delamination and a region where a change in density exists after impact damage. The latter case is used to model the effects of impact damage on the transmission of Lamb waves. All the finite element modelling was conducted using PAFEC. The program simulates the propagation of the Lamb waves and the interaction of the Lamb waves at the damage area of interest in the time domain. The results obtained from the finite element analysis were processed using the 2D-FFT (Alleyne and Cawley, 1991). The spatial and temporal FFT are used to measure the amplitudes and velocities of the individual Lamb waves.

9.3.1 MODEL DEVELOPMENT

A number of finite element analyses, using a broadband frequency excitation, to predict the transmission coefficient of the dominant mode across a bonded composite repair patch. By repeating the analyses for ranges of bond thickness and bond length, the transmission coefficients can be expressed as a function of these two parameters of the joint. Thus the aim of each finite element analysis was to propagate a broadband excitation in the transmitter plate and to measure the response of the same mode in the receiver plate, expressing the ratio of their strengths as a transmission coefficient.

The two most common composite damage model are considered in this study. The first involves the case of delamination between composite plies. The second considers the reduction of local Young's modulus after impact, which in some cases, is classified as barely visible impact damage. Barely visible impact damage can, be treated as an advanced form of multiple delaminations. In both cases the transmission of Lamb waves through the damage area is investigated using simple signal

processing methods so that future experimental work could be done towards achieving in-situ structural health monitoring with PZTs both as sensor and actuator.

The choice of frequency regime

The main aim of this preliminary study was to determine the effects of local changes in stiffness and delamination in a plate-like structure on the propagation of these Lamb wave modes. To simplify the analysis and the interpretation of the results, the composite laminate was assumed to behave like an isotropic plate with prescribed local changes in stiffness used to simulate impact damage. The elastic properties of aluminium were used in the analysis.

Figure 9.3 shows the dispersion curves for a typical composite laminate, with an eight-ply lay-up $[0]_8$. These dispersion curves are for the propagation in the 0 degree direction; some changes would be seen if propagation in other directions were to be considered. Figure 9.4 shows the dispersion curves for an aluminium plate. At low frequency thickness (less than 1 MHz.mm) both plates are able to support Lamb waves with roughly similar dispersion characteristics.

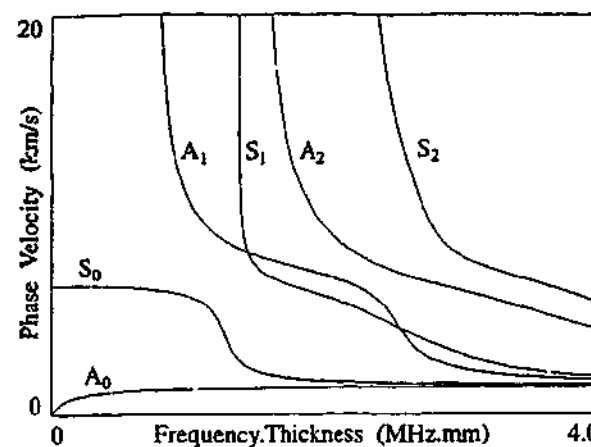


Figure 9.3: Calculated dispersion curve of an 8-ply cross ply laminate

In the work by Alleyne and Cawley (1991), a modulated sine wave was used as an input. In the work presented in this investigation, a broadband excitation was used. This is for the simplicity in implementation in practical applications involving monolithic surface-mounted PZT elements. Also, a broadband input is likely to excite

a dominant mode, the frequency of which can be later used in a more selective excitation.

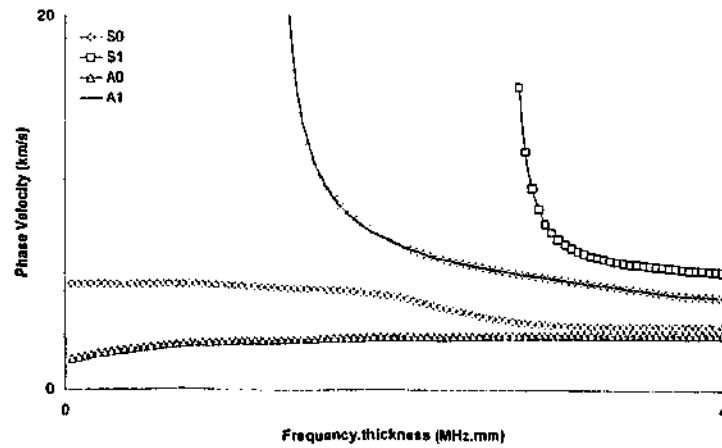


Figure 9.4: The calculated dispersion curves of aluminium plate

In explicit time marching finite-element methods, the duration of the input signal has to be finite. It was understood that the broadband excitation was likely to give rise to a variety of frequencies in the propagating Lamb wave. However, it was expected that a dominant mode would exist. To ascertain which mode of the Lamb wave was excited, the received signals were analysed using a two-dimensional Fourier transform (2D-FFT). This allowed for the decomposition of the signal into its frequency and wave number domains. It was expected that the various mode(s) of the Lamb waves would be evident in these 2D-FFT results. It is difficult to use a single frequency excitation on the PZT when it is bonded on the top surface of the plate. This is because the variation of the excitation in the y-direction at the excitation position cannot be forced into any particular mode shape of the Lamb wave. Additionally, the bottom surface of the plate is not constrained and is free to move. Equations 9.1 and 9.2 from Viktorov (1967) describe the displacement associated with Lamb waves.

$$u_x = Ak_s i \left(\frac{\cosh q_s z}{\sinh q_s d} - \frac{2q_s s_s}{k_s^2 - s_s^2} \frac{\cosh s_s z}{\sinh s_s d} \right) e^{i(k_s x - \omega t)} \quad \text{Equation 9.1}$$

$$w_x = Aq_s \left(\frac{\sinh q_s z}{\sinh q_s d} - \frac{2k_s^2}{k_s^2 + s_s^2} \frac{\sinh s_s z}{\sinh s_s d} \right) e^{i(k_s x - \omega t)} \quad \text{Equation 9.2}$$

where u_x and w_x are the displacements in the x and y directions respectively, z is $\pm d$, d is half the plate thickness, k_s is the wave number of the symmetric wave modes,

$q_s = k_s^2 - k_2^2$, and $s_s^2 = k_s^2 - k_1^2$. Similar relations for the asymmetric modes may be obtained by changing the subscript s to a and replacing \sinh by \cosh and vice versa.

Finite element models of plates

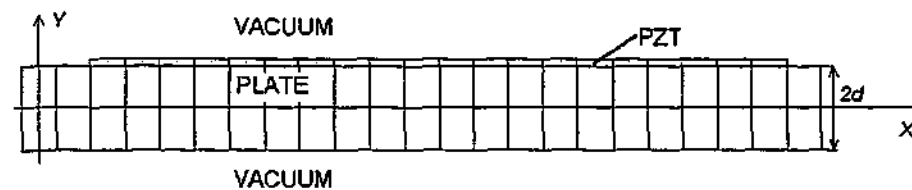


Figure 9.5 Schematic of the FE model showing the PZT transducer bonded on the aluminium host

Figure 9.5 shows a schematic of a small part of the meshed plate configuration with a piezoelectric transducer bonded to the top surface. An elastic disturbance was initiated by applying a single square x-strain pulse of 400-nanoseconds width, equating to a centre frequency of 2.5-MHz. In real impact damage scenarios, the affected area can assume arbitrary geometry, size orientation and position within the plate. However, in the finite-element investigations, only the simple case of straight-sided damage was considered.

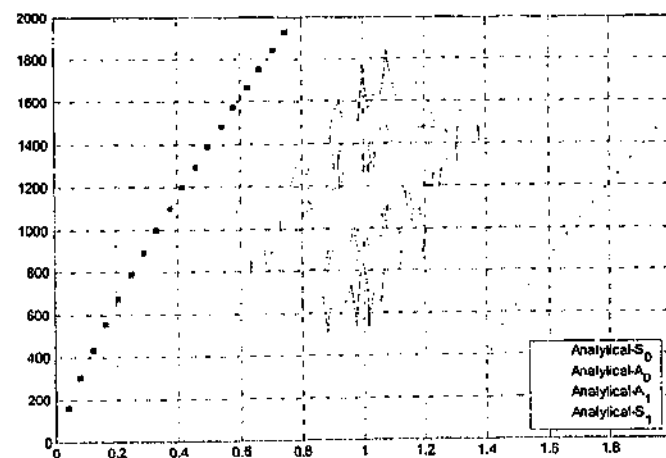


Figure 9.6 A comparison of the finite element predictions with the analytically generated dispersion curves

It was assumed that all the models had plane strain conditions. A uniform square mesh of 8-noded quadrilateral elements with more than 10 nodes per wavelength was

used. An explicit central difference approximation scheme was used by the finite element package to produce the time marching solution. The time step chosen was less than the time taken for the fastest wave to travel between two adjacent nodes. In this simulation the material properties corresponded to an aluminium alloy of grade 7075-T6, with a density of 2770-kg/m^3 , and bulk wave velocities of 6295-m/s and 3099-m/s for the longitudinal and transverse modes respectively. As shown in the results in Figure 9.6, the dominant mode excited in this plate is in the vicinity of $1\text{-MHz}\cdot\text{mm}$. It is to be noted that at frequency-thickness values below $1\text{-MHz}\cdot\text{mm}$, both aluminium and composite plates show similar characteristics in supporting only the fundamental symmetric and asymmetric modes.

The length of the plate used in the simulation of delamination-type damage was 160-mm long. A delamination was modelled with a 15-mm long slit 3-mm from the top surface of the isotropic plate.

Barely visible impact damage causes change in the local stiffness since the local region is damaged and delaminated after impact. This is independent of the impactor size but dependent upon the velocity of the impactor. By repeating simulations of BVID-type damage for a range of Young's modulus, E , as shown in Table 9.1, different intensities of impact damage were, in effect, considered.

Excitation of Lamb waves

Lamb waves were excited by subjecting the piezoelectric transducer to the excitation regime described above. In order to be able to predict Lamb wave propagation for a given mode, it is necessary to separate the multimode components in the received signal. This is facilitated by the fact that the group velocity of a_0 is significantly slower than s_0 . Accordingly, only that part of the time domain signal containing the s_0 contribution was considered.

Table 9.1 The type of impact size and intensity considered

	4-mm Damage	8-mm Damage	12-mm Damage
Low velocity	$0.9 \cdot E$	$0.9 \cdot E$	$0.9 \cdot E$
Medium velocity	$0.7 \cdot E$	$0.7 \cdot E$	$0.7 \cdot E$
High velocity	$0.5 \cdot E$	$0.5 \cdot E$	$0.5 \cdot E$

9.3.2 RESULTS AND DISCUSSION

Delamination-type damage

In the frequency-thickness region of interest in this investigation, the mode shapes of a_0 and s_0 are essentially those of flexural and extensional waves respectively. The finite-element model was 160-mm long and 1.6-mm thick. The spatial sampling interval was 0.5-mm and the sampling frequency was 20-MHz. To simplify efficient reduction of the data by Fourier transform, 1024 points were used in the time domain while 128 points was used in the spatial domain.

Figure 9.7 shows the comparison of the analytical phase velocity dispersion curve and the results from a 2D-FFT of the time histories obtained from finite element analysis. This result shows that a fundamental symmetric mode, s_0 is produced by the broadband excitation. There is a fundamental asymmetric mode that is due to the reflection from the defect (i.e. delamination). This is consistent with the findings of Guo and Cawley (1994).

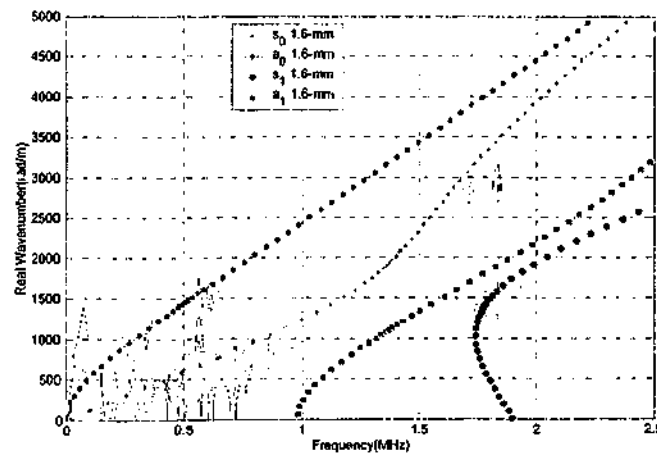


Figure 9.7 2D-FFT of the time history before the delamination zone

Figure 9.8 shows the result of a 2-D FFT on the time histories on the nodal positions above the delamination. It shows that there will be two sets of dispersion curves. The first group corresponds to the overall thickness of the plate while the second group corresponds to the thickness of the delaminated layer. These results suggest that it may be possible to quantify the depth of delamination from the surface by the

comparison of the dispersion curves with different plate thickness with the same Young's modulus.

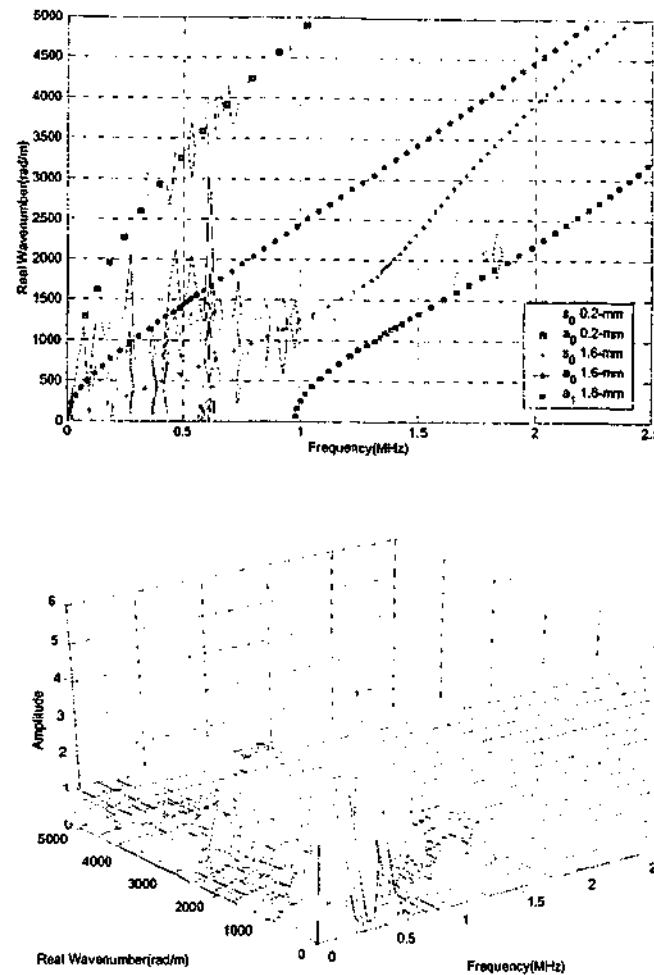


Figure 9.8 2D-FFT of the time history above the delamination zone

Figure 9.9 shows the graph obtained from Fourier transform of time histories taken from positions after the delamination. There appears to be an a_0 mode present in the time series. This is because the FFT was performed over the entire time series, which has included the reflected waves from the end of the test plate. However, the fundamental symmetric mode, s_0 dominates, which is similar to the results taken from positions before the delamination. Figure 9.10 shows the results where only a portion of the time history was analysed. The time history analysed in Figure 9.10 was such that the reflected waves will not be present in the time history of interest. This gated time series show that the incident Lamb wave, after propagating past the delamination, is essentially a pure s_0 mode.

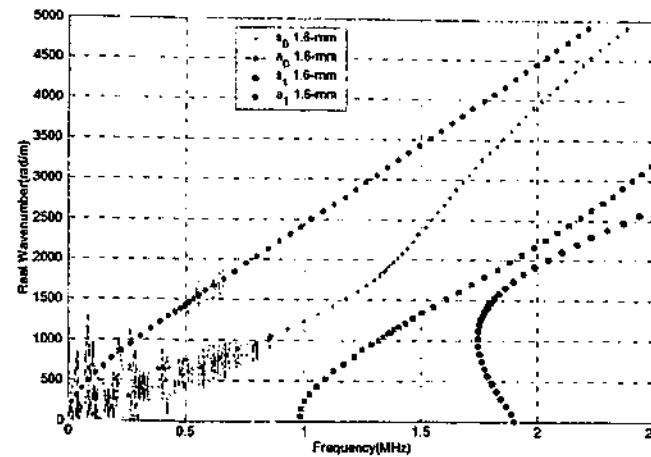


Figure 9.9 2D-FFT of the time history after the delamination zone

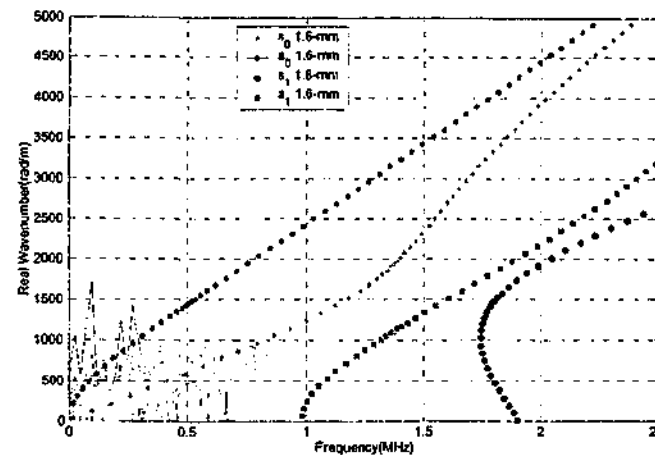


Figure 9.10 2D-FFT of the time history after the delamination zone with gating procedure

Two additional numerical analyses were conducted with the location of delamination at different depths from the surface. The choice of delamination depth was to provide results to confirm the results already obtained using the initial model, which are shown in Figures 9.7 to 9.10. The depth of the delamination used in that model was 0.2-mm from the surface of a 1.6-mm thick aluminium structure, which equated to 12.5% of the overall model thickness.

The models in the two additional numerical analyses had an overall model thickness of 1-mm. One of these models had a delamination at 0.25-mm from the surface which

was 25% of the overall thickness and the results obtained was analysed using the 2D-FFT. They are shown in Figure 9.11. The other model had a delamination at 0.375-mm from the surface which was 37.5% of the overall thickness and the results obtained was analysed using the 2D-FFT as well. They are shown in Figure 9.12.

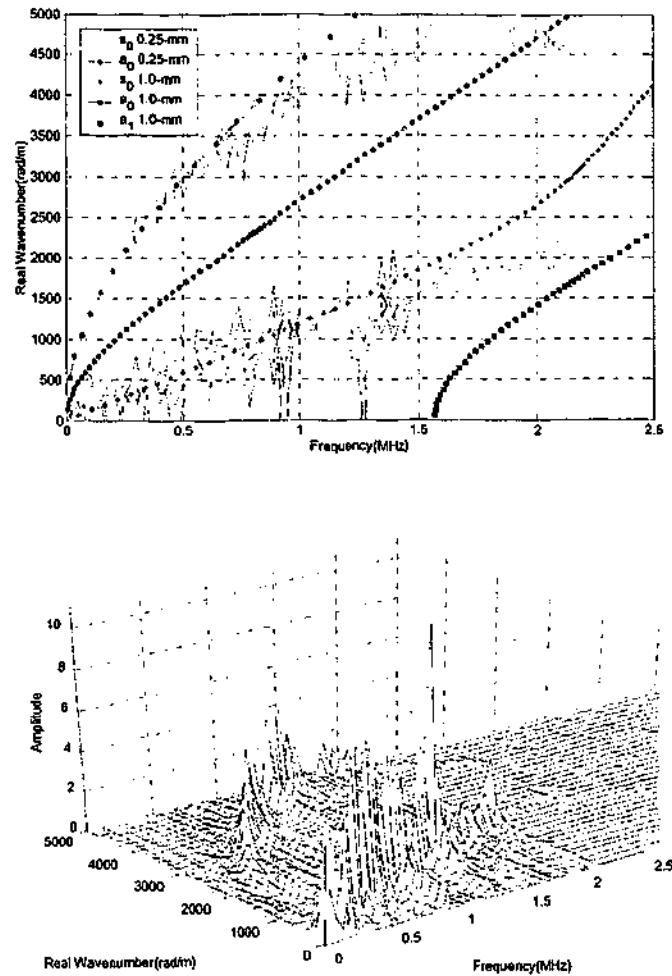


Figure 9.11 2D-FFT of the time history above a 25% delamination from the surface depth

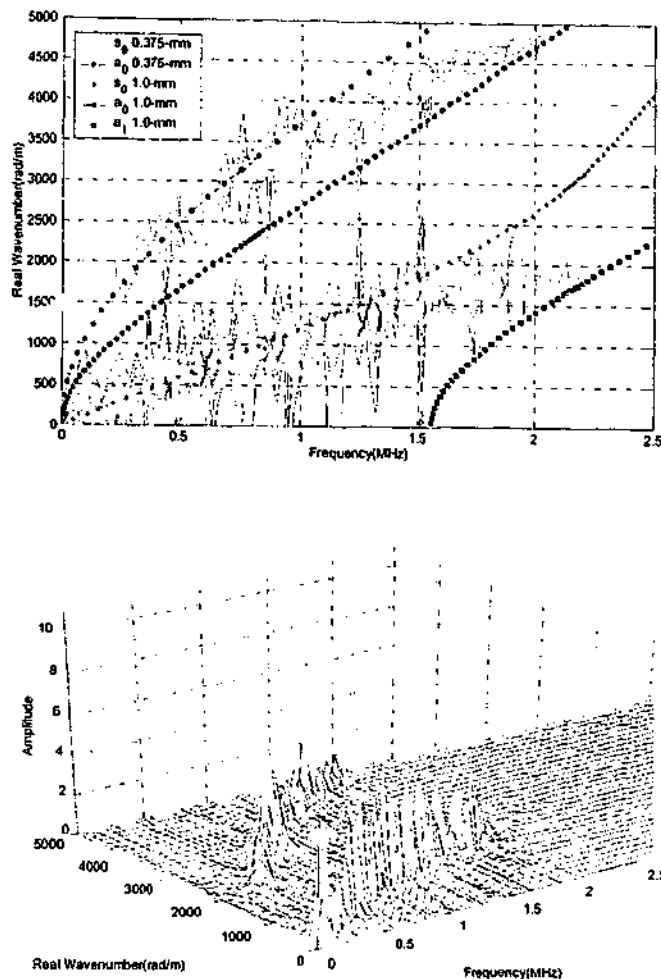


Figure 9.12 2D-FFT of the time history above a 37.5% delamination from the surface depth

The results obtained from these additional models agree with the observation made from the initial model that a second set of dispersion curves exists that corresponds to the thickness of the delaminated ply. In summary, all three models including the initial model, with the numerical analysis conducted on a variety of overall plate and delaminated ply thicknesses and the dispersion curves from the different thickness show that there was an a_0 wave mode propagating across the delaminated region.

The most important observation in this preliminary study is that mode conversion does not occur as Lamb waves travel through a delamination. Alleyne and Cawley (1992) observed mode conversion when transmitting Lamb wave through a steel plate with surface defect where the defect provided an obstruction in the propagation path

of the Lamb wave modes. This alludes to the fact that mode conversion can occur if the transmission of Lamb wave is affected by the presence of an obstacle in its path of propagation. In the case considered in this investigation, this type of discontinuity did not exist.

BVID-type damage

In this section, the impact damage was assumed to result in a local change in the stiffness of the structure. The finite-element model was 170-mm long and 1.6-mm thick. The spatial sampling interval was 0.5-mm and the sampling frequency was 20-MHz. 1024 points were used in the time domain while 128 points were used in the spatial domain. Figure 9.13 shows the comparison of the analytical phase velocity dispersion curve and the results from a 2D-FFT of the time histories obtained from finite element analysis. The results show that a fundamental symmetric mode, s_0 and a fundamental asymmetric mode, a_0 were produced by the broadband excitation.

Figure 9.13 to Figure 9.15 were obtained from the results of the no damage case and the various stages of damage considered in the simulation of impact damage. These figures show that the different intensity of the damage zone or the different size of the damage zones did not give rise to any mode conversion. However, the amplitude in the Lamb wave transmitted was attenuated. For a given mode and frequency, the power flow of the mode is proportional to the square of its amplitude (Auld, 1990). When determining how the changes in local stiffness affect the attenuation of the incident Lamb wave mode, it was assumed that a sensor was located at 30-mm after the damage. The root-mean-square of the wave transmitted to this sensor was calculated. The time history analysed was taken in such a way that the wave reflected from the end of the model was not considered.

Figure 9.16 shows the plot of the normalised power transmitted plotted against decreasing stiffness of the affected zone. The power transmitted shown in Figure 9.16 were normalised with the no-damage case. Figure 9.16 shows that power transmitted decreases with increase in damage size. The change in local stiffness has a larger impact on the attenuation of the incident Lamb wave. For a given change in the local stiffness, the apparent size of the region of lower local stiffness has a limited effect on the attenuation of the incident Lamb wave.

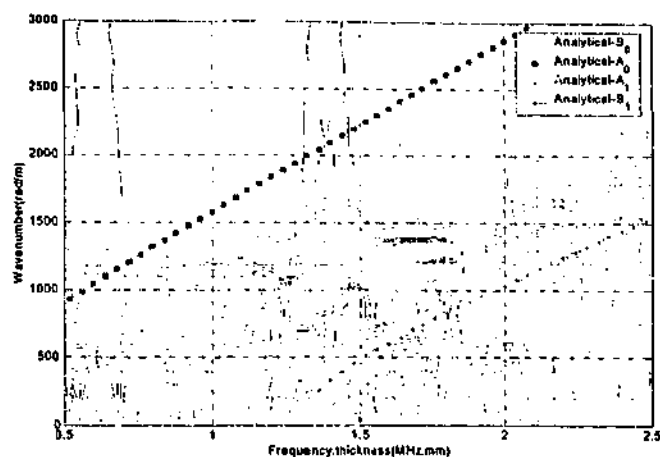


Figure 9.13: 2D-FFT from aluminium plate with no damage and 100% of Young's modulus

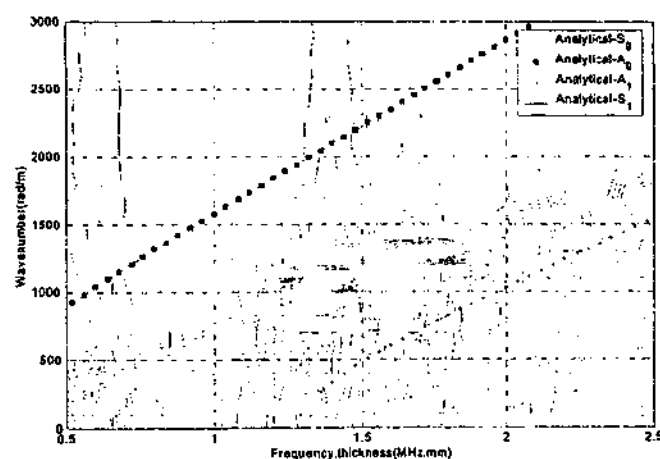


Figure 9.14: 2D-FFT from aluminium plate with 04-mm and 50% of Young's modulus

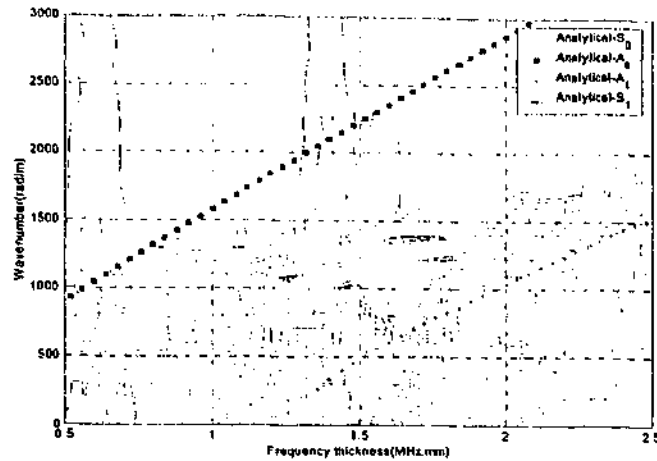


Figure 9.15 2D-FFT from aluminium plate with 12-mm and 90% of Young's modulus

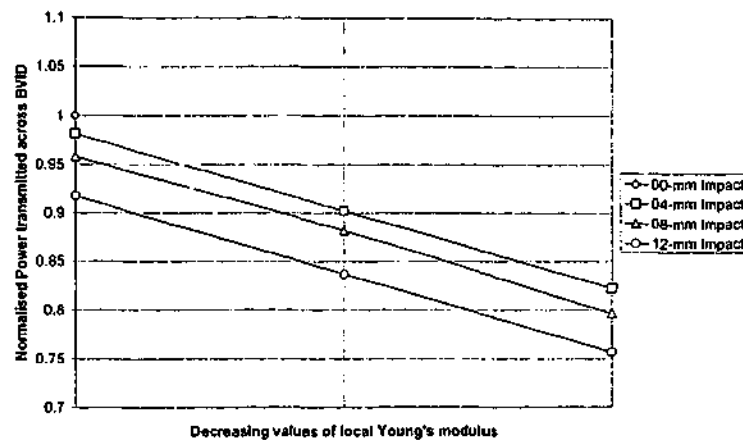


Figure 9.16 Power transmitted across BVID-type damage

9.4 MODELLING FOR DISBOND GROWTH

In this section, the results from the numerical simulation on the use of Lamb wave propagation for the detection of disbond growth beneath a composite repair patch are presented. In the model development, a description of the generation of Lamb wave in this numerical investigation was by means of a surface bonded ceramic piezoelectric transducer (PZT) is given. The change in power transmission of the Lamb wave was used to quantify the relative growth of the disbond. These results are used to predict the amount of power transmitted as a function of the disbond growth.

9.4.1 MODEL DEVELOPMENT

Development of the model for the simulation of the problem depends on a variety of factors, among them the excitation regime of the propagating Lamb wave, the geometry of the plate and the disbond shape and size. A suitable excitation regime prescribed for the surface-mounted PZT transducer is described followed by a description of the steps taken for the implementation of the finite element calculations.

Dispersion curve

Figure 9.17 shows the first four modes dispersion curves for an aluminium plate. At low frequency thickness, the group velocity of fundamental asymmetric (a_0) is slightly less than half that of fundamental symmetric (s_0) and they are only slightly dispersive. Simplifying the analysis and the interpretation of the results, the composite patch bonded on the aluminium substrate was assumed to behave perfectly elastic and isotropic, neglecting any damping properties and changes in the adhesive length to simulate disbond growth. The elastic property of aluminium is used in the analysis, and is accurately modelled.

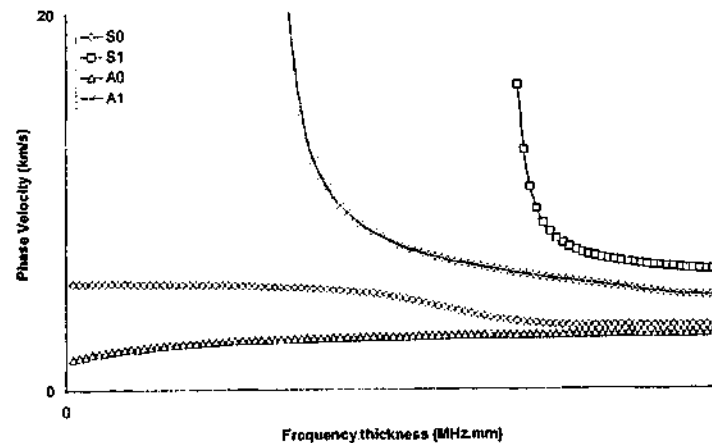


Figure 9.17 Calculated dispersion curves of aluminium plate

The first task with any method involving Lamb wave propagation is to decide on a suitable excitation scheme. In the following finite element analysis presented in this investigation a Hanning function modulated sine wave was used with a frequency-

thickness below 1-MHz.mm as the simulation above 1.5-MHz.mm could result in the spurious excitation of other modes. The centre frequency of the excitation was chosen from a dominant mode of an initial broadband excitation of Lamb wave across the composite bonded plate. This method of selection was suggested previously in the preliminary study when determining the effects of local changes in composite stiffness on propagating Lamb waves.

Broadband excitation avoids the problem of mode sensitivity to certain geometric defects, as certain symmetric or asymmetric modes will have greater power attenuation. The dominant mode from a broadband input allows a more selective excitation. In addition it is simple to implement in practical applications involving monolithic surface-mounted PZT elements.

In explicit time marching finite-element methods assuming diagonal mass-matrix, the duration of the input signal has to be finite. The received signals was analysed using a two-dimensional Fourier transform (2D-FFT). This allowed for the decomposition of the signal into its frequency and wave number domains. The various mode(s) at the centre frequency of the Lamb waves should be evident in these 2D-FFT results. The dominant mode was determined to be at the centre frequency of 0.195-MHz with a frequency-thickness of 0.312-MHz.mm for aluminium plate of 1.6-mm thickness. It is convenient to excite the s_0 mode at this frequency thickness, at its maximum whilst achieving low dispersion. It is not possible with surface bonded PZT to impose the through thickness displacement of the plate to the desired Lamb mode. Additionally, the bottom surface of the plate is not constrained and is free to move. Therefore both s_0 and a_0 will be excited at the chosen centre frequency. To enable analysis of a single mode, time history gating was carried out. Time history gating for a propagating Lamb wave was done in the previous numerical analysis above and experimental investigation (Guo and Cawley, 1994) conducted by others. This is possible since at this frequency thickness, a_0 travels at less than half the velocity of s_0 .

Finite Element Models of Plates

Figure 9.18 shows a schematic of a small section of the meshed plate configuration with a piezoelectric transducer bonded to the top surface on the transmitter plate providing the excitation. The mesh for the FM73 adhesive was chosen to be of similar

refinement to the meshes of the plate. Perfect bonding was assumed between the aluminium, the adhesive, and the composite patch. An elastic disturbance is initiated by applying five sinusoidal cycles at the centre frequency of 0.195 MHz, windowed by a Hanning function. In a large number of composite patch failures recorded by the Royal Australian Air Force (Chalkley and Geddes, 1998), disbonds initiated from the edge of the taper and grew parallel to the surface. Therefore the adhesive elements were removed starting from the edge and a straight-sided disbond was assumed in all of the finite element calculations. Seven disbond lengths were considered, ranging from 0-mm to 12-mm in 2-mm increments. By repeating the analyses for the range above the power transmission can be expressed as a function of the disbond length. The length of the plate used in all the simulations was 175-mm long.

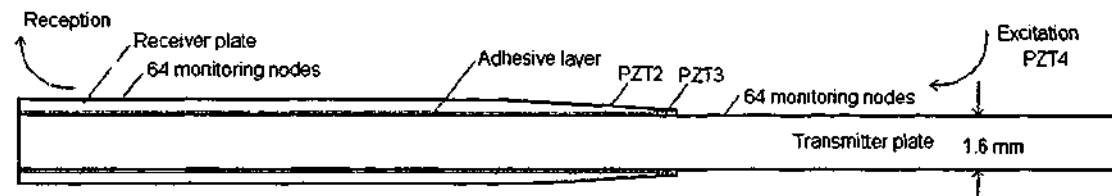


Figure 9.18 Schematic of a small section of the simulated model

As with the previous investigations, plane strain conditions were assumed. A uniform square mesh of 8-noded quadrilateral elements with more than 10 nodes per wavelength was used. An explicit central difference approximation scheme was used by the finite element package to produce the time marching solution. The time step chosen is less than the time taken for the fastest wave to travel between two adjacent nodes. In this simulation the material properties correspond to a 7075-T6 aluminium alloy, with a density of 2770-kg/m^3 , and bulk wave velocities of 6295-m/s and 3099-m/s for the longitudinal and transverse modes respectively. As shown in the results in Figure 9.19, the dominant mode excited in this plate is in the vicinity of $0.312\text{-MHz}\cdot\text{mm}$. It is to be noted that at frequency-thickness values below $1\text{-MHz}\cdot\text{mm}$, both aluminium and composite plates show similar characteristics in supporting only the fundamental symmetric and asymmetric modes.

9.4.2 RESULTS AND DISCUSSION

A prescribed displacement on the piezoelectric transducer excited a propagating Lamb wave subjected to the regime described earlier. Since our interest was to predict Lamb wave propagation for a given mode, it was necessary to separate the multimode components in the received signal. This was facilitated by the fact that the group velocity of a_0 is slightly less than half that of s_0 and they were only slightly dispersive. Accordingly, only that part of the time domain signal containing the s_0 contribution was considered. In each finite element analysis for the various damage condition similar excitation was propagated in the transmitter plate and the response measured in the receiver plate. The same bandwidth of analysis was applied to the various conditions and expressed as a ratio to the undamaged composite patch.

The dispersion curves shown in Figure 9.17 were used to design an excitation scheme that would excite the required modes. In order to excite a given mode it was necessary over a given range of frequencies and corresponding phase velocities to restrict the excitation to a box on the dispersion curve. In terms of experimental method it is practically quite difficult to maintain the wave excitation conditions within these box boundaries, but close approximations are possible.

Figure 9.19 shows the comparison between numerical and analytical calculations for symmetric and asymmetric wave modes propagating across the transmitting plate. Monitoring 64 nodes before the composite patch taper on the transmitting plate obtained the result. Zero padding which caused the graph to have a high number of points on the frequency-thickness axis compensated the lack of resolution. The initial wave propagating through is dominated by the fundamental symmetric mode. This is due to the close location of the monitoring nodes to the actuating PZT as well as the time history recorded of the propagating wave.

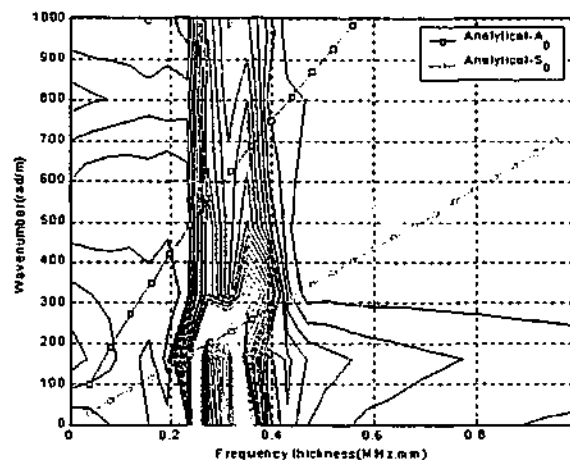


Figure 9.19: 2D-FFT on the aluminium substrate immediately next to the actuator

The following Figure 9.20 were recorded at the far field on the composite patch from 64 monitoring nodes. Distance between this set of nodes from the taper is three times the length of the taper. This is to be consistent with Saint Venant's Principle. The possibility of multimode in the overlap region and the reverberation of these modes in the overlap were first acknowledged by Lowe et al (2000). If the location of the monitoring nodes were located far enough from the discontinuity, the effect of the overlap over the propagating Lamb wave would decay. Both results show a dominant fundamental symmetric mode.

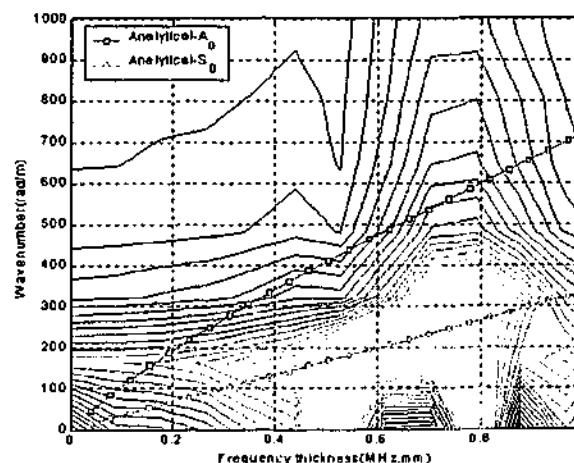


Figure 9.20: 2D-FFT on the composite repair patch after the damage

The following Figure 9.21, Figure 9.22 and Figure 9.23 show the FFT at the taper of the composite. These figure compare the numerical results and the analytical dispersion curves calculated for three different plate thicknesses. The thicknesses considered were 1.6-mm, 2.6-mm and 3.6-mm. These three thickness were the aluminium plate thickness, the total thickness of the composite patch bonded aluminium host and the average of both. The excitation frequency used was of broadband nature and allowed the propagation of multimode signals. The FFT of the numerical result for the composite patch with no disbond is shown in Figure 9.21. It is obvious that the FFT is bound by the analytical dispersion curve of the fundamental symmetric mode. The nearest fundamental asymmetric mode to the numerical results was produced by the Lamb wave propagation through a 2.6-mm plate.

As damage was introduced to the numerical model, the result for a composite patch with a 6-mm disbond is shown in Figure 9.22. The results show that the FFT of the numerical result obtained is bound by the analytical dispersion curve of the extreme thickness considered. It is found that there is no mode conversion within tapered region. The lack of reverberation and reflection in the wave propagation is expected as the geometrical condition is different from those used by Lowe et al (2000) when they simulated a double lap joint. They recorded reverberation and reflection as a result of the overlap region.

It is also noted that the 2D-FFT shown in Figure 9.22 and Figure 9.23 has a maximum value below the frequency of 500-kHz and a wave number approaching 0-rad/m. This phenomenon is not observed in the results shown in Figure 9.21. The 0-rad/m wave number could be attributed to the cantilever effect of the taper. The disbanded length of the taper thus appeared to have a very large wavelength, and a transform that approaches 0-rad/m.

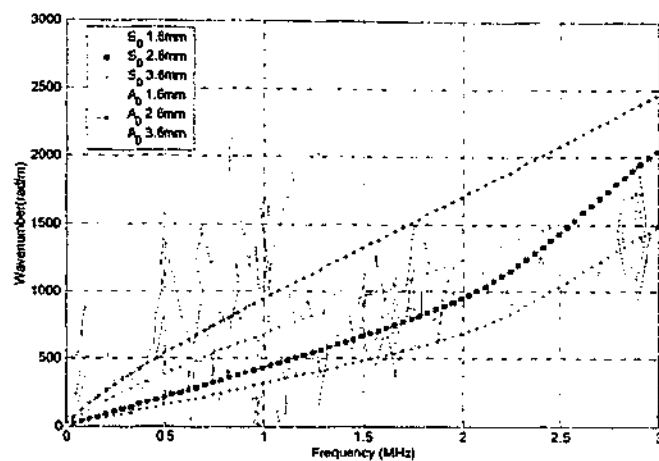


Figure 9.21 Comparison of numerical and analytical for 0-mm damage

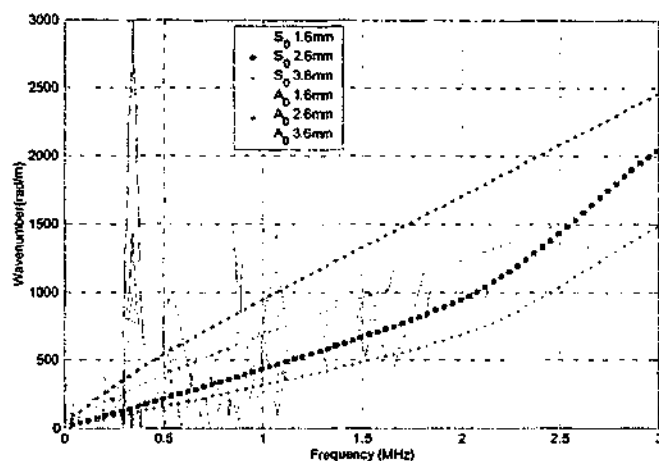


Figure 9.22 Comparison of numerical and analytical for 6-mm damage

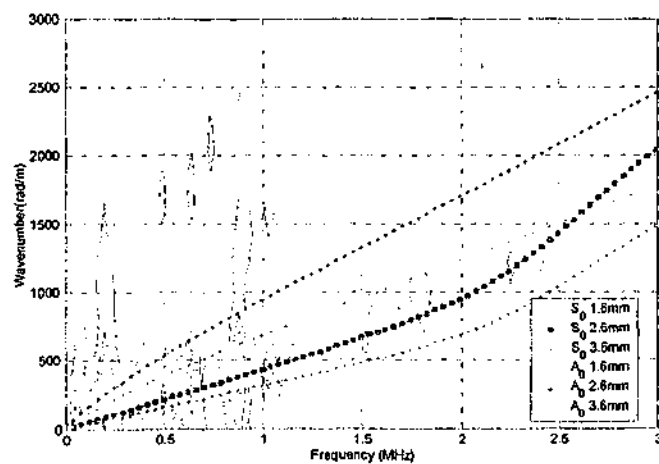


Figure 9.23 Comparison of numerical and analytical for 12-mm damage

A very recent investigation by Dalton et al (2001) on the potential of Lamb wave propagation through metallic aircraft fuselage, found that reflection is almost negligible if the taper ratio is low. They used a finite element mesh as shown in Figure 9.24 with tapering skin thickness to establish the level of reflection from the change in section with excitation of Lamb waves from the thick-end of the model. Dalton et al (2001) concluded that the reflection amplitude increases with gradient and reflection of less than 10% can be expected for gradients of up to 1:5. Therefore reflection and reverberation is a function of the gradient, which acts as a reflective surface. In the numerical simulation carried out so far the excitation of Lamb waves is from the aluminium host to the composite bonded aluminium plate, hence reflection and reverberation can be considered small to negligible.

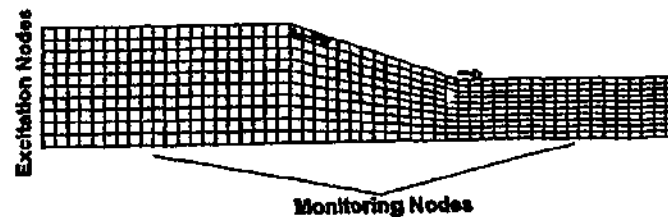


Figure 9.24 Finite element mesh used by Dalton et al (2001)

It is evident with the FFT result from the simulation taken at the three different locations – the aluminium section before the taper, tapered section of the composite repair and the composite bonded aluminium section that the fundamental symmetric mode was dominant. The same observation applies when a 12-mm disbond was the prescribed damage for the simulated model. The FFT of the numerical results obtained is bound by the analytical fundamental symmetric mode for the extreme thickness considered.

With the finite element model and the propagating Lamb modes verified, the power transmitted to both PZT2 and PZT3 were used to quantify the relative growth of the disbond. Part of the elastic energy was transmitted through the bond-line into the patch and received at the sensor locations. The expectation was that continuous monitoring of the elastic energy at these sensor locations would provide a robust basis for the assessment of disbond growth from the patch edge.

In order to obtain the power transmitted between the PZT transducers the mean square response of the sensing PZT was calculated. From the results in Figure 9.25 it is found that with increasing damage, the power transmitted decreases. As PZT3 was located at the edge of the taper, the progressive disbond growth was reflected by a decline in power transmission. The sensor PZT3 was 4-mm wide and as damage grew beyond 4-mm, the sensor was able to detect the difference in power transmitted. This was due to the reflection and diffraction of the Lamb waves by the introduced disbond. The diffraction at the semi-infinite aperture can be used to quantify disbond. These forms of reflection and diffraction of Lamb wave at a discontinuity was previously concluded by Rokhlin and Bendec (1983). They concluded that Lamb wave propagation is affected by the size of contact region between two elastic plates. Lowe et al (2000) also made similar observations regarding bond length of the lap joint.

Figure 9.26 also exhibits a decrease with progressive disbond growth. This is an important observation as the damage was located away from the PZT transducer. As the damage approached the sensor and beyond the power transmitted consistently decreases. In order to verify this observation, a second model was simulated but only one sensing PZT was used and was located at the position between the PZT2 and the PZT3 in the previous model. The result is shown in Figure 9.27. The power transmission decreases with progressive disbond growth. In summary, the PZT sensors are able to detect the change in power transmission even when the damage was not located directly beneath it.

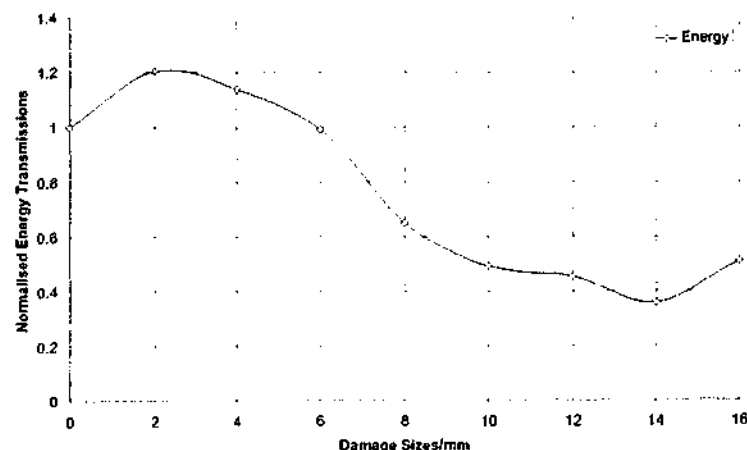


Figure 9.25: Power transmission detected by PZT3

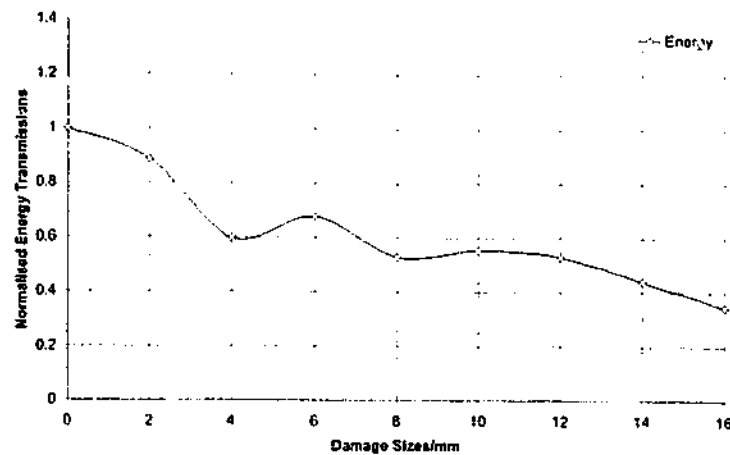


Figure 9.26 Power transmission detected by PZT2

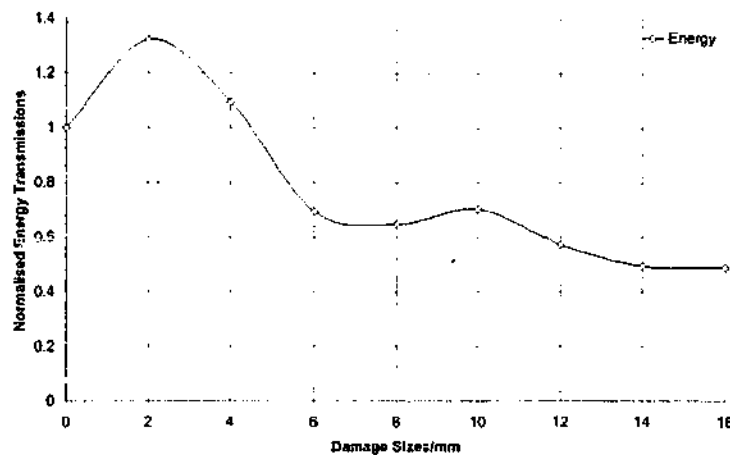


Figure 9.27 Power transmission for PZT located at the between PZT2 and PZT3

These results show that disbond growth can be predicted by the attenuation of power transmitted by means of Lamb waves. The results so far agrees with the experimental results reported by Koh et al (2002). The specimen used in that investigation can be seen in Chapter 8, Figure 8.15. In the experiments it was found that the power measurement (Figure 9.28) decreased as soon as the disbond began at the taper and the sensor was not located above the damage region. The strain gauge recordings confirmed the disbond progress as shown in Figure 9.29. The results show that the method of measuring power transmission is superior to other methods of detecting disbond. By measuring the transmission coefficient, the sensor does not need to be located immediately within the damage region.

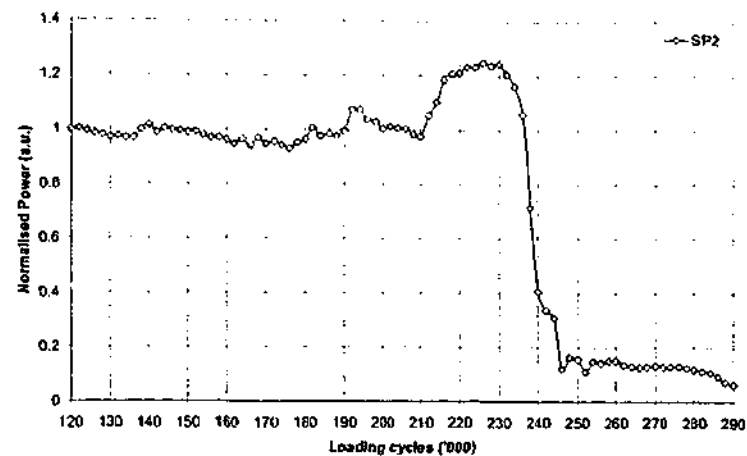


Figure 9.28: Results from the experimental investigation of the stress wave method taken from Koh et al (2002)

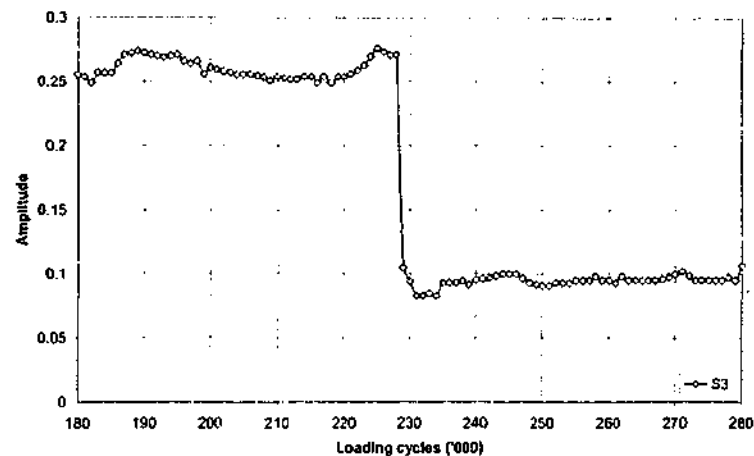


Figure 9.29: Strain gauge reading taken from edge of repair patch taper

9.5 CONCLUSIONS

The findings reported in this chapter show that stress waves excited by surface mounted piezoelectric transducers are suitable for the quantification of impact damage. The delaminated ply can be located from the surface of the composite plate based on the proposed method above. The severity of impact damage can be predicted from the power transmitted. It is shown with PZT mounted on only the top surface, both symmetric and asymmetric modes will be excited. The application of the quantification method requires time and cost resources to be spent on signal

processing. That said the results show that the proposed method can be reliably used to monitor the structural condition of a composite plate. This can be verified in the experiments by monitoring point measurements in the time domain.

This approach allows rapid inspection of a bonded composite without rigorous signal processing. It can incorporate the neural network identified in previous work to show that the dimensions of an adhesively bonded T-joint have a significant influence on the Lamb wave transmission. The reduced use of computation is to encourage practical exploitation of the proposed method. By measuring the power transmitted between a pair of surface mounted piezoelectric transducers, the initiation of the disbond can be detected as well as the progress of the disbond. The method utilising propagating Lamb wave is highly sensitive. Even when the PZT transducer is located at a distance from the damaged region, this method can be used to detect the changes due to the intrinsic properties of the propagating Lamb wave.

CHAPTER 10

EVALUATION OF STRESS WAVE METHOD USING EXPERIMENTAL ANALYSIS

10.1 INTRODUCTION

The experimental analysis for the evaluation of the stress wave method for damage detection is very different to that for the evaluation of the impedance method and the transfer function method. The experimental analysis involves a composite plate that was first impact damaged. The impact damage was expected to cause inter-ply delamination, which would provide a parallel study for disbond of composite repair. The difference between the inter-ply delamination and the disbond of composite repair is that in the former there is the same material sandwiching the delamination while in the latter these materials are different. The composite plate is made of an orthotropic material and when the plate is excited, complex wave patterns are initiated. The excitation of Lamb waves for the composite plate is by means of surface-mounted piezoelectric transducers rather than by means of a prism wedge that is traditionally used to excite both longitudinal and transverse wave. The use of surface mounted PZTs is a relatively new method.

In section 10.2, the background theory required to understand the application of the stress wave method for damage detection is presented. The experimental investigation aims to evaluate the ways of exciting a single Lamb wave mode with surface mounted PZT transducers and detecting the propagating wave using monolithic PZT transducers. In the experiments, Lamb wave propagation and detection are both measured by a single point measurement in the temporal domain whereas in the numerical analysis, measurements were made both in temporal and spatial domains.

In section 10.3, the preliminary study on the application of the stress wave method on a composite plate is presented. The aim of this study was to investigate the directional properties of the composite plate. The results obtained using the stress wave method are presented and the application of the method to determine the quasi-isotropic property of the composite laminate discussed.

In section 10.4, the damage characterisation study on the application of stress wave method on a graphite/epoxy composite plate with impact damage is presented. This plate was impacted at different velocities and loads before the characterisation process. The characterisation process measured the power attenuation in the Lamb wave when the wave was propagated through the damage region. The results obtained are used to quantify the extent of damage and to obtain a relationship between an impact damage and the residual strength in the plate.

10.2 BACKGROUND THEORY

According to Viktorov (1967), there exist four methods for the excitation of a Lamb wave on a surface. These methods are:

1. By shear perturbations: Using a Y-cut quartz or titanate specimen, the surface is excited uniformly in a strip.
2. By normal perturbations: Using a quartz or titanate specimen or an ultrasonic beam at normal incidence in liquid.

3. By a set of normal perturbations: periodical distribution with period λ_{lamb} (comb-structure method).
4. Of normal perturbations: distribution follows a sinusoidal travelling wave law (wedge method).

The first and second are non-resonance methods. For a given frequency, each normal mode is excited equally. They are usually not suitable for practical applications. The third and fourth are resonance methods. When the projections of the 'comb' or the wedge angle are adjusted, depending on the method the particular modes can be excited (Viktorov, 1967).

Stress waves are normally excited by PZT mounted on a prism wedge. One advantage of using the wedge method is that by changing the wedge angle it is easy to change the mode. This method is widely used in flaw detection but in materials such as polymers where sound travels slowly, the wedge method is difficult to use, and the comb structure method is preferred. All four methods listed above are reversible. This means that they can also be used to detect Lamb waves (Viktorov, 1967), as reported by Alleyne and Cawley (1990). However in this investigation the stress wave was excited by surface mounted PZT and the detection of stress wave was by means of a single point measurement. From sufficient measurements all the elastic stiffness components for a material of orthorhombic, or higher, symmetry could in principle be determined using a single test piece of rectangular cross-section.

Measurements of propagating Lamb waves using time and frequency domain methods were made in the experiments. This heuristic approach was adopted to provide general rules that could readily be used by practising engineers. In addition, employing tone burst excitation generally controls the frequency-thickness range of the excitation.

The phase velocity, which generally is controlled by using the coincidence principle, could not be applied in this investigation since the actuator was surface mounted on the composite specimen. With the actuator mounted on one side it was not possible to excite a single frequency or phase velocity. It was observed that increasing the number of cycles in a tone burst reduced the signal bandwidth, while windowing the

tone burst removed the side lobes present with the un-modified tone burst while broadening the main lobe.

In addition to the difficulty in exciting a pure mode, Lamb wave propagation in composite materials can be very complicated due to anisotropy, the complex attenuation mechanisms and the inhomogeneous nature of the materials through the thickness of the laminate.

10.3 PRELIMINARY STUDY OF COMPOSITE SPECIMEN

The aim of this study was to determine the quasi-isotropic property of the plate. The experimental procedures for establishing the location of the PZT and the material properties of the eight-ply carbon/epoxy laminate specimen are outlined in this section. The parameters required for the launching of the excitation, a sine function, modulated by a Hanning window, enclosing five periods of the sine wave, are also presented.

10.3.1 EXPERIMENTAL PROCEDURES

In the preliminary study, initial investigations were carried out to evaluate the directional properties of the composite specimen. This was done by measuring the speed of flight between the different points on the specimens.

Characteristics of the specimens examined

Three specimens referred to as the ID1-series were prepared for the preliminary investigation of evaluating the directional properties of the composite specimen. Figure 10.1 shows a schematic drawing of the ID1-series specimens with the PZT location and their labels. Thermal scanning of these specimens showed no prior damage. The material properties of this laminate are given in Table 10.1.

Table 10.1 Common material properties of graphite/epoxy composite

MATERIAL PROPERTIES	GRAPHITE/EPOXY AS/3501
Number of plies	8
Stacking sequence	$[0/90/\pm 45]_s$
Ply thickness	0.125 mm
Total laminate thickness	1.165 mm
Density $[\text{kg/m}^3]$	1600
E_x [GPa]	138
E_y [GPa]	8.96
α_x	0.30
α_y	0.66
E_s [GPa]	7.1
S_{xx}	7.246
S_{yy}	111.6
S_{xy}	-2.174
S_{ss}	140.8
M	1.0059
Q_{xy}	138.8
Q_{yy}	9.013
Q_{xy}	2.704
Q_{ss}	7.1

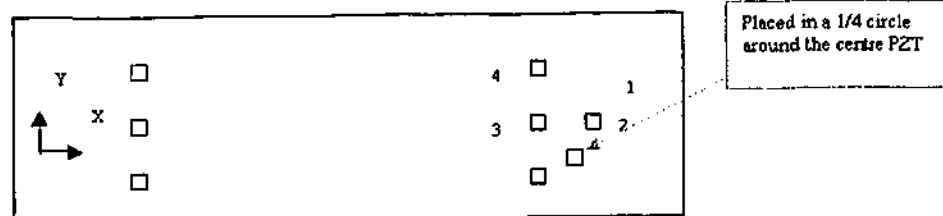


Figure 10.1 Schematic drawing of the ID1-series specimens with PZT locations

Setting the experimental conditions

In order to excite a pure Lamb mode, the input must be at the correct frequency thickness product must be appropriate for the desired mode. The characteristics of the excited signal depend on the frequency-thickness, which is the product of the frequency of the excited waveform and thickness of the specimen. An important parameter here was the thickness of the specimen to be investigated, which was measured using a micrometer gauge. The cut-off frequency-thickness of a wave mode is the smallest value of this product at which the wave mode could exist, or the value where the mode first appears. When these values had been acquired, the specific frequency-thickness corresponding to the chosen mode was divided by the measured thickness of the specimen, and the exciting frequency obtained.

To determine the dominant frequency for the modulated sine wave tone burst enclosed in a Hanning window, a simple broadband excitation was sent through the specimen. The received signal was amplified and transferred to a digital oscilloscope. In order to increase the signal-to-noise ratio, 100 successive response signals captured by the digital oscilloscope were averaged. The averaged time response on the oscilloscope recorded by the sensors at the opposite side of the specimen was then sampled and converted into frequency domain. The effect of this broadband excitation is the excitation of all the dominant modes in frequency domain. From this, the appropriate frequency to use for the excitation of the sine wave tone burst was determined.

By comparing the different response curves from the broadband frequency excitation, the dominant frequency was approximately at 210-kHz for all three specimens. Thus the frequency of 210-kHz was used as the centre frequency to excite the tone bursts in the experiments and to observe the response from the specimen.

The wave velocity along an axis was found from the following Equation 10.1.

$$c = \frac{s}{t} \quad \text{Equation 10.1}$$

where c is the wave velocity, s the distance between PZT's and t is the time travelled.

10.3.2 RESULTS AND DISCUSSION

For this experiment, a five cycle sine wave tone burst having a centre frequency of 210-kHz enclosed in a Hanning window was employed. The difference in time domain between the start of the excited burst to the start of the received signal, were measured in the time response. The signal was emitted at PZT4 and received at PZT1, PZT2 and PZT3 respectively with the PZT locations shown in Figure 10.1. The radius of the quartercircle around PZT1 was approximately 39-mm.

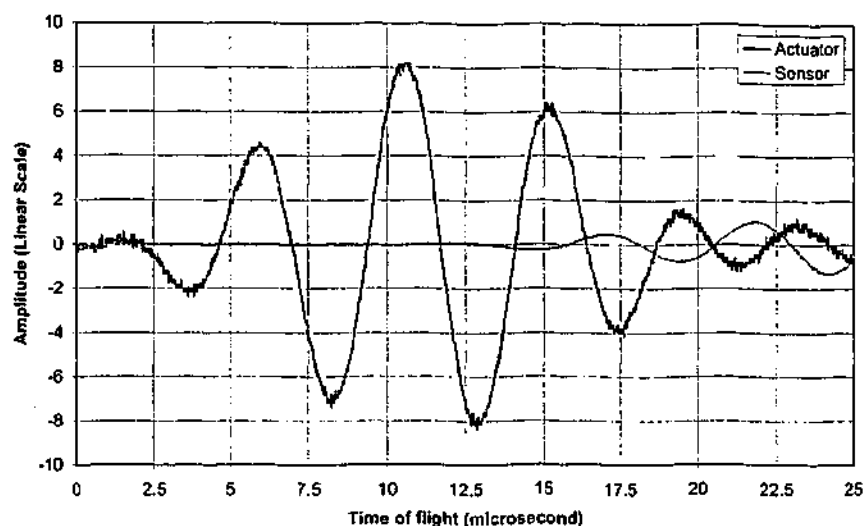


Figure 10.2 Time of flight between actuator (PZT4) and sensor (PZT1) on ID1

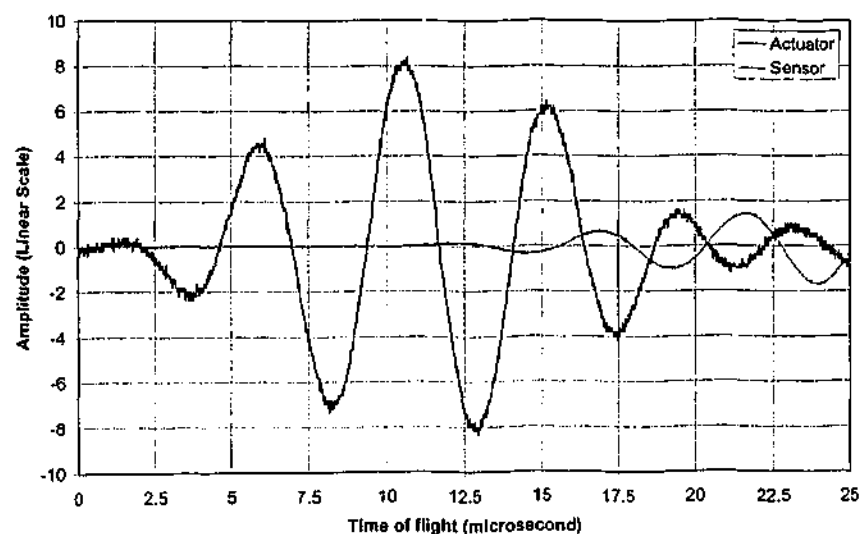


Figure 10.3 Time of flight between actuator (PZT4) and sensor (PZT2) on ID1

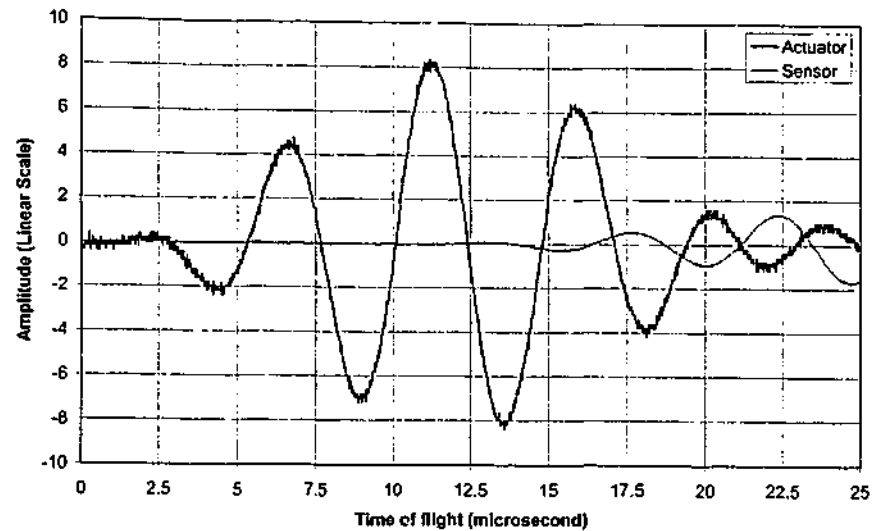


Figure 10.4 Time of flight between actuator (PZT4) and sensor (PZT3) on ID1

Table 10.2 Time delay from emitter to receiver

Emitter	Receiver	Time delay (μs)				Average (μs)
		1	2	3	4	
4	1	7.7	7.9	7.9	7.8	7.8
4	2	7.6	7.8	7.7	7.8	7.7
4	3	8.1	7.9	8.0	7.9	8.0

Table 10.3 Speed of flight in different directions

Emitter	Receiver	Travelled distance (mm)	Average time delay (μs)	Speed of flight (10^3 m/s)
4	1	39	7.8	5.0
4	2	38	7.7	4.9
4	3	39	8.0	4.9

It can be seen from these measurements that the speed of flight recorded was between the range of 4900 to 5000-m/s in all the directions measured. The time taken to travel in all three directions were close, therefore the specimen was considered to be quasi-isotropic in the xy -plane. To confirm those findings, it was decided to obtain the speed of flight over a significantly longer distance using the same input to confirm the above

findings. Measurement was taken over a significantly longer distance of up to 285-mm to record the time of flight. The signal was emitted at PZT2 and received at PZT4, in the configuration as shown in Figure 10.5.

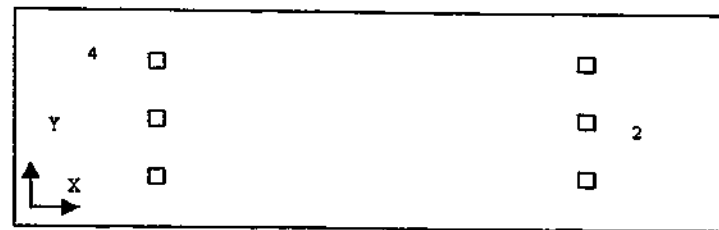


Figure 10.5 Schematic of the ID1-series specimens with new PZT labels

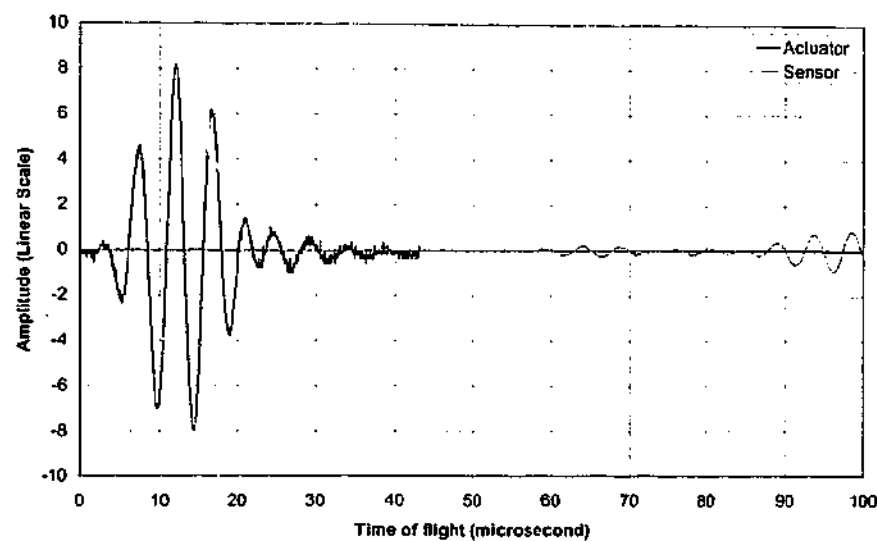


Figure 10.6 Time delay between actuator (PZT2) and sensor (PZT4) signal for a longer distance

Four consecutive tests were performed to find the average time delay and the results are shown in Table 10.4. The time delay from the start of the input signal to the response was measured to be approximately 53- μ s, thus a speed of flight approximately 5500-m/s. This indicates that the s_0 mode was excited when compared with the theoretical value of its group velocity.

Table 10.4 Time delay from emitter to receiver

Emitter	Receiver	Time delay (μ s)				Average (μ s)	Distance (m)	Speed of flight (10^3 m/s)
		1	2	3	4			

2	4	54	53	53	53	53	0.285	5.5
---	---	----	----	----	----	----	-------	-----

This theoretical value can be calculated using Equation 10.2 as follows:

$$\frac{c_t}{c_e} = 1 \quad \text{Equation 10.2}$$

where c_e is the theoretical wave velocity in the specimen.

$$c_t = \frac{\omega}{k_t} \quad \text{Equation 10.3}$$

where c_t is the transverse wave velocity and ω is the angular frequency.

$$k_t = \omega \sqrt{\frac{\rho}{\mu}} \quad \text{Equation 10.4}$$

where k_t is the transverse wave number, ρ is the density of the material and μ is an elasticity parameter

$$2d = \lambda_e \quad \text{Equation 10.5}$$

where d is the thickness of the specimen and λ_e is the wave length

By solving the above equations, the theoretical wave velocity was found to be 5760-m/s. This velocity corresponds well with the speed of flight shown previously obtained from the experiments.

Characteristics of response after FFT

A 1-D FFT was carried out over the time history shown previously in Figure 10.6. The amplitude spectrum shown in Figure 10.7 of the time history exhibit a peak at approximately 210-kHz that is equal to the centre frequency of the input signal. When the receiver was moved closer to the actuator to a distance of 3.9-mm (located in the 1/4 circle) from the actuator, the same centre frequency was observed. These amplitude spectrums for each of the three specimens was consistent and repeatable.

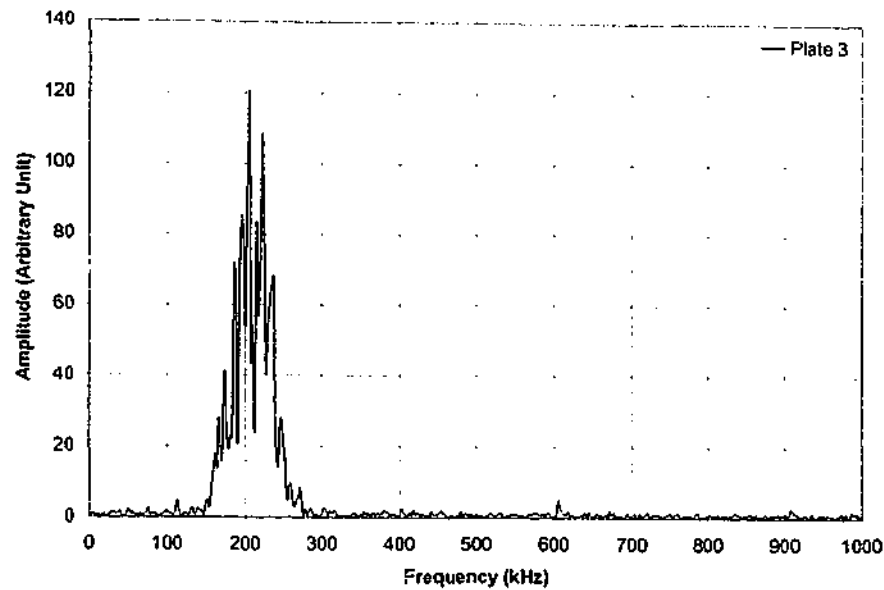


Figure 10.7 Amplitude spectrum of the time history shown in Figure 10.6

10.4 DAMAGE CHARACTERISATION STUDY

The aim of this study was to determine a relationship between the type of damage and the attenuation of stress wave. Three specimens to be evaluated were impacted to various degrees in a test rig. The impact damage in these new specimens ranged from barely visible impact damage (BVID) for specimen 4 to full penetration for specimen 6. They were inspected using the stress wave method as in the previous Section 10.3.

10.4.1 EXPERIMENTAL PROCEDURES

Three graphite/epoxy composite specimens referred to, as ID2-series were prepared with PZTs bonded as shown in the following schematic drawing (Figure 10.8). The dimensions of each PZT element were $5 \times 5\text{-mm}^2$.

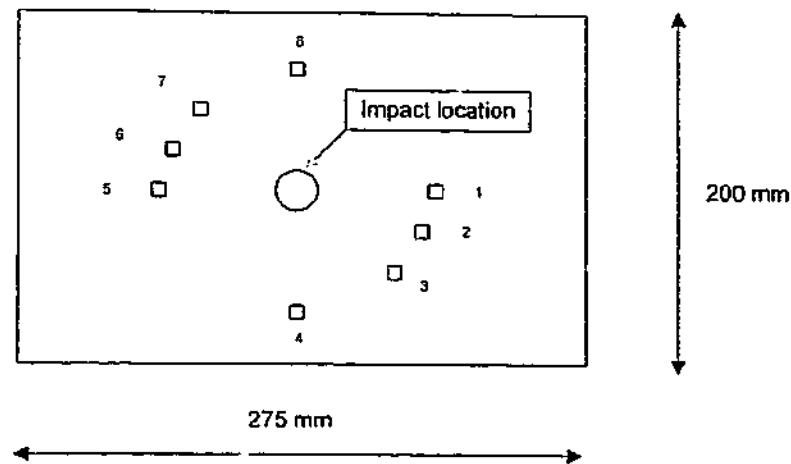


Figure 10.8 Schematic of the ID2-series specimens with PZT location labels

The PZT elements were located in two $\frac{1}{4}$ -circles placed opposite each other. They were placed at 0° , 22.5° , 45° and 90° on each quarter circle, resulting in four opposing pairs of actuators and sensors, respectively. These specimens were impacted using the drop test rig described in Section 3.7 of Chapter 3. These ID2-series specimens were labelled as specimens 4, 5 and 6. The characteristics of these specimens and impact energy experienced are shown in Table 10.5.

Table 10.5 Characteristics of the specimens after impact damage

Specimen no.	Length (m)	Width (m)	Thickness (mm)	Impact energy [J]	Impact height (mm)
4	0.280	0.200	1.165	3	65
5	0.275	0.200	1.165	6	130
6	0.260	0.200	1.165	2	43

To be consistent, comparison was made between the different impacts on a particular specimen to maintain the same boundary conditions. Thus it was decided to impact specimen 5 and 6 using different impact energies and thereby inducing more extensive damage. The specimens were then investigated again, and the response of each specimen compared with the undamaged case.

10.4.2 RESULTS AND DISCUSSION

In the first evaluation, the sensor and actuator PZT pair used was located at PZT4 and PZT8. The measured responses shown were taken before (Figure 10.9) and after the last impact (Figure 10.10). In the second evaluation, the sensor and actuator PZT pair used was located at PZT1 and PZT5. The measured responses shown were taken before (Figure 10.11) and after the last impact (Figure 10.12).

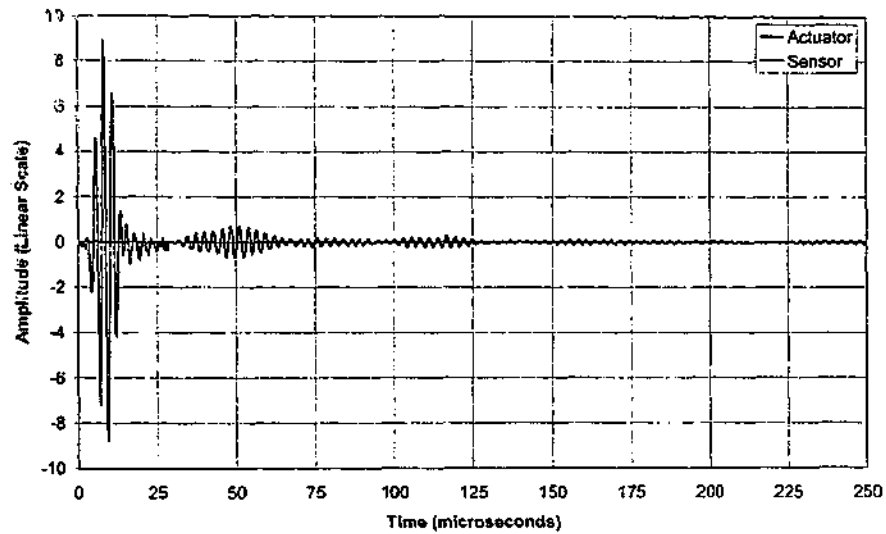


Figure 10.9 Specimen 4 Response for actuator (4) and sensor (8) before last impact

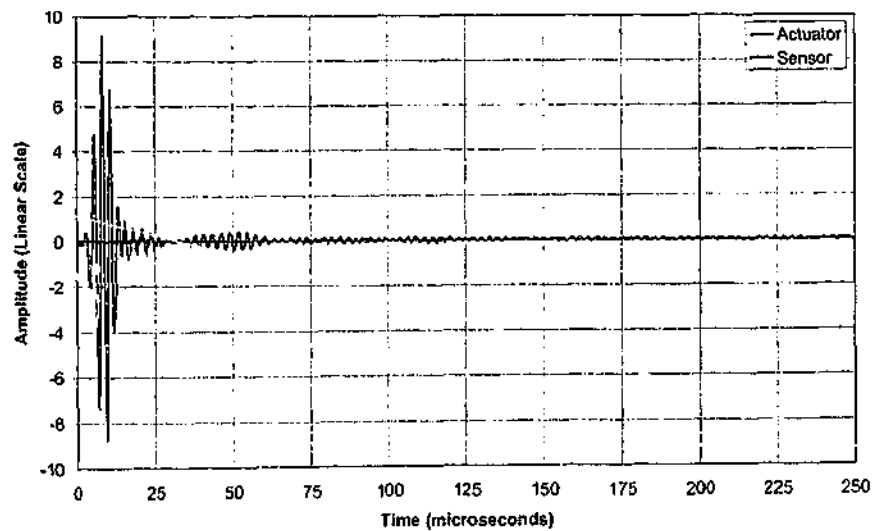


Figure 10.10 Response for actuator (4) and sensor (8) after last impact

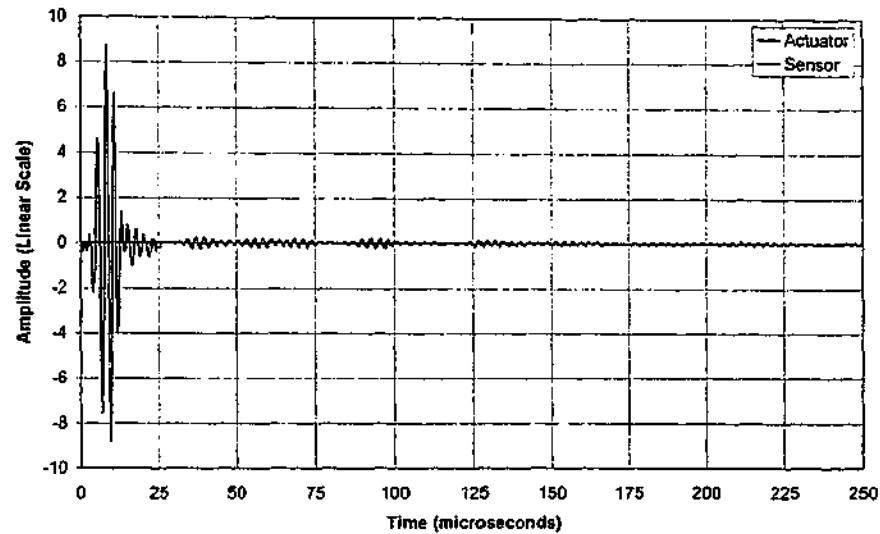


Figure 10.11 Specimen 4 Response for actuator (1) and sensor (5) before last impact

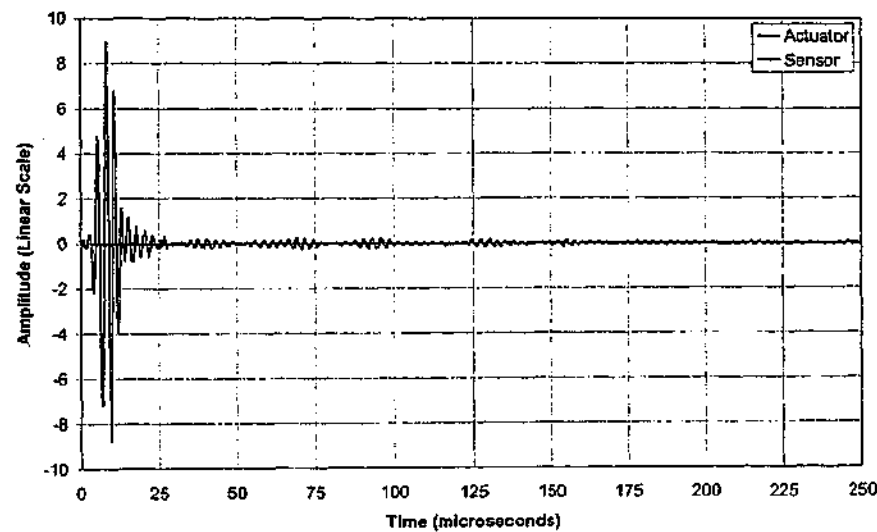


Figure 10.12 Response for actuator (1) and sensor (5) after last impact

The time of flight for the first arriving wave packet was the same for all tests thus the wave velocity was the same. The attenuation of the first wave packet with impact damage for all three specimens was further investigated. It was observed that the attenuation increased with the level of impact energy. The first wave packet was isolated in the same way for all three specimens, and the size of this before and after impact was compared using the root mean square of the measured response (RMS), in order to quantify the attenuation.

Attenuation of the measured response for the specimens

Table 10.6 RMS values for specimen 4

Actuator	Sensor	Orientation	Impact energy	RMS
1	5	0	2-J	0.134
			3-J	0.129
			4-J	0.0982
2	6	22.5°	2-J	0.190
			3-J	0.156
			4-J	0.127
3	7	45°	2-J	0.229
			3-J	0.201
			4-J	0.103
4	8	90°	2-J	0.0793
			3-J	0.0456
			4-J	0.0355

Specimen 4 was impacted in impact run 1 and 2 using impact energies of 2-J and 3-J, respectively and this had resulted in small, but detectable damage. When the specimen was impacted for a third time, increasing the impact energy to 4-J, it resulted in full penetration of the specimen. By analysing the RMS values and the time history shown previously, attenuation of the first wave packet was noted. The attenuation varied according to the actuator and sensor pair examined. The average attenuation for all the four directions was 28 %.

To evaluate the validity of the experimental findings, a thermal scan of the specimens was performed at DSTO. This provided a clearer picture of the damage development and facilitated evaluation of the size, location and orientation of the damage. The most extensive damage was discovered on the tensile (back) face of the specimen. This damage was oriented in the 45°-direction, parallel to the direction of the fibres in the lower ply. The damage area in the upper plies was smaller and round in shape, corresponding to the indent made by the impactor.

From the thermal images for specimen 4 (see Figure 10.13 and Figure 10.14), it was observed that the damage area had grown, both on the front and backside of the specimen. The damage was typically larger on the tensile face for such thin specimens.

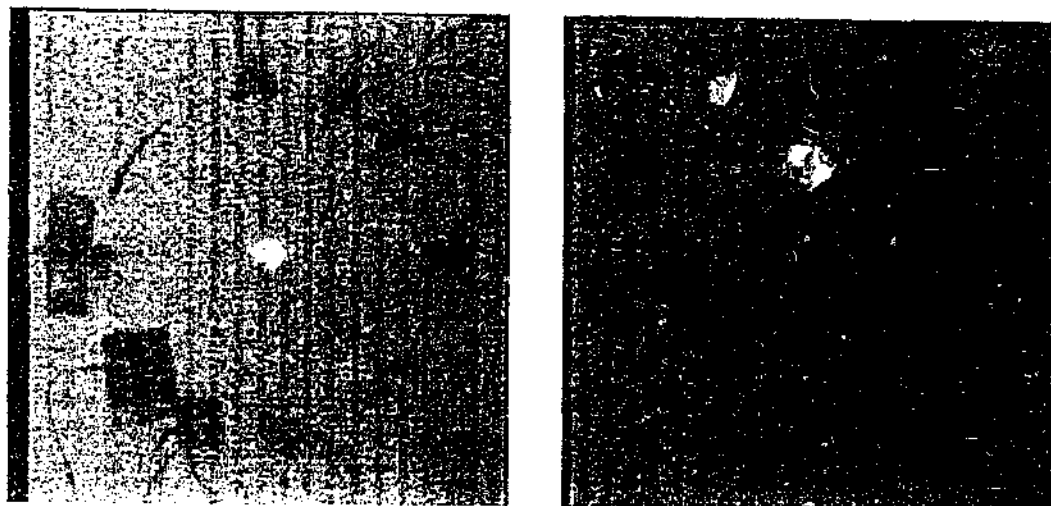


Figure 10.13 Thermal scan front face of specimen 4 before and after last impact



Figure 10.14 Thermal scan of specimen 4 (back) before and after last impact

Table 10.7 RMS values for specimen 5

Actuator	Sensor	Orientation	Impact energy	RMS
1	5	0°	2-J	0.157
			3-J	0.139
			4-J	0.0992
2	6	22.5°	2-J	0.156
			3-J	0.129
			4-J	0.0922
3	7	45°	2-J	0.183
			3-J	0.162
			4-J	0.0887
4	8	90°	2-J	0.164
			3-J	0.103
			4-J	0.0716

Specimen 5 from the ID2-series had been impacted at 2-J during the second test run. This had resulted in visible delamination damage at the back surface. The specimen was then impacted again at 4-J, resulting in full penetration of the specimen. The drop in the RMS values was larger this time where the attenuation was on average 33 %.

The damage was clearly visible on both sides of the specimen 5 as shown in Figure 10.15. This was the same as specimen 4, and the damage area was larger on the backside. Overall, the attenuation in the different directions was very similar for both specimen 4 and 5 that was being largest in the 90° direction, followed by the 22.5°, 45° and 0° direction for both specimens. The attenuation was larger for specimen 5, corresponding to the extensive damage this specimen had suffered compared to specimen 4, manifested by the full penetration of the specimen.

Figure 10.15 Thermal scan of specimen 5 after last impact (front and back)

Table 10.8 RMS values for specimen 6

Actuator	Sensor	Orientation	Impact energy	RMS
1	5	0°	2-J	0.0298
			3-J	0.0265
			4-J	0.0232
2	6	22.5°	2-J	0.0222
			3-J	0.0218
			4-J	0.0214
3	7	45°	2-J	0.2481
			3-J	0.162
			4-J	0.0759
4	8	90°	2-J	0.042
			3-J	0.0368
			4-J	0.0316

Specimen 6 from the ID2-series had been impacted at 2-J during the second test run similar to specimen 5. This had resulted in visible delamination damage at the back surface. The specimen was then impacted again at 4-J, resulting in full penetration of the specimen. The drop in the RMS values for specimen 6 of the ID2-series was much smaller than for the previous specimens, as discovered in test run 2. The attenuation resulting from the last impact was on average 13 %.

Looking at the thermal scans in Figure 10.16, the damage was clearly much less evident for this specimen compared to the previous specimens and this corresponds well with the attenuation values. The damage was here only detectable on the back; the front did not show any apparent bright spots that were related to damage. Closer examination of specimen 6 shows that the damage areas were much smaller than the previous specimens.

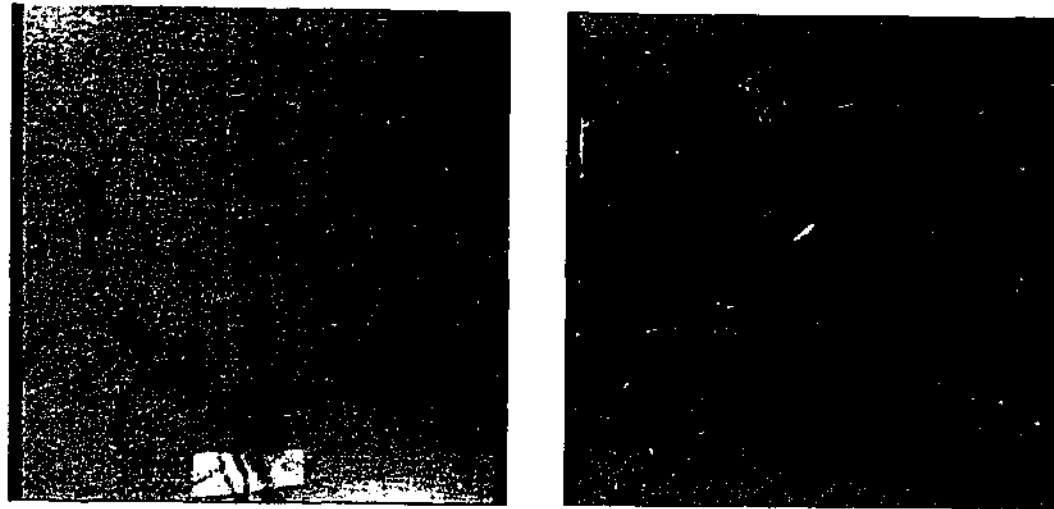


Figure 10.16 Thermal scan of specimen 6 after last impact (front and back)

Correlation between energy based indicators and attenuation of the measured response

In measuring the attenuation in the power of the propagating of the stress wave, the incremental damage development in a graphite/epoxy composite specimen resulting from impacts at different energy levels was evaluated. By using iteration it was possible to find the expected attenuation of the first response wave packet for each energy level presented in Table 10.9.

Table 10.9 Results after impact on all three specimens

Impact energy	Absorbed energy	% Energy absorbed	Attenuation (%)	Total attenuation (%)
2-J	0.5	25	19	19
3-J	1.7	57	19	34
4-J	4	100	28	52

These measurements show that a relatively small part of the impact energy was absorbed by the specimen at low impact energies, such as 2-J. Increasing the impact energy to 3-J, resulted in a relatively larger portion of the energy absorbed. At 4-J, the impactor penetrated the specimen; hence the specimen absorbed all the impact energy. It was possible to quantify the incremental damage development by looking at percentage changes of the different damage indicators as presented in Table 10.10.

Table 10.10 Results after third impact on all three specimens

change in total impact energy	change in energy absorbed (%)	change in attenuation (%)	change in impact energy (%)	change in absorbed energy (%)
0 to 2-J	128	79	50	240
2 to 3-J	75	53	33	135
3 to 4-J	75	68	100	253

In Figure 10.17 and Figure 10.18, a characteristic plateau is noted in both curves after 4-J that is a result of the full penetration of the specimen after the final impact. All the impact energy was absorbed above this value and up to our maximum test value of 6-J. It could clearly be observed from Figure 10.17 and Figure 10.18, that when the impact energy has reached the level corresponding to full penetration of the specimen approximately around 4-J, the attenuation will stabilise at a level around 55-60 %. This was expected since full penetration is the maximum damage that may be inflicted on a specimen by a single impacting object of this size. Unless the size or geometry of the impactor was altered, a further increase in impact energy would therefore not result in much further damage in the specimen. Looking at Figure 10.19, the attenuation seems to increase almost linearly with the percentage of absorbed energy.

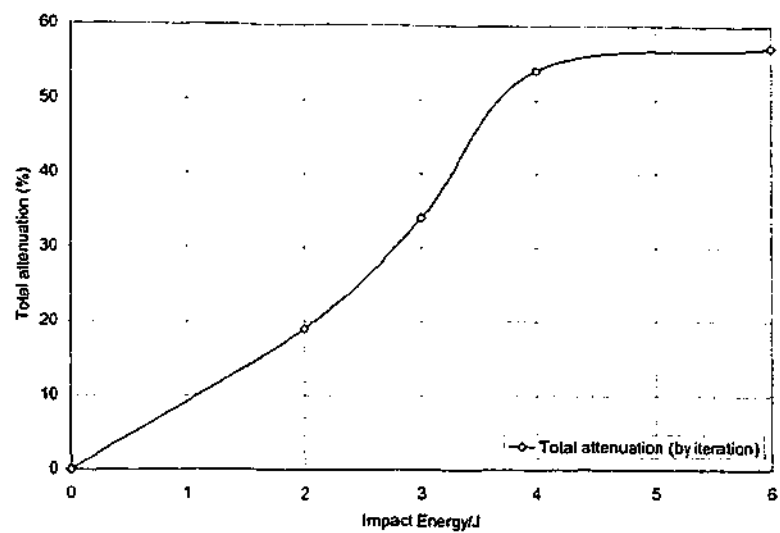


Figure 10.17 Attenuation in % as a function of impact energy (J)

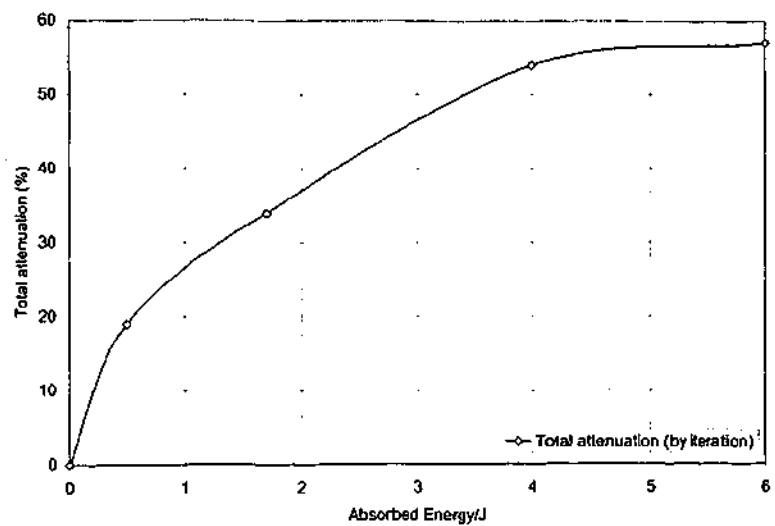


Figure 10.18 Attenuation in % as a function of absorbed energy (J)

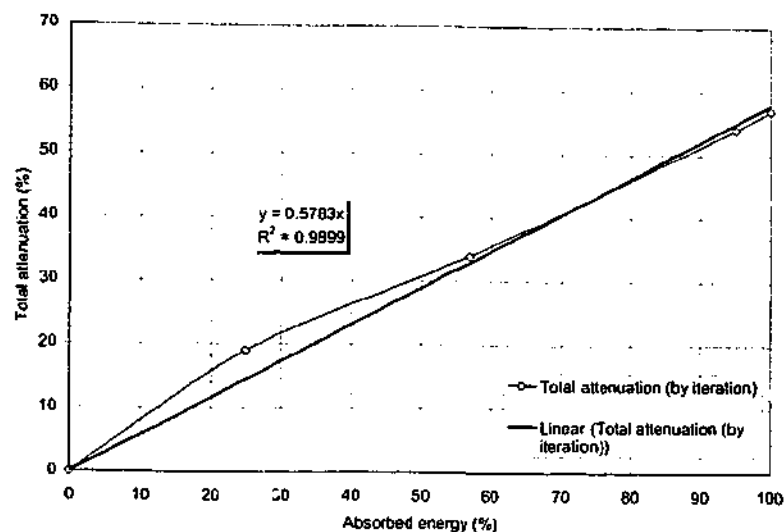


Figure 10.19 Attenuation (%) as a function of absorbed energy (%) compared to a fitted line

10.5 CONCLUSIONS

These experiments show that the point measurements provided results that were indicative of damage. The application of the stress wave method has been shown to be effective in detecting damage in a composite plate. When the attenuation of the first response wave packet was compared for the different impact energy values, a clear relationship was discovered. It was found that higher impact energy is proportionally related to a larger attenuation of the response signal.

The absorbed energy was also measured for some of the impacts. This was compared with the attenuation in order to find out if this was a better indicator of impact damage than impact energy, as some of the reviewed literature had indicated. The absorbed energy values were then divided by the corresponding impact energy values to find the actual portion of the impact energy that had been absorbed in the first impact. This represented yet another possible indicator that could be used to determine the extent of the damage induced in the laminate.

When the three indicators were compared the percentage absorbed energy seemed to show the most obvious relationship with the attenuation in response signal. The

attenuation proved to be an almost linear function of the percentage absorbed energy. This indicates that percentage absorbed energy is the best single indicator of impact damage in a graphite/epoxy laminate amongst the indicators evaluated in this project. This certainly is worth investigating further.

The specimens were scanned thermally, before and after impact, to examine whether the attenuation values gave a qualitatively good indication of the actual damage in the laminate. This definitely seemed to be the case, with high attenuation values representing extensive damage areas.

After the final impact test run, three of the specimens were placed in a tensile/compressive test rig. The specimens were pulled to failure, the maximum tensile stress values representing the residual tensile strength of the specimens. Looking at these values, it can be observed that the plate suffering full penetration damage, exhibits a considerably lower residual tensile strength than the plates containing only BVID, as expected.

CHAPTER 11

CONCLUSIONS AND RECOMMENDATIONS FOR FUTURE WORK

11.1 CONCLUSIONS

The aim of the research was to assess the viability of three methods that can be implemented as part of an *in-situ* system to monitor the structural health of bonded composite repairs on aircraft structures. This investigation of the methods also necessitated an assessment of the mechanical degradation of the PZT elements. This thesis presents the results of experimental evaluations and numerical analyses of the application of three *in-situ* methods with surface bonded piezoelectric elements for damage detection. From the results reported in this thesis, the following conclusions about each of those methods and about mechanical degradation may be drawn.

11.1.1 ELECTROMECHANICAL IMPEDANCE METHOD

The impedance method is able to accurately predict the damage condition from both the x- and y-direction and the location of the damage relative to the sensors. The measurement parameter for this impedance method is the IM-parameter, which is derived from the frequency integral. This method is dependent on the change in local

stiffness with the onset of disbonds, which leads to a decrease in IM-parameter. As the disbond approaches a PZT element, the IM-parameter decreases and as it passes the PZT element, the IM-parameter reaches an asymptote.

It has been established that a damage detectable zone exists around the PZT element. It appears that this zone is 50% of the PZT element width around the sides of the PZT element. The PZT element is able to detect the disbond when the disbond is within the damage detectable zone of the PZT element. Beyond this zone, the impedance method is not able to detect a disbond.

The dimensions of the PZT elements determine the sensitivity of the impedance method, and for optimum sensitivity, the sensor should be square or have approximately the equal length and width. In addition, the size of the PZT element has to be the same as the minimum extent of disbond to be detected.

11.1.2 TRANSFER FUNCTION METHOD

The transfer function method is able to detect damage reliably and robustly. The measurement parameter for the transfer function method is the MTF-parameter, which is derived from the frequency integral. As with the impedance method, a damage detectable zone exists whereby no changes occur in the MTF-parameter calculated by means of the transfer function method until the damage has advanced into this zone. One of the advantages of the transfer function method over the impedance method is the possibility of detecting damage between a sensor and actuator pair, which is beyond the sensitivity of a single sensor/actuator using the impedance method. This form of damage is indicated by an increase in the MTF-parameter.

An increase in MTF-parameter within the frequency range of analysis can be due to two factors, the existence of resonant frequency and the change in local stiffness. The resonant frequency is detected by both the impedance method and the transfer function method while an increase due to the change in local stiffness is only detected by the transfer function method. The increase in the MTF-parameter is a characteristic feature of the method and is attractive for the detection of disbond growth between pairs of actuator and sensor.

It has been established that the transfer function method is able to accurately determine the damage size and the relative location of the damage to the sensors. The method is highly reliant on the placement of the PZT elements within the likely disbond initiation area. When multiple sensors and actuators are used, the method is able to pinpoint the location and size of disbond of the repair patch. Another advantage of the transfer function method over the impedance method is that it enables the possible use of both PZT and PVDF elements as piezoelectric sensor and actuator pairs.

11.1.3 STRESS WAVE METHOD

The stress wave method is able to detect the extent of impact damage and disbond under a composite repair reliably. In the numerical analysis, surface mounted PZT elements appear to show promise with regard to the ability to excite surface waves for the application of the stress wave method to detect the extent of impact damage. Impact damage causes a change in local area Young's modulus as well as delamination between composite plies.

For the first case, this local area change in Young's modulus of the damaged region causes the attenuation of power transmission. When the stress wave method was applied, the power transmission decreased in its propagation between two far field sensor/actuator through the affected region. To obtain the power transmitted, the results are analysed in both the spectral and spatial domain. The severity of impact damage can be predicted from the power transmitted.

For the second case, delamination between plies causes the existence of two sets of dispersion curves. The first set of dispersion curves corresponds to the overall thickness of the structure and the second set of dispersion curves corresponds to the thickness of the delaminated ply. It appears that with the PZT element mounted on the top surface and the bottom surface unconstrained, both symmetric and asymmetric wave modes are excited.

In the experimental evaluation, the attenuation of the stress wave propagating through a thin plate of graphite/epoxy composite confirms that damage can be detected using the stress wave method. The results from the experimental evaluation show that the individual point measurements are indicative of damage. Root mean square response (RMS) of the propagating stress wave provides good prediction of the impact-damaged condition of the composite plate.

It has been established that the impact energy is directly proportional to the attenuation of the stress wave response signal. Another possible indicator to determine the extent of the damage induced in the laminate is absorbed energy. The percentage-absorbed energy seems to show promise with regard to its ability to relate the attenuation in the response signal to the damage condition. The attenuation in the response signal is a linear function of the percentage-absorbed energy. From thermally scanned specimens, it is apparent that high attenuation values represent extensive damage areas.

11.1.4 MECHANICAL DEGRADATION

Mechanical degradation of PZT occurs at strain levels above 1,850 microstrain. In the experiments the PZTs do not operate above these strain levels that lead to degradation of the sensors. In addressing mechanical degradation of piezoceramics, voltage output from the PZT is a function of the varying loads applied and the number of cycles experienced by the specimen. Voltage output decreases at the onset of degradation. It decreases proportionally with the d_{31} coupling constant, as shown in the following formula.

$$V = [d_{31}] \varepsilon$$

where V is the voltage, d_{31} the coupling constant and ε the surface strain.

The impedance method appears to be unaffected by the mechanical degradation of the PZTs perhaps because the actuation and sensing are done by a single PZT. On the other hand, the transfer function method appears to be affected by the mechanical degradation of the PZT and this may be because the actuation and sensing are done by

a pair of PZT. The change in coupling constant on each PZT is at a different rate thus making the method dependent on the voltage output from the individual PZT.

11.2 RECOMMENDATIONS FOR FUTURE WORK

The research presented in this thesis has established three viable methods that can be implemented as part of an *in-situ* system to monitor the structural health of bonded composite repairs on aircraft structures. While the characteristics of the individual methods for non-destructive evaluation have been established, opportunities for further work are numerous.

Firstly, proper formulation of mechanical degradation of PZT elements needs to be done at the threshold as it occurs. A formulation would enable the recovery of data acquired from degraded sensors and would enhance the potential of application of the PZT elements. The formulation would have to consider the number of cycles and the strain levels experienced by the PZT elements. The formulation process can be obtained by using information acquired from the impedance method and the transfer function method, since the application of the impedance method is unaffected by the degraded PZT elements while the application of the transfer function method is directly proportional to the coupling constant of the PZT elements. Any *in-situ* monitoring method requires the continuous evaluation of structural condition even at strain levels above 1,850 microstrain. Without the formulation, PZT elements can only be operated below 1,850 microstrain.

In addition, while formulating the material properties of PZT elements, the influence of temperature on the material properties of PZT should also be investigated, as it would provide an understanding of the optimum operation of the PZT elements. Temperature stability of the electrical properties is critical, as changes will affect the base-line electrical properties that can be misconstrued as damage.

Secondly, for future practical application of the impedance and transfer function method, optimisation of the sensor and actuator location needs to be done. This is

relevant, as it would determine the optimum sensor density on a component that is monitored, as well a network of sensors and actuators that would allow the visualisation of the disbond type apart from determining the perimeter of the disbond growth.

If the sensors were optimally located a viable alternative method would be provided for determining the extent of disbond growth by continuous condition monitoring. Continuous component condition monitoring from the manufacturing phase is vital in case the damage is introduced during the manufacturing phase prior to active service. Since the impedance method is dependant upon changes occurring in the underlying condition, it will not record any further changes in impedance at the individual PZT if the PZT is bonded over a damaged region, which was introduced prior to monitoring. Thus the surrounding sensors and actuators are critical, as they would function as point monitors that would allow the monitoring of the region surrounding the damaged area.

Finally, further investigation should be carried out by means of experimental evaluation to obtain information about a propagating wave in the spatial domain. This would allow comparison of results obtained by means of numerical analysis. One possible suggestion would be the use of a Laser Doppler machine to detect out-of plane vibration of a composite component during wave propagation. This Laser Doppler machine would be time stepping in space within pre-defined Cartesian coordinates. Another possibility is to use flexible interdigital PVDF transducers for the vibration detection. The PVDF sensors would be bonded on pre-defined Cartesian coordinates on the plate.

To improve the stress wave method for industrial application, the attenuation of signal should be quantified to allow the measurement of transducer pitch. An understanding of the propagation efficiency is necessary in order to determine the sensor density on the object of investigation. The signal-to-noise ratio, which is a function of the working environment, has also to be included into the decaying signal of the propagating wave. The use of PZT mounted on a probe for the detection of Lamb waves is promising. This suggestion reduces the sensor density on a particular component for *in-situ* monitoring, and thus the probe must be designed for mobility.

REFERENCES

1. Adams, R.D. and Cawley, P., (1985), *A Review of Defect Types and Non-Destructive Testing Techniques for Composites and Bonded Joints*, NDT International, Vol. 21, pp 208 – 222.
2. Alleyne, D. and Cawley, P., (1991), *A Two-Dimensional Fourier Transform Method for the Measurement of Propagating Multimode Signals*, J. Acoust. Soc. Am., Vol. 89, No. 3, pp 1159 – 1168.
3. Alleyne, D. and Cawley, P., (1992), *The Interaction of Lamb Waves with Defects*, IEEE Transactions on Ultrasonic, Ferroelectrics and Frequency Control, Vol. 39, No. 3, pp 381 – 397.
4. Alleyne, D.N. and Cawley, P., *The Practical Excitation and Measurement of Lamb Waves using Piezoelectric Transducers*. Review of Progress in Quantitative NDE 13 (1994) pp 181 – 188 edited by Thompson, D.O. and Chimenti, D.E. (Plenum, New York).
5. Arnold, W.S., Robb, M.D. and Marshall, I.H., (1995), *Failure Envelopes for Notched CSM Laminates under Biaxial Pre-stress*, Composites, Vol. 26, pp 27 – 41.
6. Auld, B.A., (1990), *Acoustic Fields and Waves in Solids*, 2nd Edition, (Krieger, Malabar, FL).
7. Badcock, R.A. and Birt E.A., (1998), *The Use of 0-3 Piezocomposite embedded Lamb Wave Sensors for Damage Detection in Advanced Fibre Composites*, 4th ESSM and 2nd MIMR Conference, Harrogate, pp 373 – 380.
8. Baker, A.A., (1997), *On the Certification of Bonded Composite Repairs to Primary Aircraft Structure*, Proceedings of ICCM-11, Gold Coast, Australia.
9. Baker, A.A., (1988), *Crack Patching: Experimental Studies, Practical Applications*, Baker, A.A. and Jones, R. (eds.), Bonded repair of aircraft structure, (Martinus Nijhoff Publishers, The Netherlands)
10. Baker, A.A., Galea, S.C. and Powlesland, I.G. Powlesland, (1998), *A Smart Patch Approach for Bonded Composite Repairs to Primary Airframe Structures*,

Proceedings of the Second Joint FAA/DOD/NASA Conference on Aging Aircraft, Williamsburg VA.

11. Baker, A.A., (1999), *Bonded Composite Repair of Fatigue-Cracked Primary Aircraft Structure*, Composite Structures, Vol. 47, pp 431 – 443.
12. Ball, D.F. and Shewring, D., (1973), *Some Problems in the Use of Lamb Waves for the Inspection of Cold-Rolled Steel Sheet Coil*, Nondestructive Testing, Vol. 6, pp 138 – 145.
13. Banks, H.T., Inman, D.J., Leo, D.J. and Wang, Y., (1996), *An Experimentally Validated Damage Detection Theory in Smart Structure*, Journal of Sound and Vibration, Vol. 191(5), pp 859 – 880.
14. Barbero, E.J. and Reddy, J.N., (1991), *Modelling of Delamination in Composite Laminates using Layerwise Plate Theory*, International Journal of Solids and Structures, Vol. 28, pp 373 – 388.
15. Bar-Cohen, Y. and Crane, R.L., (1982), *Acoustic-Backscattering Imaging of Subcritical Flaws in Composite*, Materials Evaluation, Vol. 40, pp 970 – 975.
16. Barrett, R., (1992), *Active Plate and Wing Research using EDAP Elements*, Smart Material and Structures, Vol. 1, pp 214 – 226.
17. Bartholomeusz, R., Geddes, R. and Chalkley, P., (2000), *A Compendium of Bonded Repairs Applied to the PC9/A Full Scale Fatigue Test Article During Testing*, Airframes and Engines Division Aeronautical and Maritime Research Laboratory, DSTO-TN-0324
18. Bathe, K.-J., (1982), *Finite Element Procedures in Engineering Analysis*, Prentice-Hall, New Jersey.
19. Beard, S. and Chang, F.K., (1997), *Active Damage Detection in Filament Wound Composite Tubes Using Built-In Sensors and Actuators*, Journal of Intelligent Material Systems and Structures, Vol. 8, pp 891 – 897.
20. Bennett, D.C., (1999), *Stress Corrosion Cracking of 316L Oxygen Reactor Pressure Vessels*, Pulp & Paper Canada, Vol. 100, No. 6, pp 39 – 42.
21. Berman, J., Quattrone, R., Averbuch, A., Lalande, F., Cudney, H., Raju, V. and Cohen, G.L., (1999), *Piezoelectric Patch Sensors for Structural Integrity Monitoring of Composite-Upgraded Masonry and Concrete Structures*, US Army Corps of Engineers, Construction Engineering Research Laboratory, CERL Technical Report 99/72.

22. Bond, L.J., Punjani, M. and Saffari, N., (1984), *Review of Some Recent Advances in Quantitative Ultrasonic NDT*, IEEE Proc., Vol. 131, Pt. A, No. 4, pp. 265 – 274.
23. Bork, U. and Challis, R.E., (1995), *Non-Destructive Evaluation of the Adhesive Fillet Size in a T-Peel Joint using Ultrasonic Lamb Waves and a Linear Network for Data Discrimination*, Meas. Sci. Technol., Vol. 6., pp
24. Boller, C. and Dilger, R., (1992), *In flight aircraft structure health monitoring based on smart structures technology*, AGARD Conference Proceedings 531 Smart structures for aircraft and spacecraft.
25. Bruch, J.C. Jr., Sloss, J.M., Adali, S. and Sadek, I.S., (2000), *Optimal Piezo-actuator Locations/Lengths and Applied Voltage for Shape Control of Beams*, Smart Mater. Struct., Vol. 9(2), pp 205 – 211.
26. Butcher, B.R., (1979), *Impact Resistance of Unidirectional CFRP under Tensile Stress*, Fibre Science and Technology, Vol. 12, pp 295 – 362.
27. Butts, J. and Shukla, A., (1991), *The Impact Performance of Laminated Composite Materials under Biaxial Compressive Loading*, Proceedings of the SEM Spring Conference on Experimental Mechanics, Milwaukee, Wisconsin, pp 647 – 654.
28. Cantwell, W.J. and Morton, J., (1992), *The Significance of Damage and Defects and their Detection in Composite Materials: A Review*, Journal of Strain Analysis, Vol. 57, pp 29 – 42.
29. Castanien, K.E. and Liang, C., (1996), *Application of Active Structural Health Monitoring Technique to Aircraft Fuselage Structures*, Proceedings of SPIE Symposium on Smart Structures and Materials, Vol. 2721, pp 38 – 49.
30. Cawley, P., (1984), *The Impedance Method of Non-Destructive Inspection*, Journal of NDT International, Vol. 17, pp 59 – 65.
31. Cawley, P., Woolfrey, A.M. and Adams, R.D., (1985), *Natural Frequency Measurements for Production Quality Control of Fibre Composites*, Composites, Vol. 16, pp 23 – 27.
32. Cawley, P., (1990), *Low Frequency NDT Techniques for the Detection of Disbonds and Delaminations*, British Journal of NDT, Vol. 32, No. 9, pp 454 – 460.

33. Ceravolo, R. and Stefano, A.D., (1995), *Damage Location in Structure through a Connectivistic use of FEM Modal Analyses*, The International Journal of Analytical and Experimental Modal Analysis, Vol. 10, pp 176 – 177.
34. Chalkley, P. and Geddes, R., (1998), *Service History of the F-111 Wing Pivot Fitting Upper Surface Boron/Epoxy Doublers*, Airframes and Engines Division Aeronautical and Maritime Research Laboratory, DSTO-TN-0168
35. Chaudry, Z., Lalande, F., Ganino, A., Rogers, C. and Chung, J., (1995), *Monitoring the Integrity of Composite Patch Structural Repair via Piezoelectric Actuators/Sensors*, AIAA/ASME/ASCE/AHS/ASC 36th SDM Conference, Vol. 4, New Orleans, LA, pp 2243 – 2248.
36. Cheng, J.-C. and Berthelot, Y.H., (1996), *Theory of Laser-Generated Transient Lamb Waves in Orthotropic Plates*, J. Phys. D: Appl. Phys., Vol. 29, pp 1857 – 1867.
37. Chimenti, D.E. and Martin, R.W., (1991), *Nondestructive Evaluation of Composite Laminates by Leaky Lamb Waves*, Ultrasonics, Vol. 29, pp 13 – 21.
38. Chiu, W.K., Koh, Y.L., Galea, S.C. and Rajic, N., (2000), *Smart Structure Application in Bonded Repairs*, Composite Structures, Vol. 50(4), pp. 433 – 444.
39. Chung, J.H., (1991), *Composite Repairs of Fatigue Damaged Aluminium Panels*, Proceedings, International Conference on Aircraft Damage Assessment and Repair, Melbourne, Australia, pp 134 – 139.
40. Chung, J.H., (1993), *Cost Effective Aircraft Repair: Composite Repair of Aircraft Structure*, Proceedings, Defence Manufacturing Conference, Vol. 2, San Francisco, CA, pp 551 – 574.
41. Clark, R.L. and Fuller, C.R., (1992), *Experiments on Active Control of Structurally Radiated Sound using Multiple Piezoelectric Actuators*, J. Acoust. Soc. Am., Vol. 91, pp 3313 – 3320.
42. Cohen, J. and Awerbuch, J., (1988), *Monitoring Delamination Progression in Composites through Acoustic Emission during Fatigue Loading*, Proc. of the 4th Japan/United States Conference on Composite Materials, pp 1035 – 1046.
43. Cowley, K.D. and Beaumont, P.W., (1997), *Modelling Problems of Damage at Notches and the Fracture Stress of Carbon-Fibre/Polymer Composites: Matrix, Temperature and Residual Stress Effects*, Composite Science and Technology, Vol. 57, pp 1309 – 1329.

44. Crawley, E.F. and Anderson, E.H., (1990), *Detailed Model of Piezoceramic Actuation of Beams*, Journal of Intelligent Material System and Structures, Vol. 1, pp 4 – 25.
45. Crawley, E.F., Lazarus, K.B., and Warkentin, D.J., (1989), *Embedded Actuation and Processing in Intelligent Material*, ARO/AHS/RPI 2nd International Workshop on Composite Materials and Structures for Rotorcraft, Troy, N.Y.
46. Culshaw, B., 1996, *Smart Structures and Materials*, Boston: Artech House.
47. Dalton, R.P., Cawley, P. and Lowe, M.J.S., (2001), *The Potential of Guided Waves for Monitoring Large Area of Metallic Aircraft Fuselage Structure*, Journal of Nondestructive Evaluation, Vol. 20(1) pp. 29 – 46.
48. Debling, S.W., Farrar, C.R., Prime, M.B., and Shevitz, D.W., (1995), *Damage Identification and Health Monitoring of Structural and Mechanical Systems from Changes in their Vibration Characteristics: Literature Review*, Report LA-13070-MS, Los Alamos, NM.
49. Dokun, O.D., Jacobs, L.J. and Haj-Ali, R.M., (2000), *Ultrasonic Monitoring of Material Degradation in FRP Composites*, Journal of Engineering Mechanics, pp 704 – 710.
50. Egusa, S. and Iwasawa, N., (1996), *Piezoelectric Paints as One Approach to Smart Structural Materials with Health Monitoring Capabilities*, Smart Materials and Structures, Vol. 7, pp 438 – 445.
51. Eyraud, L., Audigier, D., Lebrun, L., Guiffard, B. and Guyomar, D., (1998), *New PZT Formulation for Actuators*, IEEE, pp 281 – 284.
52. Galea, S.C., Chiu, W.K. and Paul, J.J., (1993), *Use of Piezoelectric Films in Detecting and Monitoring Damage in Composites*, Journal of Intelligent Material Systems and Structures, Vol. 4, pp 330 – 336.
53. Galea, S.C., Powlesland, I.G., Moss, S.D., Konak, S., van der Velden, B., Stade, B. and Baker, A.A., (2001), *Development of Structural Health Monitoring Systems for Composite Bonded Repairs on Aircraft Structures*, Proceedings of SPIE 8th Annual International Symposium on Smart Structures and Materials: Smart Structures and Integrated Systems Conference, Newport Beach, CA, USA, Paper 4327-33.
54. Gandhi, M.V. and Thompson, B.S., (1992), *Smart Materials and Structures*, London: Chapman & Hall.

55. Giurgiutiu, V. and Rogers, C.A., (1998), *Recent Advancements in the Electro-Mechanical (E/M) Impedance Method for Structural Health Monitoring and NDE*, Smart Structures and Materials, Smart Structures and Integrated Systems, SPIE 3329, pp 536 -- 547.
56. Guo, N. and Cawley, P., (1993), *The Interaction of Lamb Waves with Delaminations in Composite Laminates*, J Acoust Soc Am, Vol. 94, pp 2240 -- 2246.
57. Guo, N. and Cawley, P., (1994), *Lamb Wave Reflection for the Quick Non-Destructive Evaluation of Large Composite Laminates*, Materials Evaluation, Vol. 52, No. 3, pp 404 -- 411.
58. Guyott, C.C.H., Cawley, P. and Adams, R.D., (1986), *The Non-Destructive Testing of Adhesively Bonded Structure: A Review*, J. Adhesion, Vol. 20, No. 2, pp. 129 -- 159.
59. Hanagud, S. and Luo, H., (1994), *Modal Analysis of a Delaminated Beam*, SEM Conference on Experimental Mechanics, Baltimore, MD.
60. Hart-Smith, L.J., (1974), *Advances in the Analysis and Design of Adhesive-Bonded Joints in Composite Aerospace Structures*, SAMPE Process Engineering Series, Vol. 19, SAMPE, Azusa, pp 722 -- 737.
61. Hart-Smith, L.J., (1978), *Adhesive Bond Stresses and Strains at Discontinuities and Cracks in Bonded Structures*, Transactions of the ASME, Journal of Engineering Materials and Technology, Vol. 100, pp 15 -- 24.
62. Hart-Smith, L.J., (1986), *Adhesively Bonded Joints in Fibrous Composite Structures*, Douglas Aircraft Paper 7740; Proceedings of International Symposium on Joining and Repair of Fibre-Reinforced Plastics, Imperial College, London.
63. Hart-Smith, L.J., (1991), *An Engineers Viewpoint on Design and Analysis of Aircraft Structural Joints*, Douglas Paper MDC91K0067; Proceedings of International Conference on Aircraft Damage Assessment and Repair, Institute of Engineers Australia, Melbourne, Australia.
64. Huber, J.E., Fleck, N.A. and Ashby, M.F., (1997), *The Selection of Mechanical Actuators Based on Performance Indices*, Proc. R. Soc. Am., Vol. 453, pp. 2185 -- 2205.

65. Islam A.S. and Craig, K.C., (1994), *Damage Detection in Composite Structures using Piezoelectric Materials*, Smart Materials and Structures, Vol. 3, pp. 318 – 326.
66. Isometsa, J. and Stig-Goran, S., (1999), *A Continuum Damage Mechanics Model for Fibre Reinforced Composites*, International Journal of Damage Mechanics, Vol. 8, pp 2 –17.
67. Jones, T.S., Polansky, D. and Berger, H., *Radiation Inspection Methods for Composites*, NDT International, 1988, Vol. 4, pp 227 – 232.
68. Kelkar, A.D., Sankar, J. and Rajeev, K., (1998), *Analysis of Tensile Preloaded Composites Subjected to Low Velocity Impact Load*, AIAA Journal-98-1944, pp 1978 – 1987.
69. Kinsler, L.E., Frey, A.R., Coppens, A.B., Sanders, J.V. (1982) *Fundamentals of Acoustics*, (John Wiley & Sons, New York).
70. Koh, Y.L., Chiu, W.K., Rajic, N. and Galea, S.C., (2002), *The Application of Piezoceramic Elements to the Detection of Disbond Growth in a Bonded Composite Repair Patch*, 3rd Australasian Congress on Applied Mechanics, Sydney, Australia, 20 - 22 February 2002.
71. Kuang, K.S.C., Kenny, R., Whelan, M.P., Cantwell, W.J. and Chalker, P.R., (2001), *Embedded Fibre Bragg Grating Sensors in Advanced Composite Materials*, Composites Science and Technology, Vol. 61, pp 1379 – 1387.
72. Ladeveze, P., (1995), *A Damage Computational Approach for Composites: Basic Aspects and Micro Mechanical Relations*, Computational Mechanics, Vol. 17, pp 142 – 150.
73. Lamb, H., (1917), *On Waves in an Elastic Plate*, Proc. R. Soc. London, Ser. A, Vol. 93, pp 114 – 128.
74. Lange, Y.V. and Moskovenko, I.B., (1978), Soviet J. Nondestr. Test. (English Trans), Vol. 14, pp 788 – 797.
75. Lichtenwalner, P.F., Dunne J.P., Becker R.S. and Baumann E.W., (1997), *Active Damage Interrogation System for Structural Health Monitoring*, SPIE, Vol. 3044, pp186 - 194.
76. Liu, Xiaozhou, Ye, Shigong, Gong, Xiufen, Zhang, Weiya and Lu, Rongrong, (1999), *Study of Polymer Ultrasonic Transducer and Complex Ultrasonic Transducer with PZT/PVDF Multilayer Structure*, Acustica, Vol. 85 pp 420 – 426.

77. Lowe, M.J.S., Challis, R.E. and Chan, C.W., (2000), *The Transmission of Lamb Waves across Adhesively Bonded Lap Joints*, J Acoust Soc Am, Vol. 107(3), pp 1333 – 1345.
78. Mal, A.K. and Bar-Cohen, Y., (1991), *Characterisation of Composite Laminates using Combined LLW and PBS Methods*, Rev Progress in Quantitative NDE, Vol. 10B, pp 1555 - 1560.
79. Mansfield, T.L., (1975), *Lamb Wave Inspection of Aluminium Sheet*, Materials Evaluation, Vol. 33, pp 96 - 100.
80. Mitrovic, M., Carman, G.P., Hickman, G.A. and Bar-Cohen, Y., (1995), *Influence of Damage on the Vibration Response of Composite Laminates*, ASME International Mechanical Engineering Congress & Exposition.
81. Monkhouse, R.S.C., Wilcox, P.D. and Cawley, W.P., (1997), *Flexible Interdigital PVDF Transducers for the Generation of Lamb Waves in Structures*, Ultrasonics, Vol. 35, pp 489 – 498.
82. Morey, W.W., Meltz, G. and Glenn, W.H., (1989), *Fibre Optic Bragg Grating Sensors*, SPIE, Vol. 1169, pp 98 – 107.
83. Moss, S.D., Galea, S.C., Powlesland, I.G., Konak, M. and Baker, A.A., (2000) *In-situ Health Monitoring of a Bonded Composite Patch using the Strain Ratio Technique*, Proceedings of the SPIE 2000 Symposium on Smart Materials and MEMS, Smart Structures and Devices Conference, Melbourne, Australia. Paper 4235-41.
84. Nagesh Babu, G.L. and Hanagud, S., (1990), *Delaminations in Smart Composite Structures: A Parametric Study on Vibrations*, Proceedings of the 31st AIAA/ASME/ASCE/AHS/ASC SDM Conference, Part 4, pp 2417 - 2426.
85. Nayfeh, A.H. and Chimenti, D.E., (1988), *Propagation of Guided Waves in Fluid Coupled Plates of Fibre Reinforced Composites*, Journal of Acoustic Society America, Vol. 83, pp 1736 - 1743.
86. Newnham, R.E. and Ruschau, G.R., (1991), *Smart electroceramics*, Journal of American Ceramic Society, Vol. 74, pp 463 - 480.
87. Newland, D.E. *Transmission of Random Vibration. An Introduction to Random Vibrations, Spectral & Wavelet Analysis* (Prentice Hall, Singapore, 1993).

88. O'Donnell, M., Jaynes, E.T. and Miller, J.G., (1978), *General Relationships between Ultrasonic Attenuation and Dispersion*, Journal Acoustic Society of America, Vol. 63, pp 1935 - 1937.
89. Pardo de Vera, C. and Guemes, J.A., (1998), *Embedded Self-Sensing Piezoelectrics for Damage Detection*, J Int Mater Syst Struct, Vol. 9, pp. 876 - 882.
90. Pell, R., (1996), *Examination of an F111 Boron Doubler*, DSTO Publication DSTO-DDP-0167.
91. Penn, L.S., Jump, J.R., Greenfield, M.J., Blandford, G.E., (1999), *Use of the Free Vibration Spectrum to Detect Delamination in Thick Composites*, Journal of Composite Materials, Vol. 33 pp 54 - 72.
92. Pierce, S.G., Staszewsik, W.J., Gachagan, A., James, I.R., Philip, W.R., Worden, K., Culshaw, B., McNab, A., Tomlinson, G.R., Hayward, G. (1997), *Ultrasonic Condition Monitoring of Composite Structures using a Low Profile Acoustic Source and an Embedded Optical Fibre Sensor*, SPIE Vol. 3041, pp 437 - 448.
93. Pohl, J., Herold, S., Mook, G. and Michel, F., (2001), *Damage Detection in Smart CFRP Composites using Impedance Spectroscopy*, Smart Material and Structure, Vol. 10, pp 834 - 842.
94. Rogers, C. and Lalande, F., (1996), *Solid-State Active Sensing for In-situ Health Monitoring*, Society for Machinery Failure Prevention Technology Showcase, pp. 1 - 7.
95. Rokhlin, S.I. (1991), *Lamb Wave Interaction with Lap-Shear Adhesive Joints: Theory and Experiment*, J Acoust Soc Am, Vol. 89, pp 2758 - 2765.
96. Rokhlin, S.I. and Bendec, F., *Coupling of Lamb Waves with the Aperture between Two Elastic Sheets*. J Acoust Soc Am 73(1) (1983) pp 55 - 60.
97. Rytter, A. and Kinkegaard, J. (1994), *Vibrational-Based Inspection of a Steel Mast*, Proceedings of the 12th International Modal Analysis Conference, Hawaii, pp 1602 - 1608.
98. Salawu, O.S., (1997), *Detection of Structural Damage Through Changes in Frequency: A Review*, Engineering Structures, Vol. 19, pp 718 - 723.
99. Sanders, D.R., Kim, Y.I., Stubbs, N., (1992), *Non-destructive Evaluation of Damage in Composite Structures using Modal Parameters*, Experimental Mechanics, Vol. 32, pp 240 - 251.

100. Sandhu, R.S., (1985), *Impact Damage of Composites Laminates Preloaded in Tension*, AFWAL-TM-85-254-FIBC.
101. Sato, H., (1993), *Free Vibration of Beams with Abrupt Changes of Cross-Section*, Journal of Sound and Vibration, Vol. 89, pp 59 – 64.
102. Schulz, M., Pai, P.F., Smith, E.C. and Tu, P.K.C., (1998), *Adaptive Real-Time Structural Health Monitoring*, AIAA Journal.
103. Sessler, G.M., (1982), *Piezoelectricity in Polyvinylidene fluoride*, Journal of Acoustic Society America, Vol. 70, pp 1596 - 1607.
104. Shen, M.H.H. and Grady, J.E., (1992), *Free Vibration of Delaminated Beams*, AIAA Journal, Vol.30, pp 1361 - 1370.
105. Sivanesan, P., Sirkis, J., Venkat, V., Shi Y.C., Reddy, C.J. and Sankaran, S., (1999), *Simultaneous Measurement of Temperature and Strain using a Single Bragg Grating*, SPIE, Vol. 3670, pp 92 – 103.
106. Speake, J.H., Arridge, R.G.C., and Curtis, G.J., (1974), *Measurement of the cure of resins by ultrasonic techniques*, J Phys D: Appl Phys, Vol. 7, pp 412 - 424.
107. Spillman, W.B., Sirkis, J.S. and Gardiner, P.T., (1996), *Smart Materials and Structures: What are they?*, Smart Materials and Structures, Vol. 5, pp. 247 – 254.
108. Srivastava, V.K. and Prakash, R., (1987), *Fatigue Life Prediction of Glass Fibre-Reinforced Plastics using the Acousto-Ultrasonic Technique*, International Journal of Fatigue, Vol. 9, pp 175 – 178.
109. Stone, D.E.W. and Clark, B., (1987), *Non-Destructive Evaluation of Composite Structures - An Overview*, Proc. of the ICCM6, pp 128 - 159.
110. Summerscales, J., (1987), *Non-Destructive Testing of Fibre-Reinforced Plastics*, Composites London, Elsevier Applied Science
111. Tappet, P.M., Snyder, T.D. and Robertshaw, H.H., (1995), *Attacking the Damage Identification Problem*, Proceedings of SPIE - The International Society for Optical Engineering Smart Structures and Materials: Smart Sensing, Processing and Instrumentation, Vol. 2443, pp. 286 – 294.
112. Temple, J.A.G., (1988), *Modelling the Propagation and Scattering of Elastic Waves in Inhomogeneous Anisotropic Media*, J. Phys. D: Appl. Phys., Vol. 21, pp. 857 – 874.
113. Timoshenko, S., Young, D.H. and Weaver, Jr. W., (1974), *Vibration Problems in Engineering*, 4th Edition, John Wiley & Sons.

114. Todd, C.P.D. and Challis, R.E., (1999), *Quantitative Classification of Adhesive Bondline Dimensions using Lamb Waves and Artificial Neural Networks*, IEEE Trans. Ultrason. Ferroelectr. Freq. Control, Vol. 46, pp. 167 – 181.
115. Vary, A. and Bowles, K.J., (1977), *Ultrasonic Evaluation of the Strength of Unidirectional Graphite-Polyimide Composites*, NASA TM X-73646
116. Viktorov, I.A., (1967), *Rayleigh and Lamb Waves Physical Theory and Application*, Plenum Press.
117. Worlton, D.C., (1957), *Ultrasonic Testing with Lamb Waves*, Non-Destructive Testing, Vol. 15, pp 218 – 222.
118. Yin, L., Wang, X. and Shen, Y., (1996), *Damage-Monitoring in Composite Laminates by Piezoelectric Films*, Computers & Structures, Vol. 59, No. 4, pp 623 – 630.
119. Zou, Y., Tong, L. and Simon, G.P., (2000), *Vibration-Based Model-Dependent Damage (Delamination) Identification and Health Monitoring For Composite Structures – A Review*, Journal of Sound and Vibration, Vol. 230, No. 2, pp 357 – 378.

LIST OF PUBLICATIONS

1. Koh, Y.L., Rajic, N., Chiu, W.K. and Galea, S.C., (1999), Smart Structure for Composite Repair, *Composite Structures*, 47(1), pp. 745 – 752.
2. Chiu, W.K., Koh, Y.L., Galea, S.C. and Rajic, N., (2000), Smart Structure Application in Bonded Repairs, *Composite Structures*, 50(4), pp. 433 – 444.
3. Koh, Y.L., Chiu, W.K., Marshall, I.H., Rajic, N. and Galea, S.C., (2001), Detection of Disbonding in a Repair Patch by Means of an Array of Lead Zirconate Titanate and Polyvinylidene Fluoride Sensors and Actuators, *Smart Materials and Structures*, Vol. 10.
4. Galea, S.C., Rajic, N., Powlesland, I.G., Moss, S., Konak, M.J., Van der Velden, S., Baker, A.A., Wilson, A.R., Burke, S.K., McKenzie, I., Koh, Y.L. and Chiu, W.K., (2001), HUMS 2001 – DSTO International Conference on Health and Monitoring Usage Monitoring, Melbourne, 19 – 20 February 2001.
5. Galea, S.C., Rajic, N., Moss, S., McKenzie, I., Koh, Y.L. and Chiu, W.K., (2001), In-Situ Structural Health Monitoring of Composite Bonded Repair, 3rd International Workshop on Structural Health Monitoring
6. Koh, Y.L., Chiu, W.K. and Rajic, N., (2001), Effects of Local Stiffness Changes and Delamination on Lamb Wave Transmission using Surface-Mounted Piezoelectric Transducers, *Composite Structures*.
7. Koh, Y.L., Chiu, W.K., Rajic, N. and Galea, S.C., (2002), The Application of Piezoceramic Elements to the Detection of Disbond Growth in a Bonded Composite Repair Patch, ACAM 2002, Sydney, Australia. February 2002.

8. Koh, Y.L. and Chiu, W.K., (2002), Numerical Study of Detection of Disbond Growth under Composite Repair Patch, Smart Materials and Structure.
9. Wibowo, N, Chiu, W.K. and Koh, Y.L., (2002), Crack monitoring of a structural component, ACAM 2002, Sydney, Australia. February 2002.